

Université du Québec
Institut National de la Recherche Scientifique
Centre Énergie Matériaux Télécommunications

**Ferroelectric Tunnel Junctions:
Models for Memory and Neuromorphic Applications**

Par

Andreas Dörfler

Thèse présentée pour l'obtention du grade de
Philosophiae doctor (Ph.D.)
en sciences de l'énergie et des matériaux

Jury d'évaluation

Président du jury et
examinateur interne

Professeur José Azaña
Institut National de la Recherche Scientifique
Centre Énergie Matériaux Télécommunications

Examinateur externe

Professeur Ashish Garg
Indian Institute of Technology Kanpur
Department of Materials Science & Engineering

Examinateur externe

Professeur Alfred Kersch
Munich University of Applied Sciences
Department of Applied Sciences and Mechatronics

Directeur de recherche

Professeur Andreas Ruediger
Institut National de la Recherche Scientifique
Centre Énergie Matériaux Télécommunications

Codirecteur de recherche

Professeur Ulrich Wagner
Munich University of Applied Sciences
Department of Applied Sciences and Mechatronics

Acknowledgments

Firstly, I would like to thank Prof. Dr. Ruediger, who has been an outstanding mentor during my research. Many thanks also go to Prof. Dr. Feiertag and Prof. Dr. Wagner, who both diligently supported my research, especially in the initial phase of the project, and initiated the collaboration with Prof. Dr. Ruediger.

I especially appreciate the close collaboration with Dr. Kolhatkar, the invaluable scientific discussions we had as well as her inexhaustible positive attitude. Special thanks go to Mr. Gonzalez and Dr. Katoch for their scientific contributions, as well as Ms. Dekermenjian and Dr. Youssef for their assistance with the french translation. The Nanophotonics research team at the INRS and the Micromechanics Laboratory staff at MUAS provided an enjoyable work environment.

Last, but not least I would like to thank my friends and family for their encouragement and support during my research.

Résumé

Les ferroélectriques sont des matériaux qui manifestent une polarisation spontanée et inversible. Les plus célèbres représentants de ces matériaux sont les cristaux ioniques ayant une structure de pérovskite telle que le titanate de baryum et le titanate de zirconate de plomb, qui sont utilisés dans des capteurs et actionneurs [1–3], dans des applications électro-optiques [4], et dans des applications spécialisées de technologie de mémoire [5, 6]. Un de ces dispositifs de mémoire émergents est de type ferroélectrique à jonction de tunnel. Ce dispositif utilise l'état ferroélectrique pour moduler des courants tunnel entre les deux électrodes, constituant un dispositif de mémoire résistive non volatile et compact. Malgré le fait que cela a été prédit de façon théorique par T. Esaki en 1971, d'un point de vue pratique, le fait qu'un film ferroélectrique doive avoir une épaisseur nanométrique a fait en sorte que ce n'est aux débuts des années 2000 que cela a été démontré expérimentalement. Un des plus grands défis reliés aux pérovskites ferroélectriques consiste leur intégration dans les dispositifs semiconducteurs, particulièrement dans des applications telles que des dispositifs de mémoire, des enjeux de compatibilité avec les procédés de fabrication des semiconducteurs et des restrictions reliées à leur extensibilité à de plus grandes échelles ont entravé l'application industrielle étendue des ferroélectriques.

Un nouveau matériau était nécessaire pour atténuer ces obstacles. Une alternative prometteuse est devenue disponible avec la découverte d'une phase ferroélectrique dans le HfO₂ dopé de silicium en 2011 par T. Böscke [7]. Cela a été une surprise puisque le matériau avait fréquemment été utilisé comme diélectrique dans l'industrie des semiconducteurs. Cependant, une multitude de conditions de traitement et de transformation devaient être satisfaites pour obtenir une phase ferroélectrique.

Tandis que la plupart des ferroélectriques perdent leurs caractéristiques à l'échelle nanométrique, des dimensions nanométriques sont nécessaires pour le HfO₂ dopé pour la formation d'une phase ferroélectrique suffisante, ce qui fait de ce matériau un candidat idéal pour la construction de minces couches de cellules de mémoire, notamment le type ferroélectrique à jonction de tunnel. Cependant, malgré les progrès significatifs, la compréhension actuelle de cette structure métastable et polycristalline demeure incomplète.

Ce travail se penche sur certaines des exigences de conception théoriques et pratiques de la jonction de tunnel ferroélectrique à base de Hf_{0.5}Zr_{0.5}O₂. Nous évaluons ce dispositif de mémoire à deux terminaux à la lumière de ce nouveau matériau dans le but de comprendre et d'optimiser ses fonctionnalités et ses défauts en fonction de l'application d'une mémoire ou d'une configuration de réseau neutre. En fonction de sa polarisation, le film ferroélectrique induit des charges image dans les électrodes ce qui module la hauteur effective de la barrière de potentiel. En utilisant des matériaux avec des propriétés d'écrantage différentes, la barrière de potentiel effective est abaissée ou élevée, selon la polarisation. Pour fixer le dispositif à un certain état résistif, une tension est appliquée au-dessus du seuil du champ coercitif. L'état est lu à l'aide des voltages sous-coercitifs.

Malgré ses excellentes propriétés prédites par la théorie, notamment une longue rétention, un affichage non-destructif, une adaptabilité excellente à grande échelle, une compatibilité aux CMOS et des vitesses d'écriture élevées prédites par la théorie, il existe plusieurs défis tels que la dégradation des électrodes, l'induction de sites vacants et des variations dans la performance électrique. Le dernier point est partiellement inhérent aux films polycristallins dans lesquels la hauteur des structures approche la taille du grain. À cause de sa capacité à commuter graduellement, le dispositif peut aussi être utilisé comme synapse pour le calcul neuromorphique. Dans ce contexte, nous étudions et quantifions la réponse d'apprentissage de la jonction tunnel ferroélectrique (FTJ).

Mots-clés jonction tunnel ferroélectrique, mémoire résistive, couche mince de hafnia, changement de valence, modélisation numérique, synapse artificielle.

Abstract

Ferroelectrics are materials that exhibit spontaneous, switchable polarization. Their most prominent representatives are ionic crystals with perovskite structure such as barium titanate and lead zirconate titanate, which are used in sensors and actuators [1–3], electrooptical applications [4], as well as in specialized applications of memory technology [5, 6]. One of these emerging memory devices is the ferroelectric tunnel junction type. This device uses the ferroelectric state to modulate tunneling currents between two electrodes, constituting a compact, non-volatile resistive memory device. Despite being theoretically predicted by T. Esaki in 1971, the practical requirement of a ferroelectric film with a nanometer thickness meant that it was not experimentally demonstrated until the early 2000s. One of the biggest challenges of the ferroelectric perovskites is their integration into semiconductor devices. Especially in applications such as memory devices, compatibility issues with the semiconductor manufacturing process, as well as scalability limitations impeded ferroelectrics from widespread industrial application.

A new material was required to alleviate these roadblocks. A promising alternative became available with T. Böscke’s discovery of a ferroelectric phase in Si-doped HfO₂ in 2011 [7]. This came as a surprise, since the material had frequently been used as a dielectric in the semiconductor industry. However, a number of processing conditions must be met in order to obtain the ferroelectric phase. While most ferroelectrics lose their characteristics at the nanoscale, scales in the nanometer region are required for doped HfO₂ to build up significant amounts of ferroelectric phase, which makes it a prime candidate to construct thin film memory cells, including the ferroelectric tunnel junction type. However, despite significant progress, the current understanding of this metastable, polycrystalline structure is still incomplete.

This work investigates some of the theoretical and practical design requirements of the Hf_{0.5}Zr_{0.5}O₂

based ferroelectric tunnel junction. We evaluate this two-terminal memory device in light of the new material in order to understand and optimize its features and shortcomings with respect to applications in a memory or neural network configuration. Depending on its polarization, the ferroelectric film induces mirror charges within the electrodes which modulate the effective height of the potential barrier. Using materials with different shielding properties, the effective potential barrier is lowered or raised, depending on the polarization. To set the device to a certain resistive state, a voltage above the coercive field threshold is applied. The state is then read using sub-coercive voltages.

Despite its theoretically excellent properties, such as long retention, non-destructive readout, excellent scalability, CMOS compatibility and high write speeds, there exist a number of challenges in the form of electrode degradation, induced vacancies, and variations in electrical performance. The last point is partially inherent to polycrystalline films where structure heights approach the grain size. Due to its ability to switch gradually, the device can also be used as a synapse for neuromorphic computing. In this context, we investigate and quantify the learning response of the FTJ.

Keywords Ferroelectric Tunnel Junction, Resistive Memory, Thin Film Hafnia, Valency Switching, Numerical Modeling, Artificial Synapse

Contents

Acknowledgments	ii
Résumé	iii
Abstract	v
Contents	vii
List of figures	x
List of Tables	xii
Acronyms	xiii
1 Introduction	1
1.1 The Search for Alternative Memories	1
1.2 FTJ Operation	3
1.3 Ferroelectrics	4
1.4 Electrical Properties of Metallic Oxide Insulators	6
1.5 Thesis Objectives	7
2 Fundamentals	8
2.1 Ferroelectricity	8
2.1.1 Ferroelectric Materials	9
2.1.2 Kay-Dunn Law	10
2.2 State of the Art	11
2.2.1 Conduction in Ferroelectrics	13
2.2.2 The Ferroelectric Tunnel Junction	15
2.2.3 Ionic resistive switching	16
2.3 Ferroelectric Crystals	16
2.3.1 Ferroelectric Domain Walls	17
2.3.2 The Ferroelectric Phase in Doped HfO ₂	18
2.4 Tunneling Mechanisms	19
2.4.1 The Tsu-Esaki Model	19
2.4.2 Supply Function Modeling	20
2.4.3 The Energy Barrier	21
2.5 Ferroelectric Switching Models	22
2.5.1 Landau-Khalatnikov Double Potential Well	23
2.5.2 Kolmogorov-Avrami-Ishibashi (KAI) Model	26

2.5.3	Nucleation Limited Switching (NLS) Model	27
2.5.4	Inhomogeneous Field Mechanism (IFM) Model	27
2.6	Resistive Vacancy Switching	29
2.6.1	Valency Model	30
2.6.2	Phonon-Assisted Tunneling between Traps	31
2.7	Conduction Models	33
2.7.1	WKB approximation	33
2.7.2	Quantum Transmitting Boundary Method	36
2.7.3	Tight Binding Model	39
2.7.4	Thermionic Conduction	42
2.8	Practical Considerations	42
3	Materials and Methods	44
3.1	Hf _x Zr _{1-x} O ₂ Material Characterization	44
3.2	Depolarization Field	46
3.3	Read and Write Rate	47
3.4	FTJ Manufacturing	48
3.5	Annealing	49
3.6	Electrode Materials	49
4	Results	50
4.1	The Effects of Thin Film Homogeneity on the Performance of FTJs	51
4.1.1	Hf _x Zr _{1-x} O ₂ Structural Homogeneity	51
4.1.2	Results	55
4.2	Valency Mechanism and Endurance	63
4.2.1	Drift-Diffusion Valency Change Model	63
4.2.2	Measurements	65
4.2.3	Valency Mechanism Model	67
4.3	CMOS Compatible Hf _{0.5} Zr _{0.5} O ₂ FTJs for Neuromorphic Devices	70
4.3.1	Spike-Timing-Dependent Plasticity	70
4.3.2	Partial Switching and Model of Domain Polarization	73
4.3.3	Modeling the STDP Switching Behavior	76
4.3.4	Conclusion	79
5	Summary and Outlook	81
5.1	Summary	81
5.2	Conclusion and Outlook	83
References		84
A	Appendix	106
A.1	Probing	106
A.1.1	X-ray Photoelectron Spectroscopy (XPS)	106
A.1.2	X-ray Spectroscopy (XRD)	107
A.1.3	X-ray reflectivity (XRR)	109
A.1.4	Atomic and Piezoresponse Force Microscopy	110
A.1.5	Transmission Electron Microscopy (TEM)	111
A.2	Manufacturing methods	113
A.2.1	Magnetron Sputter deposition	113

A.2.2	Atomic Layer Deposition (ALD)	115
A.3	FTJ Measurement Setup	116
A.3.1	Switching Behavior	117
A.3.2	FTJ Valency Switching	117
A.3.3	Endurance	117
A.4	Work Function in Electrode Materials	123
Sommaire récapitulatif: La Jonction Tunnel Ferroélectrique:		
Modèles pour les Applications Mémoires et Neuromorphiques		124
Introduction		124
Contexte théorique		127
Résultats		138
Résumé et Conclusions		153

List of figures

1.1	The LRS and HRS states of resistive switching	4
1.2	Ferroelectric hysteresis loops	5
1.3	Domain switching process	6
2.1	Ferroelectric orthorhombic phase (No. 29) in HfO_2	10
2.2	Kay-Dunn law: Coercive field over thickness	11
2.3	Crystal Classification hierarchy of ferroelectricity	17
2.4	Domain switching process	18
2.5	Potential barrier with distribution functions	20
2.6	Potential barrier deviation from idealized trapezoid	22
2.7	LGD energy density	24
2.8	$\text{Hf}_x\text{Zr}_{1-x}\text{O}_2$ equivalent circuit diagram	25
2.9	MGLK switching dynamics	26
2.10	IFM switching dynamics	29
2.11	Trapezoidal potential barrier	35
2.13	3D tight binding model	40
2.14	Tight binding current density	41
3.1	$\text{Hf}_x\text{Zr}_{1-x}\text{O}_2$ crystal phases	45
3.2	Phase diagram, grain radius over temperature	45
3.3	Sputtering deposited layers	48
4.1	Tunneling over voltage and thickness for LRS and HRS states	53
4.2	Potential barrier for LRS and HRS	54
4.3	J-V curve according to the WKB approximation	55
4.4	Thickness variation conductivity model	57
4.5	Current density distribution for thickness variations	58
4.6	Mean current density of LRS state and HRS state	59
4.7	Probability of electrical breakdown	61
4.8	TER over pinned domain fractions	62
4.9	Sequence of alternating write and read pulses.	66
4.10	Pulse sequence over write voltage	66
4.11	Vacancy density FDM model	67
4.12	Current density, valency mechanism	68
4.13	Synapse between neurons	70
4.14	Resistive switching over pulse duration and amplitude	71
4.15	Pre- and post-synaptic action potential creating synaptic plasticity in STDP	72
4.16	STDP switching response	74

4.17	STDP parameters over action potential amplitude	75
4.18	STDP parameters over action potential width	76
4.19	Resistive switching for varying STDP pulses	77
4.20	STDP switching response from NLS model	79
A.1	XPS spectra on TiN, HZO, Pt and interfaces	107
A.2	Grazing incidence XRD maps on $\text{Hf}_x\text{Zr}_{1-x}\text{O}_2$	108
A.3	Grazing incidence XRD measurements on $\text{Hf}_x\text{Zr}_{1-x}\text{O}_2$	109
A.4	XRR measurements on $\text{Hf}_x\text{Zr}_{1-x}\text{O}_2$	110
A.5	PFM surface, phase and switching measurements.	111
A.6	PFM endurance measurements on $\text{Hf}_{0.5}\text{Zr}_{0.5}\text{O}_2$	111
A.7	TEM images of various $\text{Hf}_x\text{Zr}_{1-x}\text{O}_2$ films on SiO_2	112
A.8	TEM image of 3 nm $\text{Hf}_x\text{Zr}_{1-x}\text{O}_2$ film	113
A.9	Sputtering deposition system SPT310	114
A.10	Sputtering System (geometric model)	115
A.11	Measurement Microscope	116
A.12	Two Tip Measurement	117
A.13	FTJ, microscope view	118
A.14	Resistive switching over pulse duration and amplitude	119
A.15	Vacancy density FDM model	120
A.17	Endurance over Pulses	120
A.16	Current density, valency mechanism	121
A.18	Endurance Pulse Sequence	121
A.19	Delamination of top electrode	122
A.20	Current over write voltage	122
A.21	Work function over electron density	123
A.22	Crystal classification hierarchy	129
A.23	Ferroelectric hysteresis loops	131
A.24	Ferroelectric orthorhombic phase (No. 29) in HfO_2	132
A.25	Kay-Dunn law: Coercive field over thickness	133
A.26	The LRS and HRS states of resistive switching	136
A.27	Domain switching process	138
A.28	Thickness variation conductivity model	141
A.29	Mean current density of LRS state and HRS state	142
A.30	Sequence of alternating write and read pulses.	145
A.31	Vacancy density FDM model	146
A.32	Current density, valency mechanism	146
A.33	Synapses and neurons	148
A.34	Pre- and post-synaptic action potential creating synaptic plasticity in STDP	150
A.35	Resistive switching for varying STDP pulses	152

List of Tables

2.1	Survey of FTJs in literature	12
2.2	L-K model parameters	25
2.3	IFM model parameters	28
2.4	$\text{Hf}_x\text{Zr}_{1-x}\text{O}_2$ tight binding model parameters	41
4.1	Interface potentials	54
4.2	Valency mechanism model parameters.	68
4.3	IFM model parameters, fitting	78
A.1	Sputtering parameters	114
A.2	Valency mechanism model parameters.	118

Acronyms

AFM atomic force microscopy. 29, 87

ALD atomic layer deposition. 8, 87

BEOL back-end-of-line. 8, 87

CAFM conductive atomic force microscopy. 71, 87

CMOS complementary metal-oxide semiconductor. 2, 8, 87

DRAM dynamic random-access memory. 3, 87

DWGN domain-wall geometric nucleation. 87

DWM domain-wall motion. 87

E_c conduction band. 87

E_g band gap. 87

EEPROM electrically erasable programmable read-only memory. 87

EPROM erasable programmable read-only memory. 87

f-phase ferroelectric phase. 26, 87

FE ferroelectric. 3, 4, 87

FeFET ferroelectric field effect transistor. 10, 87

FEOL front-end-of-line. 8, 87

FeRAM ferroelectric random-access memory. 10, 87

FTJ ferroelectric tunnel junction. 2, 3, 10, 45, 52, 53, 55, 87

GIXRD grazing incidence X-ray diffraction. 87

HRS high resistance state. 4, 49, 87

HZO hafnium zirconium oxide. 3, 27, 45, 46, 49, 87

IFM inhomogeneous field mechanism. 18, 87

- IV loop** current-voltage loop (measurement). 87
- KAI** Kolmogorov-Avrami-Ishibashi. 17, 87
- LRS** low resistance state. 4, 49, 87
- LTP** long term potentiation. 54, 87
- MLP** multilayer perceptron. 10, 87
- NLS** nucleation-limited switching. 17, 45, 87
- P_O** oxygen partial pressure. 87
- P_r** remanent polarization. 87
- PE loop** polarization-electric field loop (measurement). 87
- PFM** piezoresponse force microscopy. 29, 71, 87
- PLD** pulsed laser deposition. 87
- PRSPAP** switching promotion effect between adjacent parts. 87
- PZT** lead zirconate titanate. 87
- RAM** random-access memory. 87
- ReRAM** resistive random-access memory. 10, 55, 87
- rms** root mean square. 87
- ROM** read only memory. 87
- sccm** standard cubic centimeter per minute. 87
- SNN** spiking neural network. 55, 87
- SRAM** static random-access memory. 3, 87
- STDP** Spike-timing-dependent plasticity. 45, 55, 87
- T_M** melting temperature. 87
- TER** tunneling electroresistance. 3, 4, 45, 49, 52, 53, 87
- U** barrier height energy. 87
- u.c.** unit cell. 87
- VBM** valence band maximum. 87
- VBO** valence band offset. 87

WKB Wentzel-Kramer-Brillouin. 46, 49, 87

XPS X-ray photoelectron spectroscopy. 87

XRD X-ray diffraction. 87

XRR X-ray reflectivity. 87

Chapter 1

Introduction

The historically exponential increase in electronic device performance in information technology is beginning to slow down. In the past decades, both power consumption and production costs were improved with smaller feature sizes, a correlation that is no longer true with classical transistor technology. This makes the exponential predictions of Moore's law increasingly difficult to keep up with. Generally, there are two orthogonal ways to alleviate this situation: Either by improving the classical silicon-based logic units, or by finding architectural solutions to the Von Neumann bottleneck. The Ferroelectric Tunnel Junction (FTJ) is a type of resistive switching unit that shows favorable characteristics which apply to both scenarios.

1.1 The Search for Alternative Memories

Ferroelectric thin films are a prime research area, offering a wide array of technological applications in the microelectronics and semiconductor industry. However, up to recently, there were limits either with regards to scalability (e.g. thin films losing their ferroelectric phase) or compatibility with complementary metal-oxide semiconductor (CMOS) manufacturing technology, amongst them the requirements of moderate processing temperatures and process-compatible formation gas. With the discovery of a ferroelectric phase in Hafnium-Oxide films by Böscke et al. [7] in 2011, a material that is already widely used as a dielectric now became available that could potentially overcome these limitations.

This new material has sparked renewed interest in ferroelectric tunnel junctions (FTJs). The theoretical concept of the FTJ was first proposed by Esaki et al. in 1971 [8], who predicted tunneling currents through this junction could depend on polarization. The simple design layers a ferroelectric thin film between two electrodes and relies on the interaction between the polarization and asymmetric mirror charges induced in the electrodes to modulate the effective tunneling barrier. With nanometer scales being a requirement for practical FTJs, the newly discovered HfO₂ phase fits this requirement well.

The switching between resistive states is also known as the TER effect. It was first experimentally demonstrated on ultrathin ferroelectric BaTiO₃ films in 2009 by Garcia et al. [9]. Their findings sparked extensive research efforts, which found that the FTJ concept shows a series of promising features for memory applications, such as good endurance (10⁶ cycles), [10, 11] high write speeds (<10 ns), [12] excellent scalability, [13] and simple architecture [14].

However, several limitations have so far prevented FTJ memory from being adopted in commercial devices. The perovskite ferroelectrics (BTiO₃, BiFeO₃ or Pb(Zr_{1-x}Ti_x)O₃) are difficult to process on silicon, because of their elevated crystallization temperatures (over 650°C) and the incompatibility of forming gases with silicon [15–21]. The discovery of ferroelectricity in HfO₂ by Böscke et al. [7] was both unexpected and astonishing for two reasons: First, both hafnium and zirconium oxides have long been studied and used in the semiconductor industry with no indications of ferroelectricity [22]. Second, its simple stoichiometry is exceptional in forming a ferroelectric structure. With respect to FTJs, this novel material allows a CMOS compatible manufacturing, while maintaining the excellent scalability which allows for a sufficiently large tunneling effect for memory applications. Since both ZrO₂ and HfO₂ are already used in semiconductor memories as dielectrics, [22–25], an Hf_{0.5}Zr_{0.5}O₂-based FTJ memory can easily be integrated into an existing CMOS process. The first experimental demonstration of an HfO₂-based FTJ was done by Fujii et al. [26], quickly followed by Chernikova et al. [27] in 2016, who experimentally demonstrated the scalability of the ferroelectric (FE) film down to 2.5 nm.

Standard computer memory stores information as charge state. The dynamic random-access memory (DRAM) memory is compact, consisting of a single transistor and capacitor, but requires periodic refresh cycles. The much bigger static random-access memory (SRAM) requires 6 transistors and requires a constant voltage supply to maintain its information. The non-volatile NOR and NAND flash memories require high write voltages (5-12V) to inject charges onto the charge trapping layer and have moderate program/erase durability of typically 10³-10⁶ cycles.

The FTJ memory is persistent, possesses very high write/erase speeds, and operates on moderate voltages. Only consisting of a nanometer scale ferroelectric tunneling barrier with two electrodes, the device is extremely thin and requires few lithographic steps.

Despite its promising features, however, the composition of the ferroelectric $\text{Hf}_x\text{Zr}_{1-x}\text{O}_2$ phase and structure exhibits some theoretical and technical challenges which have shunted its application in industry. For one, the ferroelectric phase depends on its polycrystallinity and other extrinsic factors, which means that it is not intrinsically stable. Additionally, obtaining reproducible electrical characteristics of a polycrystalline nanostructure is challenging, as the coercive fields required for polarization switching represent a significant fraction of the breakdown voltage, which can induce defects and degradation of the device over time. This thesis investigates the design of a ferroelectric tunnel junction and attempts to quantify these issues. While we exemplarily study the $\text{TiN}/\text{Hf}_{0.5}\text{Zr}_{0.5}\text{O}_2/\text{Pt}$ structure in this thesis, the results mostly generalize to all types of tunnel junctions.

1.2 FTJ Operation

The resistive switching properties of the HfO_2 -based FTJs is highly sensitive to certain design parameters. The resistive switching mechanism is a result of the FE polarization [13], which induces surface charges at the metal-FE interface. This induces screening charges within the metal, inducing a depolarization field within the FE that opposes the FE polarization [28]. When using electrode metals with different screening lengths, this modulates the interface potentials in unequal magnitudes (see Fig. 1.1). Due to the exponential dependency between tunneling current and potential barrier, two distinct resistance states, the high resistance state (HRS) and the low resistance state (LRS) can be observed. A large difference between these which is beneficial for memory applications. The ratio of HRS and LRS resistivities is also known as the tunneling electroresistance (TER) ratio. Especially reading the state of the device also depends in the magnitude of the LRS. Since a certain amount of charge is required to measure resistivity, lower LRS resistivities and a larger tunneling surface improve read speeds, while the voltage must remain below the coercive field. Compared to that, the write speeds only depend on FE switching speeds at the write voltage. Since switching domains propagate with the speed of the transverse optical phonon, the write speed is for all practical concerns only limited by the nucleation rate and sideways growth of the domain

wall (see sections 2.3.1, 3.3).

HfO_2 typically starts breaking down at electric fields between 4 to 7 MV/cm [29], depending on its crystalline structure and interface types. This value is only slightly above the coercive field of at least 1 MV/cm, which is typically exceeded to improve switching speeds. For this reason, the write cycle endurance requires a careful selection of the write voltage.

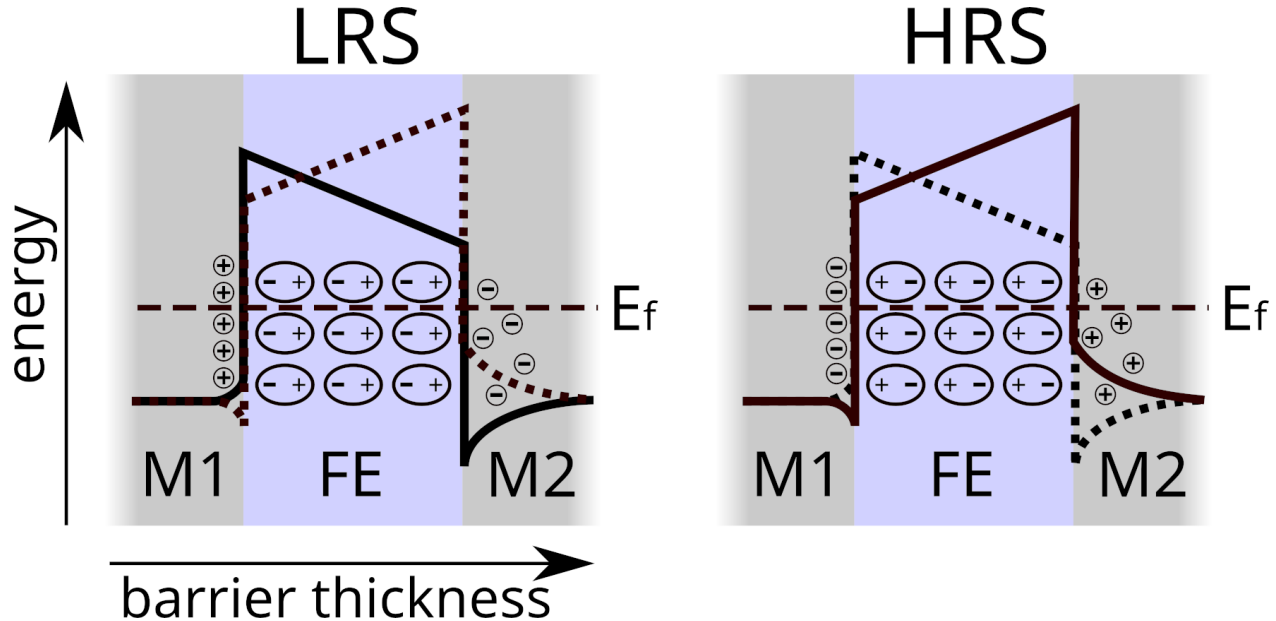


Figure 1.1: The LRS and HRS states of resistive switching (schematic). The solid line is the tunneling barrier. Left: The ferroelectric layer FE is polarized towards the electrode of weaker electrostatic shielding M2, causing the potential barrier to significantly drop at the M2 interface, with a smaller, opposite effect at M1. Right: When the polarization is flipped, the potential barrier increases significantly at M2, with the smaller, opposite effect at M1.

The size of the space charge regions that bend the conduction band inside the electrodes is extremely exaggerated for visualization purposes in Fig. 1.1. Their scale is quantified by Thomas-Fermi screening, which is extremely small in metallic electrodes. We therefore do not include this effect in our calculations.

1.3 Ferroelectrics

Ferroelectric materials possess a permanent electrical dipole moment that can be reoriented by application of an external voltage. Ferroelectricity occurs in crystals in which the crystalline symmetry allows a polar axis. This spontaneous polarization is due to the relative displacement of

differently charged ions in the crystal lattice. The electrical polarization in ferroelectrics can be reversed by applying an external electric field. Ferroelectric materials are intrinsically pyroelectric and piezoelectric, but become paraelectric at high temperatures. When the paraelectric material cools down below the ferroelectric Curie temperature, spontaneous polarization occurs and the relative permittivity increases considerably. The characteristic ferroelectric polarization response can be obtained from periodic P-E loops. Fig. 1.2a shows a typical hysteresis curve for $\text{Hf}_{0.5}\text{Zr}_{0.5}\text{O}_2$. In multigrain structures with varying orientations and grain shapes, the coercive field strength becomes a stochastic distribution, which smoothes the switching transition (lowering the curve slopes at x-axis intersections). The permittivity spikes proportional to the slope of the polarization as the switching progresses (Fig. 1.2b).

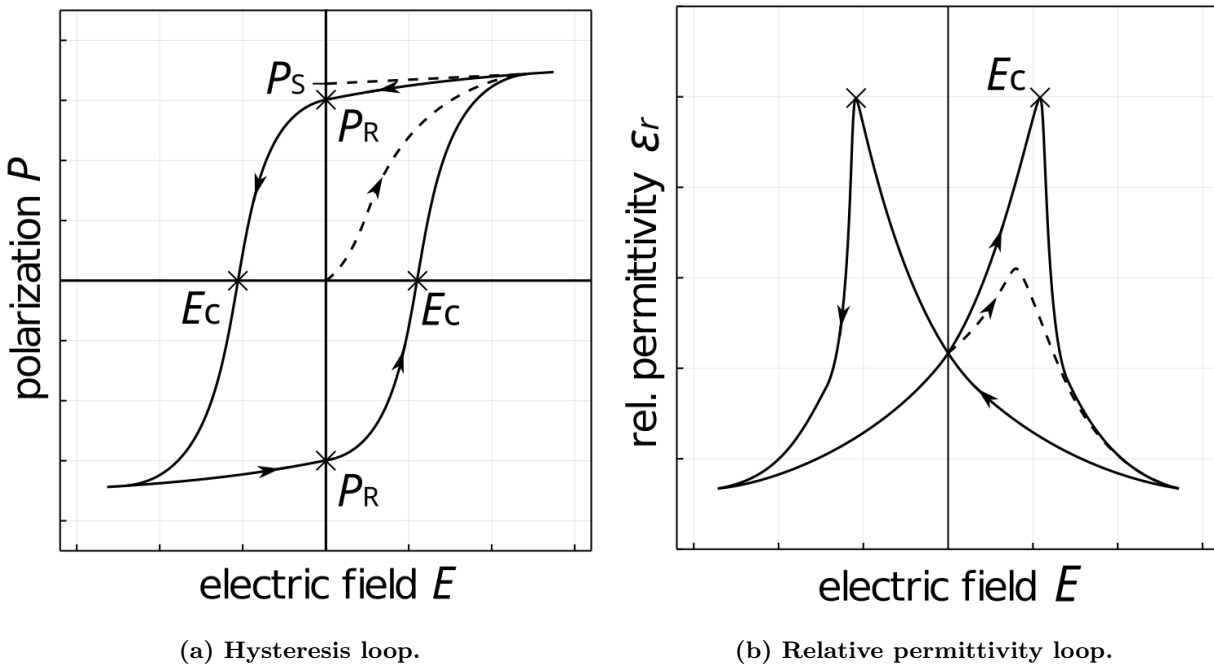


Figure 1.2: Characteristic ferroelectric hysteresis loop. Initially, randomly oriented FE domains may exhibit no macroscopic polarization (dashed line). Under the effect of an external electric field, the crystal becomes increasingly polarized, asymptotically approaching the saturation limit $\partial P / \partial E = \varepsilon_0 \chi$. The remanent polarization P_R remains, which can be toggled by an opposing electric field. The smoothness of the switching transition depends on the nucleation and growth behavior of the flipped domains, which depends on the ferroelectric material and parameters, such as the applied frequency.

Ferroelectric crystals form domains, i.e. regions with similar polarization directions. From domain to domain, the direction of polarization changes in the region of a few atomic layers where the polarization transitions. The ferroelectric Curie-Weiss domain walls are typically only a few

nanometers wide. Therefore, the storable information density can be much higher than on ferromagnetic substrates, where the Néel walls are significantly larger. Uniaxial ferroelectrics, such as FE $\text{Hf}_x\text{Zr}_{1-x}\text{O}_2$, have one possible polarization axis and can be switched by 180° with an applied electric field. In some biaxial ferroelectrics, stress can also reorient the polarization [30]. The evolution of domains during the switching process can be divided into steps as shown in Fig. 1.3.

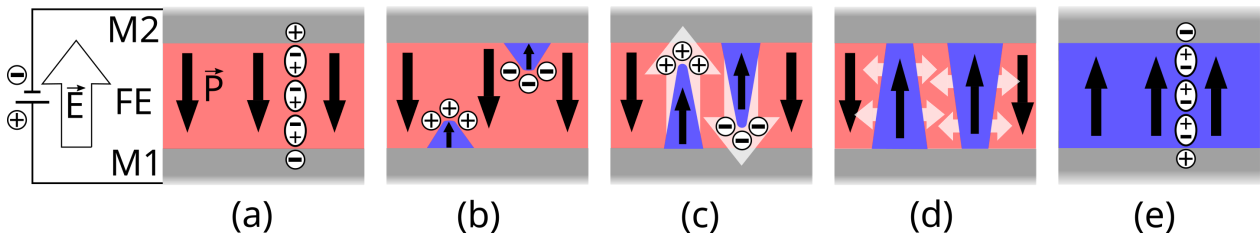


Figure 1.3: Domain switching process (schematic). Five states of polarization switching are presented. (a) Initially fully downwards polarized ferroelectric. (b) When a certain voltage threshold is exceeded, nucleation of a flipped domain initiates. (c) Driven by charges at the domain wall, it quickly propagates through the domain. (d) With polarizations mostly oriented parallel to the domain wall, an energetically much more stable state is formed, resulting in slow lateral growth. (e) Fully switched domain.

1.4 Electrical Properties of Metallic Oxide Insulators

Resistance changes in ultrathin ferroelectric films may occur for different reasons [31] that need to be carefully discriminated against each other to control and predict the device operation:

- (1) Direct tunneling for which the tunnelling electroresistance effect occurs due to a modulation of the average barrier height in an asymmetric electrode configuration
- (2) Fowler Nordheim tunneling, which dominates for larger fields
- (3) Thermionic (Schottky) charge transport across the barrier

- (4) Within the film, variable range hopping between defects
- (5) Valency change: local electroforming of extended defects (agglomeration of oxygen vacancies) is generally possible in oxide-based thin films and yields local semiconductor properties
- (6) Conductive bridge effects, where a metal filament is electrochemically driven.

In an FTJ, the direct tunneling mechanism is the desirable conduction regime that forms the basis of the FTJ operation. While the tunneling mechanisms are only marginally affected by temperature, thermionic and diffusion-based conduction sharply increases with temperature. The energy distribution of charge carriers in insulators follows Boltzmann statistics, which is valid if the conduction band edge for electrons (valence band edge for holes) approaches the Fermi energy. While nanometer scale films exhibit strong tunneling behavior, preexisting or electrochemically induced vacancies are also known to contribute to the conduction in thin films, which can lead to device degradation and breakdown [32–34].

1.5 Thesis Objectives

This work investigates the challenges and characteristic properties of ferroelectric tunnel junctions (FTJs) based on the recently discovered ferroelectric phase of $\text{Hf}_{0.5}\text{Zr}_{0.5}\text{O}_2$. Specifically, we address the following questions: First, what degree of structural homogeneity is required in the deposited thin film is required to create reproducible devices? Second, how can the degradation within the device, and the resulting resistive switching behavior be understood? And third, to what extent can the gradual switching characteristic be used in a neural network application? To approach these questions, We outline the fundamental physical mechanisms and explore the design parameter space. From this theoretical basis, we develop a model to quantify thin film homogeneity requirements. Next, we describe the electrochemical durability of the device by approaching breakdown voltages, including the operation under gradual failure. We aim to describe and quantify the operation under soft breakdown by developing a simulation model. Suitable models were to be found by the author. With the resulting insights, the suitability of the FTJs with regards to applications in memory, as well as in a case study of a spiking neural network were to be investigated.

Chapter 2

Fundamentals

The resistive switching in FTJs, also known as tunneling electroresistance (TER), is a mechanism that exists in principle in all types of ferroelectric materials interfaced by two electrodes with asymmetric material properties. This electrode property is the electric field screening which occurs as a response to the adjacent ferroelectric charge. It is characterized by Thomas-Fermi screening and its characteristic Debye screening length, which depends exclusively on the Fermi level and electron density.

This chapter discusses the status quo of research on FTJs. Next, the material properties polarization, ferroelectricity and piezoelectricity in crystals are discussed. Traditional perovskite ferroelectrics are contrasted to the new fluorite structure $\text{Hf}_{0.5}\text{Zr}_{0.5}\text{O}_2$ and its phases. We proceed to describe the XPS measurement to determine interface potentials, and proceed with a presentation of the Tsu-Esaki description of tunneling currents. A formula to approximate the more realistic, smooth barrier shape is shown.

2.1 Ferroelectricity

A ferroelectric is defined as a material that exhibits permanent polarization which can be reoriented by application of an electric field. Contrary to the other groups presented in Fig. 2.3, the distinction from the pyroelectrics is not found in its crystal structure, but merely in the feasibility of polarization switching. This polarization reversal can be visualized by hysteresis loops as shown in Fig. 1.2a. In

a non-polarized crystal, the polarization is randomly oriented, i.e. the macroscopic polarization is zero. If one applies a very small electric field, the relationship between polarization P and electric field E will behave like a normal dielectric, and removing the field will revert the total polarization to zero. Increasing the electric field sufficiently will cause the polarization to be aligned in one direction [35]. In this saturation state, the polarization is proportional to the applied electric field

$$\partial P_i = \chi_{ij} \partial E_j = (\varepsilon_{ij} - 1) \partial E_j \quad (2.1)$$

The polarization P_i describes permanent and induced electric dipole moments in the material. It is measured in units of surface charge density C/m². One approach to describe the ferroelectric hysteresis loop is derived from the Ginzburg-Landau theory [36] (see section 2.5.1) or heuristic models [37].

2.1.1 Ferroelectric Materials

From a crystallographic point of view, only non-centrosymmetric polar crystals can be ferroelectric. This is due to the intrinsic polarization axis that is incompatible with inversion symmetry. The polarization in a ferroelectric develops as a result of charge separation within the crystal phase. When the polarization is flipped, a relative displacement of atoms between two thermodynamically stable states occurs.

The most prominent representatives of ferroelectrics are perovskites such as BaTiO₃ and Pb(Zr, Ti)O₃, as well as organic materials, such as polytrifluoroethylene (PVDF) [38]. The orthorhombic fluorite structure of ferroelectric HfO₂ and ZrO₂ is shown in Fig. 2.1. Closely related to ferroelectrics are antiferroelectrics, which also exhibit switchable dipoles within the crystal. However, as opposed to ferroelectrics, adjacent dipoles align in an antiparallel pattern, cancelling out any macroscopic polarization.

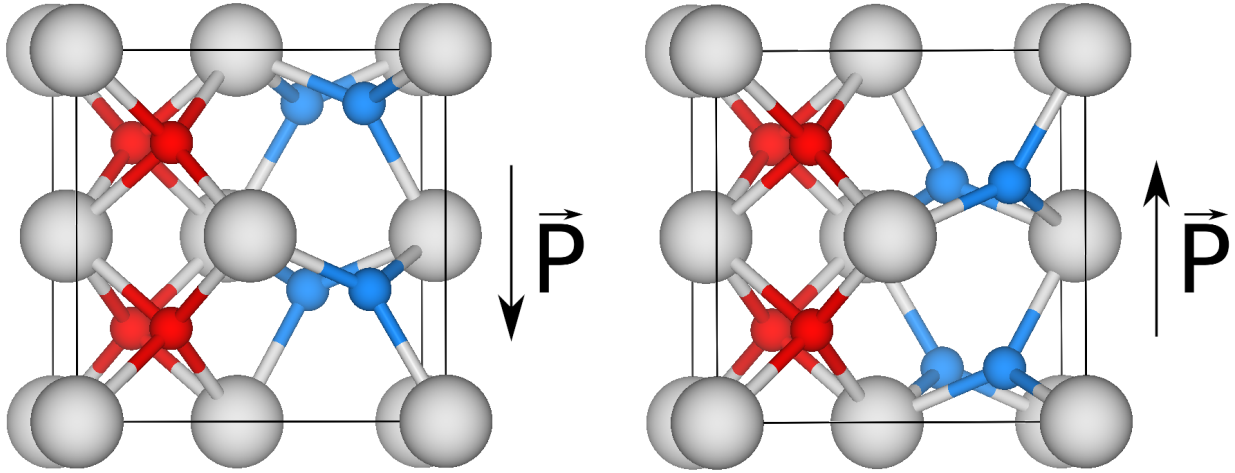


Figure 2.1: Ferroelectric orthorombic phase (No. 29) as observed in $\text{Hf}_{0.5}\text{Zr}_{0.5}\text{O}_2$. Grey: Hf/Zr atoms. Red/blue: Oxygen. Blue: Oxygen in bistable, switchable location. Left: Downward polarization. Right: Upward polarization. The horizontal axis aligns with lattice parameter b , the vertical axis is lattice parameter c .

The various transducing properties of ferroelectric materials make them useful in many applications, such as classical infrared detectors which exploit pyroelectricity, surface acoustic wave (SAW) devices and microactuators, based on piezoelectricity, high permittivity insulators in integrated capacitors and DRAM, optical modulators and frequency doublers, using their electrooptic properties, and finally the applications that are directly based on the ferroelectric effect.

2.1.2 Kay-Dunn Law

Back in 1962, H. Kay and J. Dunn described the dependence of the coercive field E_c on the film thickness d by a semi-empirical law [39]

$$E_c \propto d^{-2/3} \quad (2.2)$$

The derivation assumes idealized electrodes that induce no internal electric fields in the ferroelectric film, which makes the measured coercive field through the electrodes identical to that of the sample. Dawber et al. [40] have shown that the law holds true for various materials (PVDF, $\text{Pb}[\text{Zr}_x\text{Ti}_{1-x}]\text{O}_3$, KNO_3) for films ranging from 100 μm down to 1 nm (see Fig. 2.2). Interface effects, such as screening charges over finite distances have the effect of altering the measured coercive field. In the case of large spontaneous polarization compared to the dielectric constant of the film $4\pi P_s \gg \epsilon_0 \epsilon_r E$, the

effective coercive field is reduced since the depolarization field assists the switching process [40]. In this case, the Kay-Dunn law can be taken as an upper limit to the coercive field. Recent findings confirm that this law extends to hafnia-based ferroelectrics [41].

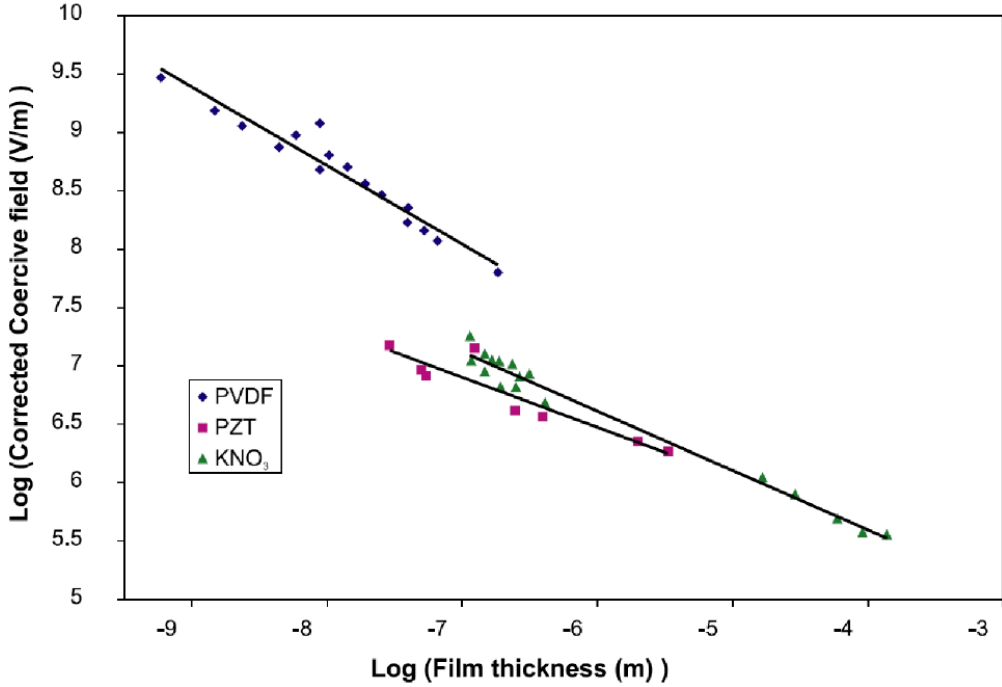


Figure 2.2: Kay-Dunn law: Coercive field over thickness for various ferroelectric films (logarithmic) [42].

2.2 State of the Art

Various types of FTJ have been investigated in literature. Their TER values are typically found in the range of 10 to 100 [43–45]. A giant TER ratio has been demonstrated in FTJ memories based on BiFeO₃,[11] PbTiO₃ [46] and BaTiO₃ [9].

A crucial condition to fabricate FTJ memory devices is to achieve ferroelectricity in ultrathin film form [13, 47]. Non-centrosymmetric perovskite materials in their thin film form such as BaTiO₃, [48–50] BiFeO₃ [51, 52] and PbTiO₃ [46] are well known for their outstanding ferroelectric properties. However, their ferroelectricity starts to disappear as their layer thickness decreases [13, 47]. For many years, it was believed that ferroelectricity exists only in films with a film thickness above a certain critical thickness (around 10 nm) [53]. Recently, strain engineering studies had proved that the ferroelectricity is compatible with ultrathin films. This is possible, due to the strain forces

generated between the film and substrate which distort the crystal structure lattice of the ultra-thin film [53]. This in turn reduces the symmetry of the crystal structure, which enhances the ferroelectricity in the ultrathin films. In 2009, Garcia et al. [9] experimentally demonstrated robust ferroelectricity in a 1 nm thick, highly strained BaTiO₃ film. This discovery allowed the experimental demonstration of the tunneling electroresistance effect in a metal-ferroelectric-semiconductor structure. Starting at that point, perovskite materials such as BaTiO₃, [9, 45] PbTiO₃, [46] BiFeO₃ [11] and Pb(Zr, Ti)O₃ [54] have been used successfully as ultrathin ferroelectric barriers in FTJ devices. Besides the perovskites and the fluorite structure HfO₂, organic ferroelectrics, such as PVDF [55], have also been demonstrated to show significant TER switching (table 2.1).

Bottom/Top El.	FE	d	T _s	Remarks	Ref.
La _{0.67} Sr _{0.33} MnO ₃ Cr/Pt	BaTiO ₃	PLD, 1 nm	775°C	PLD, highly strained FE	[9] 2009
Nb:SrTiO ₃ Au/Ti	BaTiO ₃	10 u.c.	775°C	PLD, TER demonstration	[45] 2016
SrRuO ₃ AFM tip	PbTiO ₃	3.6 nm	700°C	PLD, Giant TER, 72h retention	[46] 2010
La _{0.67} Sr _{0.33} MnO ₃ Co/Au	BaTiO ₃	2 nm	700°C	PLD, TER=64, 900 cycles	[12] 2012
Au/Co La _{0.67} Sr _{0.33} MnO ₃	PbZr _{0.3} Ti _{0.8} O ₃	1.6 nm	700°C	PLD, TER=300 at ±0.4 V, WKB model	[54] 2012
Ca _{0.96} Ce _{0.04} MnO ₃ Co	BiFeO ₃	4.6 nm	750°C	PLD, TER=10 ³ , cycles=10 ⁶	[10] 2014
Ca _{0.96} Ce _{0.04} MnO ₃ Co/Pt	BiFeO ₃	7 u.c.	750°C	PLD, TER=10 ⁴ , cycles=10 ³ , retention=68 h	[11] 2013
La _{0.67} Sr _{0.33} MnO ₃ graphene	BaTiO ₃	6 u.c.	680°C	PLD, TER=6000 at ±0.2 V	[56] 2014
La _{0.67} Sr _{0.33} MnO ₃ Cu	BaTiO ₃	3 nm	700°C	PLD, TER=10 ³ , WKB model	[57] 2014
Au W	PVDF	2.2 nm	RT	Langmuir-Blodgett, TER=3, monolayer	[55] 2016
n ⁺ -Si TiN	Hf _{0.5} Zr _{0.5} O ₂	2.5 nm	400°C	ALD, U _c =0.8 V, suspected SiO ₂ formation	[27] 2016
TiN Pt	Hf _{0.5} Zr _{0.5} O ₂	2.8 nm	425°C	RF sputtering, TER=15 at ±0.2 V	[58] 2017
TiN Pt	Hf _{0.5} Zr _{0.5} O ₂	4 nm	600°C	ALD, TER=3 at ±0.2 V	[59] 2019

Table 2.1: Survey of FTJs in literature. T_s is the substrate deposition temperature, d the thickness of the ferroelectric.

2.2.1 Conduction in Ferroelectrics

While all ferroelectric materials are insulators, there are a series of mechanisms that permit conduction [60]. Here, we summarize some that are relevant for our study of tunnel junctions.

Thermionic Conduction

The Schottky mechanism describes the thermal excitation of charge carriers into the conduction band of an insulator [61]. An equation describing the thermionic current is given in section 2.7.4. The mechanism depends on barrier height and temperature, but is independent of barrier thickness and typically becomes negligible at nanometer-scale barrier thicknesses, as tunneling mechanisms grow exponentially [54].

Direct Tunneling

The direct tunneling mechanism results from the quantum mechanical transmission probability of charge carriers through potential barriers, and becomes relevant for thin films in the nanometer regime [62]. Direct tunneling directly transports particles between the electrodes, assuming negligible scattering within the barrier. In case of a trapezoidal potential barrier, the Wentzel-Kramers-Brillouin (WKB) approximation yields [63]

$$j_{DT} = C \frac{\exp \left[\alpha \left(\left(\phi_2 - \frac{eV}{2} \right)^{3/2} - \left(\phi_1 + \frac{eV}{2} \right)^{3/2} \right) \right]}{\alpha^2 \left[\sqrt{\phi_2 - \frac{eV}{2}} - \sqrt{\phi_1 + \frac{eV}{2}} \right]^2} \sinh \left[\frac{3eV}{4} \alpha \left(\sqrt{\phi_2 - \frac{eV}{2}} - \sqrt{\phi_1 + \frac{eV}{2}} \right) \right] \quad (2.3)$$

where $C = -\frac{4em_e^*}{9\pi^2\hbar^3}$, $\alpha = \frac{4d\sqrt{2m_e^*}}{3\hbar(\phi_1+eV-\phi_2)}$, m_e^* is the effective tunneling electron mass, ϕ_1 and ϕ_2 the interface potentials.

The equation only depends on the two interface potentials $\phi_{1,2}$ per polarization and the effective mass m_e^* , while showing an exponential behavior with thickness d .

Fowler-Nordheim Tunneling

Compared to direct tunneling, Fowler-Nordheim tunneling requires increased fields [64, 65]. The applied voltage reduces one interface potential of the insulator below the energy level of electrons in the opposing electrode. Therefore, the tunneling distance is reduced. The resulting current is given by [63]

$$j_{FN} = \frac{e^3 m}{8\pi h m_e^* \phi_{1,2}} E^2 \exp \left[-\frac{8\pi \sqrt{2m_e^*} \phi_{1,2}^{3/2}}{3he} \frac{E}{E} \right] \quad (2.4)$$

where $\phi_{1,2}$ is the barrier potential of the interface of negative voltage.

Besides this classical Fowler-Nordheim Tunneling equation, there exist updated variants that provide improved accuracy, such as Forbes and Deane [66]. Since we operate our device at voltages below the Fowler-Nordheim Tunneling regime, these equations are not reproduced here.

Defect Mechanisms

Defects locally distort the shape of the potential barrier. These defects can be a result of intrinsic polycrystallinity, as well as manufacturing or fatigue induced defects due to repeated polarization switching. Ferroelectric domain walls can also exhibit conductive behavior [67]. Besides degrading the ferroelectric switching properties, point defects such as oxygen vacancies enable Poole-Frenkel as well as trap-assisted tunneling (TAT), amongst others [60]. Hopping conduction has previously been linked to leakage currents in hafnium oxides $Hf_{0.5}Zr_{0.5}O_2$ [68–72]. A quantitative model based on the hopping mechanism is developed in section 4.2.

Other Mechanisms

At high voltages, hard dielectric breakdown occurs, which generates additional charge carriers within the dielectric and rapidly degrades the insulator [73, 74]. This forms semiconductive or metallic filaments within the insulator, leading to the instant destruction of the device.

2.2.2 The Ferroelectric Tunnel Junction

A ferroelectric tunnel junction consists of a ferroelectric film of few nanometers thickness, sandwiched between two asymmetric metal electrodes, or one metal and one semiconductor electrode [75]. Depending on its polarization direction, the thin ferroelectric film between the electrodes modulates the resistance across the electrodes significantly. This effect is known as the tunneling electroresistance (TER) effect [76]. While theoretically predicted by Esaki in 1971 [8], the first experimental demonstration was achieved in 2009 by Garcia et al. [9]. While initially ferroelectrics perovskites, such as BaTiO_3 and $\text{Pb}(\text{Zr}, \text{Ti})\text{O}_3$ were used, the unique and advantageous properties of the recently discovered ferroelectric orthorhombic phase in HfO_2 in 2011 by Böck et al. [7] has sparked new interest in the concept of ferroelectric memories and FTJs.

The physical mechanism of TER switching is based on the effect of the polarization on the tunneling barrier. The asymmetric nature of the electrodes yields different distributions of mirror charges building up at the interfaces, depending on the polarization direction. When the polarization points towards an electrode, a positive space charge region forms, which elevates the interface potential. The opposite electrode shows an inverse effect, decreasing its interface potential. The asymmetric shielding properties of the electrodes cause different magnitudes of change, resulting in a change of average barrier height. The polarization state with lower average barrier height is called the low resistive state (LRS), the one with higher barrier height is the high resistive state (HRS).

This mechanism is sketched in Fig. 1.1.

The schematic of Fig. 1.1 presents the change in the tunneling barrier. Two basic tunneling regimes can be directly derived from this model: In case of a moderate bias voltage, the direct tunneling mechanism, where tunneling current traverses a trapezoidal barrier of switchable height. This mechanism is independent of bias polarity. In case of a large bias voltage, one side of the barrier drops below the conduction band of the opposite electrode. This effectively reduces the tunneling barrier to a triangle shape of reduced width, also known as Fowler-Nordheim Tunneling (FNT).

Besides the FNT mechanism, there exist two additional mechanisms affecting the effective barrier width: The electrode screening length, and the converse piezoelectric effect.

The ferroelectric polarization is screened over a finite distance by the electrodes, resulting in a space charge region and a corresponding bending of the conduction band. The bending is downwards in

case of the polarization pointing towards the interface, and vice versa. Since the screening length decreases with the free carrier density, it is typically negligible for ideal metallic electrodes. However, in case of semiconductor electrodes or poor electrode interfaces, this effect can significantly impact the device [77]. The converse piezoelectric effect directly couples the applied electric field to the barrier width. Peak values in Si:HfO₂ of $d_{33} = 20 \text{ pm/V}$ [78] and fields of 300 MV/m mean that this effect remains in the sub-percent range of the initial thickness.

2.2.3 Ionic resistive switching

The ionic resistive switching mechanisms constitute an important part in studying FTJs, since their similar nature allows for the FTJ to potentially exhibit this ionic based switching component simultaneously. The cation-type ReRAM is known as conductive bridge RAM and structured similar to the FTJ. The oxide-based switching layer is sandwiched between two electrode materials with uneven electronegativities, one of which forms a Redox pair with the insulator. Using the field-driven formation and rupture of a metallic conductive filament, an abrupt change of cell resistance is observed. The anion-type ReRAM mechanism works similarly, but instead of metallic ions, positively charged oxygen vacancies are created in the Redox reaction that make up the conductive filaments [79–82].

2.3 Ferroelectric Crystals

Half of the crystal classes which exhibit the piezoelectric effect undergo spontaneous electrical polarization in the absence of an applied stress or electrical field. The spontaneous polarization involves a small shift of the positive ions relative to the negative ions, thus creating an electric dipole in the unit cell. The spontaneous polarization may only occur below a certain temperature threshold that induces a phase change.

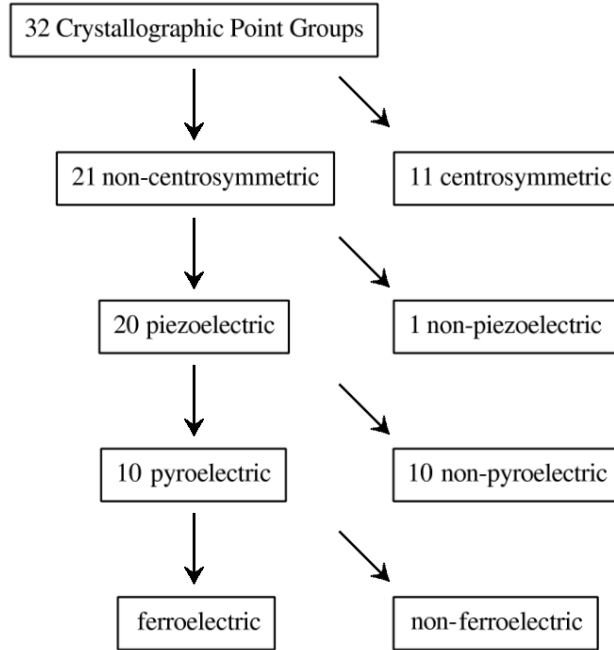


Figure 2.3: Classification hierarchy of materials exhibiting the ferroelectric effect

A small region in which the adjacent unit cells have an identical polarization axis is called a domain. In small grains, only a single FE domain is present. Within larger grains or within adjacent grains, it is energetically favorable to form domains of alternating polarization [83]. In case of a single ferroelectric axis, the domains align in an anti-parallel pattern, while more ferroelectric axes yield more complex patterns [84]. By applying an external electric field, the FE domains can be aligned. This poled state is energetically unfavorable and tends to return to the multidomain state, in a process that is aided by temperature.

2.3.1 Ferroelectric Domain Walls

Ferroelectric switching progresses through the crystal by expanding or receding domains with a specific polarization alignment [84]. Domain walls describe the interfaces between these domains. Depending on the alignment of the domain wall and its neighboring polarizations, different types of domain walls and domain wall motion can be distinguished [85]. The simplest case of switching in a uniaxial ferroelectric without defects is shown in Fig. 2.4. In general, domain walls can be seen as moving elastic surfaces that can be slowed or pinned by charged defects within the crystal [86, 87], leading to reduced switching capability [85].

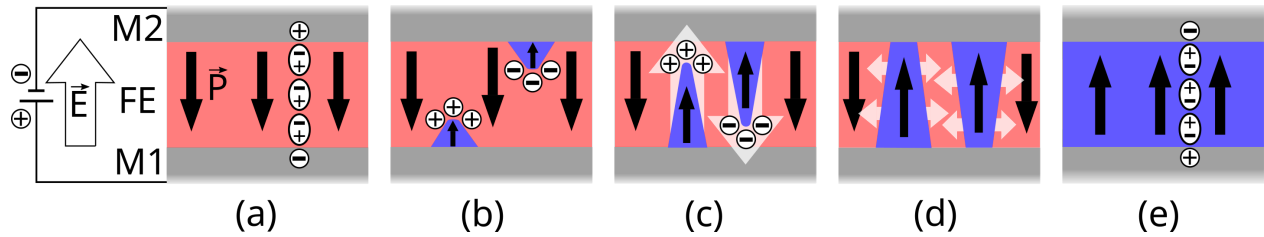


Figure 2.4: Domain switching process (schematic). Five states of polarization switching are presented. (a) Initially fully downwards polarized ferroelectric. (b) When a certain voltage threshold is exceeded, nucleation of a flipped domain initiates. (c) Driven by charges at the domain wall, it quickly propagates through the domain. (d) With polarizations mostly oriented parallel to the domain wall, an energetically much more stable state is formed, resulting in slow lateral growth. (e) Fully switched domain.

2.3.2 The Ferroelectric Phase in Doped HfO_2

Since the ferroelectric orthorhombic phase in HfO_2 without modification is unstable, it was not discovered until 2011. Since then, the main factors affecting the ferroelectric properties have been identified and comprehensively reviewed. These include doping, interface materials and mechanical encapsulation, film thickness, grain size, deposition method and process temperatures [88].

Notable dopants in $\text{Hf}_{1-x}\text{B}_x\text{O}_2$ films include $\text{B} = \text{Si}, \text{Zr}, \text{Y}, \text{Al}, \text{Gd}, \text{Sr}, \text{La}$ [89]. Of these, the Zr dopant has some highly unique features. Its physical and chemical similarity to Hf allows for large doping concentrations, minimizing relative statistical concentration gradients. In case of atomic layer deposition (ALD), a cyclic Hf:Zr deposition provides an especially homogeneous doping of equal Hf and Zr content. Another important feature of the Zr doped oxide is that relatively low processing temperatures (400°C - 600°C) suffice to yield a stable orthorhombic phase, making it compatible with both CMOS front-end-of-line (FEOL) and back-end-of-line (BEOL) manufacturing [89]. Current research indicates that high tensile stresses of 3-5 GPa are required to form the ferroelectric phase. This phase exhibits a coercive field of 1-2 MV/cm, and a polarization of up to about $P_r = 30 \mu\text{C}/\text{cm}^2$ [89].

To obtain the ferroelectric hafnium zirconium oxide (HZO) phase, several energetic contributions are required to stabilize this otherwise energetically unfavorable phase. Amongst them, a mixture with about equal parts of Hf:Zr atoms, combined with substrate and grain boundary contributions are thought to be key factors for this stabilization. The effects of other dopants and oxygen vacancy defects are also being researched for their ability to increase the FE phase. Fig. 2.1 shows the bistable locations of the oxygen atoms. Since oxygen carries negative fractional charge, the polarization aligns in opposite direction to the oxygen offset.

Compared to the perovskites, there are some notable technological advantages of HfO_2 -based ferroelectrics [90]. Most notably, it does not spontaneously form dead layers on interfaces, which limits the scalability of perovskites. Additionally, an increased breakdown threshold due to a bandgap of 5.6 eV compared to 3-5 eV in perovskites [91]. Finally, its comparatively low dielectric constant [92] allows switching at lower voltages, despite higher coercive field strengths [93].

2.4 Tunneling Mechanisms

With two electrodes in sufficient proximity, the conduction between them is characterized by the tunnel effect. Tunneling conduction can be separated into direct tunneling (DT) and Fowler-Nordheim (FN) tunneling. In addition, the trap-assisted tunneling mechanism can transport charge carriers over a wider distance using the tunneling between intermediary defects within the insulator. There exist two types of trap assisted tunneling (TAT), namely the elastic (energy-conserving) and inelastic (phonon-emitting) variant. In case of the metallic electrodes, the relevant charge carriers are electrons, while semiconductor electrodes could also show hole valency-valency tunneling and valency-conduction band tunneling.

2.4.1 The Tsu-Esaki Model

The Tsu-Esaki Model describes the tunneling current density between two metallic or semiconducting electrodes separated by an insulator with barrier height $q\Phi_B$, measured from the Fermi energy to the conduction band edge of the insulating layer. Electrons tunnel from electrode 1 to electrode 2. The distribution functions at both sides of the barrier are indicated in Fig. 2.5.

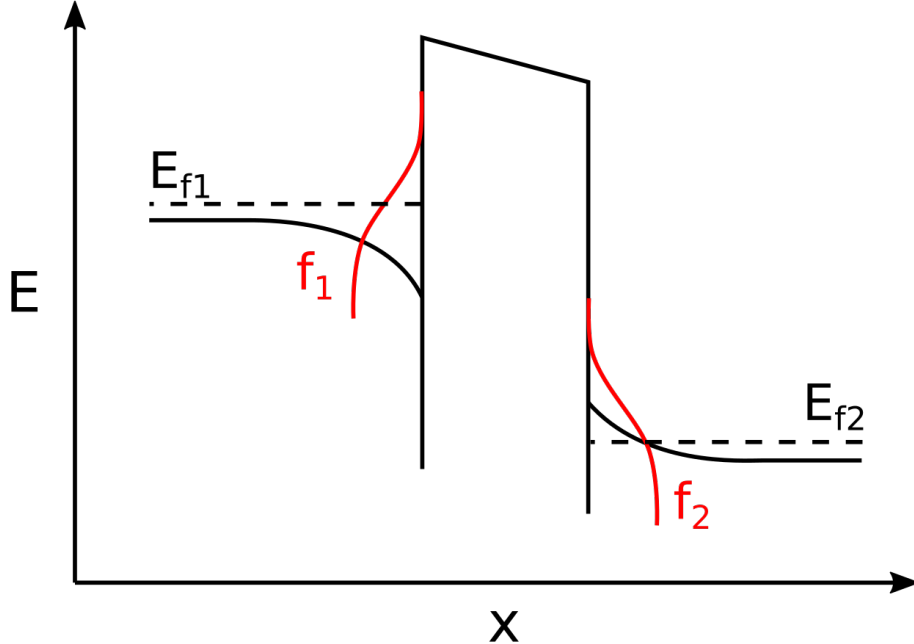


Figure 2.5: Potential barrier with distribution functions f_1 , f_2 of both electrodes.

According to the Tsu-Esaki model [94], the net current through the interface is

$$J = \frac{4\pi m_{eff}q}{h^3} \int_{E_{min}}^{E_{max}} T(E_x)N(E_x)dE_x \quad (2.5)$$

where E_x is the wavevector energy perpendicular to the interface, $T(E_x)$ is the transmission coefficient, $N(E_x)$ is the supply function. This expression approximates the band structure by m_{eff} , such that the dispersion relation is parabolic $E = \frac{\hbar\vec{k}^2}{2m_{eff}}$ in the electrodes, and the transition is uniaxial, which means that only the perpendicular wavevector k is considered in the tunneling process.

2.4.2 Supply Function Modeling

The general form of the supply function can be expressed as [95, 96]

$$N(E) = \int_0^\infty f_1(E_\rho) - f_2(E_\rho)dE_\rho \quad (2.6)$$

where E_ρ is the wavevector energy component perpendicular to E_x and f_1 , f_2 are the energy distribution functions near the respective interface.

With energies above the Fermi level, the energy distribution functions f are approximated by the

well-known Fermi-Dirac statistics

$$f(E) = \frac{1}{1 + \exp\left(\frac{E - E_f}{k_B T}\right)} \quad (2.7)$$

which allows analytic integration of 2.6 to yield a supply function of

$$N(E_x) = k_B T \log \left(\frac{1 + \exp(-\frac{E_x - E_{f1}}{k_B T})}{1 + \exp(-\frac{E_x - E_{f2}}{k_B T})} \right) \quad (2.8)$$

2.4.3 The Energy Barrier

In very small scales, image forces that appear on the metal-insulator interface that smoothen the barrier shape. This especially affects the trapezoidal and triangular potential barriers [97, 98]. The question arises whether it is possible to reproduce the image force effect on the tunnel current curves with only a change in the barrier height, the value of which is usually used as a fitting parameter in tunneling problems. Studies performed by Jiménez-Molinos et al. [99] show that different oxide thicknesses yield results that appear to show decreasing barrier potentials with decreasing oxide thickness, and which are quantitatively explained by considering the interface image energies.

The energy offset within the insulator is [100]

$$\Delta\Phi_d = -\frac{q^2}{16\pi\varepsilon_d} \sum_{i=0}^{\infty} \left((k_l k_r)^i \left[\frac{k_l}{x + it_d} + \frac{k_r}{(i+1)t_d - x} + \frac{2k_l k_r}{(i+1)t_d} \right] \right) \quad (2.9)$$

where x is the position within the dielectric from left to right interface $x = 0..t_d$, t_d being the thickness of the dielectric, ε_d , $\varepsilon_{l/r}$ is the dielectric and left and right electrode permittivities, respectively.

In the electrodes, we have

$$\begin{aligned} \Delta\Phi_l &= -\frac{q^2}{16\pi\varepsilon_l} \sum_{i=0}^{\infty} \left((k_l k_r)^i \left[\frac{-k_l}{it_d - x} + \frac{k_r}{(i+1)t_d - x} \right] \right) \\ \Delta\Phi_r &= -\frac{q^2}{16\pi\varepsilon_r} \sum_{i=0}^{\infty} \left((k_l k_r)^i \left[\frac{-k_r}{(i+1)t_d - x} + \frac{k_l}{it_d + x} \right] \right) \end{aligned} \quad (2.10)$$

The parameters k_l , k_r are permittivity ratios at the left and right interface

$$k_{l/r} = \frac{\varepsilon_d - \varepsilon_{l/r}}{\varepsilon_d + \varepsilon_{l/r}} \quad (2.11)$$

which are close to -1 for ideal metallic interfaces.

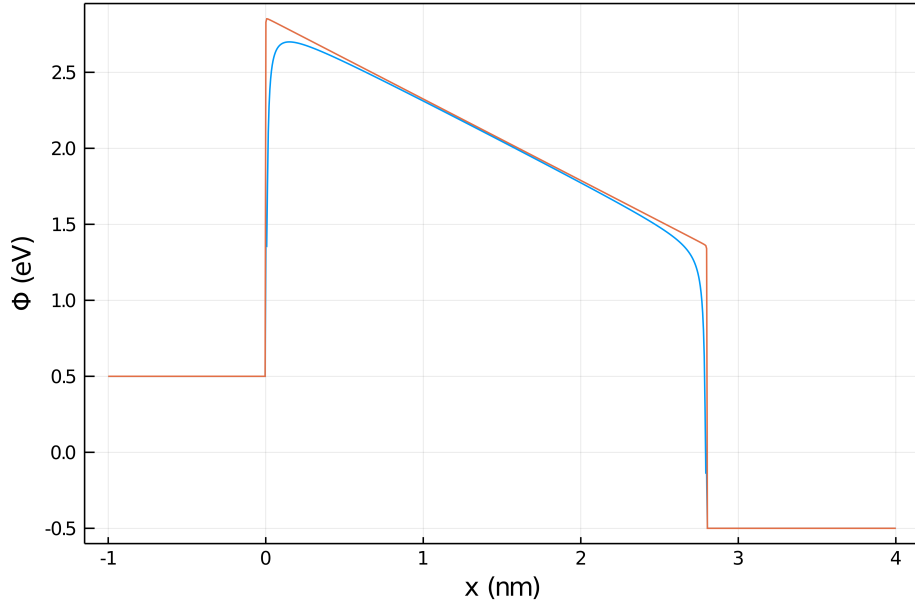


Figure 2.6: Potential barrier deviation from idealized trapezoid. The deviation is estimated assuming a relative permittivity of $\varepsilon_r = 30$ at a potential difference of 1 V.

2.5 Ferroelectric Switching Models

A ferroelectric domain is a region of equal polarization. Domains are separated by domain walls. The interaction between ferroelectric unit cells is governed by two forces: First, a lattice mismatch between adjacent cells of different polarization. This relatively short-ranged effect reaches an energetically favorable state by growing domains. Second, the electrostatics of polarization. This longer-range effect drives the dipoles to align in a heads-to-tails pattern.

When a switching process is initiated, the system has to cross over an intermediary state of higher energy: The first unit cells that flip will be oriented in a head-to-head or tail-to-tail polarization pattern, generating a charged region within the crystal. This charged, 180° domain wall propagates through the ferroelectric at the speed of an optical phonon, thereby transporting charge to the other side.

In general, the process of polarization reversal requires three steps. First, new domains nucleate at energetically favorable points. Second, these domains grow along the polarization axis, and third, the formed pillars expand orthogonally to the applied electric field.

Mulaosmanovic et al. [101] demonstrated that ferroelectric $\text{Hf}_{0.5}\text{Zr}_{0.5}\text{O}_2$ exhibits multiple ferroelectric domains with distinct switching characteristics in the polycrystalline material layer. In these small ferroelectric crystallites the polarization reversal can be described by a nucleation limited process [102]. That is, the growth of the ferroelectric domains is not a dominant factor and hence the individual domains switch very abruptly. From that behavior one might deduce that a smooth transition between many different resistance states requires the existence of a large number of domains inside the FTJ, and which will have an influence on the scalability of the polycrystalline $\text{Hf}_{0.5}\text{Zr}_{0.5}\text{O}_2$ based FTJ. Relief could be found by introduction of epitaxial growth of monocrystalline ferroelectric layers [103] where a domain might extend over a larger area and where domain wall motion might allow a more analogue switching behavior even in smaller devices.

In the ferroelectric hafnium oxide layers there exists a trade-off between switching speed and applied switching voltage [102] to achieve switching of these films in the ns-regime [104]. The typically measured current density of an FTJ is in the range of $1 \mu\text{A cm}^{-2}$. Thus, scaling the FTJ to the nm^2 -regime would result in very small read currents in the range below 1 pA . Hence, a very precise probing operation has to be ensured by the sensing circuitry. Accumulative switching effects might lead to a degradation of the TER after multiple subsequent read operations [105]. The retention behavior of the FTJ is limited by the depolarization field that might yield to a back-flipping of ferroelectric domains. Furthermore, especially in semiconductor electrodes, it was reported that charge trapping into the interfacial region between the ferroelectric layer and the dielectric layer can lead to a degradation of the TER.

2.5.1 Landau-Khalatnikov Double Potential Well

The Landau-Khalatnikov (LK) model can be used to describe the energy density of the whole polycrystalline ferroelectric film according to Hoffmann et al. [106]. The total energy density u of a grain can be expressed by a Landau-Ginzburg-Devonshire (LGD) polynomial

$$u(Q) = a_1 P^2 + a_{11} P^4 + a_{111} P^6 - (E_F - E_b) P \quad (2.12)$$

where E_b is the bias field observed within $\text{Hf}_{0.5}\text{Zr}_{0.5}\text{O}_2$ -based ferroelectric thin films (see Schenk et al. [107]), and E_F is the externally applied voltage. Using parameters according to table 2.2, this yields the bistable polarization states shown in Fig. 2.7.

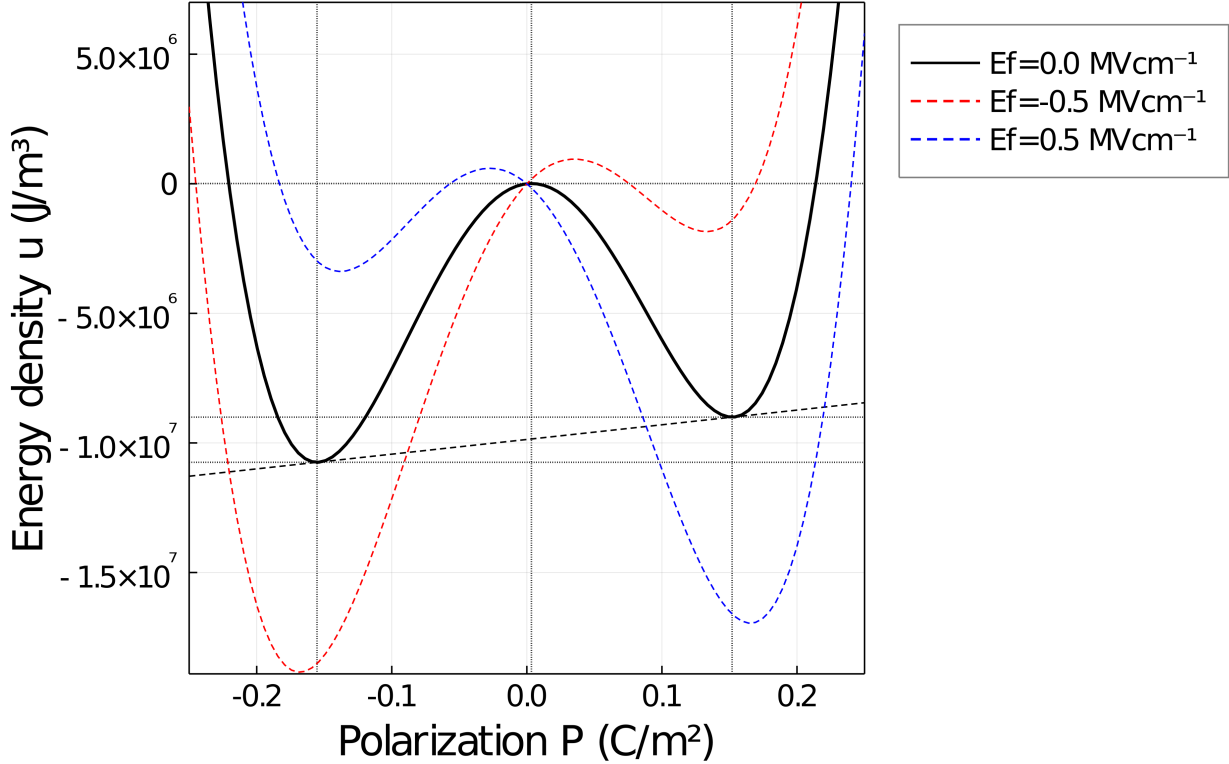


Figure 2.7: Energy density according to the Landau-Ginzburg-Devonshire model and additional bias field without external voltage $E_F = 0$ (black), negative and positive voltages (red, blue).

From 2.12, the total energy of an individual grain can be expressed in terms of the grain charge $Q = PA$

$$U(V_F) = \alpha Q^2 + \beta Q^4 + \gamma Q^6 - (V_F - V_b) Q \quad (2.13)$$

where A is the grain area, d its thickness, $\alpha = a_1 d/A$, $\beta = a_{11} d/A^3$, $\gamma = a_{111} d/A^5$ are the Landau coefficients normalized to the grain geometry, V_b is the bias field observed with $\text{Hf}_x\text{Zr}_{1-x}\text{O}_2$ -based ferroelectrics (see Schenk et al. [107]), and V_F is the externally applied voltage.

Assuming an internal grain resistance $\rho = \rho_G d/A$, the grain charge is expressed as the differential equation

$$\rho \frac{\partial Q}{\partial t} = -\frac{\partial U}{\partial Q} = -\left(2\alpha Q + 4\beta Q^3 + 6\gamma Q^5 - (V_F - V_b)\right) = V_F - V_i(Q) \quad (2.14)$$

where $V_i(Q)$ is the charge-dependent internal voltage component

$$V_i(Q) = 2\alpha Q + 4\beta Q^3 + 6\gamma Q^5 + V_b \quad (2.15)$$

The equivalent circuit of the model expressed by Eq. 2.14 is shown in Fig. 2.8. The characteristic model response for a distribution of grains is graphed in Fig. 2.9. For the modeling of an FTJs, the network of parallel grains is supplemented by a voltage-dependent parallel resistor to describe leakage currents.

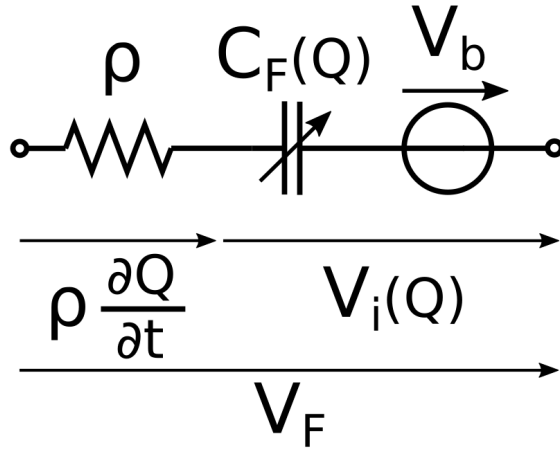


Figure 2.8: Equivalent circuit diagram model for a single, non-leaking $\text{Hf}_x\text{Zr}_{1-x}\text{O}_2$ grain. The ferroelectrically bound charges are represented by a bistable capacity.

The capacity of the tunable capacitor (Fig. 2.8) depends on the amount of charge. Its value can even be negative when the ferroelectric has passed a certain threshold polarization for which the polarization flipping process self-reinforces.

Parameter	mean value	unit	description
a_1	-8.36×10^8	$\text{mF}^{-1}\text{C}^{-2}$	polynomial coeff. order 2
a_{11}	1.77×10^{10}	$\text{m}^5\text{F}^{-1}\text{C}^{-2}$	polynomial coeff. order 4
a_{111}	0.0	$\text{m}^9\text{F}^{-1}\text{C}^{-2}$	polynomial coeff. order 6
ρ_G	1.776×10^7	Ωm	grain internal resistivity
$E_b = V_b/d$	5.67×10^6	Vm^{-1}	bias field

Table 2.2: Geometry-independent parameters: Landau coefficients, intrinsic bias field and resistivity, according to Hoffmann et al. [106]

While a single crystal can be described by a single set of model parameters, the polycrystalline ferroelectric requires a statistical distribution of model parameters across the individual grains [108].

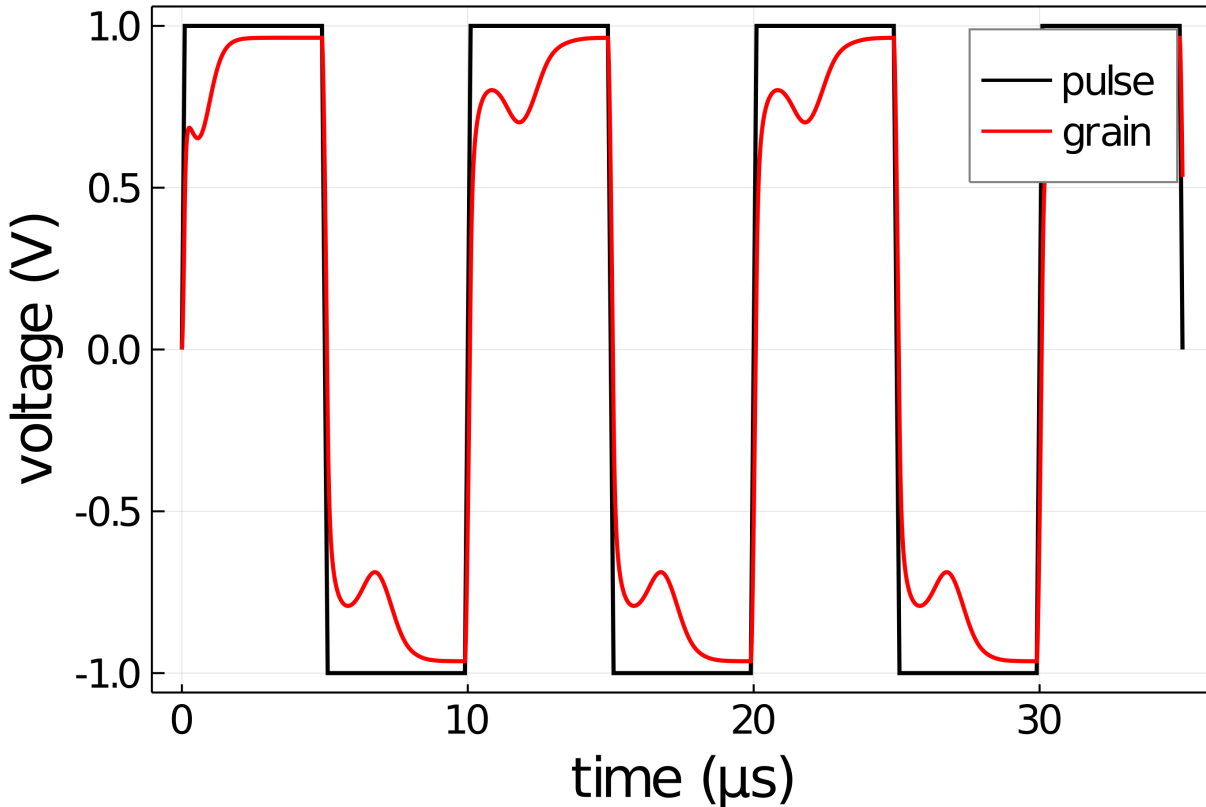


Figure 2.9: MGLK switching dynamics. At the point of ferroelectric switching, a sudden increase in the time-dependent capacity leads to a voltage drop.

2.5.2 Kolmogorov-Avrami-Ishibashi (KAI) Model

The Kolmogorov-Avrami-Ishibashi (KAI) model describes the switching kinetics of ferroelectrics by a simple Arrhenius expression [109–113]:

$$\frac{\Delta P(t)}{2P_s} = 1 - \exp \left[\left(-\frac{t}{\tau} \right)^n \right] \quad (2.16)$$

where n is the effective dimensionality of the domain growth, τ is the characteristic time and P_s is the spontaneous polarization. This model differentiates into two cases [109]: The α -model, where nucleation occurs with a constant rate during switching ($n = D + 1$) and the β -model, where nucleation occurs only at $t = 0$ ($n = D$). D is the geometrical growth dimensionality of the system. $D = 1$ for stripe-like domains, $D = 2$ for circular domains, and $D = 3$ for spherical domains.

Although the KAI model gives a good description of the switching kinetics of ferroelectric single crystals and sometimes epitaxial thin films [113, 114], it encounters problems when it comes to correctly describing the domain reversal behavior of polycrystalline thin films [115–117]

The strong retardation of the switching curves at medium or low fields for these films has been explained via polarization processes with a broad distribution of relaxation times [115], the nucleation-limited switching (NLS) model, [118] or the Lorentzian distribution of logarithmic switching times [116].

2.5.3 Nucleation Limited Switching (NLS) Model

The Nucleation limited switching (NLS) model describes the transient behavior in polycrystalline ferroelectrics using a statistical distribution of grain properties, such as switching times. Both thin films and bulk materials can be modeled, including effects such as negative capacitance. The model can be quantified by a parallel and serial network of individual grains with a distribution of properties.

2.5.4 Inhomogeneous Field Mechanism (IFM) Model

Although the NLS and KAI models are able to describe experimental measurements with high accuracy, they neglect several crucial physical aspects of the poling problem. A disordered granular structure in a polarized state is unavoidably accompanied by charge formation on grain boundaries (GB), therefore giving rise to additional electric fields. Charges on grain boundaries should vary depending on polarization, therefore depolarization fields should be also time dependent. The latter fact, however, is omitted in the NLS as well as in the KAI models.

The IFM model remedies these limitations by replacing the constant electric field by an distribution of fields within the domain. It is based on Merz' law to describe the local switching time τ

$$\tau(E) = \tau_0 \exp(E_a/E)^n \quad (2.17)$$

with a characteristic time τ_0 , activation field E_a and $n = 1$ to 2.5. With an applied field $E - F$, and a generalized distribution of the electric field $Z(E, E_F)$, the total polarization is expressed as

$$\Delta P(E_F, t) = \int_0^\infty (p(t, \tau(E)), Z(E, E_F)) dE \quad (2.18)$$

Assuming a Heaviside step function shape $p(t, \tau) = 2P_s H(E - E_{th}(t))$ and the peak polarization P_s , the threshold field E_{th} is expressed by restating Merz' law

$$E_{th}(t) = E_a \log(t/\tau_0)^{-1/n} \quad (2.19)$$

Using a Gaussian distribution of field values E/E_F with standard deviation σ to describe the nonuniform nature of the $\text{Hf}_x\text{Zr}_{1-x}\text{O}_2$ film, the polarization from Eq. 2.18 is solved as [119]

$$\Delta P(E_F, t) = P_s \operatorname{erfc} \left(\frac{1}{\sqrt{2}\sigma} \left(\frac{E_{th}(t)}{E_F} - 1 \right) \right) \quad (2.20)$$

where erfc is the complementary error function. IFM model parameters from literature are summarized in table 2.3. The corresponding switching behavior is shown in Fig. 2.10.

Parameter	value	unit	description
P_s	0.25	Cm^{-2}	ferroelectric polarization
σ	0.22	1	standard deviation of local field
E_a	3.91×10^8	Vm^{-1}	activation field
τ_0	137×10^{-12}	s	characteristic time

Table 2.3: IFM model parameters for $\text{Hf}_x\text{Zr}_{1-x}\text{O}_2$, according to Li et al. [119]

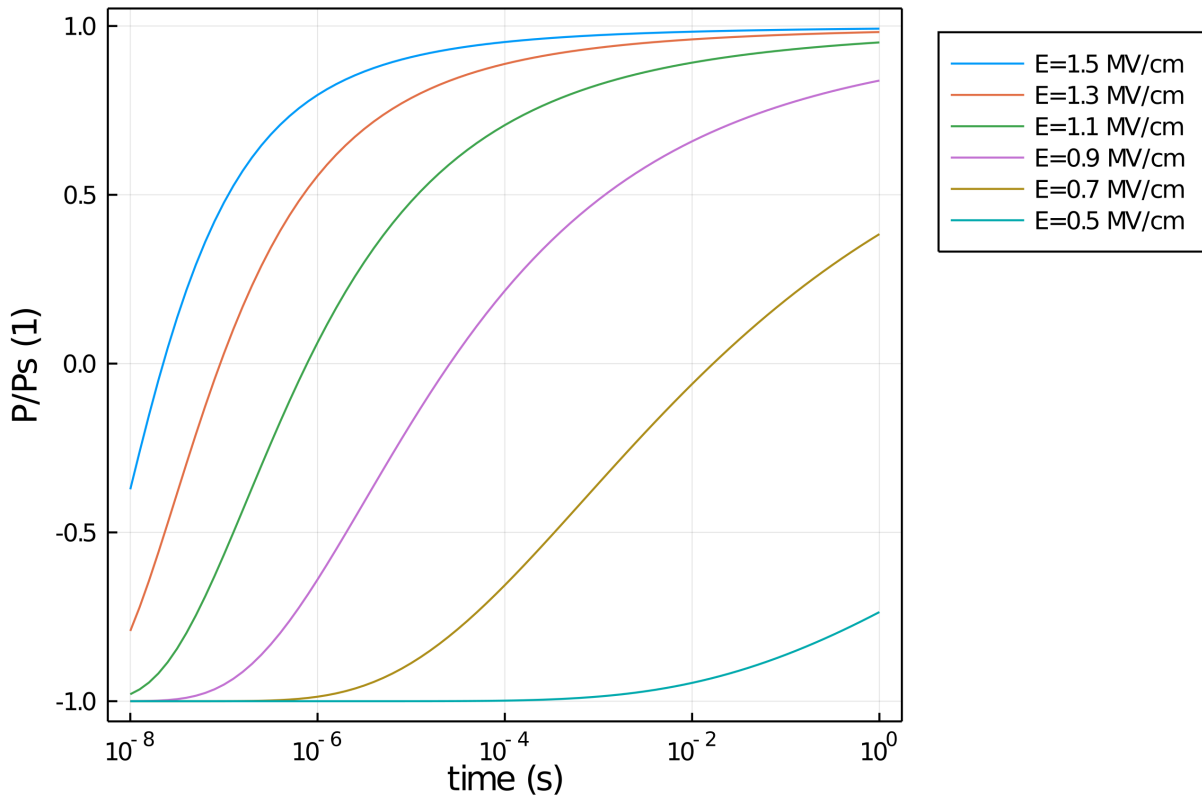


Figure 2.10: IFM switching dynamics. With a constant external field, the polarization switching initiates slowly. The switching accelerates approximately until half of the domains are flipped, after which it approaches the opposite polarization asymptotically.

2.6 Resistive Vacancy Switching

The resistive switching effect in transition metal oxides is frequently linked to the valence change mechanism (VCM). Three physical phenomena are involved in this process: The forming of the conductive filament, the conduction mechanism and the transient evolution under the Joule heating effects. Both the filament formation and rupture process are driven by an electrochemical reduction-oxidation reaction combined with oxygen vacancy migration [120]. Despite that, the conduction mechanism substantially depends on the dielectric and electrodes materials. In $\text{Hf}_x\text{Zr}_{1-x}\text{O}_2$ -based thin-films that contain sufficient traps, the phonon-assisted tunneling between traps (PATT) model has recently been shown to accurately model these thin-film devices [121, 122].

In the following sections, we extend this model by coupling it with the valency mechanism.

2.6.1 Valency Model

Besides the idealized, pristine insulator, direct tunneling mechanisms discussed in section 2.4, we can also observe a voltage and cycle dependent component of the conduction mechanism. This mechanism is identified in literature [123–126] by electrochemical reactions forming and annihilating oxygen vacancies at the metal/insulator interfaces.

This phenomenon is used in metal oxide-based ReRAM devices, resistive switching is typically based on the drift of oxygen vacancies. These vacancies can either be produced during an electroforming cycle, or initially be present in the insulator [127–130]. The difference in chemical properties between the electrodes determines the asymmetry of the device switching behavior.

The reduction within the insulator in terms of the Kröger-Vink-Notation starts with the dislocation of an oxygen atom at the interface with an externally applied positive voltage U



where $\frac{1}{2} \text{O}_2$ denotes the oxygen originating from the insulator, physisorbed to the grain of the electrode. Once vacancies near the interface have formed, they form a migration path for deeper oxygen, allowing the reaction to continue. With a metallic electrode that is inert and impermeable to oxygen diffusion, the oxygen accumulates within the interface. Since typical top electrode metals, such as Pt or Au are relatively soft, thin, and have only weak adhesive characteristics, this recombed oxygen can locally detach the interface [131, 132]. For this reason, Cr, Ni or Ti intermediary adhesion layer are sometimes used in thin film electrodes to strengthen the bond[133, 134]. However, due to their lower work function, these materials would not form a an effective switching ratio with the bottom TiN electrode. From this, an irreversible loss of oxygen within the insulator and permanent degradation of the device is the consequence.

While this mechanism is not based on the ferroelectric switching of FTJs, it must be considered when describing conductivity and provides a link to device degradation. Besides that, it also offers a secondary mode of operation for the device. In fact, despite its relatively high bond strength, HfO_2 has also been employed in valency switching devices [123, 135–137].

In case of the simple FTJ structure, we assess the phenomenon as a means to distinguish switching modes and to predict device parameter drift and breakdown. With the asymmetric electrodes

required for the ferroelectric switching, this mechanism will be dominated by the electrode with the lower activation energy. In our case, the TiN structure is relatively inert and highly rigid, which makes the bottom electrode highly impermeable to oxygen from the insulator, both with respect to interstitial positions as well as oxygenation. With noble top electrode metals, such as Pt and Au (electronegativity of 2.28 eV and 2.54 eV, as compared to 1.2 eV and 1.3 eV in Hf and Zr), the accumulation of interstitial oxygen at the Pt-interface is likely the predominant mechanism of reducing the insulator.

2.6.2 Phonon-Assisted Tunneling between Traps

To determine a relationship between trap density and the leakage currents, we use the PATT model initially proposed by proposed by Makram-Ebeid and Lannoo [138]. It has been shown that this transport model offers an accurate description of electrical behavior in both ferroelectric and non-ferroelectric $\text{Hf}_{0.5}\text{Zr}_{0.5}\text{O}_2$ [68–72]. The charge transport system can be described by the Shockley-Read-Hall model, and a potential according to Poisson’s equation [139, 140]

$$\frac{\partial n}{\partial t} = -\nabla(nv) + n_t P_{ion} - \sigma nv(N - n_t) \quad (2.22a)$$

$$\frac{\partial n_t}{\partial t} = \sigma nv(N - n_t) - n_t P_{ion} - a\nabla(n_t(1 - n_t/N)P) \quad (2.22b)$$

$$\Delta U = -e\frac{n + n_t}{\epsilon_r \epsilon_0} \text{ and } F = -\nabla U \quad (2.22c)$$

with the electron concentration in the conduction band and traps n, n_t , v the electron velocity, and P_{ion}, P_{tun} the trap ionization and intertrap tunneling rates. The trap capture cross section, trap density and voltage potential are σ, N and U , respectively. The average trap distance is $a = 1/\sqrt[3]{N}$, and F is the electric field.

In deep traps and sufficient trap density, the ionized conduction band transport will be negligible compared to the hopping transport, and we can reduce Eq. 2.22b into

$$\left(\frac{\partial n_t}{\partial t}\right)_{tun} = -a\nabla(n_t(1 - n_t/N)P) = -\frac{1}{q}\nabla J \quad (2.23)$$

where the rightmost identity follows as a result of charge conservation. From this, the stationary transport equation for a 1D uniform trap distribution $N = a^{-3}$ follows as

$$J = \frac{q}{a^2} \frac{n_t}{N} (1 - n_t/N) P \quad (2.24)$$

The parameter P is the transmission rate between traps, which is given by [70, 121]:

$$P = \int_{\varepsilon>0} \frac{\hbar\varepsilon}{m^*a^2kTQ_0} \exp\left(-\frac{(Q-Q_0)^2 - (Q-qFa/Q_0)^2}{2kT}\right) - \frac{4}{3} \frac{\sqrt{2m^*}(\varepsilon^{3/2} - (\varepsilon - qFa)^{3/2})}{qF\hbar} dQ \quad (2.25a)$$

$$\varepsilon = Q_0(Q - Q_0) + W_{opt} \quad (2.25b)$$

$$Q_0 = \sqrt{2(W_{opt} - W_t)} \quad (2.25c)$$

m^* is the charge carrier effective mass, T is the temperature, Q is the configuration coordinate of a trapped-electron-phonon system, F is the local electric field, $-\varepsilon$ is the energy of trapped electrons below the conduction band, Q_0 is the configuration coordinate quantifying electron-phonon interaction [121].

The general non-uniform transitions between traps n_t is obtained by solving the partial differential equation [140]

$$\frac{\partial(n_t)}{\partial t} = -a(x) \frac{\partial(n_t)}{\partial x} \left[\frac{n_t}{N} \left(1 - \frac{n_t}{N} \right) P(t) \frac{\vec{F}}{F} \right] \quad (2.26)$$

which depends exponentially on the applied voltage and temperature due to $P(t) = P(T(t), F(t))$.

2.7 Conduction Models

2.7.1 WKB approximation

The WKB method is an approximative semiclassical approach to compute the stationary solution of the Schrödinger equation without struggling with the difficulties of a second order differential equation. Taking the time-independent, one-dimensional Schrödinger equation

$$-\frac{\hbar^2}{2m_e} \partial_x^2 \psi(x) + (\phi(x) - E)\psi(x) = 0 \quad (2.27)$$

with the ansatz function

$$\psi(x) = R(x) \exp\left(i \frac{S(x)}{\hbar}\right) \quad (2.28)$$

we find the real and imaginary components

$$\partial_x^2 R \frac{R}{\hbar^2} (\partial_x S)^2 + \frac{2m_e(E - \phi(x))}{\hbar^2} R = 0 \quad (2.29)$$

$$R \partial_x^2 S + 2\partial_x R \partial_x S = 0 \quad (2.30)$$

for Eq. 2.27. Combining the solution of Eq. 2.30

$$\partial_x S = \frac{C}{R^2} \quad (2.31)$$

into 2.29 yields

$$1/R \partial_x^2 R - 1/\hbar^2 (\partial_x S)^2 + \frac{2m_e(E - \phi(x))}{\hbar^2} = 0. \quad (2.32)$$

Applying the approximation

$$1/R \partial_x^2 R \ll 1/\hbar^2 (\partial_x S)^2 \quad (2.33)$$

for 2.29 yields

$$S(x) \approx \int \sqrt{2m(E - \phi(x))} dx \quad (2.34)$$

and the ansatz 2.28 becomes

$$\psi(x) = R(x) \exp\left(i/\hbar \int \sqrt{2m(E - \phi(x))} dx\right) \quad (2.35)$$

With an energy barrier between points $x_{1,2}$, the incoming and transmitted waves $\psi_{1,2}$ become

$$\psi_1(x \leq x_1) \sim \exp\left(i/\hbar \int_{-\infty}^{x_1} \sqrt{2m(E - \phi(x'))} dx'\right) \quad (2.36)$$

$$\psi_2(x \geq x_2) \sim \exp\left(i/\hbar \int_{-\infty}^{x_2} \sqrt{2m(E - \phi(x'))} dx'\right) \quad (2.37)$$

With this, the transmission $T(E)$ can be expressed as [141]

$$T(E) = \left| \frac{\psi_2(x_2)}{\psi_1(x_1)} \right|^2 = \exp\left(-2/\hbar \int_{x_1}^{x_2} \sqrt{2m(\phi(x') - E)} dx'\right) \quad (2.38)$$

This formula also applies to classical forbidden regions where the particle energy E lies below the potential barrier $\phi(x)$. Assuming a negligible amount of charges in the potential barrier, the potential barrier can be written as a linear function

$$\phi(x) = \phi_1 + \frac{\phi_2 - \phi_1}{x_2 - x_1}(x - x_1) = \phi_1 + q_0 F_{ox}(x - x_1) \quad (2.39)$$

where ϕ_1, ϕ_2 are the edge potentials of the barrier located between x_1, x_2 , which can also be expressed in terms of an internal electric field F_{ox} .

If the edge potentials $\phi_{1,2}$ are higher than the particle energy E , the width of the potential barrier is fixed by the oxide thickness, yielding a trapezoidal barrier (Fig. 2.11 left).

For this trapezoidal case, Eq. 2.38 yields

$$T(E) = \exp\left(-4 \frac{2\sqrt{2m_e}}{3\hbar q F_{ox}} (q\phi_2 - E)^{3/2} - (q\phi_1 - E)^{3/2}\right) \quad (2.40)$$

When the edge potential ϕ_2 drops below the particle energy E , the barrier effectively becomes triangular, decreasing the effective barrier width to

$$x_m = x_1 + \frac{qF - \phi_1}{q_0 F_{ox}} \quad (2.41)$$

This case is called Fowler-Nordheim Tunneling (Fig. 2.11 middle). Evaluating Eq. 2.38 with the upper integral bound of x_m then yields

$$T(E) = \exp\left(-4\frac{2\sqrt{2m_e}}{3\hbar qF_{ox}}(q\phi_1 - E)^{3/2}\right) \quad (2.42)$$

The case of opposite polarity (Fig. 2.11 right) follows from interchanging ϕ_1 with ϕ_2 .

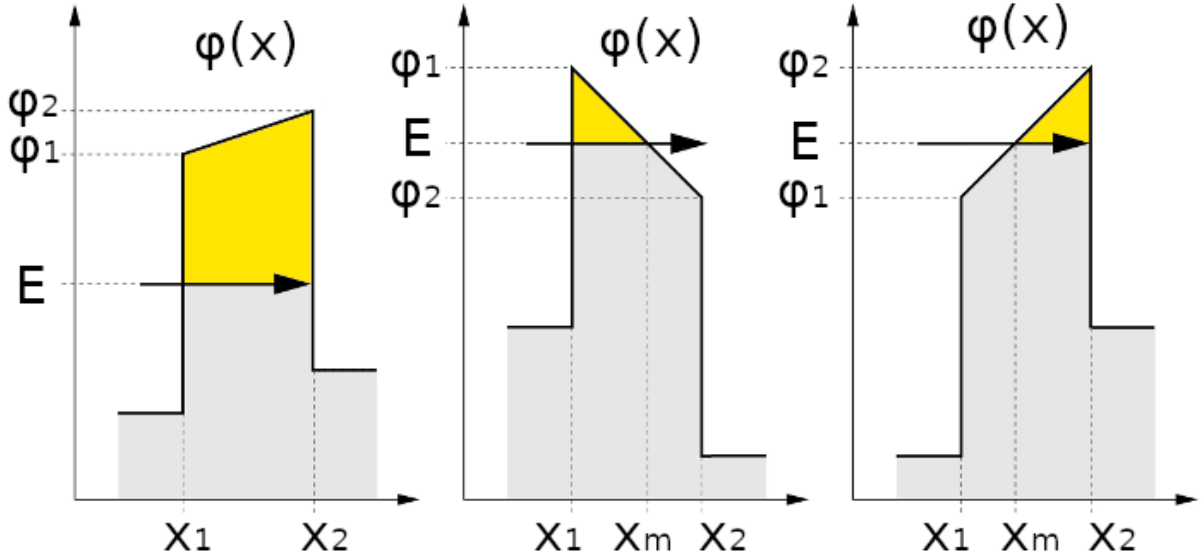


Figure 2.11: Schematic representation of a trapezoidal (left) and a triangular barrier for a negative (middle) and a positive (right) bias voltage.

Tunneling across a Trapezoidal Barrier: Inserting the Trapezoidal Barrier WKB Approximation into the Esaki Equation, the tunneling current density can be expressed as [59]

$$j_{DT} = C \frac{\exp\left[\alpha\left(\left(\phi_2 - \frac{eV}{2}\right)^{3/2} - \left(\phi_1 + \frac{eV}{2}\right)^{3/2}\right)\right]}{\alpha^2 \left[\sqrt{\phi_2 - \frac{eV}{2}} - \sqrt{\phi_1 + \frac{eV}{2}}\right]^2} \sinh\left[\frac{3eV}{4}\alpha\left(\sqrt{\phi_2 - \frac{eV}{2}} - \sqrt{\phi_1 + \frac{eV}{2}}\right)\right] \quad (2.43)$$

where $C = -\frac{4em_e^*}{9\pi^2\hbar^3}$, $\alpha = \frac{4d\sqrt{2m_e^*}}{3\hbar(\phi_1 + eV - \phi_2)}$, m_e^* is the effective electron tunneling mass, ϕ_1 and ϕ_2 are the interface potential barriers. It is noteworthy that this equation only depends only on these three material parameters, and shows an exponential relationship with the thickness d .

Tunneling across a Triangular Barrier (Fowler-Nordheim Tunneling): This equation is derived analogous to the trapezoidal case:

$$j_{FN}(d) = \frac{e^3 m_e}{8\pi h m_e^* \Phi_B} E^2 \exp\left(-\frac{8\pi\sqrt{2m_e^*}}{3he} \frac{\Phi_B^{3/2}}{E}\right) \quad (2.44)$$

with the electric field comprising the applied and band components $E = E_{ap} + E_{Band} = -U/d + \frac{\phi_2 - \phi_1}{ed}$ and the potential barrier Φ_B that the electrons must overcome across the ferroelectric, ϕ_1 for $U > 0$ and ϕ_2 for $U < 0$ [142].

The effective tunneling distance decreases with increasing electric field E , creating an even larger dependence of tunneling currents on the electric field.

2.7.2 Quantum Transmitting Boundary Method

The Quantum Transmitting Boundary Method (QTBM) method provides a relatively simple method to generalize the WKB results from the previous section to potential barriers of arbitrary shape. Starting from the 1D effective-mass Schrödinger Equation

$$\left(-\frac{\hbar^2}{2}\nabla \frac{1}{m^*(x)}\nabla + V(x)\right)\Psi(x) = E\Psi(x) \quad (2.45)$$

we build a finite difference approximation

$$\left.\frac{\partial\Psi}{\partial x^2}\right|_{x_i} \approx \frac{1}{\Delta x^2} [\Psi_{i-1} - 2\Psi_i + \Psi_{i+1}] \quad (2.46)$$

where subscript i is the value at the position of the corresponding lattice point x_i . Considering that Ψ must be differentiable, one obtains diagonal matrix elements

$$d_i = \frac{\hbar^2}{4\Delta x^2} \left(\frac{1}{m_{i-1}^* + m_i^*} + \frac{1}{m_i^* + m_{i+1}^*} \right) + V_i \quad (2.47)$$

and off-diagonal symmetric elements

$$s_i = \frac{\hbar^2}{4\Delta x^2} \frac{1}{m_{i-1}^* + m_i^*} \quad (2.48)$$

The boundary elements $i = 1$ and $i = n$ are described in terms of

$$\begin{aligned}\psi_1 &= a_1 \exp(-ik_1 x_1) + b_1 \exp(-ik_1 x_1) \\ \psi_n &= a_n \exp(-ik_n x_n) + b_1 \exp(-ik_n x_n)\end{aligned}\tag{2.49}$$

where a_0, a_n are the amplitudes of incoming waves, b_0, b_n amplitudes of outgoing waves. The boundary conditions are subject to the steady-state constraints

$$\begin{aligned}\Psi_1 &= a_1 + b_1 \\ \Psi'_1 &= ik_1 (a_1 + b_1) \\ \Psi_n &= a_n + b_n \\ \Psi'_n &= ik_n (a_n + b_n)\end{aligned}\tag{2.50}$$

Choosing the incoming waves a_0, a_n of our system, we obtain Robin boundary conditions of our system:

$$\begin{aligned}a_1 &= \frac{1}{2} (\Psi_1 - i\Psi'_1/k_1) \\ a_n &= \frac{1}{2} (\Psi_n - i\Psi'_n/k_n)\end{aligned}\tag{2.51}$$

Abbreviating $z_i := \exp(-ik_i x_i)$, and solving the Schrödinger Equation at the boundaries, we obtain

$$\begin{aligned}E &= d_1 - s_1(z_1 + z_1^{-1}) \\ E &= d_n - s_n(z_n + z_n^{-1})\end{aligned}\tag{2.52}$$

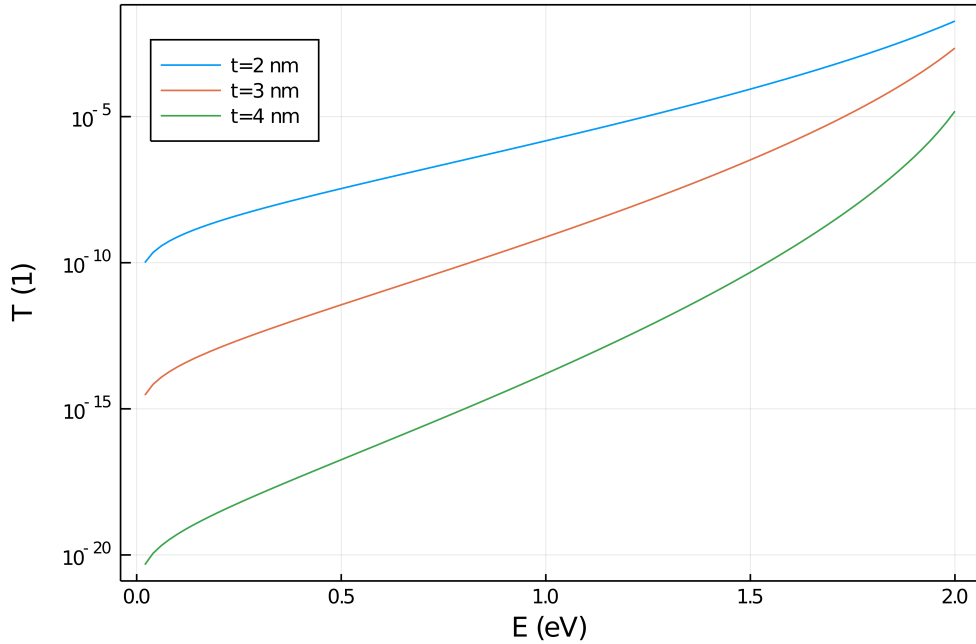
This implicit set of equations is used calculate z_i, z_n for a given energy E . Choosing the solution with $|z| \leq 1$, $\text{im}(z) \geq 0$, we obtain for the Matrix elements for the discretized system as

$$\begin{aligned}a_1 &= \frac{\Psi_1 - z_1 \Psi_2}{z_1^2 + 1} = \alpha_1 \Psi_1 + \beta_1 \Psi_2 \\ a_n &= \frac{\Psi_n - z_n \Psi_{n-1}}{z_n^2 + 1} = \alpha_n \Psi_n + \beta_n \Psi_{n-1}\end{aligned}\tag{2.53}$$

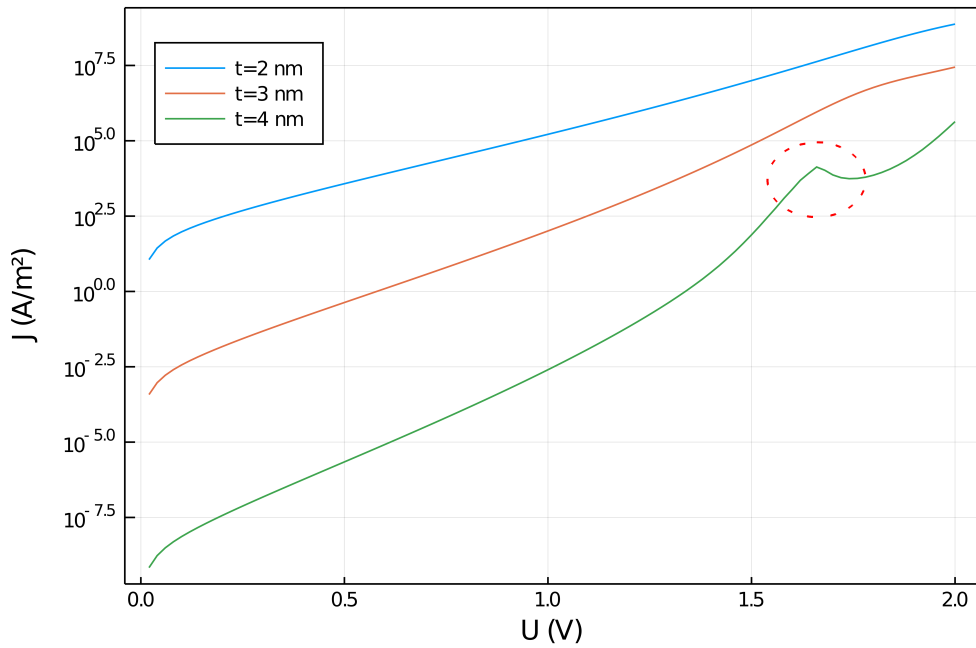
which yields the discretized $n \times n$ tridiagonal complex-valued system

$$G_{i,j}^{-1} \dot{\Psi}_j = a_i \tag{2.54}$$

where G is Green's function for the Schrödinger equation, with additional QTBM boundaries. Besides transmission, the system's eigenstates describe the resonant states of the system.



(a) QTBM transmission coefficient over thickness.



(b) QTBM tunneling current over thickness. The 4 nm thick barrier (green line) exhibits a slight resonance peak at 1.7 V

2.7.3 Tight Binding Model

The tight binding method allows the calculation of the electronic band structure by describing valency electrons with wave functions for each atomic site within the lattice [143]. Essentially, a tight binding model consists of a graph of vertices and edges that correspond to lattice sites and hopping transitions. These can be described by onsite and hopping Hamiltonians [144].

The complex band structure in the bandgap region describes the evanescent electron wave. This allows for efficient device simulations. The Hamiltonian describing the system can be parametrized by ab initio simulations. Dong et al. [77] demonstrated that the effective mass approximation using a $2 \times 2 k \cdot p$ Hamiltonian describes the bands contributing to charge transport adequately in orthorhombic $\text{Hf}_x\text{Zr}_{1-x}\text{O}_2$. The Hamiltonian is expressed as

$$H(k_x, k_y) = \begin{pmatrix} E'_C + \frac{\hbar^2 k_z^2}{2m_{Cz}} & \hbar k_z \nu \\ \hbar k_z \nu & E'_V + \frac{\hbar^2 k_z^2}{2m_{Vz}} \end{pmatrix} \quad (2.55)$$

where $E'_C = E_{C0} + \frac{\hbar^2 k_x^2}{2m_{Cx}} + \frac{\hbar^2 k_y^2}{2m_{Cy}}$, and $E'_V = E_{V0} + \frac{\hbar^2 k_x^2}{2m_{Cx}} + \frac{\hbar^2 k_y^2}{2m_{Cy}}$. m_{Cx} , m_{Cy} , m_{Vx} , m_{Vy} are the fitted effective mass at the Γ point along the x- and y-direction, ν is a fitting parameter, and E_{C0} and E_{V0} are the minimum and maximum value of conduction band and valence band at the Γ point that provide the minimum decay constant κ in the band gap region, and m_{Cz} and m_{Vz} are the corresponding fitted effective masses.

We use the Kwant Project tight binding simulator [145] to support the WKB and QTBM solutions.

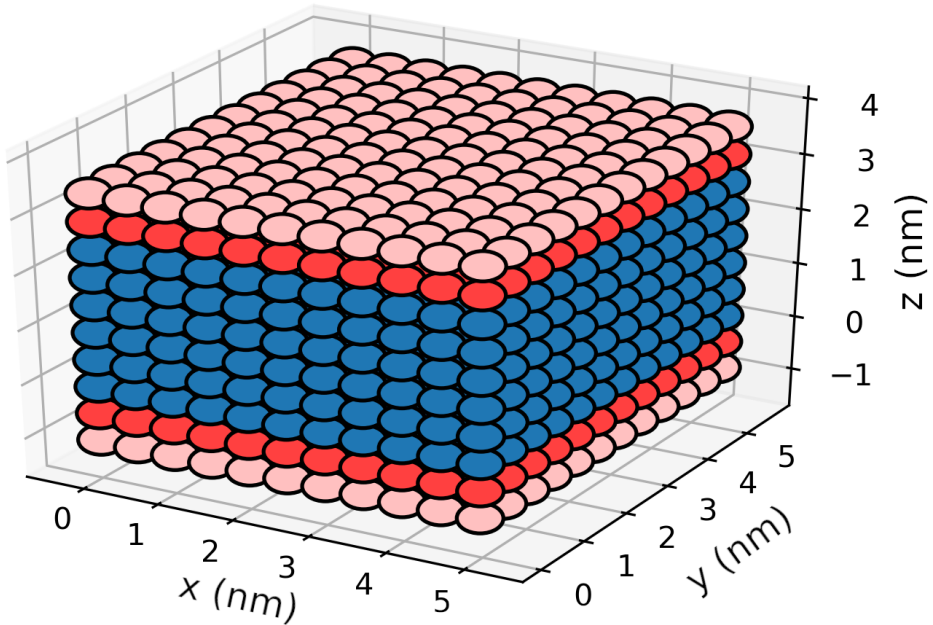


Figure 2.13: Tight binding model, 3D lattice of the 6 unit cell insulator (blue) and infinite electrodes (red)

Using the Non-Equilibrium Green Function (NEGF) formalism, the scattering matrix $S_{n,m}$ and the wave function ϕ_n of the system is calculated by Kwant. The current density is then obtained by the energy integral

$$J = \int (f_S - f_D) T_{SD} dE \quad (2.56)$$

where f_S , f_D are the Fermi functions of the source and drain lead, and T_{SD} is the transmission coefficient between the two.

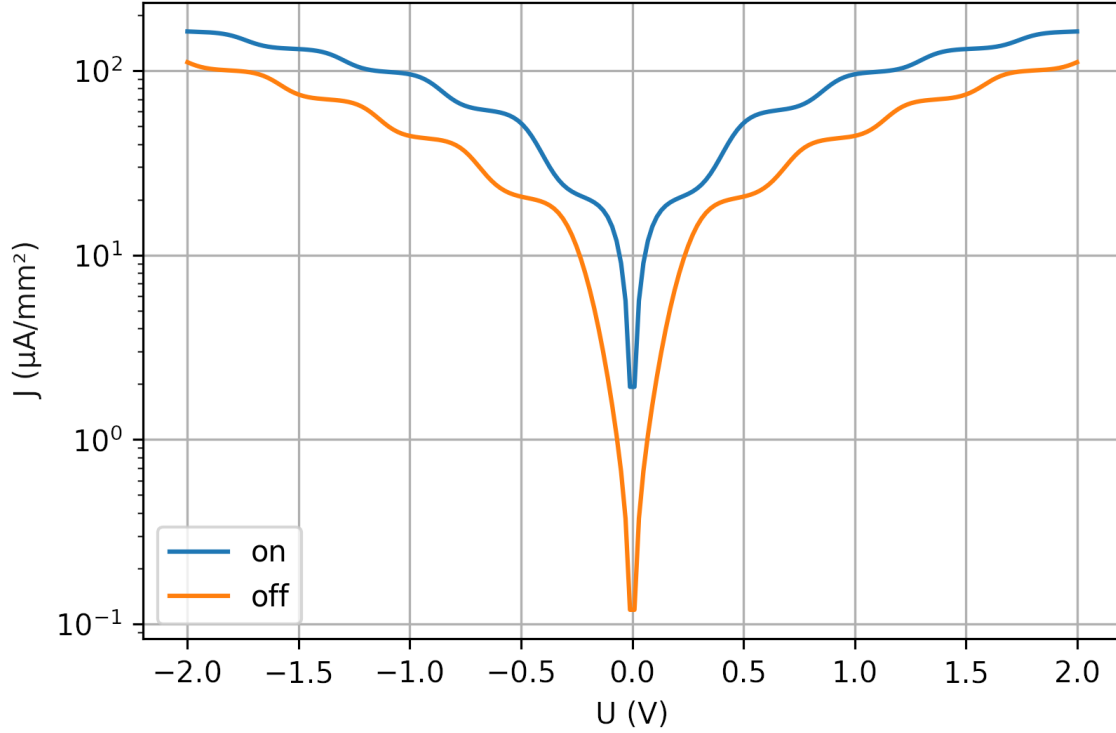


Figure 2.14: Current density, obtained from 3D Tight binding model. The step structure indicates discrete energy steps of the quantum system. The resulting current densities are on the same order of magnitude as obtained from the 1D QTBM approximation, however the curve shape remains slightly subexponential over the full voltage regime.

Parameter	value	unit	description
a	4.9619	Å	lattice constant
b	5.1695	Å	lattice constant
c	4.9749	Å	lattice constant
m_C^x	0.4205	m_0	eff. mass, conduction band, along x
m_V^x	7.6609	m_0	eff. mass, valency band, along x
m_C^y	0.5785	m_0	eff. mass, conduction band, along y
m_V^y	1.2132	m_0	eff. mass, valency band, along y
m_C^z	0.4086	m_0	eff. mass, conduction band, along z
m_V^z	0.5914	m_0	eff. mass, valency band, along z
v	8.7×10^5	m/s	coupling factor (off-diagonal 2x2 Hamiltonian)

Table 2.4: $\text{Hf}_x\text{Zr}_{1-x}\text{O}_2$ tight binding model parameters for the orthorhombic phase according to Yoon et al. [59]. The effective masses are specified with regards to the Γ point.

2.7.4 Thermionic Conduction

Thermionic conduction occurs when the thermal (kinetic) energy of charge carriers suffices to reach the conduction bands of the insulator. The barrier height is lowered by image force lowering, called the Schottky effect. For voltage potentials much higher than the thermal energy (>100 mV at RT), this is described by[142]

$$J(E, T) = AT^2 \exp\left(-\frac{1}{k_B T} \left(\Phi_B - \sqrt{\frac{q^3 E}{4\pi\varepsilon_0\varepsilon_r}}\right)\right) \quad (2.57)$$

where A is the effective Richardson's constant, ϕ is the potential barrier facing towards the larger charge carrier density (side of negative voltage in case of electrons), and T is the temperature. This current scales with temperature, but not with barrier thickness. For this reason, this current becomes negligible at very small thicknesses. It has been shown that this is typically the case for devices below 4 nm [54], making it unobservable in practical FTJs.

2.8 Practical Considerations

Effective Work Function Engineering

The presence of point defects can modulate this dipole and the Effective Work Function (EWF), thus affecting the threshold voltage. Among the HfO₂ native defects, the O vacancy is a dominant intrinsic electronic defect [146]. There have been some studies of the EWF computation, and the effects of O vacancies on the Schottky barrier height and EWF modulation, using the phenomenological theory of band offset – the so-called Metal Induced Gap States (MIGS) model developed by Robertson [147–149]. This method describes the charge transfer at the metal-insulator interface in terms of the alignment of a charge neutrality level with the metal Fermi level.

Dependence on the Crystalline State of the TiN Electrode

According to Sun et al. [150], it is found that Pt/HfO₂/TiN devices with crystallized TiN electrode exhibited a typical bipolar resistive switching behavior, while the I-V curves of the Pt/HfO₂/TiN devices with amorphous TiN electrode showed the unipolar resistive switching behavior regardless of

voltage polarity, which is similar to the Pt/HfO₂/Pt devices. It is believed that this originates from the different oxygen reservoir ability of TiN with different fabricating process. Moreover, the resistive random-access memory (ReRAM) device with the new structure of TiN (amorphous)/HfO₂/TiN (crystallized) exhibited the bipolar resistive switching behavior [150]. When conductive filaments are formed, the unipolar mechanism is called fuse-antifuse.

Chapter 3

Materials and Methods

This chapter describes the manufacturing process and requirements to obtain the ferroelectric phase within the $\text{Hf}_x\text{Zr}_{1-x}\text{O}_2$ thin film, as well a quantitative estimation of the effect of dead layers on the metal-insulator interface.

3.1 $\text{Hf}_x\text{Zr}_{1-x}\text{O}_2$ Material Characterization

To obtain the ferroelectric $\text{Hf}_x\text{Zr}_{1-x}\text{O}_2$ phase, several energetic contributions have been observed to stabilize this otherwise energetically unfavorable phase. Amongst them, a mixture with about equal parts of Hf:Zr atoms [151], combined with substrate and grain boundary contributions are thought to be key factors for this stabilization. Besides Zr, a range of other dopants [152, 153] and oxygen vacancies [132] can stabilize this metastable phase. An overview of the crystal phases in HfO_2 is shown in Fig. 3.1. As shown in Fig. 3.2, the energetically favourable phase depends on grain radius, and only a small window allows for the formation of the orthorhombic phase, which requires a consistent annealing process, while pure ZrO_2 does not form a stable orthorhombic phase.

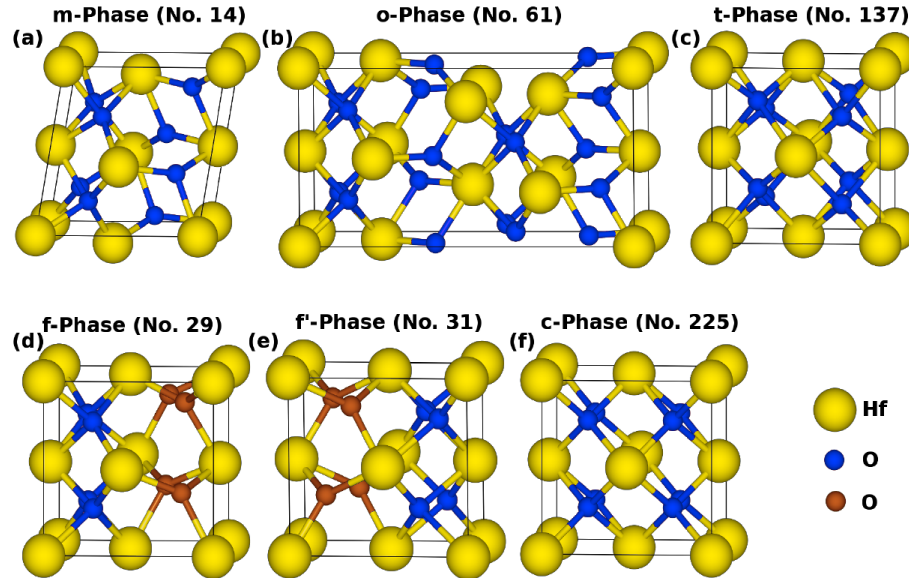


Figure 3.1: (a) monoclinic (b) orthorhombic, (c) tetragonal, (d) ferroelectric (down), (e) ferroelectric (up) (f) cubic phase. Figure adapted from Materlik [154].

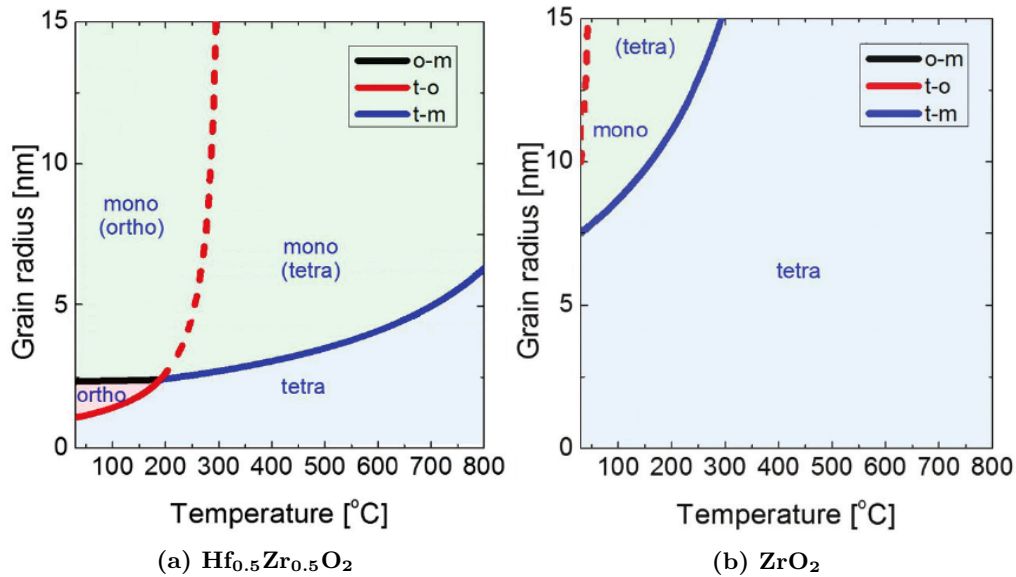


Figure 3.2: Phase diagram, grain radius over temperature, according to the thermodynamic model of Park et al. [155]. Left: The ferroelectric, orthorhombic phase of $\text{Hf}_{0.5}\text{Zr}_{0.5}\text{O}_2$ is stable only in a small window with grains of around 2 nm diameter. For larger grain sizes, the thermodynamic model predicts the monoclinic phase. However, experiments show significant amounts of orthorhombic phase. b) With reduced HfO_2 content, the tetragonal phase region extends to smaller temperatures and larger grains. For pure ZrO_2 , there is practically no stable orthorhombic phase left at temperatures above 25°C. Adapted from [155].

3.2 Depolarization Field

Besides the ferroelectric tunnel junction where miniaturization is a prerequisite, the demand for thin film ferroelectrics is to shrink with its incorporating electronics. Various types of ferroelectric thin-film capacitors are thus required to shrink to the nanometer scale [156–158].

The continuing requirement for the miniaturization of electronic devices, ferroelectric thin-film capacitors are required to shrink to nanometer scale [156–158]. Generally, this size reduction allows to achieve a lower operating voltage. However, at a certain size, most materials entail a size effect which may affect the polarization stability, initially lowering the coercive field, until the ferroelectricity is lost. This size effect limits the practical applications and affects all of the commonly used perovskite ferroelectrics. This means that the intrinsic ferroelectric polarization exceeds the coercive field. In this context, the field opposing the intrinsic polarization is called the depolarizing field, which can be screened to reduce this effect Yang et al. [159]. For this reason, metallic electrodes that closely mirror the surface charges are used to stabilize the polarization states. In other words, insufficient screening of the polarization charge at the ferroelectric surface is likely the cause of this size effect [160, 161], leading to so-called "dead layers" which is effectively non-ferroelectric and has low permittivity. Even with individual domains in the material remaining ferroelectric, their stability is dependent on adjacent domains of the opposite polarity, forming a polydomain structure that effectively diminishes the ferroelectricity. The dead layer is equivalent to an additional capacitor [162], which is detrimental to the total polarization and capacitance properties. Besides the formation of polydomains [163], electrical fatigue [117, 164], imprint [165] and leakage problems [166] are associated with this effect. Consequently, the existence of dead layer greatly limits the scaling-down of ferroelectric thin films and hinders the miniaturization and integration of ferroelectric-based electronic devices.

Quantitatively, the potential barrier changes at the interface are

$$\Delta\phi_{top} = \frac{l_{top}Q_sq}{\varepsilon_{top}} \quad \text{and} \quad \Delta\phi_{bot} = \frac{l_{bot}Q_sq}{\varepsilon_{bot}} \quad (3.1)$$

where l_{top} and l_{bot} are the screening lengths of the top and bottom electrodes

$$l_{top} = \sqrt{\frac{\varepsilon_{top}k_BT}{q^2n}} \quad \text{and} \quad l_{bot} = \sqrt{\frac{\varepsilon_{bot}k_BT}{q^2n}} \quad (3.2)$$

and Q_s is the screening charge density that is derived from the remnant polarization and screening length [59]

$$Q_s = \frac{Pt_{FE}}{\varepsilon_{FE} \left(\frac{l_{top}}{\varepsilon_{top}} + \frac{l_{bot}}{\varepsilon_{bot}} \right) + t_{FE}} \quad (3.3)$$

The depolarization field results from the difference between polarization and screening charge

$$E_{depol} = -\frac{P - Q_s}{\varepsilon_{FE}} \quad (3.4)$$

with the remnant polarization P and screening charge density Q_s from Eq. 3.3.

The electric field is then within the ferroelectric is then

$$E_{FE} = E_{appl} \pm E_{depol} \quad (3.5)$$

with the externally applied field $E_{appl} = V_{FE}/t_{FE}$ and the depolarization field E_{depol} from Eq. 3.4.

3.3 Read and Write Rate

Writing is limited by the domain switching process in the device. Due to its very small thickness, the nucleation process and domain wall motion are the defining factors in this scenario. While the domain wall propagation along the polarization direction occurs at the speed of phonon propagation, the sideways motion can be described as a relatively slow, viscous process that can be stopped ("pinned") at defects. Thus, the switching speed of a polycrystalline ferroelectric thin film is dominated by nucleation. This is also known as nucleation-limited switching (NLS), which can span several orders of magnitude (see Fig 2.10), depending on voltage [105, 167].

Reading the resistive device is done by charge integration at sub-coercive voltages and thus requires the current density

$$J = \frac{Q}{tA} \quad (3.6)$$

to acquire the charge Q over time t transported through area A . We can roughly estimate that reading the resistive state requires on the order of $Q = 10^3 e^-$ elementary charges [168, 169]. On a $100 \text{ nm} \times 100 \text{ nm}$ device area and a read speed of 100 ns , the required current density is 16 A/cm^2 .

This is within the feasible range of FTJ current densities [14]. A tradeoff between read time and voltage must be maintained to avoid degrading the polarization state.

3.4 FTJ Manufacturing

The TiN/Hf_{0.5}Zr_{0.5}O₂/Pt and TiN/Hf_{0.5}Zr_{0.5}O₂/Au stacks were deposited using a Plasmionique Inc. (SPT310 model) system. A polycrystalline Hf_{0.5}Zr_{0.5}O₂ 1" ceramic disc was used as a sputtering target. Prior to deposition, the chamber was evacuated at a base pressure of 10 mbar. The inert sputtering gas Ar and is mixed with O₂ to equal partial pressures ($n_{O_2}/(n_{Ar} + n_{O_2}) = 50\%$) where an operating pressure of 6 – 40 mbar is maintained. The RF power was fixed to 20 W on the target and the substrate temperature was maintained at 500°C during deposition. The target surface is cleaned by pre-sputtering. During deposition, a target-substrate distance of 11 cm is used to reduce inhomogeneities due to backspattering. The deposition data is summarized in table A.10.

The TiN bottom electrode is deposited on silicon substrate by sputtering Ti in a nitrogen atmosphere and annealing for 30 min at 650°C. The Hf_{0.5}Zr_{0.5}O₂ layer is then deposited, using sputtering-rate compensated Hf and Zr sputtering in oxygenated gas. To obtain the precise thickness, the deposition rate of this sputtering process is calibrated using X-ray reflectivity (XRR) thickness measurements. Finally, a dot-pattern shadow mask is used to deposit the top electrode. One of the first surveys of fully-sputtered ferroelectric hafnium-based MIM-device was demonstrated by Olsen et al. [170].

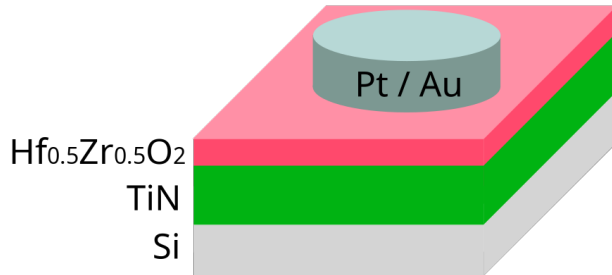


Figure 3.3: Sputtering deposited layers on top of the silicon substrate. The top electrode is structured using a 150 μm diameter dot-pattern shadow mask.

3.5 Annealing

After deposition of the TiN bottom electrode, a short annealing cycle is required for the TiN to crystallize and increase conductivity. However, this process should be kept short and at moderate temperatures, since individual grains grow on the surface, increasing surface roughness.

Typically, after deposition of the top electrode, annealing the $\text{Hf}_{0.5}\text{Zr}_{0.5}\text{O}_2$ film is required to form the ferroelectric orthorhombic phase. Previous annealing experiments, as well as literature indicates that temperatures between 500°C and 650°C yield the largest amount of ferroelectric phase [155], which is consistent with resistive switching experiments previously performed with our setup. However, depending on the electrode and manufacturing process, significantly lower (370°C [171]) and higher (800°C [132]) temperatures have been reported.

Since the second annealing step requires higher temperatures, both components in the TiN/ $\text{Hf}_{0.5}\text{Zr}_{0.5}\text{O}_2$ interface undergo recrystallization, likely further degrading the surface planarity and inducing localized strains. Since both the top and bottom electrodes have higher CTEs than the $\text{Hf}_{0.5}\text{Zr}_{0.5}\text{O}_2$ -compound, the polycrystalline oxide remains in an in-plane compression state. Theoretical models suggest that this compression is an important contribution to stabilize the otherwise unstable ferroelectric phase [90]. Besides the annealing-induced strains and grain interface energies, doping with the chemically similar Zr or other dopants can improve the thermodynamic stability of the desired f-phase [172, 173].

3.6 Electrode Materials

The physical principle of FTJ resistive switching requires the structure to exhibit an asymmetry in electron potentials when switching polarization. The materials TiN/Pt and TiN/Au are prime candidates, since they remain stable at elevated temperatures, they exhibit low oxygen affinity, yet have a significant difference in work functions. Additionally, these materials do not migrate or form filaments. Since TiN is porous, it can potentially absorb oxygen from ZrO_2 at elevated temperatures [107, 174], especially if the electrode is nitrogen deficient. Probing techniques applicable to FTJs, such as XPS, XRR and AFM are detailed in Appendix A.1. An overview of work functions is given in Appendix A.4.

Chapter 4

Results

The following sections include the three main research topics: The first section describes our findings of the theoretical impact of thin film thickness homogeneity on the FTJ electrical parameters [175]. The effects of this parameter is quantified, and its effect on the electrical characteristics analyzed. The second section investigates switching at elevated voltages in a Au/Hf_{0.5}Zr_{0.5}O₂/TiN structure. In this regime, we identify switching that is dominated by the vacancy mechanism and develop a vacancy hopping model to describe the time-dependent switching behavior. The model describes the generation of oxygen vacancies and device degradation in the context of trap-assisted tunneling. This vacancy mechanism exhibits switching behavior that, while it is larger in magnitude, leads to device degradation upon operation, especially at elevated voltages. An article with our findings is in preparation. Finally, we investigate TiN/Hf_{0.5}Zr_{0.5}O₂/Pt-based FTJs in a neural network configuration [176]. Two neuron spikes overlap to produce a time dependent Spike-timing-dependent plasticity (STDP) at the FTJ. The FTJ response as a synapse is observed. An NLS model is used to describe the experimentally observed resistivity change. The description of neural switching behavior defines key parameters, such as the learning rate, switching stability and symmetry.

4.1 The Effects of Thin Film Homogeneity on the Performance of FTJs

As the thickness of the ferroelectric thin film applied to a ferroelectric tunnel junction (FTJ) device reduces to several nanometers, the electron transport behavior, causing two different electrical resistance states known as the tunneling electroresistance (TER) effect, can be predominantly explained by the direct tunneling mechanism. However, to accurately predict the TER ratio, while it is necessary to precisely define the parameters of the $\text{Hf}_x\text{Zr}_{1-x}\text{O}_2$ -based material applied to the conduction model, it is still insufficient to fully account for the device operation. In the following section, we present the theoretical results of thickness variations in an FTJ device with a Pt/ $\text{Hf}_x\text{Zr}_{1-x}\text{O}_2$ /TiN structure, using 3 nm thick $\text{Hf}_{0.5}\text{Zr}_{0.5}\text{O}_2$ tunnel barrier with stochastic thickness inhomogeneities and the resulting effects on the electrical performance [175].

4.1.1 $\text{Hf}_x\text{Zr}_{1-x}\text{O}_2$ Structural Homogeneity

We describe a three-layer TiN/ $\text{Hf}_{0.5}\text{Zr}_{0.5}\text{O}_2$ /Pt structure with a 3 nm ferroelectric layer that is operated within the limits of the trapezoidal Wentzel-Kramer-Brillouin (WKB) model, which we separate into analytical small and large voltage approximations. As a basis to quantify the effects of inhomogeneities in the ferroelectric layer, we derive a statistical, closed form expression for the distribution of current densities based on the WKB approximation, based on a predefined distribution of tunneling barrier thicknesses. The consistency of these results was numerically checked using the MonteCarloMeasurements library from the Julia programming language [177, 178].

The ferroelectric phase in $\text{Hf}_x\text{Zr}_{1-x}\text{O}_2$ deposited by atomic layer deposition or sputtering processes has been attributed to the film's polycrystalline grain structure [179]. While $\text{Hf}_x\text{Zr}_{1-x}\text{O}_2$ films much thicker than 10 nm are mostly composed of the non-ferroelectric monoclinic and tetragonal structures, smaller thicknesses increasingly favor the formation of the ferroelectric orthorhombic phase. A polycrystalline film with a thickness in a range of 2 nm to 4 nm inherently induces significant relative thickness fluctuations in the ferroelectric layer. Imperfections in the surface homogeneity of the base electrode may increase this effect. Magnetron-sputtered TiN/ $\text{Hf}_{0.5}\text{Zr}_{0.5}\text{O}_2$ /Pt

heterostructure with an $\text{Hf}_{0.5}\text{Zr}_{0.5}\text{O}_2$ thickness of 3 nm exhibit a root mean square (rms) interface roughness of 0.2 nm on the TiN bottom electrode, and 0.1 nm on the thereon deposited $\text{Hf}_{0.5}\text{Zr}_{0.5}\text{O}_2$ [180]. This results in thickness variations in the $\text{Hf}_x\text{Zr}_{1-x}\text{O}_2$ film. To understand the impact of this inhomogeneity, we developed a model that describes the tunneling current behavior in $\text{Hf}_x\text{Zr}_{1-x}\text{O}_2$ using the WKB approximation. The WKB approximation across a trapezoidal barrier quantifies the current density J as a function of barrier thickness d and voltage U . The analytical expression [57, 59, 88] can be written as

$$J(d) = \frac{C}{d^2} e^{Dd} \times \sinh(Ed) \quad (4.1)$$

with the parameters C , D , E

$$C = \frac{4em_e}{9\pi^2\hbar^3} \frac{1}{\alpha^2 \left[\left(\phi_2 - \frac{eU}{2} \right)^{1/2} - \left(\phi_1 + \frac{eU}{2} \right)^{1/2} \right]^2} \quad (4.2a)$$

$$D = \alpha \left[\left(\phi_2 - \frac{eU}{2} \right)^{3/2} - \left(\phi_1 + \frac{eU}{2} \right)^{3/2} \right] \quad (4.2b)$$

$$E = \frac{3}{4} \left| U \alpha \left[\left(\phi_2 - \frac{eU}{2} \right)^{1/2} - \left(\phi_1 + \frac{eU}{2} \right)^{1/2} \right] \right| \quad (4.2c)$$

where α is

$$\alpha = \left(\frac{-4\sqrt{2m_e}}{3\hbar \left[\left(\phi_2 - \frac{eU}{2} \right) - \left(\phi_1 + \frac{eU}{2} \right) \right]} \right) \quad (4.2d)$$

In this equation, ϕ_1 and ϕ_2 are the trapezoidal interface potential barriers shown in Fig. 4.2, m_e the (effective) electron mass, and U and d the operating voltage and ideally homogeneous thickness, respectively. Fig. 4.1 shows the resulting LRS, HRS and TER ratio.

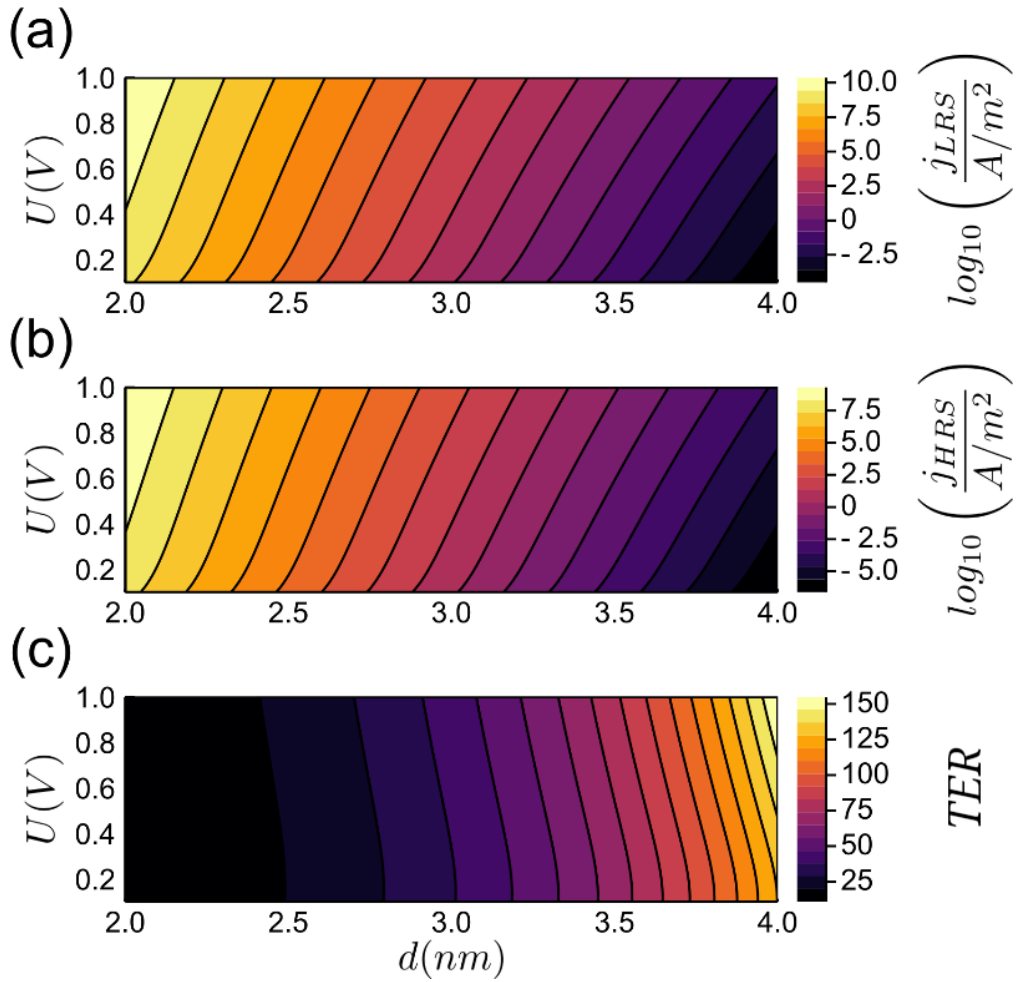


Figure 4.1: Semi-logarithmic plots of the effect of the voltage and the $\text{Hf}_{0.5}\text{Zr}_{0.5}\text{O}_2$ thickness on the (a) LRS current density, (b) HRS current density, and (c) linear plot of the TER ratio of LRS and HRS current densities. Tunneling currents are calculated from Eqn. 4.1. over varying thickness and voltages. Increasing voltage and thickness improves the TER.

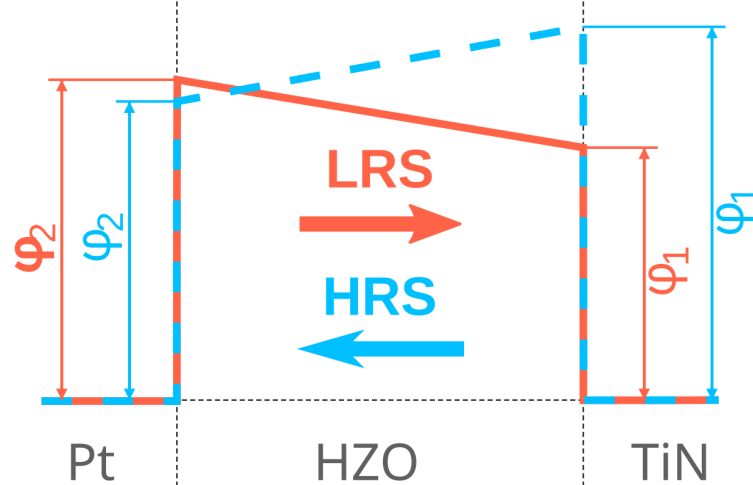


Figure 4.2: Modulation of potential barrier for the low resistance state (LRS), where the polarization is in the direction of the TiN interface (red), and the high resistance state (HRS), where the polarization is oriented towards of the Pt interface (blue). The barrier heights represent the mean values from table 4.1.

	Vargas 2018	Yoon 2019	mean	change
$\varphi_{Pt}^\downarrow(eV)$	1.86	2.14	2.000	0.585
$\varphi_{Pt}^\uparrow(eV)$	2.75	2.42	2.585	
$\varphi_{TiN}^\downarrow(eV)$	2.36	2.33	2.345	-0.110
$\varphi_{TiN}^\uparrow(eV)$	2.20	2.27	2.235	

Table 4.1: Interface potentials from Ambriz-Vargas et al. [181] and Yoon et al. [59]. The arrows symbolize the polarization towards the TiN interface (\downarrow , LRS) and Pt interface (\uparrow , HRS). The rightmost column shows the impact of polarization reversal.

Using ϕ_1 , ϕ_2 as shown in table 4.1, and Eqn. 4.1, the J-V curves in the HRS and LRS were reconstructed for a 3 nm $Hf_{0.5}Zr_{0.5}O_2$ film, as illustrated in Fig. 4.3 (gray curves). The J-V curve follows a large exponential slope that tapers off into a shallower exponential. At higher voltages, the current density increases exponentially with the voltage. To represent these two regions, the approximations $\sinh(Ed) \approx Ed$ and $\sinh(Ed) \approx \frac{1}{2}e^{Ed}$ were used, which approximate the regions for U smaller and larger than $\log((2)/E)$, respectively. The current density of Eqn. 4.1 is thus split into the two following equations:

$$J_s \approx \frac{CE}{d} e^{Dd} \quad \text{if } U < \log(2)/E \quad (4.3a)$$

$$J_l \approx \frac{C}{2d^2} e^{(D+E)d} \quad \text{if } U > \log(2)/E \quad (4.3b)$$

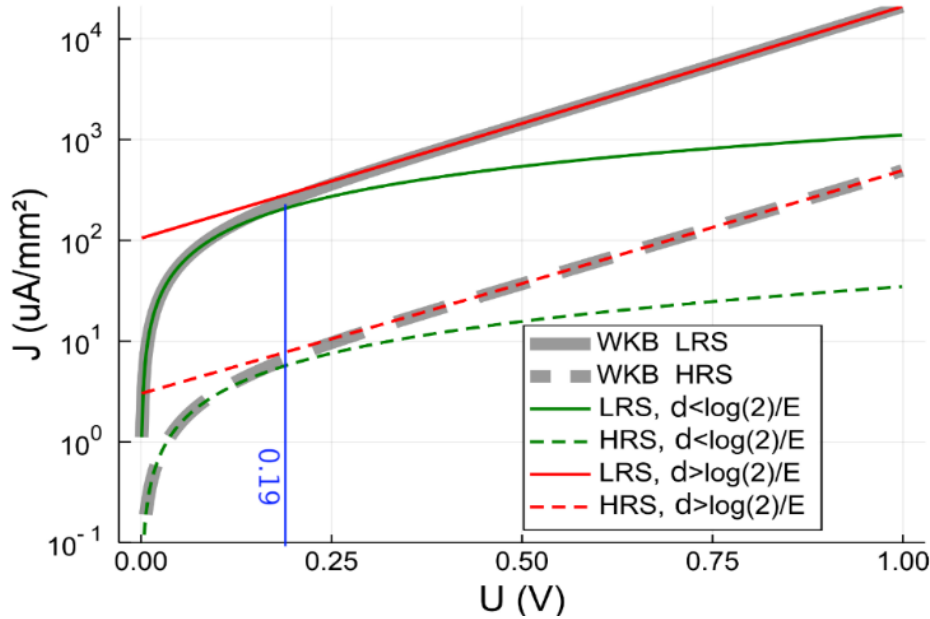


Figure 4.3: J-V behavior in the HRS (dashed line) and the LRS (full line) according to the WKB approximation (gray), as well as with the small (green) and large voltage approximations (red) for an ideally homogeneous insulator with a thickness of 3 nm. The transition point between the small and large voltage approximation $\log(2)/E$ is indicated for each curve by the blue line.

4.1.2 Results

A comparison between the WKB model Eqn. 4.1 and the approximations Eqns. 4.3(a),(b) is shown in Fig. 4.3 (gray line with green and red approximations, respectively). The calculations and figures are shown exemplary for a ferroelectric film thickness of 3 nm. Limiting factors for the thickness are prohibitively high resistivity for larger thicknesses for acceptable readout speed as discussed in section 3.3, and electrical instability/breakdown for smaller thicknesses. A good agreement is obtained in each region, showing that for a barrier width of $d = 3\text{nm}$, the WKB formula is accurately described by the approximations, as long as each approximation is used within its threshold of

$U = \log(2)/E$ (blue vertical lines). These approximations can be exploited to calculate the current density distribution in a closed form in the next section.

Using these approximations, the exponential dependency of the current density on both barrier width and operating currents can be calculated for the LRS and HRS, respectively. For both LRS and HRS, the current density increases exponentially when decreasing the $\text{Hf}_{0.5}\text{Zr}_{0.5}\text{O}_2$ thickness. Also, the current density increases exponentially with the voltage above a certain threshold, consistent with the curves shown in Fig. 4.3, see also Hyuk Park et al. [18]. The TER ratio is critical for distinguishing the two resistive states. It can be defined as the ratio of current densities

$$\text{TER} = \frac{\overline{j_{LRS}}}{\overline{j_{HRS}}}. \quad (4.4)$$

The TER ratio grows with voltage and barrier width. A plot of the LRS, HRS and TER over voltage and material thickness is shown in Fig. 4.1. Higher currents are beneficial for a fast readout of the resistivity state, which is assisted by lower thicknesses. In addition, the voltage is limited by the breakdown threshold of the device. Therefore, the TER ratio can be optimized by adjusting the $\text{Hf}_{0.5}\text{Zr}_{0.5}\text{O}_2$ thickness while remaining below the device breakdown voltage, neglecting the effect of roughness induced field enhancement [182]. In the Eqns. 4.1-4.3, variations of the $\text{Hf}_{0.5}\text{Zr}_{0.5}\text{O}_2$ thickness are not yet taken into consideration.

To account for these effects, we model the TER device as a series of parallel resistors with resistances dependent on the local film thickness (see Fig. 4.4). Since the total resistance is predominantly defined by the smallest parallel resistance, the distribution of thicknesses is crucial parameter.

The effect of varying local film thicknesses, and therefore the film surface roughness, on the current density is thus crucial in understanding the total device conductance. Since the current density J is a monotone function with respect to d , its probability distribution $pdf_J(j)$ for a distribution of thicknesses $pdf_d(d)$ can be expressed as [183]

$$pdf_J(j) = pdf_d(J^{-1}(j)) \left| \frac{dJ^{-1}(j)}{dj} \right|, \quad (4.5)$$

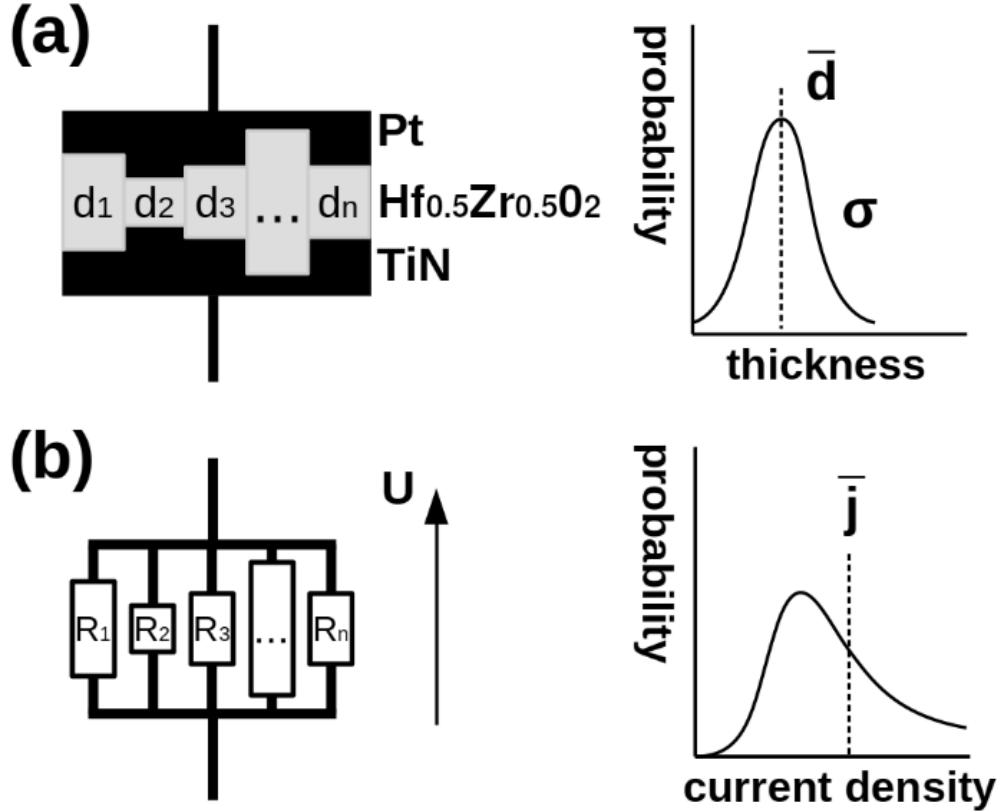


Figure 4.4: Hf_xZr_{1-x}O₂ conductivity model. The local film thickness results in a local current density at voltage U. (a) Representation of roughness as a distribution of thicknesses. (b) Parallel resistor model yielding the current density distribution for a fixed voltage.

where $J^{-1}(j)$ is the inverse of function $J(d)$. Using the closed form invertibility of Eqns. 4.3a, b, this yields the generic distributions

$$pdf_{Js}(j) = pdf_d \left(-\frac{W_{Js}}{D} \right) \times \left| \frac{W_{Js}}{jD(W_{Js} + 1)} \right| \quad (4.6a)$$

$$pdf_{Jl}(j) = pdf_d \left(-\frac{2W_{Jl}}{D + E} \right) \times \left| \frac{W_{Jl}}{j(D + E)(W_{Jl} + 1)} \right| \quad (4.6b)$$

with $W_{Js} = W \left(\frac{-CDE}{j} \right)$ and $W_{Jl} = W \left(\frac{-\sqrt{2}C(D+E)}{4\sqrt{j}} \right)$, where W is the principal branch Lambert W function [184]. Assuming a normal distribution of thickness pdf_d

$$pdf_d(d) = \frac{1}{\sqrt{2\pi\sigma^2}} \exp \left(-\frac{(d - d_0)^2}{2\sigma^2} \right) \quad (4.7)$$

for small deviations σ around the mean thickness d_0 , the current density distribution is calculated from Eqn. 4.6(a) and 4.6(b). Both are shown in Fig. 4.5(a), (b) at voltages according to their applicable scope. Even for unphysically small values of $\sigma = 5 \text{ pm}$, the current density probability shows a visible spread that resembles a Gaussian centered at $\sqrt{170} \text{ A/m}^2$. When σ increases to 10 pm , the current density probability peak decreases by half and becomes broader. As the thickness deviation further increases, the curve becomes broader and the maximum significantly decreases, while shifting to lower current densities. Contrary to the visual shift, the mean conductivity increases in this process, since the distributions increasingly stretch to higher current densities, as shown in the inset on the right-hand side of Fig. 4.5(b). This shows that for real-world FTJs, much of the $\text{Hf}_{0.5}\text{Zr}_{0.5}\text{O}_2$ film will not contribute significantly to the tunneling current.

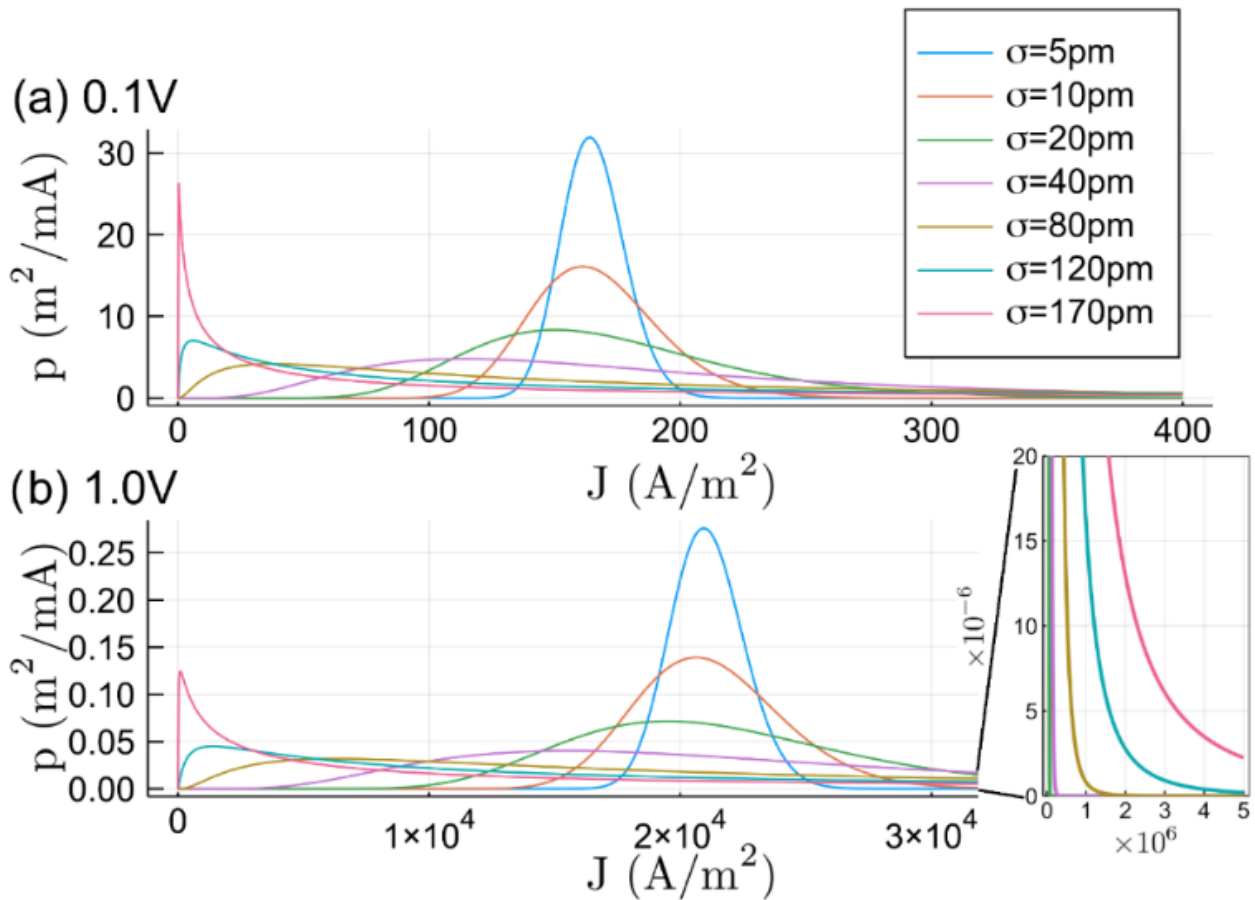


Figure 4.5: Probability density functions of the current density distribution pdf_J for a mean thickness $d_0 = 3 \text{ nm}$ at varying standard deviations of thickness σ . Even for unphysically small values of $\sigma = 5 \text{ pm}$, significant variations in current density can be observed. At $\sigma = 170 \text{ pm}$ for (a) $U = 100 \text{ mV}$ and (b) $U = 1 \text{ V}$ in the LRS. While the peak probability moves to lower current densities with increasing σ , the probability distribution increasingly stretches to high current densities (shown in the magnified inset).

The mean current density through a distribution of parallel grains can be extracted from Fig. 4.5 according to the first moments

$$\bar{j} = \int_0^\infty j p\text{df}_J(j) dj. \quad (4.8)$$

The results of j_{LRS} and j_{HRS} for both LRS and HRS are illustrated in Fig. 4.6(a) over the thickness standard deviation σ . It shows that the current densities increase exponentially with thickness standard deviation σ . The thickness of the FTJ thus needs to be extremely homogeneous to permit reproducible conductivities. This requirement occurs as the grains function as a parallel resistor network. As a result, the resistance of the network is defined by that of the smallest parallel resistors.

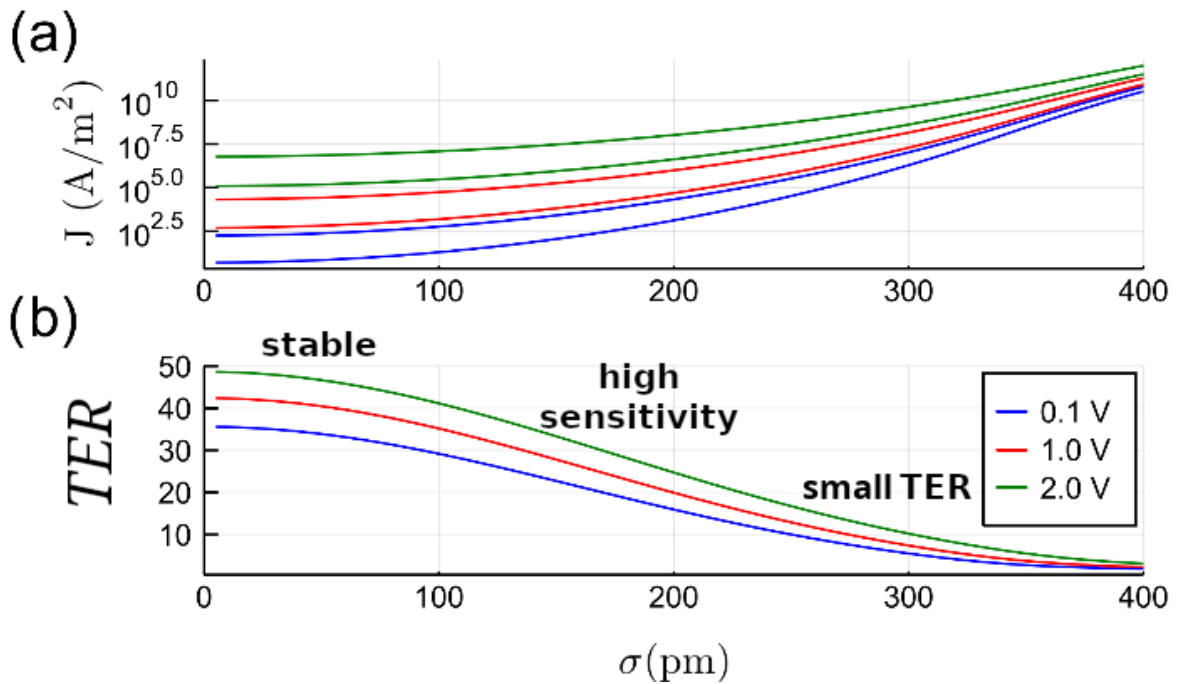


Figure 4.6: (a) Mean current density of LRS state and HRS state for three voltages at a thickness of $d_0 = 3\text{nm}$. (b) Mean TER ratio over standard deviation. The ratio is stable for small deviations and drops quickly above when σ exceeds $\approx 0.1\text{nm}$. The TER ratio follows a Gaussian-shaped decay of resistive switching with increasing thickness variations. It can be seen that the thickness inhomogeneity has a significant impact on the TER ratio. This decay results from the fact that the smallest resistances determine the TER, which in return exhibits the lowest TER ratio (Fig. 4.1(c)).

Due to a non-epitaxial film growth of $\text{Hf}_{0.5}\text{Zr}_{0.5}\text{O}_2$ on the bottom electrode, and a crystal structure with a typical lateral grain size comparable to the film thickness [15, 103, 185], ferroelectric

$\text{Hf}_{0.5}\text{Zr}_{0.5}\text{O}_2$ intrinsically exhibits structural thickness variations between the electrode interfaces. As shown in the previous section, this can greatly affect the electrical performance of the device. Another aspect of this analysis is the increased probability of electrical breakdowns. Literature specifications of breakdown voltages in hafnium and zirconium oxide thin films vary between 7 MV/cm and 20 MV/cm [73, 186–188], whereby typical coercive fields require at least 1 MV/cm to 2.5 MV/cm [189, 190]. At this point, higher fields allow increased switching speeds and help switching pinned domains. Switching a 3 nm device by application of 2 V could however already exceed the electric breakdown threshold. Going by these numbers, just approaching the coercive field could already reach 13% to 36% of the breakdown field. Defects in the $\text{Hf}_{0.5}\text{Zr}_{0.5}\text{O}_2$ narrowing the barrier can thus increase the likelihood of an electrical breakdown as observed by Kracklauer et al. [191].

Besides the decay of the TER ratio, FTJs are typically operated at voltages within a significant percentage of their electrical breakdown threshold. For an individual site of random thickness, the cumulative probability of failure over the thickness is

$$p_{site} = \int_0^{\frac{U}{E_{crit}}} pdf_d(d)dd = \int_0^{\frac{E}{E_{crit}}} pdf_d(\sigma_n)d\sigma_n \quad (4.9)$$

where E_{crit} is the critical field strength, $E = U/d_0$ the mean field strength, and $\sigma_n = \sigma/d_0$ the relative thickness standard deviation. Thus, the accumulated breakdown probability p_N for a device with N sites is

$$p_N = 1 - (1 - p_{site})^N \quad (4.10)$$

This relation is detailed in Fig. 4.7, showing linear equipotential lines between field E and standard deviation σ .

We find an increasing chance of breakdown with increasing the operating voltage and decreasing the mean thickness, as well as with the device area and the surface roughness. When operating a device with 7% thickness standard deviation at 60% of the critical voltage, 10 out of a million devices will surpass the critical value.

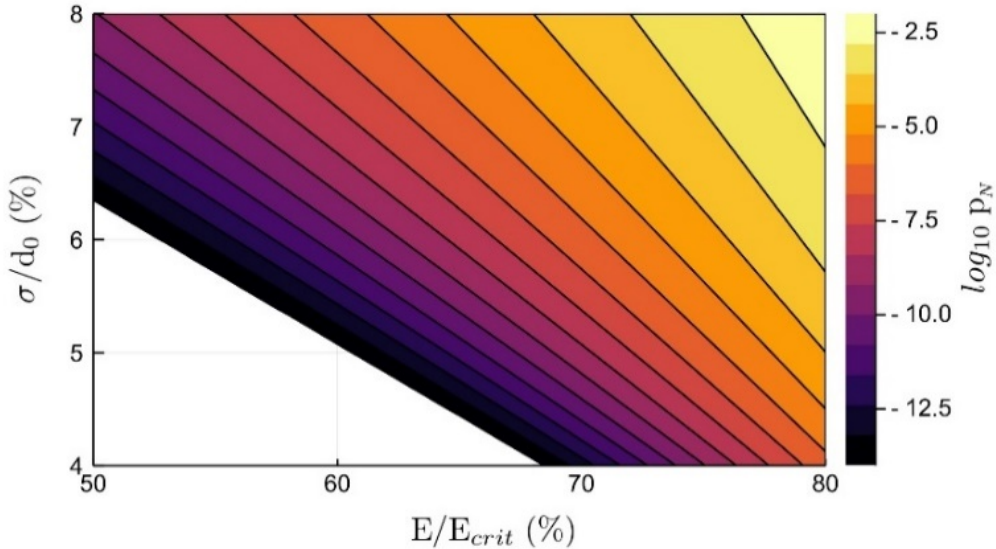


Figure 4.7: Probability of an electrical breakdown in a device p_N , assuming $N = 10^6$ statistically independent sites with independent lattice thicknesses. The x-axis measures the mean electric field relative to the critical field E/E_{crit} while the y-axis is the relative standard deviation of the thickness σ/d_0 . The plot corresponds to a $3\mu m \times 3\mu m$ device with an average 3 nm in-plane grain diameter, assuming one statistically independent height per grain.

Non-Ferroelectric and Pinned Domains

With real ferroelectric switching devices, an effect known as domain pinning is observed. This pinning effect happens due to the interaction between a charged domain wall and a charged defect. This effectively leads to portions of the ferroelectric domain to become "frozen", i.e. exempt from switching. Here, we present an estimation of the effects of these frozen domains on the total conductivity and TER ratio. Using Kirchhoff's circuit laws and assuming domain walls oriented alongside the thickness of the ferroelectric, the effective TER is the ratio of parallel current density fractions and can be expressed as:

$$TER_{f,g} = \frac{R_{HRS}}{R_{LRS}} = \frac{j_{HRS}f + j_{LRS}g + j_{LRS}(1-f-g)}{j_{HRS}f + j_{LRS}g + j_{HRS}(1-f-g)} = \frac{TER - (TER - 1)f}{1 + (TER - 1)g} \quad (4.11)$$

with a phase fraction f permanently in HRS state, and g permanently in LRS state, and a switchable remainder. The pristine current densities are j_{LRS} , j_{HRS} . When we also account for a non-

ferroelectric phase component e with current density j_{nonFE} , this becomes

$$TER_{f,g,e} = \frac{j_{nonFE}e + j_{HRS}f + j_{LRSg} + j_{LRS}(1-e-f-g)}{j_{nonFE}e + j_{HRS}f + j_{LRSg} + j_{HRS}(1-e-f-g)} \quad (4.12)$$

The TER dependence on f and g is shown in Fig. 4.8. We can conclude that if any pinning is inevitable, pinning in the HRS state is favourable with respect to its impact on the TER.

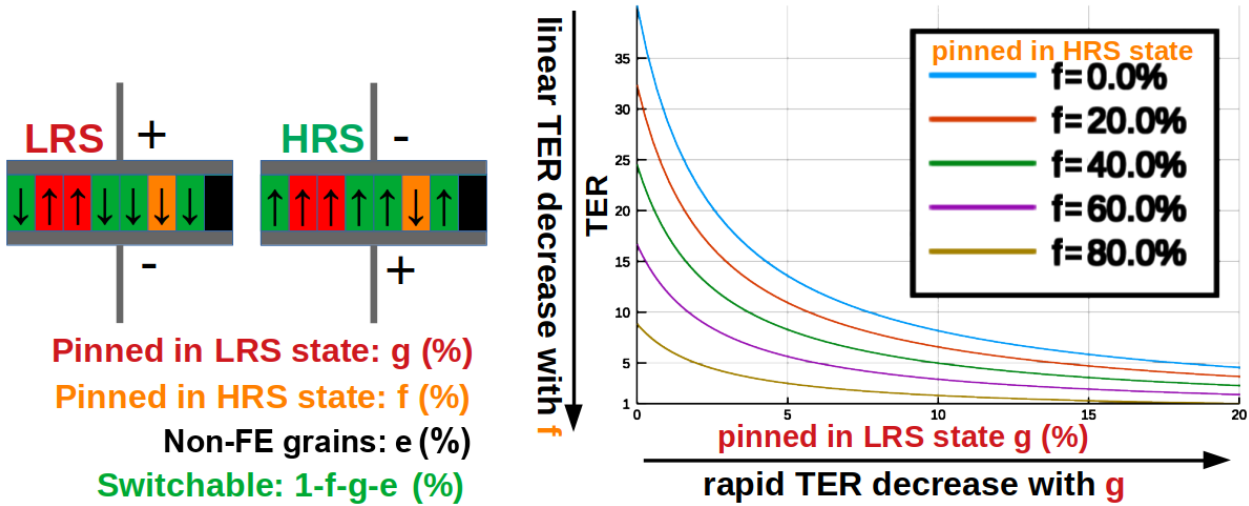


Figure 4.8: Left: Model of parallel resistors with domain fractions f, g pinned in LRS and HRS states, and the non-ferroelectric component e. Right: TER over pinned domain fractions at $e = 0$. The tunneling electroresistance ratio degrades rapidly with the fraction g pinned in LRS state, and linearly with the fraction f pinned in HRS state.

In the model description of Eqn. 4.11, we assume that the non-ferroelectric domains do not significantly contribute to device conductivity. These regions could be taken into account by adding another parallel resistor that contributes similarly to the pinned domains.

Conclusion

We quantitatively estimate the effect of thickness variations on the device performance. From the high sensitivity of the tunneling process, we can conclude that these statistical variations are generally significant and cannot be eliminated, especially in a polycrystalline structure. Our TEM measurements (Appendix figure A.7) provide a visual representation of these inhomogeneities. A comparison with literature shows a surface roughness of sputtered HfO₂ [192] of 0.2 nm. This means that most of the tunneling current will tend towards a small area of hotspots, which increases the

likelihood of device failure by dielectric breakdown. The deposition on a polycrystalline, nonplanar bottom electrode such as TiN will further increase this issue. For our estimations, we assumed smooth thickness variations. Local thicknesses of zero are considered to be device failures. The effects of sharp edges and points in the interface can create significant field enhancements, further amplifying the tunneling currents[182, 193]. Furthermore, we assume idealized metallic electrodes and neglect secondary current channels. Quantitatively, we find that thickness standard deviations of $\sigma = 0.2 \text{ nm}$ halves the TER while increasing current densities by 2 orders of magnitude. A doubling of σ from 0.1 nm to 0.2 nm will increase the breakdown probability by a factor of 500, and LRS-pinned domains can quickly degrade the TER. Since $\sigma = 0.2 \text{ nm}$ corresponds to ca. 1 atomic defect per 20 surface sites, any application will have to take into tolerate significant inter-device variations.

4.2 Valency Mechanism and Endurance

When considering voltages considerable above the coercive voltage, the resistive switching mechanism changes to valency switching. This is a form of soft electrical breakdown, initiated when the electric field strength is large enough to extract significant amounts of oxygen from the insulator. The thereby created oxygen vacancies propagate within the bulk insulator. We describe this process by modeling the drift of the positively charged vacancy by an isotropic diffusion term with a convection contribution according to the electric field. From this model, a distribution of vacancies is derived, which is then used to calculate the electrical conductivity.

4.2.1 Drift-Diffusion Valency Change Model

A Finite Difference Model of the $\text{Hf}_{0.5}\text{Zr}_{0.5}\text{O}_2$ domain is constructed. This model is used to solve for the vacancy distribution. This time-dependent drift-diffusion model encompasses the voltage-driven vacancy migration in the simulation domain, as well as the chemical vacancy generation/annihilation mechanism at the boundaries.

Starting from Eq. 2.21 to model the FTJ with Au top electrode, the vacancy generating reaction when a positive voltage is applied to the top electrode is



and the vacancy annihilation at negative voltage is



We model the rate equations of this physisorption process with voltage dependent Arrhenius-type equations

$$J_{gen} = -k^+(c_{\text{O}_\text{O}^\times} - c_{\text{V}_\text{O}^{\bullet\bullet}}) \exp\left(\frac{f(2-\beta)(qU - \varphi^+)}{k_B T}\right) \quad (4.15a)$$

$$J_{ann} = k^- c_{\text{V}_\text{O}^{\bullet\bullet}} \exp\left(\frac{f\beta(-qU - \varphi^-)}{k_B T}\right) \quad (4.15b)$$

$$J = J_{gen} + J_{ann} \quad (4.15c)$$

with the rate prefactors k^+ , k^- , vacancy and oxygen concentrations $c_{\text{V}_\text{O}^{\bullet\bullet}}$ and $c_{\text{O}_\text{O}^\times}$, and the applied voltage U working against the activation energies φ^+ , φ^- . The parameter β allows for a slight asymmetry between the exponential behaviors, and is approximately one. Finally, f is a heuristic exponential parameter that is identical for both equations.

Similar to the Au top electrode, the TiN bottom electrode interface is relatively inert. However, its ionic structure is assumed to be too rigid to incorporate significant amounts of oxygen. This circumstance is supported experimentally, since a negative applied voltage at the TiN electrode does not affect resistivity.

The total reaction rate $J_{gen} + J_{ann}$ is the boundary condition for a finite difference, voltage driven

drift diffusion model of vacancies across the insulator domain. The equation and its boundary conditions are expressed by

$$\frac{\partial c}{\partial t} = \nabla(D\nabla c) - \nabla v_t c \quad (4.16a)$$

$$\text{where } \left. \frac{\partial c}{\partial t} \right|_{x=x_0} = (J(x_0) + c(x_0)v_t)/D(x_0) \quad (4.16b)$$

$$\text{and } \left. \frac{\partial c}{\partial t} \right|_{x=x_1} = c(x_1)v_t/D(x_1) \quad (4.16c)$$

where $c = c(x, t)$ is the vacancy concentration, $v_t = v_t(U)$ is the voltage dependent drift velocity, $U(t)$ is the externally applied voltage, $D = D(T)$ is the diffusion coefficient, $T = T(x)$ is the temperature, x_0 and x_1 are the locations interface boundary conditions. $J(x_0) = J(c(x_0), U, T)$ is the rate equation of the vacancy mechanism at the active interface x_0 , given by Eq. 4.15c.

4.2.2 Measurements

A sequence of alternating voltage pulses U_w is applied to the FTJ according to Fig. 4.9. The pulses increase by 0.01 V This sequence rising sequence is repeated multiple times for rising read voltages U_r , shown in Fig. 4.10. A polar asymmetry in is visible. The currents measured after a write pulse of positive polarity increase rapidly above 1.5 V, while for negative polarity, the resistivity gradually increases over the full voltage range. This trend continues for the full span of read voltages. As can be seen in Fig. 4.12, the current progression transistions to a more noisy transistion which may hint at the onsetting electrochemical process.

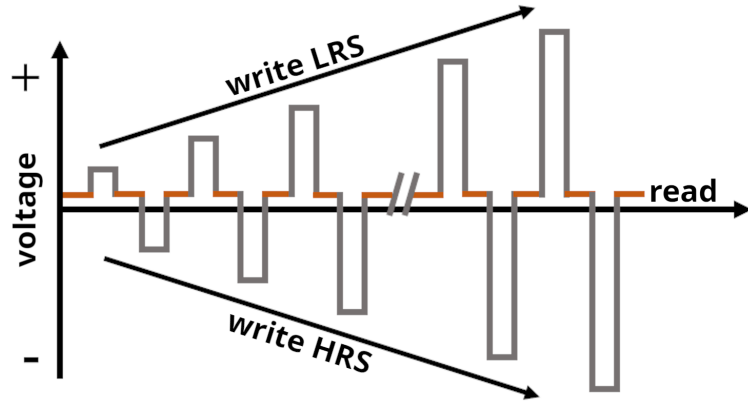


Figure 4.9: Sequence of alternating write and read pulses. The write pulse voltage is successively increased. After each write pulse, the current is measured over a constant read pulse (red lines). Both read and write pulses have a fixed length of 100 ms.

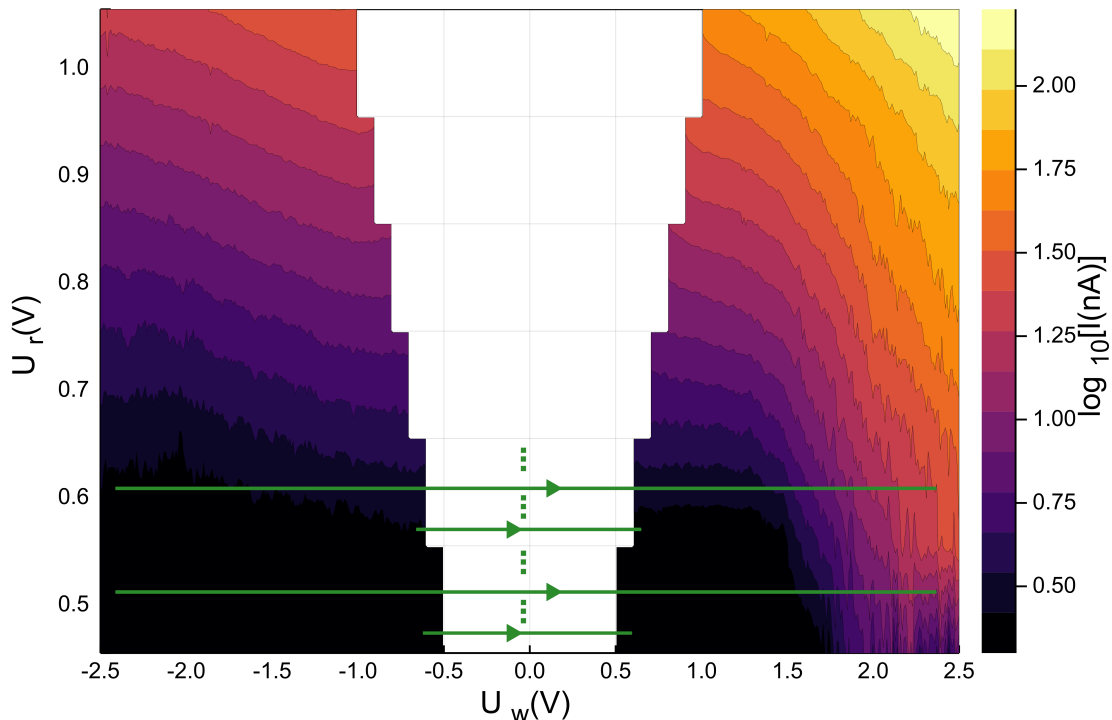


Figure 4.10: Pulse sequence for varying write voltages (± 0.5 V.. ± 2.5 V). After each write pulse of length 100 ms and varying voltage (x-axis), the current is measured at (± 0.5 V.. ± 1.0 V) (y-axis) over 100 ms. The green lines indicate the measurement progression analogous to Fig. 4.9

4.2.3 Valency Mechanism Model

We describe our measurements with the vacancy model in the following steps: A distribution of vacancies is calculated by solving the FDM model 4.16 and Eq. 4.15.

With this distribution of traps, the fraction of filled traps is calculated by solving the FDM model Eq. 2.26 with Eq. 2.25. From this, the electrical current J through the traps is obtained.

Fitting this model to the measured currents presented in Fig. 4.10, we obtain a vacancy distribution as shown in Fig. 4.11.

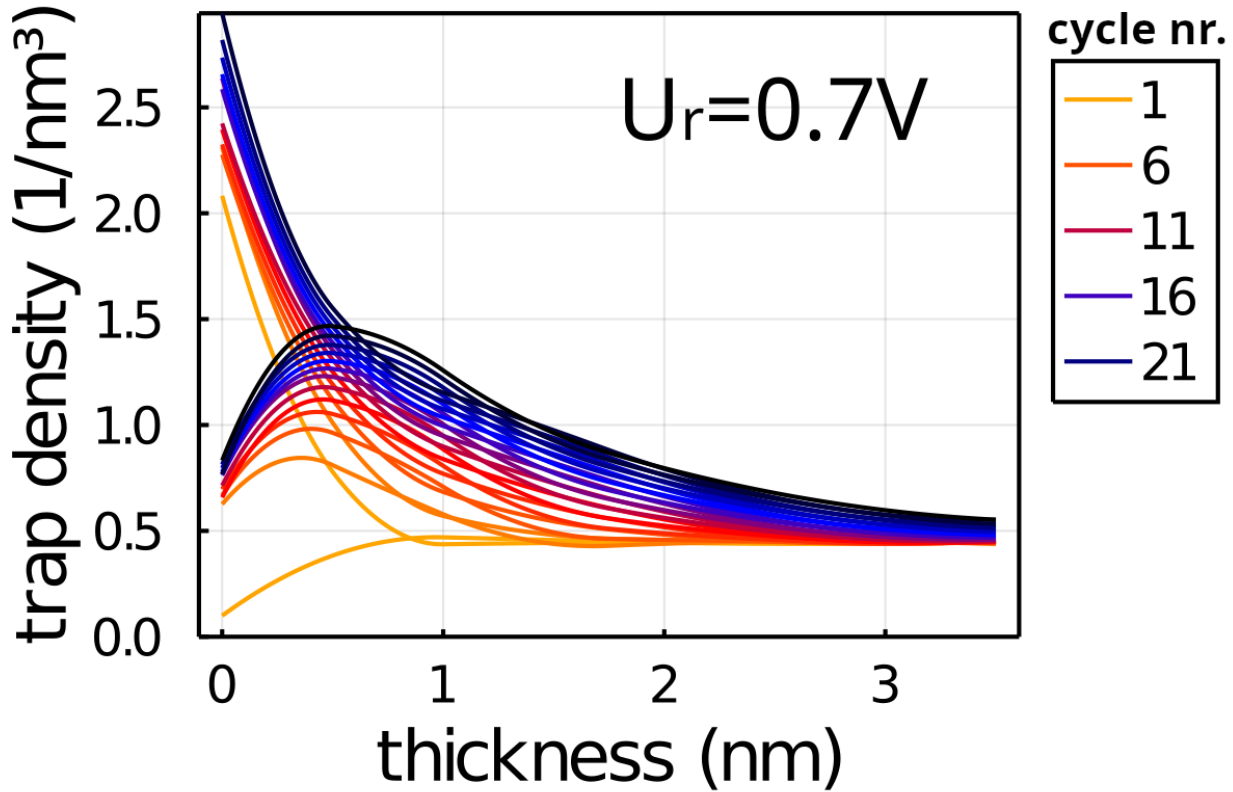


Figure 4.11: Vacancy convection-diffusion FDM model for the pulse sequence, fitted to the measured pulse sequence at $U_r = 0.7V$. The left side is the chemically active $\text{Hf}_{0.5}\text{Zr}_{0.5}\text{O}_2/\text{Au}$ interface, while the right TiN electrode is assumed to be inert.

Conclusion

We developed a finite difference model to describe valency-based resistive switching in our devices. The model describes the formation of oxygen vacancies at the electrodes above 1.5 V, and their field-

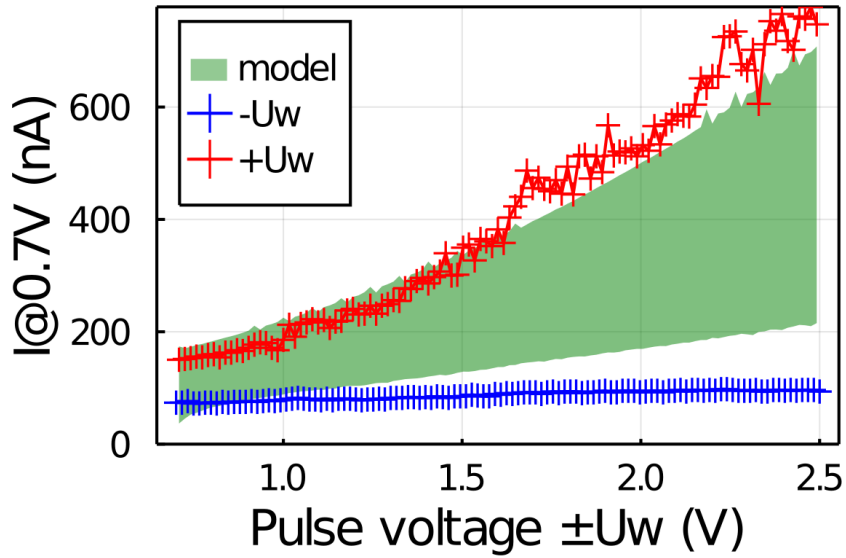


Figure 4.12: Current density from the valency switching model (red) compared to the measured values of the pulse sequence at a read voltage of $U_r = 0.7V$ (Fig. 4.10).

parameter	value	unit	description
u_i	0.445	nm^{-3}	Initial concentration
k^+	0.00338	s^{-1}	Generation rate
k^-	0.560	s^{-1}	Annihilation rate
β	0.914	1	Asymmetry factor
f	0.0120	1	Exponential factor
φ^+	2.94	eV	Vacancy generation barrier
φ^-	1.11	eV	Vacancy annihilation barrier
D	0.0320	$\text{nm}^2 \text{s}^{-1}$	Diffusion coefficient
v_d	3.77×10^{-4}	$\text{nm s}^{-1} \text{V}^{-1}$	Voltage-induced drift

Table 4.2: Valency mechanism model parameters.

enhanced drift-diffusion within the domain. Coupled with the spatially-resolved phonon-assisted tunneling between traps (PATT) model [122, 194] and the Shockley-Read-Hall equations [139, 140], we are able to reproduce the trends observed in our measurements. This allows us to predict the gradual drift in electrical parameters and eventual device breakdown. From the model, we obtain plausible results for the oxygen vacancy density, parameters such as reaction rates, diffusion and drift coefficient. However, the 1D approximation has certain limitations in accuracy which can be attributed to the fact that vacancies cannot agglomerate and dissolve into the two in-plane dimensions. For further refinement of the model, we suggest the following: Extension to 3D,

accounting for the discrete nature of the lattice, and considering the formation of oxynitrides in the bottom electrode.

4.3 CMOS Compatible $\text{Hf}_{0.5}\text{Zr}_{0.5}\text{O}_2$ FTJs for Neuromorphic Devices

While machine learning algorithms are becoming increasingly sophisticated, they are in most cases still based on the binary von Neumann computer architecture. This presents a serious bottleneck of energy efficiency and data processing speeds. In contrast to that, a neural network combines processing and storage in a system of gradually switching artificial synapses. We investigate the viability of $\text{Hf}_{0.5}\text{Zr}_{0.5}\text{O}_2$ ferroelectric tunnel junctions as artificial synapses. The neuromorphic behavior of an individual synapse level is quantitatively characterized by its spike-timing-dependent plasticity (STDP). Resistive switching devices, such as the $\text{Hf}_{0.5}\text{Zr}_{0.5}\text{O}_2$ tunnel junction have been shown to be able to mimic a similar synaptic behavior [176, 195, 196]. Learning in biological neural systems can be understood in terms of Hebb's law: When two neurons fire at once, their connection becomes stronger. This is also known as long term potentiation (LTP), where the amount of neurotransmitters and postsynaptic receptors is increased (Fig. 4.13). There are short-term and long-term modifications in the system, such as the activation of additional receptors, and changes in protein synthesis and gene expression, as well as the ability to grow new connections [197].

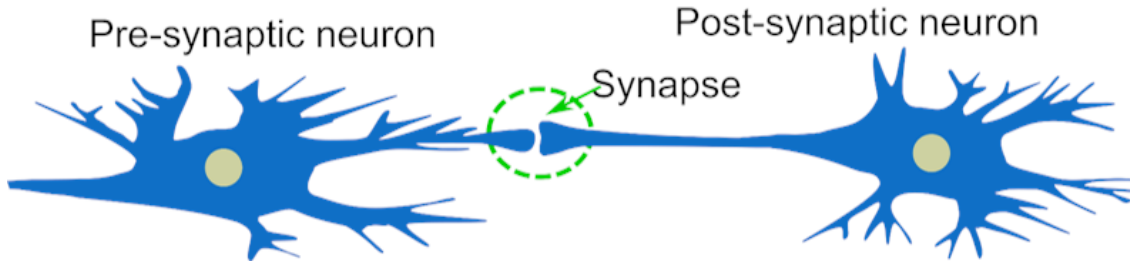


Figure 4.13: Synapse between neurons. The neurons produce electrical pulses. When both pulses overlap at the synapse (see Fig. 4.14), its conductivity is strengthened or weakened, depending on a positive or negative delay between the two. This constitutes the "learning" of a temporal relation between the neurons.

4.3.1 Spike-Timing-Dependent Plasticity

To evaluate the ability of the device to mimic synaptic plasticity, the STDP tests are the technique of choice [198, 199]. The STDP is modeled after the brain's neuronal activity, where the synapse is stimulated by two neurons which each apply a voltage pulse [196, 200, 201]. Also known as action potentials, these pulses and their relative time difference (see Fig. 4.14) induce a strengthening or

the weakening of the synapse, analogous to resistive switching in FTJs. The learning rate is an key parameter of a neural network, and is directly quantified by STDP measurements. This parameter has a crucial impact on the training efficiency and algorithms during the training process. While there exist studies investigating the learning behavior of ReRAM cells using STDP [196, 200, 201], a quantitative study describing the relationship between action potential and learning rate has yet to be reported.

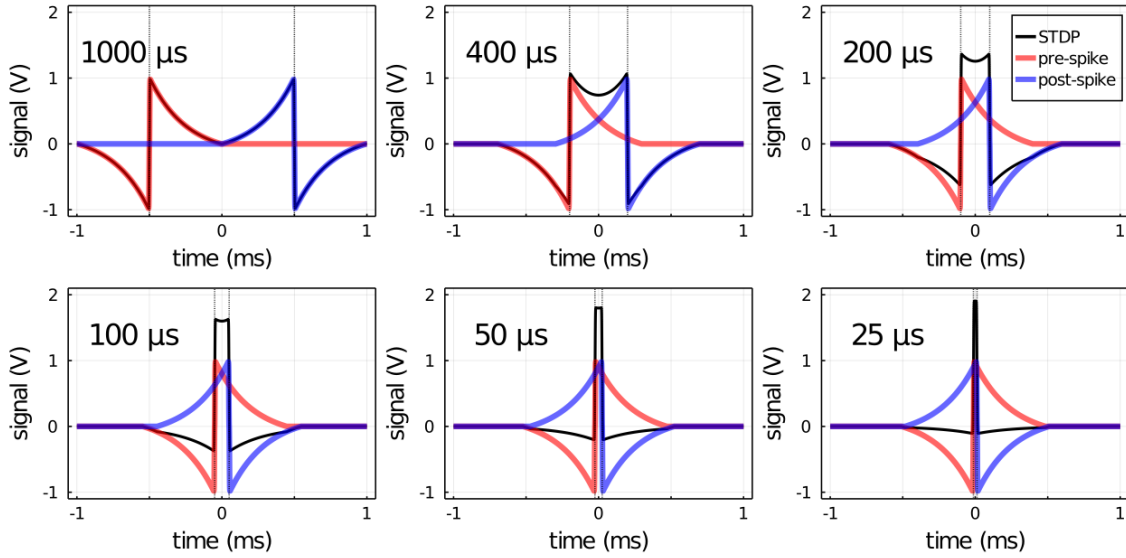


Figure 4.14: Formation of the STDP by two equal spikes on opposite sides of the synapse/FTJ. Their temporal proximity creates up to twice the amplitude of the individual spikes, with the time averaged signal remaining zero. For negative relative times, the resulting voltage pulse is inverted.

A schematic of the STDP mechanism is shown in Fig. 4.15. Since each action potential (red/blue curve) is too small to induce a change in resistance, their temporal superposition (black curves) is required to exceed the threshold voltage (black dashed curve) that allows changing its resistance. The central plot in Fig. 4.15 shows the STDP, more specifically the relative change in resistance as a function of Δt . For a small positive Δt , the pre-synaptic action potential precedes the post-synaptic potential, which describes a causal relation between two neurons. In this way, a large positive superposition of the two spikes (small positive Δt , right part of Fig. 4.15) lowers the resistance of the synapse and enhances future interactions between the neurons. Vice versa, short negative Δt increase the resistance. If $|\Delta t|$ is too large, no causal relation between the two neurons can be established, and the superposition voltage is insufficient to alter the synapse (negative Δt , left part of Fig. 4.15).

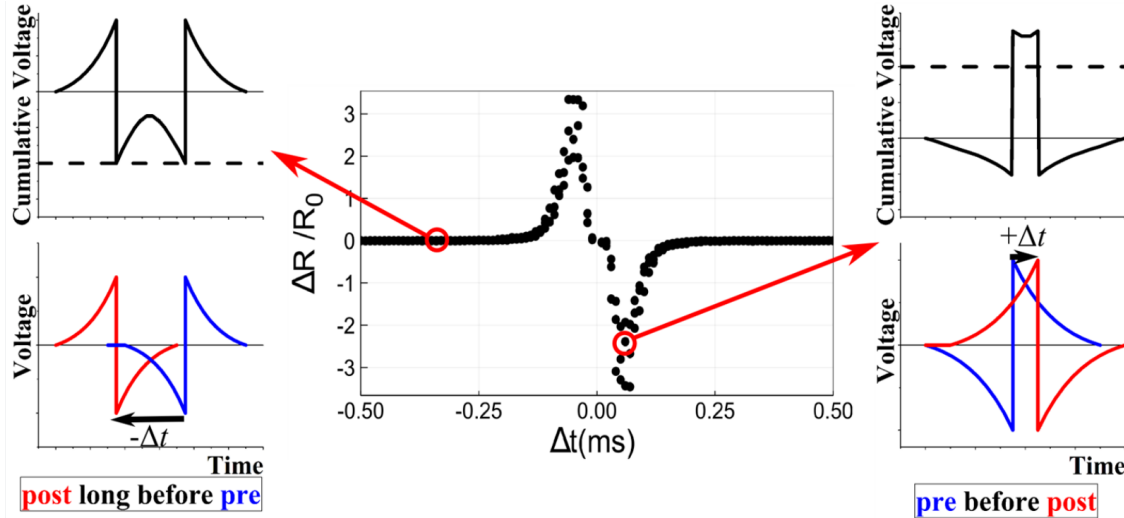


Figure 4.15: Schematic of varying time difference Δt between pre- and post-synaptic action potential creating synaptic plasticity in STDP. The scatter plot shows the change in resistance of the FTJ over Δt (STDP function). For a small positive Δt , the overlap of the two action results in a decrease in the resistance. The red and blue curves represent the pre- and post-synaptic action potential, respectively. The black curve is the superposition of the two action potentials for a given Δt . For a larger negative Δt , the resulting voltage is too small to trigger a change in resistance.[176]

In the following sections, we investigate the spike-timing-dependent plasticity of $\text{Hf}_{0.5}\text{Zr}_{0.5}\text{O}_2$ cells. We perform measurements with varying amplitude and width of the action potentials. From this, we obtain STDP functions that quantitatively show that the learning rate of the synapse depends exponentially on the action potential amplitudes, while the temporal relation can be controlled linearly by the action potential width. This experimental result is supported with a NLS-based physical model of the gradual switching behavior, which relies on gradual switching of grain polarization. The NLS-based IFM model concurs with the experimental results.

The synaptic plasticity in a spiking neural network (SNN), i.e. change in the synapse's resistance, is a function of the time difference Δt between pre- and post-synaptic action potentials as shown in Fig. 4.14. The key measurement in this setup is the resistivity response $\frac{\Delta R}{R_0}$ for a superposition of two action potentials with time offset Δt . We define

$$\frac{\Delta R}{R_0}(\Delta t) = \frac{R_{\text{after}}(\Delta t) - R_{\text{before}}(\Delta t)}{\min\{R_{\text{before}}(\Delta t), R_{\text{after}}(\Delta t)\}} \quad (4.17)$$

where R_{before} and R_{after} are the synapse resistances measured before and after exposure to the action potentials. The minimum of both values is used for normalization.

The STDP measurements $\Delta R/R_0(\Delta t)$ are fitted using the STDP functions

$$\frac{\Delta R}{R_0}(\Delta t) = A_+ \exp(\Delta t/\tau_+) \text{ for } \Delta t > 0 \quad (4.18a)$$

$$\frac{\Delta R}{R_0}(\Delta t) = A_- \exp(\Delta t/\tau_-) \text{ for } \Delta t < 0 \quad (4.18b)$$

with the two linear scaling factors A_+ , A_- and the two characteristic times τ_+ , τ_- . These fitting parameters allow a quantitative comparison between individual measurements.

4.3.2 Partial Switching and Model of Domain Polarization

To describe our experimental results, we employ a physical model of gradual polarization switching. We first express the resistance change as a change in ferroelectric polarization. Polarization switching in the polycrystalline grain structure of $\text{Hf}_{0.5}\text{Zr}_{0.5}\text{O}_2$ includes certain statistical factors that are expressed by the IFM model (see section 2.5.4). The model describes the fractional switching of domains, depending on pulse time and amplitude. We assume a columnar grain structure due to the small film thickness, since the grain diameters are typically at least as large as the film thickness [15, 179]. Thus, the structure can be described as a series of parallel resistors, i.e. the total current is the sum of currents over the individual domains. These individual currents are calculated from the WKB direct tunneling model through a trapezoidal potential profile [63]. The polarization-dependent LRS and HRS current densities are calculated from the trapezoidal tunneling function (section 2.2.1). The linear combination with fraction g in the LRS polarization state then reads

$$j(g) = g j_{LRS}(U, d) + (1 - g) j_{HRS}(U, d) \quad (4.19)$$

where $j(g)$ is the current density, and g is the fraction of ferroelectric domains polarized towards the LRS. The current densities j_{LRS} and j_{HRS} are adjusted to the experimental measurements, using a common scaling factor. The resistance can be expressed as

$$R(g) = \frac{U}{A j(g)} \quad (4.20)$$

where $A=150\text{ }\mu\text{m}^2$ is the FTJ surface area, and $U=200\text{ mV}$ is the applied voltage. Solving by g yields

$$g(R) = \frac{U/(RA) - j_{HRS}}{j_{LRS} - j_{HRS}} \quad (4.21)$$

This equation provides the fraction g corresponding to the measured resistivities, as shown in Fig. 4.19 (green region). This shows that the amount of switched grains initially increases and then decreases with larger Δt .

A typical STDP measurement on the TiN/Hf_{0.5}Zr_{0.5}O₂/Pt FTJ shows a maximum relative resistance change of approximately ± 3.5 (see Fig. 4.16). The STDP curve parameters are obtained by fitting Eq. 4.18 (Fig. 4.16, red curve). We obtain values of -16 and 12 for parameters A_+ and A_- , and -0.034 ms and 0.033 ms for parameters τ_+ and τ_- , respectively. The exponential parameters τ_\pm indicate the dependence between STDP function and Δt , while the linear factors A_\pm measure the peak change in resistance per pulse, and are thus a direct expression of the learning rate. The heuristic Eq. 4.18 provides parameters to quantitatively compare individual STDP measurements. The transition region between the exponential functions $|\Delta t| < 0.05\text{ ms}$ occurs when the increasing amplitudes of the can no longer sufficient to compensate for the decreasing time of the effective superimposed pulse.

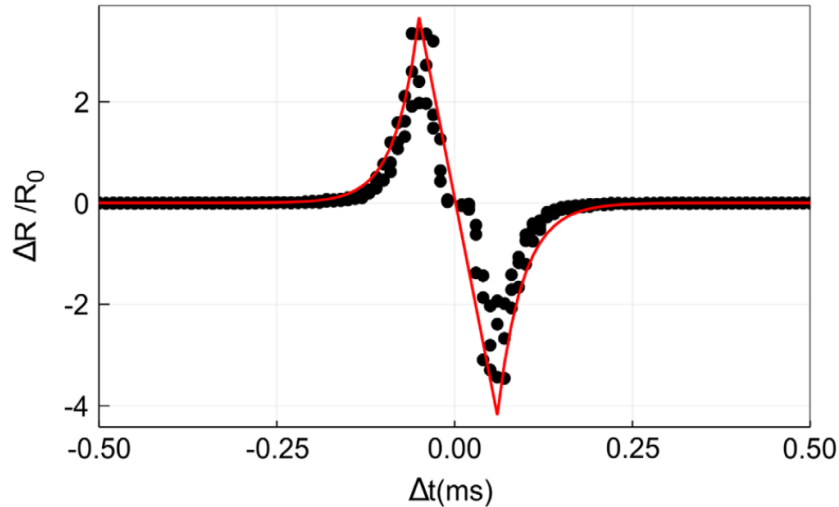


Figure 4.16: STDP switching response as measured at an action potential amplitude of 0.9 V and a width of 2 ms. Red lines are fits of Eq. 4.18.

The influence of the amplitude of both action potentials on the fitted parameters of the STDP function is shown in Fig. 4.17. Fig. 4.17a depicts the change in scaling parameters with the ac-

tion potential peak amplitude, which ranges from 0.05 to over 100 for action potential amplitudes between 0.7 V and 1.2 V. For each voltage value, three measurements are performed. The three measurements show good reproducibility over the STDP curve, as shown in Fig. 4.17a. Furthermore, the logarithmic plot reveals an approximately linear correlation up to 1.1 V, corresponding to an exponential dependence of the scaling parameters on the amplitude of the action potentials. For higher amplitudes, the scaling parameter saturates. Since the superposition scales linear with its components for a constant Δt , this induces a larger change in resistance that we attribute to ferroelectric switching within the FTJ. Analogous, the relationship between action potential amplitude and exponential parameters is shown in Fig. 4.17b. The exponential parameters τ_{\pm} remain approximately constant for action potential amplitudes in the 0.7 V to 1.2 V range.

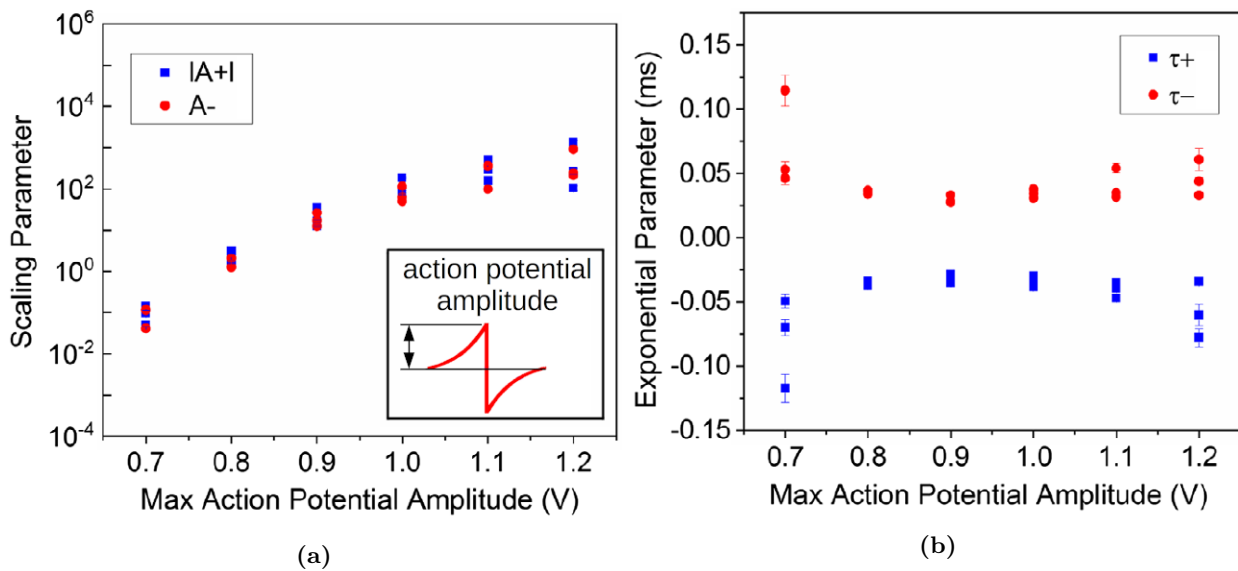


Figure 4.17: STDP scaling parameters over maximum action potential amplitude at a constant action potential width of 1 ms. (a) Scaling parameters A_{\pm} over action potential amplitude. (b) Exponential parameters τ_{\pm} over action potential amplitude.

Fig. 4.18 shows the dependence between the action potential width and the STDP function. The pulse width is varied between 0.8 ms and 2.0 ms at a fixed action potential of 0.7 V. While the parameters A_{\pm} only show negligible variations (Fig. 4.18a), the exponential parameters τ_{\pm} naturally show a linear dependence on the action potential width (Fig. 4.18b). Thus, the width of the incoming stimulus does not affect the learning rate, while the change in the exponential parameters can be used to control the decay of the STDP function.

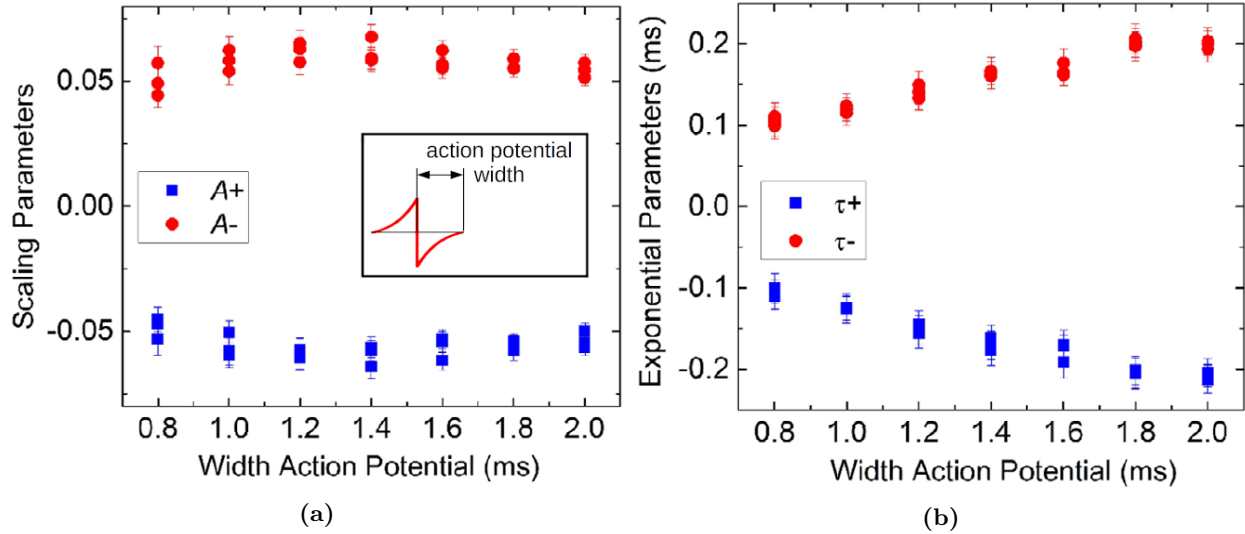


Figure 4.18: STDP scaling parameters over action potential width at a constant maximum action potential amplitude of 0.7 V. (a) Scaling parameters A_{\pm} over action potential width. (b) Exponential parameters τ_{\pm} over action potential width.

4.3.3 Modeling the STDP Switching Behavior

We use the IFM model [202] to describe our measurements from the previous section. The model provides an analytical description of the time- and field-dependent polarization reversal in ferroelectric thin films (see section 2.5.4) [119]

$$\Delta P(t) = P_s \operatorname{erfc} \left\{ \left[\frac{E_a}{E_f(t) [\log(t/\tau_0)]^{1/n}} - 1 \right] / \sqrt{2}\sigma \right\} \quad (4.22)$$

where $E_f(t)$ is the electric field, P_s , E_a , τ_0 , n , and σ are material parameters and $\operatorname{erfc}(x)$ is the complementary error function.

During the measurements, the FTJ is probed by a sequence of STDPs with positive and negative time delays Δt between 20 μ s to 320 μ s and spike amplitudes ranging from 0.8 V to 1.1 V. For small delays Δt , the resulting signal is approximately a rectangular pulse of width Δt with an exponentially decaying voltage amplitude with increasing Δt . The resistivity is measured before and after each pulse at 0.2 V. The induced polarization change is determined by Eq. 4.21, resulting in a switching range shown in Fig. 4.19 (green area).

While this equation describes the polarization reversal starting from $\Delta P(t) = 0$ at time $t = 0$, our devices possess an intrinsic bias that leaves an initial non-zero mean polarization. Thus, we

determine the initial time t_{init} that corresponds to our device's initial polarization. Starting from this value, the part of the STPD pulse that exceeds the threshold can be approximated by a rectangular pulse, and the evolution of the polarization is simply obtained by solving Eq. 4.22 with a time step of Δt . Due to the asymmetric switching behavior, we determine two sets of parameters as shown in table 4.3. The polarization fraction g is then obtained from Eq. 4.22. Fig. 4.19 compares the model with our experimental data. The figure shows that switching starting from Δt of $20 \mu\text{s}$. The device is switched between LRS (lower curve) and HRS (upper curve) by $+\Delta t$ and $-\Delta t$ for each time step.

Switching to the maximum HRS takes about $60 \mu\text{s}$. For Δt above $150 \mu\text{s}$ and action potential amplitudes of 1.0 and 1.1 V , switching towards the LRS increases. This could indicate that it takes larger $+\Delta t$ to switch certain remaining domains in the LRS, which could indicate a slower mechanism such as a sideways growth of ferroelectric domains [203]. The asymmetric behavior can be explained by the different electronic and mechanical properties of the interfaces or contributions from charged defects.

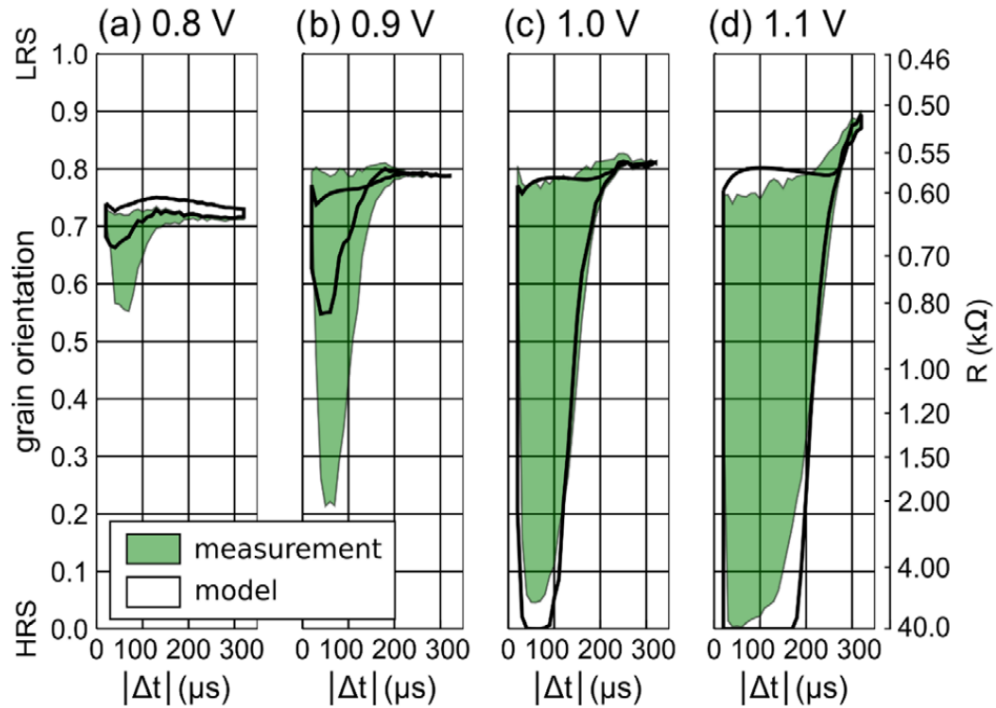


Figure 4.19: Resistive switching for varying STDP pulses with amplitudes a) 0.8 V b) 0.9 V c) 1.0 V , and d) 1.1 V and offsets Δt . The green area corresponds to the grain orientation switching induced by two overlapping spikes with Δt in the positive and negative orientations. The black line shows the model prediction when starting from the measured value [176]

Parameter	P_s ($\mu\text{C}/\text{cm}^2$)	τ_0 (μs)	E_a (MV/cm)	σ (1)	n (1)
HRS to LRS	$2P_0$	6.9	3.85	0.60	1.72
LRS to HRS	$2P_0$	22	4.53	0.089	3.77

Table 4.3: IFM model fitting parameters

Using the polarization switching model from Eq. 4.22, we are able to reproduce the STDP curves Fig. 4.20a. This is again done by computing the polarization component g aligned with the LRS, and using the WKB model to compute the total resistance. Fig. 4.20a shows that the approximate behavior of our measurements is reproduced.

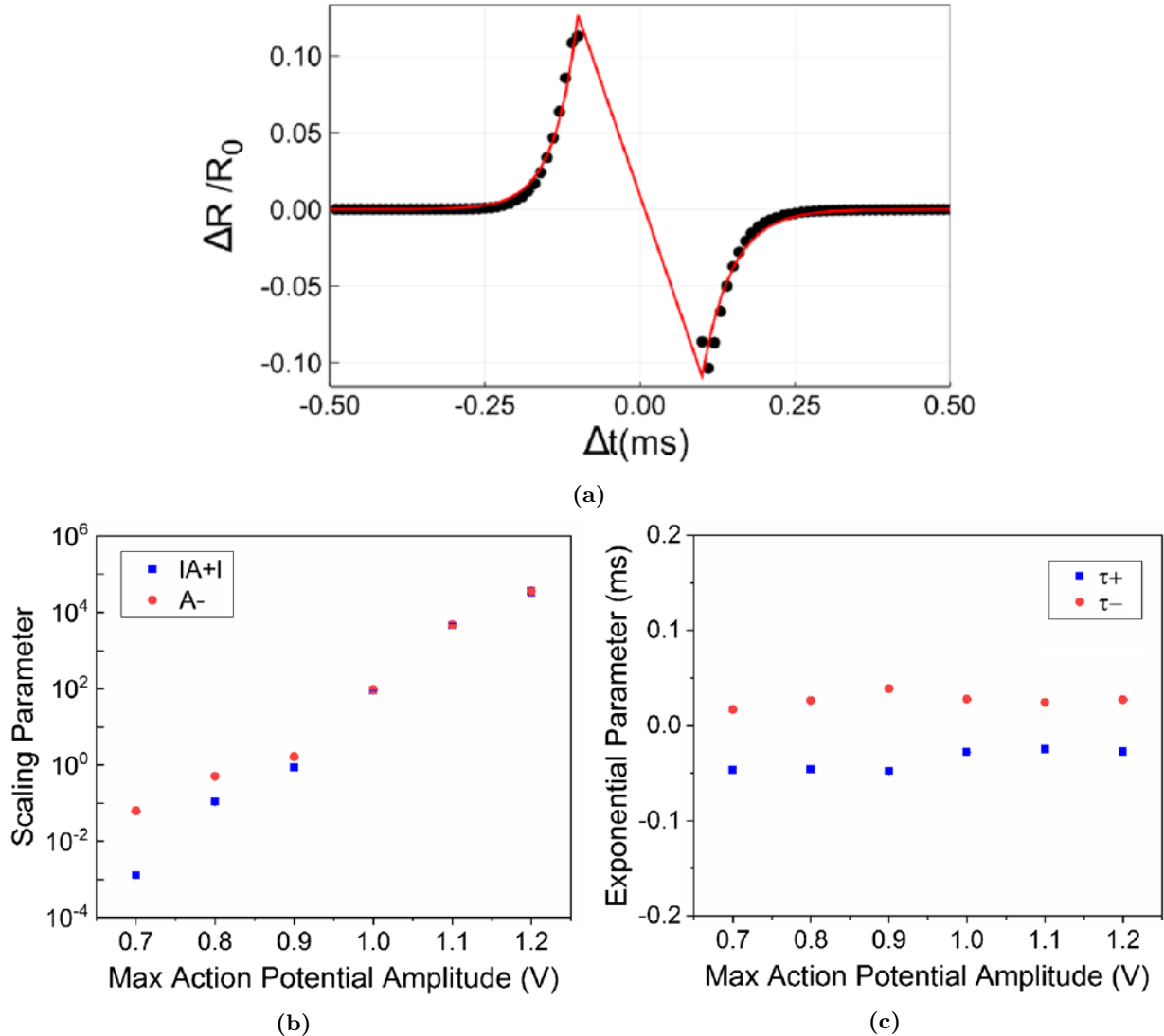


Figure 4.20: STDP switching response obtained from NLS model. (a) Switching response at an action potential amplitude of 0.9 V and a width of 2 ms. Red lines are fits of Eq. 4.18. (b) Scaling parameters A_\pm over action potential amplitude. (c) Exponential parameters τ_\pm over action potential amplitude [132].

4.3.4 Conclusion

We investigate the neuromorphic properties of a TiN/Hf_{0.5}Zr_{0.5}O₂/Pt ferroelectric tunnel junction acting as an artificial synapse. The resistive switching properties are determined using Spike-timing-dependent plasticity measurements with varying amplitude and width of the action potentials. We find reproducible multilevel switching with a synaptic learning rate that mainly depends on the voltage amplitude of the applied stimulus. The experimental result is supported by the IFM model

that describes the nucleation limited ferroelectric switching process (see section 2.5.4). The model is capable of reproducing our experimental findings up to spike voltages of 1 V, most notably the exponential dependence between spike amplitude and learning rate. These results will be useful in the design of a hardware spiking neural network.

Chapter 5

Summary and Outlook

While FTJs have long been theoretically predicted, they have only been experimentally demonstrated in 2009 [9]. With the 2011 discovery of a ferroelectric phase in doped HfO₂ [7], a material with unique characteristics became available. While research into this material is still ongoing, its advantageous scalability and CMOS compatibility make Hf_{0.5}Zr_{0.5}O₂ an excellent candidate for FTJ devices. We build on previous works of Vargas [180], who developed a quantitative model of the tunneling barrier that has since been supported by Yoon et al. [59]. A metal-insulator-metal ferroelectric tunnel junction design has been demonstrated. A film thickness of 3 nm allows for significant tunneling currents. The mechanism transitions from direct tunneling to a trap-assisted tunneling at elevated voltages.

5.1 Summary

First, we have investigated a Pt/Hf_xZr_{1-x}O₂/TiN FTJ with regards to its electronic charge transport properties. The polycrystalline nature of the TiN bottom electrode, as well as the polycrystalline Hf_xZr_{1-x}O₂ crystallization inevitably result in inhomogeneities within the ferroelectric layer. Based on the WKB equation, we have developed an analytical model that estimates the impact of surface thickness on its electrical performance [175]. The straightforward analytical expression describes the impact of thickness inhomogeneities on electrical conductivity, TER switching ratios which are key to information recovery, and probability of electrical breakdown. From this, man-

ufacturing requirements for a reproducible design are derived. The results are exemplified on the TiN/Hf_{0.5}Zr_{0.5}O₂/Pt heterostructure. The exponential nature of tunneling currents with respect to the thickness makes this effect critical when designing devices and investigating and stability, where a thickness reduction by a single unit cell in a \sim 3 nm insulator may increase the conductance by up to 3 orders of magnitude, and significantly diminishes the TER ratio. This critical effect on the electrical performance is not easily mediated by the averaging effect of a large device area, but rather increases the chances of electrical breakdown. We estimate the effect of pinned domains, non-ferroelectric phases and the probability of local short circuits. Our model shows that producing integrated circuits with large numbers of operational devices with comparable electrical properties is a major challenge that is partially intrinsic to the polycrystalline nature of the FTJ.

In the second part, we investigate the switching behavior at voltages significantly exceeding the coercive field on a 3.5 nm Au/Hf_{0.5}Zr_{0.5}O₂/TiN FTJ. We find that the valency switching mechanism supersedes ferroelectric switching. Oxygen is ejected from Hf_{0.5}Zr_{0.5}O₂ into the Hf_{0.5}Zr_{0.5}O₂/Au interface, leaving positively charged holes that can trap electrons. We develop a numerical model that describes the generation of these vacancies at the interface, and a drift-diffusion process dispersing them throughout the insulator. Using the By fitting this model to the experimental data, we obtain reaction rates, diffusion and a field dependent drift velocity of these vacancies. Combined with the phonon-assisted tunneling between traps (PATT) model [122, 194], we describe the time-dependent resistive switching behavior. The resulting model is in good agreement with our experimental results.

Our third study is dedicated to the FTJ application in a spiking neural network [176]. Its gradual switching characteristic makes the FTJ viable for multilevel or analog applications [11, 12] and as such a viable candidate for a spiking neural network [204]. In our setup, the TiN/Hf_{0.5}Zr_{0.5}O₂/Pt FTJ acts as an artificial synapse. We perform spike-timing-dependent plasticity measurements [196, 200, 201] over varying amplitudes and widths of the action potential. A quantitative analysis of the resulting STDP functions shows that the learning rate of the synapse mainly depends on the amplitude of the action potential. We find the nucleation-limited switching (NLS) model [119, 202] to be in good agreement with our experimental findings. The gradual switching ability makes the FTJ a well-suited candidate for this type of application.

5.2 Conclusion and Outlook

A ferroelectric tunnel junction design was demonstrated. A ferroelectric film thin enough to enable quantum-mechanical tunneling is stacked between two metal electrodes. This thesis investigates practical and theoretical design contributions, interactions and physical mechanisms and substantiates models to describe the observed conduction, switching and degradation behavior. Manufacturing of these devices proves challenging for two major reasons. The employed sputtering-induced growth mechanism of TiN forms non-planar surface structures, which are further enhanced by annealing-induced crystal growth. Based on this, the thereon deposited $\text{Hf}_x\text{Zr}_{1-x}\text{O}_2$ layer exhibits a variation in thickness.

The successful preparation of FTJs is demonstrated, even though the reproducibility remains low within and between batches. Using ferroelectric conductivity models, direct tunneling is identified as the dominant conduction mechanism in pristine, sub-3nm devices. This is supported by its magnitude, as well as the measured TER ratio. This also demonstrates that the much more cost-efficient sputtering process can be used, as opposed to the commonly used ALD approach.

Important model parameters for polarization switching, such as the coercive field, and the resulting potential profile were determined, as well as time dependent polarization reversal processes, confirming a significantly biased switching behavior in our FTJs.

Future research could address the field device consistency, the effects of electrode interface oxidation that represent additional screening layers, as well as increasing the long-term stability of the device. Improved models of both tunneling and electrochemistry should also consider the discrete nature and quantum properties of the crystal.

References

- [1] J.M Herbert. *Ferroelectric transducers and sensors*. Gordon and Breach, New York, 1982. ISBN 978-0-677-05910-5. OCLC: 839404967.
- [2] D. Damjanovic, P. Muralt, and N. Setter. Ferroelectric sensors. *IEEE Sensors Journal*, 1(3): 191–206, October 2001. ISSN 1558-1748. doi: 10.1109/JSEN.2001.954832. Conference Name: IEEE Sensors Journal.
- [3] A. K. Sarin Kumar, P. Paruch, J.-M. Triscone, W. Daniau, S. Balandras, L. Pellegrino, D. Marré, and T. Tybell. High-frequency surface acoustic wave device based on thin-film piezoelectric interdigital transducers. *Applied Physics Letters*, 85(10):1757–1759, September 2004. ISSN 0003-6951. doi: 10.1063/1.1787897. URL <https://aip.scitation.org/doi/abs/10.1063/1.1787897>. Publisher: American Institute of Physics.
- [4] Vladimir M. Fridkin. *Photoferroelectrics*. Springer Series in Solid-State Sciences. Springer-Verlag, Berlin Heidelberg, 1979. ISBN 978-3-642-81353-5. doi: 10.1007/978-3-642-81351-1. URL <https://www.springer.com/gp/book/9783642813535>.
- [5] James F. Scott. *Ferroelectric Memories*. Springer Science & Business Media, May 2000. ISBN 978-3-540-66387-4. Google-Books-ID: 9FT06UFHWZwC.
- [6] Rainer Waser and Andreas Rüdiger. Pushing towards the digital storage limit. *Nature Materials*, 3(2):81–82, February 2004. ISSN 1476-4660. doi: 10.1038/nmat1067. URL <https://www.nature.com/articles/nmat1067>. Number: 2 Publisher: Nature Publishing Group.
- [7] T. S. Böscke, J. Müller, D. Bräuhaus, U. Schröder, and U. Böttger. Ferroelectricity in hafnium oxide thin films. *Applied Physics Letters*, 99(10):102903, September 2011. ISSN 0003-6951, 1077-3118. doi: 10.1063/1.3634052. URL <http://aip.scitation.org/doi/10.1063/1.3634052>.
- [8] a L Esaki, RB Laibowitz, and PJ Stiles. Polar switch. *IBM Tech. Disc. Bull*, 13(2161):114, 1971.
- [9] V. Garcia, S. Fusil, K. Bouzehouane, S. Enouz-Vedrenne, N. D. Mathur, A. Barthélémy, and M. Bibes. Giant tunnel electroresistance for non-destructive readout of ferroelectric states. *Nature*, 460(7251):81–84, May 2009. doi: 10.1038/nature08128. URL <https://doi.org/10.1038%2Fnature08128>.
- [10] S. Boyn, S. Girod, V. Garcia, S. Fusil, S. Xavier, C. Deranlot, H. Yamada, C. Carrétéro, E. Jacquet, M. Bibes, A. Barthélémy, and J. Grollier. High-performance ferroelectric memory

- based on fully patterned tunnel junctions. *Applied Physics Letters*, 104(5):052909, February 2014. ISSN 0003-6951, 1077-3118. doi: 10.1063/1.4864100. URL <http://aip.scitation.org/doi/10.1063/1.4864100>.
- [11] Hiroyuki Yamada, Vincent Garcia, Stéphane Fusil, Sören Boyn, Maya Marinova, Alexandre Gloter, Stéphane Xavier, Julie Grollier, Eric Jacquet, Cécile Carrétéro, Cyrile Deranlot, Manuel Bibes, and Agnès Barthélémy. Giant Electroresistance of Super-tetragonal BiFeO₃-Based Ferroelectric Tunnel Junctions. *American Chemical Society NANO*, 7(6):5385–5390, June 2013. ISSN 1936-0851. doi: 10.1021/nn401378t. URL <https://doi.org/10.1021/nn401378t>. Publisher: American Chemical Society.
 - [12] André Chanthbouala, Arnaud Crassous, Vincent Garcia, Karim Bouzehouane, Stéphane Fusil, Xavier Moya, Julie Allibe, Bruno Dlubak, Julie Grollier, Stéphane Xavier, Cyrile Deranlot, Amir Moshar, Roger Proksch, Neil D. Mathur, Manuel Bibes, and Agnès Barthélémy. Solid-state memories based on ferroelectric tunnel junctions. *Nature Nanotechnology*, 7(2):101–104, February 2012. ISSN 1748-3387, 1748-3395. doi: 10.1038/nnano.2011.213. URL <http://www.nature.com/articles/nnano.2011.213>.
 - [13] Evgeny Y. Tsymbal and Hermann Kohlstedt. Tunneling Across a Ferroelectric. *Science*, 313 (5784):181–183, July 2006. ISSN 0036-8075, 1095-9203. doi: 10.1126/science.1126230. URL <https://science.sciencemag.org/content/313/5784/181>.
 - [14] Vincent Garcia and Manuel Bibes. Ferroelectric tunnel junctions for information storage and processing. *Nature Communications*, 5(1):4289, September 2014. ISSN 2041-1723. doi: 10.1038/ncomms5289. URL <http://www.nature.com/articles/ncomms5289>.
 - [15] Han Joon Kim, Min Hyuk Park, Yu Jin Kim, Young Hwan Lee, Woojin Jeon, Taehong Gwon, Taehwan Moon, Keum Do Kim, and Cheol Seong Hwang. Grain size engineering for ferroelectric Hf_{0.5}Zr_{0.5}O₂ films by an insertion of Al₂O₃ interlayer. *Applied Physics Letters*, 105(19):192903, November 2014. ISSN 0003-6951, 1077-3118. doi: 10.1063/1.4902072. URL <http://aip.scitation.org/doi/10.1063/1.4902072>.
 - [16] Min Hyuk Park, Han Joon Kim, Yu Jin Kim, Woongkyu Lee, Taehwan Moon, and Cheol Seong Hwang. Evolution of phases and ferroelectric properties of thin Hf_{0.5}Zr_{0.5}O₂ films according to the thickness and annealing temperature. *Applied Physics Letters*, 102(24):242905, June 2013. doi: 10.1063/1.4811483. URL <https://doi.org/10.1063%2F1.4811483>.
 - [17] Takao Shimizu, Tatsuhiko Yokouchi, Takahiro Oikawa, Takahisa Shiraishi, Takanori Kiguchi, Akihiro Akama, Toyohiko J. Konno, Alexei Gruverman, and Hiroshi Funakubo. Contribution of oxygen vacancies to the ferroelectric behavior of Hf_{0.5}Zr_{0.5}O₂ thin films. *Applied Physics Letters*, 106(11):112904, March 2015. doi: 10.1063/1.4915336. URL <https://doi.org/10.1063%2F1.4915336>.
 - [18] Min Hyuk Park, Han Joon Kim, Yu Jin Kim, Taehwan Moon, and Cheol Seong Hwang. The effects of crystallographic orientation and strain of thin Hf_{0.5}Zr_{0.5}O₂ film on its ferroelectricity. *Applied Physics Letters*, NCFET2019(1):072901, February 2014. ISSN 0003-6951. doi: 10.1063/1.4866008@apl.2019.NCFET2019.issue-1. URL <https://aip.scitation.org/doi/abs/10.1063/1.4866008%40apl.2019.NCFET2019.issue-1>. Publisher: American Institute of Physics.

- [19] G. Velu, D. Remiens, P. Tronc, E. Cattan, and B. Thierry. Influence of annealing treatment on the ferroelectric and piezoelectric properties of PZT thin films grown on silicon substrates by sputtering. In *ISAF '96. Proceedings of the Tenth IEEE International Symposium on Applications of Ferroelectrics*, volume 1, pages 503–506 vol.1, August 1996. doi: 10.1109/ISAF.1996.602799.
- [20] Linghua Jin, Xianwu Tang, Dongpo Song, Renhuai Wei, Jie Yang, Jianming Dai, Wen-hai Song, Xuebin Zhu, and Yuping Sun. Annealing temperature effects on (111)-oriented BiFeO₃ thin films deposited on Pt/Ti/SiO₂/Si by chemical solution deposition. *Journal of Materials Chemistry C*, 3(41):10742–10747, 2015. ISSN 2050-7526, 2050-7534. doi: 10.1039/C5TC02379C. URL <http://xlink.rsc.org/?DOI=C5TC02379C>.
- [21] Zhen Zheng, Yuhao Shi, Xinyu Liang, and Chunqing Wang. The Anneal Temperature Effect on the BTO and NZFO Flims and Their Capacitance - Inductance Integrated Device. *Semiconductor Science and Information Devices*, 1(1), October 2019. ISSN 2661-3212. doi: 10.30564/ssid.v1i1.606. URL <https://ojs.bilpublishing.com/index.php/ssid/article/view/606>.
- [22] Johannes Müller, Tim S. Böscke, Uwe Schröder, Stefan Müller, Dennis Bräuhaus, Ulrich Böttger, Lothar Frey, and Thomas Mikolajick. Ferroelectricity in Simple Binary ZrO₂ and HfO₂. *Nano Letters*, 12(8):4318–4323, August 2012. ISSN 1530-6984, 1530-6992. doi: 10.1021/nl302049k. URL <http://pubs.acs.org/doi/10.1021/nl302049k>.
- [23] J. Müller, T. S. Böscke, U. Schröder, M. Reinicke, L. Oberbeck, D. Zhou, W. Weinreich, P. Kücher, M. Lemberger, and L. Frey. Improved manufacturability of ZrO₂ MIM capacitors by process stabilizing HfO₂ addition. *Microelectronic Engineering*, 86(7):1818–1821, July 2009. ISSN 0167-9317. doi: 10.1016/j.mee.2009.03.076. URL <http://www.sciencedirect.com/science/article/pii/S0167931709002494>.
- [24] Xinyuan Zhao and David Vanderbilt. First-principles study of structural, vibrational, and lattice dielectric properties of hafnium oxide. *Physical Review B*, 65(23):233106, June 2002. doi: 10.1103/PhysRevB.65.233106. URL <https://link.aps.org/doi/10.1103/PhysRevB.65.233106>. Publisher: American Physical Society.
- [25] Deok-Yong Cho, Hyung-Suk Jung, and Cheol Hwang. Structural properties and electronic structure of HfO₂-ZrO₂ composite films. *Physical Review B - PHYS REV B*, 82, September 2010. doi: 10.1103/PhysRevB.82.094104.
- [26] Shosuke Fujii, Yuuichi Kamimuta, Tsunehiro Ino, Yasushi Nakasaki, Riichiro Takaishi, and Masumi Saitoh. First demonstration and performance improvement of ferroelectric HfO₂-based resistive switch with low operation current and intrinsic diode property. In *2016 IEEE Symposium on VLSI Technology*, pages 1–2, June 2016. doi: 10.1109/VLSIT.2016.7573413. ISSN: 2158-9682.
- [27] Anna Chernikova, Maksim Kozodaev, Andrei Markeev, Dmitrii Negrov, Maksim Spiridonov, Sergei Zarubin, Ohheum Bak, Pratyush Buragohain, Haidong Lu, Elena Suvorova, Alexei Gruverman, and Andrei Zenkevich. Ultrathin Hf_{0.5}Zr_{0.5}O₂ Ferroelectric Films on Si. *ACS Applied Materials & Interfaces*, 8(11):7232–7237, March 2016. ISSN 1944-8244, 1944-8252. doi: 10.1021/acsami.5b11653. URL <http://pubs.acs.org/doi/10.1021/acsami.5b11653>.

- [28] Dong Zhao, Thomas Lenz, Gerwin H. Gelinck, Pim Groen, Dragan Damjanovic, Dago M. de Leeuw, and Ilias Katsouras. Depolarization of multidomain ferroelectric materials. *Nature Communications*, 10(1):2547, December 2019. ISSN 2041-1723. doi: 10.1038/s41467-019-10530-4. URL <http://www.nature.com/articles/s41467-019-10530-4>.
- [29] J. McPherson, J. Kim, A. Shanware, H. Mogul, and J. Rodriguez. Proposed universal relationship between dielectric breakdown and dielectric constant. In *Digest. International Electron Devices Meeting*,, pages 633–636, San Francisco, CA, USA, 2002. IEEE. ISBN 978-0-7803-7462-1. doi: 10.1109/IEDM.2002.1175919. URL <http://ieeexplore.ieee.org/document/1175919/>.
- [30] Zibin Chen, Qianwei Huang, Feifei Wang, Simon P. Ringer, Haosu Luo, and Xiaozhou Liao. Stress-induced reversible and irreversible ferroelectric domain switching. *Applied Physics Letters*, 112(15):152901, April 2018. ISSN 0003-6951. doi: 10.1063/1.5020534. URL <https://aip.scitation.org/doi/10.1063/1.5020534>. Publisher: American Institute of Physics.
- [31] Doo Seok Jeong, Reji Thomas, Ram Katiyar, J Scott, H Kohlstedt, Adrian Petraru, and Cheol Hwang. Emerging memories: Resistive switching mechanisms and current status. *Reports on progress in physics. Physical Society (Great Britain)*, 75:076502, July 2012. doi: 10.1088/0034-4885/75/7/076502.
- [32] R. Ranjan, K. L. Pey, C. H. Tung, L. J. Tang, D. S. Ang, G. Groeseneken, S. De Gendt, and L. K. Bera. Breakdown-induced thermochemical reactions in HfO₂ high-k/polycrystalline silicon gate stacks. *Applied Physics Letters*, 87(24):242907, December 2005. ISSN 0003-6951. doi: 10.1063/1.2146071. URL <https://aip.scitation.org/doi/10.1063/1.2146071>. Publisher: American Institute of Physics.
- [33] K. L. Pey, C. H. Tung, L. J. Tang, W. H. Lin, and M. K. Radhakrishnan. Size difference in dielectric-breakdown-induced epitaxy in narrow n- and p-metal oxide semiconductor field effect transistors. *Applied Physics Letters*, 83(14):2940–2942, September 2003. ISSN 0003-6951. doi: 10.1063/1.1616195. URL <https://aip.scitation.org/doi/10.1063/1.1616195>. Publisher: American Institute of Physics.
- [34] J. D. Baniecki, T. Shioga, K. Kurihara, and N. Kamehara. Investigation of the importance of interface and bulk limited transport mechanisms on the leakage current of high dielectric constant thin film capacitors. *Journal of Applied Physics*, 94(10):6741–6748, October 2003. ISSN 0021-8979. doi: 10.1063/1.1620377. URL <https://aip.scitation.org/doi/10.1063/1.1620377>. Publisher: American Institute of Physics.
- [35] N. Setter, D. Damjanovic, L. Eng, G. Fox, S. Gevorgian, S. Hong, A. Kingon, H. Kohlstedt, N. Y. Park, G. B. Stephenson, I. Stolitchnov, A. K. Taganstev, D. V. Taylor, T. Yamada, and S. Streiffer. Ferroelectric thin films: Review of materials, properties, and applications. *Journal of Applied Physics*, 100(5):051606, September 2006. ISSN 0021-8979. doi: 10.1063/1.2336999. URL <https://aip.scitation.org/doi/10.1063/1.2336999>.
- [36] Premi Chandra and Peter B. Littlewood. A Landau Primer for Ferroelectrics. In *Physics of Ferroelectrics*, volume 105, pages 69–116. Springer Berlin Heidelberg, Berlin, Heidelberg, 2007. ISBN 978-3-540-34590-9. doi: 10.1007/978-3-540-34591-6_3. URL http://link.springer.com/10.1007/978-3-540-34591-6_3.

- [37] Hang Ting Lue, Chien Jang Wu, and Tseung Yuen Tseng. Device modeling of ferroelectric memory field-effect transistor (FeMFET). *IEEE Transactions on Electron Devices*, 49(10):1790–1798, October 2002. ISSN 0018-9383. doi: 10.1109/TED.2002.803626. URL <https://scholar.lib.ntnu.edu.tw/en/publications/device-modeling-of-ferroelectric-memory-field-effect-transistor-f>. Publisher: Institute of Electrical and Electronics Engineers Inc.
- [38] K. Tashiro, K. Takano, M. Kobayashi, Y. Chatani, and H. Tadokoro. Structural study on ferroelectric phase transition of vinylidene fluoride-trifluoroethylene copolymers (III) dependence of transitional behavior on VDF molar content. *Ferroelectrics*, 57(1):297–326, June 1984. ISSN 0015-0193. doi: 10.1080/00150198408012770. URL <https://doi.org/10.1080/00150198408012770>. Publisher: Taylor & Francis _eprint: <https://doi.org/10.1080/00150198408012770>.
- [39] H. F. Kay and J. W. Dunn. Thickness dependence of the nucleation field of triglycine sulphate. *Philosophical Magazine*, 7(84):2027–2034, 1962.
- [40] M. Dawber, P. Chandra, P. B. Littlewood, and J. F. Scott. Depolarization corrections to the coercive field in thin-film ferroelectrics. *Journal of Physics: Condensed Matter*, 15(24):L393–L398, June 2003. ISSN 0953-8984. doi: 10.1088/0953-8984/15/24/106. URL <https://doi.org/10.1088%2F0953-8984%2F15%2F24%2F106>. Publisher: IOP Publishing.
- [41] Monica Materano, Patrick D. Lomenzo, Halid Mulaosmanovic, Michael Hoffmann, Akira Toriumi, Thomas Mikolajick, and Uwe Schroeder. Polarization switching in thin doped HfO₂ ferroelectric layers. *Applied Physics Letters*, 117(26):262904, December 2020. ISSN 0003-6951. doi: 10.1063/5.0035100. URL <https://aip.scitation.org/doi/abs/10.1063/5.0035100>. Publisher: American Institute of Physics.
- [42] M Dawber, Izabela Szafraniak-Wiza, Marin Alexe, and J Scott. Self-patterning of arrays of ferroelectric capacitors: Description by theory of substrate mediated strain interactions. *Journal of Physics: Condensed Matter*, 15:L667, October 2003. doi: 10.1088/0953-8984/15/44/L03.
- [43] X. Lu, H. Li, and W. Cao. Current-voltage Characteristics and ON/OFF Ratio in Ferroelectric Tunnel Junctions. *Journal of Applied Physics*, 112(5):054102, 2012.
- [44] I.D. Bilc, J. Iniguez, P. Ordejon, and P. Ghosez. *Electroresistance Effect in Ferroelectric Tunnel Junctions with Symmetric Electrodes*, volume 6. American Chemical Society NANO, 2012.
- [45] L. Wang, M.R. Cho, Y.J. Shin, J.R. Kim, S. Das, J.-G. Yoon, J.-S. Chung, and T.W. Noh. Overcoming the Fundamental Barrier Thickness Limits of Ferroelectric Tunnel Junctions Through BaTiO₃/SrTiO₃ Composite Barriers. *Nano letters*, 16:3911–3918, 2016.
- [46] A. Crassous, V. Garcia, K. Bouzehouane, S. Fusil, A.H.G. Vlooswijk, G. Rispens, B. Noheda, M. Bibes, and A. Barthé lémuy; Giant Tunnel Electroresistance with PbTiO₃ Ferroelectric Tunnel Barriers. *Applied Physics Letters*, 96(4):042901, 2010.
- [47] E.Y. Tsymbal and A. Gruverman. Ferroelectric Tunnel Junctions: Beyond the Barrier. *Nature Materials*, 12:602–604, 2013.

- [48] F. Ambriz-Vargas, I. Velasco-Davalos, R. Thomas, and A. Ruediger. Nucleation and Growth of Ultrathin BaTiO₃ Films on Single Terminated Nb:SrTiO₃ (100) Substrates for Ferroelectric Tunnel Junction. *Journal of Vacuum Science & Technology B, Nanotechnology and Microelectronics: Materials, Processing, Measurement, and Phenomena*, 34(2):02 101, 2016.
- [49] I. Velasco-Davalos, F. Ambriz-Vargas, C. Gómez-Yáñez, R. Thomas, and A. Ruediger. Polarization Reversal in BaTiO₃ Nanostructures Synthesized by Microwave-assisted Hydrothermal Method. *Journal of Alloys and Compounds*, 667:268–274, 2016.
- [50] I.A. Velasco-Davalos, A. Ruediger, J.J. Cruz-Rivera, and C. Gomez-Yanez. Mechanical Niobium Doping in Barium Titanate Electroceramics. *Journal of Alloys and Compounds*, 581: 56–58, 2013.
- [51] I. Velasco-Davalos, F. Ambriz-Vargas, G. Kolhatkar, R. Thomas, and A. Ruediger. Synthesis of BiFeO₃ Thin Films on Single-terminated Nb:SrTiO₃ (111) Substrates by Intermittent Microwave Assisted Hydrothermal Method. *AIP-Advances*, 6(6):065117, 2016.
- [52] I.A. Velasco-Davalos, M. Moretti, M. Nicklaus, C. Nauenheim, S. Li, R. Nechache, C. Gomez-Yanez, and A. Ruediger. Polar Properties of Hydrothermally Synthesized BiFeO₃ Thin Films. *Applied Physics A*, 115(3):1081–1085, 2013.
- [53] K.J. Choi, M. Biegalski, Y.L. Li, A. Sharan, J. Schubert, R. Uecker, P. Reiche, Y. Chen, W.Q. Pan, V. Gopalan, L.-Q. Chen, D.G. Schlom, and C.B. Eom. Enhancement of Ferroelectricity in Strained BaTiO₃ Thin Films. *Science*, 306:1005–1008, 2004.
- [54] D. Pantel, H. Lu, S. Goetze, P. Werner, D.J. Kim, A. Gruverman, D. Hesse, and M. Alexe. Tunnel Electroresistance in Junctions with Ultrathin Ferroelectric Pb(Zr_{0.2}Ti_{0.8})O₃ Barriers. *Applied Physics Letters*, 100(23):232902, 2012.
- [55] B. B. Tian, J. L. Wang, S. Fusil, Y. Liu, X. L. Zhao, S. Sun, H. Shen, T. Lin, J. L. Sun, C. G. Duan, M. Bibes, A. Barthélémy, B. Dkhil, V. Garcia, X. J. Meng, and J. H. Chu. Tunnel electroresistance through organic ferroelectrics. *Nature Communications*, 7(1):11502, May 2016. ISSN 2041-1723. doi: 10.1038/ncomms11502. URL <https://www.nature.com/articles/ncomms11502>. Number: 1 Publisher: Nature Publishing Group.
- [56] H. Lu, A. Lipatov, S. Ryu, D.J. Kim, H. Lee, M.Y. Zhuravlev, C.B. Eom, E.Y. Tsymbal, A. Sinitskii, and A. Gruverman. Ferroelectric Tunnel Junctions with Graphene Electrodes. *Nature Communications*, 5:5518, 2014.
- [57] Rohit Soni, Adrian Petraru, Paul Meuffels, Ondrej Vavra, Martin Ziegler, Seong Keun Kim, Doo Seok Jeong, Nikolay A. Pertsev, and Hermann Kohlstedt. Giant electrode effect on tunnelling electroresistance in ferroelectric tunnel junctions. *Nature Communications*, 5(1):5414, December 2014. ISSN 2041-1723. doi: 10.1038/ncomms6414. URL <http://www.nature.com/articles/ncomms6414>.
- [58] Fabian Ambriz-Vargas, Gitanjali Kolhatkar, Maxime Broyer, Azza Hadj-Youssef, Rafik Nouar, Andranik Sarkissian, Reji Thomas, Carlos Gomez-Yáñez, Marc A. Gauthier, and Andreas Ruediger. A Complementary Metal Oxide Semiconductor Process-Compatible Ferroelectric Tunnel Junction. *ACS Applied Materials & Interfaces*, 9(15):13262–13268, April 2017. ISSN 1944-8244, 1944-8252. doi: 10.1021/acsami.6b16173. URL <https://pubs.acs.org/doi/10.1021/acsami.6b16173>.

- [59] Jungkyu Yoon, Seunghyeon Hong, Yong Won Song, Ji-Hoon Ahn, and Seung-Eon Ahn. Understanding tunneling electroresistance effect through potential profile in Pt/Hf_{0.5}Zr_{0.5}O₂/TiN ferroelectric tunnel junction memory. *Applied Physics Letters*, 115(15):153502, October 2019. ISSN 0003-6951, 1077-3118. doi: 10.1063/1.5119948. URL <http://aip.scitation.org/doi/10.1063/1.5119948>.
- [60] Fu-Chien Chiu. A Review on Conduction Mechanisms in Dielectric Films. *Advances in Materials Science and Engineering*, 2014:1–18, 2014. ISSN 1687-8434, 1687-8442. doi: 10.1155/2014/578168. URL <http://www.hindawi.com/journals/amse/2014/578168/>.
- [61] E. L. Murphy and R. H. Good. Thermionic Emission, Field Emission, and the Transition Region. *Physical Review*, 102(6):1464–1473, June 1956. doi: 10.1103/PhysRev.102.1464. URL <https://link.aps.org/doi/10.1103/PhysRev.102.1464>. Publisher: American Physical Society.
- [62] W. F. Brinkman, R. C. Dynes, and J. M. Rowell. Tunneling Conductance of Asymmetrical Barriers. *Journal of Applied Physics*, 41(5):1915–1921, April 1970. ISSN 0021-8979. doi: 10.1063/1.1659141. URL <https://aip.scitation.org/doi/10.1063/1.1659141>.
- [63] A. Gruverman, D. Wu, H. Lu, Y. Wang, H. W. Jang, C. M. Folkman, M. Ye. Zhuravlev, D. Felker, M. Rzchowski, C.-B. Eom, and E. Y. Tsymbal. Tunneling Electroresistance Effect in Ferroelectric Tunnel Junctions at the Nanoscale. *Nano Letters*, 9(10):3539–3543, October 2009. ISSN 1530-6984. doi: 10.1021/nl901754t. URL <https://doi.org/10.1021/nl901754t>. Publisher: American Chemical Society.
- [64] R. H. Fowler and L. Nordheim. Electron Emission in Intense Electric Fields. *Proceedings of the Royal Society of London. Series A, Containing Papers of a Mathematical and Physical Character*, 119(781):173–181, 1928. URL <http://www.jstor.org/stable/95023>.
- [65] V. Di Lecce, S. Krishnamoorthy, M. Esposto, T.-H. Hung, A. Chini, and S. Rajan. Metal-oxide barrier extraction by Fowler-Nordheim tunnelling onset in Al₂O₃-on-GaN MOS diodes. *Electronics Letters*, 48(6):347, 2012. ISSN 00135194. doi: 10.1049/el.2011.4046. URL <http://digital-library.theiet.org/content/journals/10.1049/el.2011.4046>.
- [66] Richard Forbes and Jonathan Deane. Reformulation of the standard theory of Fowler–Nordheim tunnelling and cold field electron emission. *Proceedings of The Royal Society A: Mathematical, Physical and Engineering Sciences*, 463:2907–2927, August 2007. doi: 10.1098/rspa.2007.0030.
- [67] Peter Maksymovych, Jan Seidel, Ying Chu, Pingping Wu, Arthur Baddorf, Long-Qing Chen, Sergei Kalinin, and Ragashravanthi Ramesh. Dynamic Conductivity of Ferroelectric Domain Walls in BiFeO₃. *Nano letters*, 11:1906–12, May 2011. doi: 10.1021/nl104363x.
- [68] D. R. Islamov, T. V. Perevalov, V. A. Gritsenko, C. H. Cheng, and A. Chin. Charge transport in amorphous Hf_{0.5}Zr_{0.5}O₂. *Applied Physics Letters*, 106(10):102906, March 2015. ISSN 0003-6951, 1077-3118. doi: 10.1063/1.4914900. URL <http://aip.scitation.org/doi/10.1063/1.4914900>.
- [69] D.R. Islamov, A.G. Chernikova, M.G. Kozodaev, A.M. Markeev, T.V. Perevalov, V.A. Gritsenko, and O.M. Orlov. Charge transport mechanism in thin films of amorphous and ferroelectric Hf_{0.5}Zr_{0.5}O₂. *JETP Lett*, 102, 2015. doi: 10.1134/S0021364015200047. URL <https://doi.org/10.1134/S0021364015200047>.

- [70] K. A. Nasyrov and V. A. Gritsenko. Charge transport in dielectrics by tunneling between traps. *Journal of Experimental and Theoretical Physics*, 112(6):1026–1034, June 2011. ISSN 1063-7761, 1090-6509. doi: 10.1134/S1063776111040200. URL <http://link.springer.com/10.1134/S1063776111040200>.
- [71] K.A. Nasyrov, V.A. Gritsenko, Y.N. Novikov, E.-H. Lee, S.Y. Yoon, and C.W. Kim. Two-bands charge transport in silicon nitride due to phonon-assisted trap ionization. *J. Appl. Phys*, 96(8):4293–4296, 2004. URL <https://doi.org/10.1063/>.
- [72] N. Novikov, V.A. Gritsenko, and K.A. Nasyrov. Charge transport mechanism in amorphous alumina. *Appl. Phys. Lett*, 94, 2009. doi: 10.1063/1.3151861. URL <https://doi.org/>.
- [73] Li-Mo Wang. Relationship between Intrinsic Breakdown Field and Bandgap of Materials. In *2006 25th International Conference on Microelectronics*, pages 576–579, Belgrade, Serbia and Montenegro, 2006. IEEE. ISBN 978-1-4244-0117-8. doi: 10.1109/ICMEL.2006.1651032. URL <http://ieeexplore.ieee.org/document/1651032/>.
- [74] S. Starschich, S. Menzel, and U. Böttger. Pulse wake-up and breakdown investigation of ferroelectric yttrium doped HfO₂. *Journal of Applied Physics*, 121(15):154102, April 2017. ISSN 0021-8979, 1089-7550. doi: 10.1063/1.4981893. URL <http://aip.scitation.org/doi/10.1063/1.4981893>.
- [75] Mohammad Abuwasib, Haidong Lu, Tao Li, Pratyush Buragohain, Hyungwoo Lee, Chang-Beom Eom, Alexei Gruverman, and Uttam Singisetti. Scaling of electroresistance effect in fully integrated ferroelectric tunnel junctions. *Applied Physics Letters*, 108(15):152904, April 2016. ISSN 0003-6951. doi: 10.1063/1.4947020. URL <https://aip.scitation.org/doi/full/10.1063/1.4947020>.
- [76] Xuan Tian and Akira Toriumi. New opportunity of ferroelectric tunnel junction memory with ultrathin HfO₂-based oxides. In *2017 IEEE Electron Devices Technology and Manufacturing Conference (EDTM)*, pages 36–64, Toyama, Japan, February 2017. IEEE. ISBN 978-1-5090-4660-7. doi: 10.1109/EDTM.2017.7947507. URL <http://ieeexplore.ieee.org/document/7947507/>.
- [77] Zhipeng Dong, Xi Cao, Tong Wu, and Jing Guo. Tunneling current in HfO₂ and Hf_{0.5}Zr_{0.5}O₂-based ferroelectric tunnel junction. *Journal of Applied Physics*, 123(9):094501, March 2018. ISSN 0021-8979, 1089-7550. doi: 10.1063/1.5016823. URL <http://aip.scitation.org/doi/10.1063/1.5016823>.
- [78] S. Kirbach, K. Kühnel, and W. Weinreich. Scalable Piezoelectric Effect in Silicon Doped Hafnium Oxide for Acoustic Wave Applications. In *2019 Thirteenth International Congress on Artificial Materials for Novel Wave Phenomena (Metamaterials)*, pages X–197–X–199, September 2019. doi: 10.1109/MetaMaterials.2019.8900872.
- [79] Katsumasa Kamiya, Moon Young Yang, Seong-Geon Park, Blanka Magyari-Köpe, Yoshio Nishi, Masaaki Niwa, and Kenji Shiraishi. Physical origins of ON-OFF switching in ReRAM via VO based conducting channels. *AIP Conference Proceedings*, 1566(1):11–12, December 2013. ISSN 0094-243X. doi: 10.1063/1.4848260. URL <https://aip.scitation.org/doi/10.1063/1.4848260>.
- [80] Rulin Zhang, Hong Huang, Qing Xia, Cong Ye, Xiaodi Wei, Jinzhao Wang, Li Zhang, and Li Qiang Zhu. Role of Oxygen Vacancies at the TiO₂/HfO₂ Interface in Flexible Oxide-Based

- Resistive Switching Memory. *Advanced Electronic Materials*, 5(5):1800833, 2019. ISSN 2199-160X. doi: 10.1002/aelm.201800833. URL <https://onlinelibrary.wiley.com/doi/abs/10.1002/aelm.201800833>.
- [81] D.H. Kwon, K.M. Kim, J.H. Jang, J.M. Jeon, M.H. Lee, G.H. Kim, X.S. Li, G.S. Park, B. Lee, S. Han, M. Kim, and C.S. Hwang. Atomic Structure of Conducting Nanofilaments in TiO₂ Resistive Switching Memory. *Nature Nanotechnology*, 5(2):148–53, 2010.
 - [82] A López, A De Andrés, and P Ramos. Finite Element Model of a Ferroelectric. In *Proceedings of the COMSOL Conference*, page 5, Paris, 2010.
 - [83] A. Safari, R. K. Panda, and V. F. Janas. Ferroelectricity: Materials, Characteristics & Applications. *Key Engineering Materials*, 122-124:35–70, 1996. ISSN 1662-9795. doi: KEM.122-124.35. URL <https://www.scientific.net/KEM.122-124.35>. Conference Name: Advanced Ceramic Materials ISBN: 9780878497454 Pages: 35-70 Publisher: Trans Tech Publications Ltd Volume: 122-124.
 - [84] Jill Guyonnet. *Ferroelectric Domain Walls*. Springer Theses. Springer International Publishing, Cham, 2014. ISBN 978-3-319-05749-1 978-3-319-05750-7. doi: 10.1007/978-3-319-05750-7. URL <http://link.springer.com/10.1007/978-3-319-05750-7>.
 - [85] Myung-Geun Han, Matthew S. J. Marshall, Lijun Wu, Marvin A. Schofield, Toshihiro Aoki, Ray Tweten, Jason Hoffman, Frederick J. Walker, Charles H. Ahn, and Yimei Zhu. Interface-induced nonswitchable domains in ferroelectric thin films. *Nature Communications*, 5(1):1–9, August 2014. ISSN 2041-1723. doi: 10.1038/ncomms5693. URL <https://www.nature.com/articles/ncomms5693>.
 - [86] Patrycja Paruch and Jill Guyonnet. Nanoscale studies of ferroelectric domain walls as pinned elastic interfaces. *Comptes Rendus Physique*, 14(8):667–684, October 2013. ISSN 1631-0705. doi: 10.1016/j.crhy.2013.08.004. URL <http://www.sciencedirect.com/science/article/pii/S1631070513001321>.
 - [87] Fumitaka Kagawa, Nao Minami, Sachio Horiuchi, and Yoshinori Tokura. Athermal domain-wall creep near a ferroelectric quantum critical point. *Nature Communications*, 7(1):10675, February 2016. ISSN 2041-1723. doi: 10.1038/ncomms10675. URL <https://www.nature.com/articles/ncomms10675>. Number: 1 Publisher: Nature Publishing Group.
 - [88] Patrick Polakowski and Johannes Müller. Ferroelectricity in undoped hafnium oxide. *Applied Physics Letters*, 106(23):232905, June 2015. ISSN 0003-6951, 1077-3118. doi: 10.1063/1.4922272. URL <http://aip.scitation.org/doi/10.1063/1.4922272>.
 - [89] Si Joon Kim, Jaidah Mohan, Scott R. Summerfelt, and Jiyoung Kim. Ferroelectric Hf_{0.5}Zr_{0.5}O₂ Thin Films: A Review of Recent Advances. *JOM*, 71(1):246–255, January 2019. ISSN 1047-4838, 1543-1851. doi: 10.1007/s11837-018-3140-5. URL <http://link.springer.com/10.1007/s11837-018-3140-5>.
 - [90] R. Materlik, C. Künneth, and A. Kersch. The origin of ferroelectricity in Hf_{1-x}Zr_xO₂: A computational investigation and a surface energy model. *Journal of Applied Physics*, 117(13):134109, April 2015. ISSN 0021-8979. doi: 10.1063/1.4916707. URL <https://aip.scitation.org/doi/full/10.1063/1.4916707>. Publisher: American Institute of Physics.

- [91] John Robertson. High dielectric constant gate oxides for metal oxide Si transistors. *Reports on Progress in Physics*, 69:327–396, February 2006. doi: 10.1088/0034-4885/69/2/R02. URL <http://adsabs.harvard.edu/abs/2006RPPh...69..327R>.
- [92] Stefan Mueller, Johannes Mueller, Aarti Singh, Stefan Riedel, Jonas Sundqvist, Uwe Schroeder, and Thomas Mikolajick. Incipient Ferroelectricity in Al-Doped HfO₂ Thin Films. *Advanced Functional Materials*, 22(11):2412–2417, 2012. ISSN 1616-3028. doi: 10.1002/adfm.201103119. URL <https://www.onlinelibrary.wiley.com/doi/abs/10.1002/adfm.201103119>. eprint: <https://onlinelibrary.wiley.com/doi/pdf/10.1002/adfm.201103119>.
- [93] D. Zhou, J. Müller, J. Xu, S. Knebel, D. Bräuhaus, and U. Schröder. Insights into electrical characteristics of silicon doped hafnium oxide ferroelectric thin films. *Applied Physics Letters*, 100(8):082905, February 2012. ISSN 0003-6951. doi: 10.1063/1.3688915. URL <https://aip.scitation.org/doi/10.1063/1.3688915>. Publisher: American Institute of Physics.
- [94] R. Tsu and L. Esaki. Tunneling in a finite superlattice. *Applied Physics Letters*, 22:562–564, June 1973. ISSN 0003-6951. doi: 10.1063/1.1654509. URL <http://adsabs.harvard.edu/abs/1973ApPhL..22..562T>.
- [95] C. B Duke. *Tunneling in solids*. Academic Press, New York, 1969. URL <http://catalog.hathitrust.org/api/volumes/oclc/23932.html>. OCLC: 680219821.
- [96] S.M. Sze and N.K. Kwok. *Physics of Semiconductor Devices*. Wiley- Intercience (A John Wiley & Sons, inc, publications, ISBN-13, 3er edition, 2007.
- [97] G. Binnig, N. Garcia, H. Rohrer, J. M. Soler, and F. Flores. Electron-metal-surface interaction potential with vacuum tunneling: Observation of the image force. *Physical Review B*, 30(8):4816–4818, October 1984. doi: 10.1103/PhysRevB.30.4816. URL <https://link.aps.org/doi/10.1103/PhysRevB.30.4816>. Publisher: American Physical Society.
- [98] Andreas Schenk and Gernot Heiser. Modeling and simulation of tunneling through ultra-thin gate dielectrics. *Journal of Applied Physics*, 81(12):7900–7908, June 1997. ISSN 0021-8979. doi: 10.1063/1.365364. URL <https://aip.scitation.org/doi/abs/10.1063/1.365364>. Publisher: American Institute of Physics.
- [99] F. Jiménez-Molinos, F. Gámiz, A. Palma, P. Cartujo, and J. A. López-Villanueva. Direct and trap-assisted elastic tunneling through ultrathin gate oxides. *Journal of Applied Physics*, 91(8):5116–5124, April 2002. ISSN 0021-8979, 1089-7550. doi: 10.1063/1.1461062. URL <https://aip.scitation.org/doi/10.1063/1.1461062>.
- [100] M. Kleefstra and G. C. Herman. Influence of the image force on the band gap in semiconductors and insulators. *Journal of Applied Physics*, 51(9):4923–4926, September 1980. ISSN 0021-8979, 1089-7550. doi: 10.1063/1.328366. URL <https://aip.scitation.org/doi/10.1063/1.328366>.
- [101] H. Mulaosmanovic, S. Slesazeck, J. Ocker, M. Pesic, S. Muller, S. Flachowsky, J. Muller, P. Polakowski, J. Paul, S. Jansen, S. Kolodinski, C. Richter, S. Piontek, T. Schenk, A. Kersch, C. Kunnen, R. van Bentum, U. Schröder, and T. Mikolajick. Evidence of single domain switching in hafnium oxide based FeFETs: Enabler for multi-level FeFET memory cells. In *2015 IEEE International Electron Devices Meeting (IEDM)*. IEEE, December 2015. doi: 10.1109/iedm.2015.7409777. URL <https://doi.org/10.1109%2Fiedm.2015.7409777>.

- [102] Halid Mulaosmanovic, Johannes Ocker, Stefan Müller, Uwe Schröder, Johannes Müller, Patrick Polakowski, Stefan Flachowsky, Ralf van Bentum, Thomas Mikolajick, and Stefan Slesazeck. Switching Kinetics in Nanoscale Hafnium Oxide Based Ferroelectric Field-Effect Transistors. *ACS Applied Materials & Interfaces*, 9(4):3792–3798, February 2017. ISSN 1944-8244, 1944-8252. doi: 10.1021/acsami.6b13866. URL <http://pubs.acs.org/doi/10.1021/acsami.6b13866>.
- [103] Yingfen Wei, Pavan Nukala, Mart Salverda, Sylvia Matzen, Hong Jian Zhao, Jamo Monmand, Arnoud S. Everhardt, Guillaume Agnus, Graeme R. Blake, Philippe Lecoeur, Bart J. Kooi, Jorge Íñiguez, Brahim Dkhil, and Beatriz Noheda. A rhombohedral ferroelectric phase in epitaxially strained $\text{Hf}_{0.5}\text{Zr}_{0.5}\text{O}_2$ thin films. *Nature Materials*, 17(12):1095–1100, December 2018. ISSN 1476-1122, 1476-4660. doi: 10.1038/s41563-018-0196-0. URL <http://www.nature.com/articles/s41563-018-0196-0>.
- [104] Ekaterina Yurchuk, Johannes Muller, Jan Paul, Till Schlosser, Dominik Martin, Raik Hoffmann, Stefan Mueller, Stefan Slesazeck, Uwe Schroeder, Roman Boschke, Ralf van Bentum, and Thomas Mikolajick. Impact of Scaling on the Performance of HfO_2 -Based Ferroelectric Field Effect Transistors. *IEEE Transactions on Electron Devices*, 61(11):3699–3706, November 2014. doi: 10.1109/ted.2014.2354833. URL <https://doi.org/10.1109%2Fted.2014.2354833>.
- [105] Halid Mulaosmanovic, Thomas Mikolajick, and Stefan Slesazeck. Accumulative Polarization Reversal in Nanoscale Ferroelectric Transistors. *ACS Applied Materials & Interfaces*, 10(28):23997–24002, June 2018. doi: 10.1021/acsami.8b08967. URL <https://doi.org/10.1021%2Facsami.8b08967>.
- [106] Michael Hoffmann, Milan Pešić, Korok Chatterjee, Asif I. Khan, Sayeef Salahuddin, Stefan Slesazeck, Uwe Schröder, and Thomas Mikolajick. Direct Observation of Negative Capacitance in Polycrystalline Ferroelectric HfO_2 . *Advanced Functional Materials*, 26(47):8643–8649, December 2016. ISSN 1616301X. doi: 10.1002/adfm.201602869. URL <http://doi.wiley.com/10.1002/adfm.201602869>.
- [107] Tony Schenk, Michael Hoffmann, Johannes Ocker, Milan Pešić, Thomas Mikolajick, and Uwe Schroeder. Complex Internal Bias Fields in Ferroelectric Hafnium Oxide. *ACS Applied Materials & Interfaces*, 7(36):20224–20233, September 2015. ISSN 1944-8244, 1944-8252. doi: 10.1021/acsami.5b05773. URL <https://pubs.acs.org/doi/10.1021/acsami.5b05773>.
- [108] Michael Hoffmann, Franz P. G. Fengler, Melanie Herzog, Terence Mittmann, Benjamin Max, Uwe Schröder, Raluca Negrea, Pintilie Lucian, Stefan Slesazeck, and Thomas Mikolajick. Unveiling the double-well energy landscape in a ferroelectric layer. *Nature*, 565(7740):464–467, January 2019. ISSN 0028-0836, 1476-4687. doi: 10.1038/s41586-018-0854-z. URL <http://www.nature.com/articles/s41586-018-0854-z>.
- [109] George W Taylor, 1942 Scott, J. F. (James Floyd), and Carlos Paz de Araujo. *Ferroelectric thin films: Synthesis and basic properties*. Amsterdam : Gordon and Breach, 1996. ISBN 288449197X (pbk.).
- [110] Yoshihiro Ishibashi and Yutaka Takagi. Note on Ferroelectric Domain Switching. *Journal of the Physical Society of Japan*, 31(2):506–510, August 1971. doi: 10.1143/jpsj.31.506. URL <https://doi.org/10.1143%2Fjpsj.31.506>.

- [111] Hiroshi Orihara, Shigeharu Hashimoto, and Yoshihiro Ishibashi. A Theory of D-E Hysteresis Loop Based on the Avrami Model. *Journal of the Physical Society of Japan*, 63(3):1031–1035, March 1994. doi: 10.1143/jpsj.63.1031. URL <https://doi.org/10.1143%2Fjpsj.63.1031>.
- [112] Melvin Avrami. Kinetics of Phase Change. II Transformation-Time Relations for Random Distribution of Nuclei. *The Journal of Chemical Physics*, 8(2):212–224, February 1940. doi: 10.1063/1.1750631. URL <https://doi.org/10.1063%2F1.1750631>.
- [113] Shigeharu Hashimoto, Hiroshi Orihara, and Yoshihiro Ishibashi. Study on D-E Hysteresis Loop of TGS Based on the Avrami-Type Model. *Journal of the Physical Society of Japan*, 63(4):1601–1610, April 1994. doi: 10.1143/jpsj.63.1601. URL <https://doi.org/10.1143%2Fjpsj.63.1601>.
- [114] Y. W. So, D. J. Kim, T. W. Noh, Jong-Gul Yoon, and T. K. Song. Polarization switching kinetics of epitaxial $\text{Pb}(\text{Zr}_{0.4}\text{Ti}_{0.6})\text{O}_3$ thin films. *Applied Physics Letters*, 86(9):092905, February 2005. doi: 10.1063/1.1870126. URL <https://doi.org/10.1063%2F1.1870126>.
- [115] O. Lohse, M. Grossmann, U. Boettger, D. Bolten, and R. Waser. Relaxation mechanism of ferroelectric switching in $\text{Pb}(\text{Zr},\text{Ti})\text{O}_3$ thin films. *Journal of Applied Physics*, 89(4):2332–2336, February 2001. doi: 10.1063/1.1331341. URL <https://doi.org/10.1063%2F1.1331341>.
- [116] J. Y. Jo, H. S. Han, J.-G. Yoon, T. K. Song, S.-H. Kim, and T. W. Noh. Domain Switching Kinetics in Disordered Ferroelectric Thin Films. *Physical Review Letters*, 99(26), December 2007. doi: 10.1103/physrevlett.99.267602. URL <https://doi.org/10.1103%2Fphysrevlett.99.267602>.
- [117] A.K. Tagantsev, I. Stolichnov, E.L. Colla, and N. Setter. Polarization fatigue in ferroelectric films: Basic experimental findings, phenomenological scenarios, and microscopic features. *Journal of Applied Physics*, 90(3):1387–1402, 2001. doi: 10.1063/1.1381542.
- [118] Alexander K. Tagantsev, Igor Stolichnov, Nava Setter, Jeffrey S. Cross, and Mineharu Tsukada. Non-Kolmogorov-Avrami switching kinetics in ferroelectric thin films. *Physical Review B*, 66(21), December 2002. doi: 10.1103/physrevb.66.214109. URL <https://doi.org/10.1103%2Fphysrevb.66.214109>.
- [119] Yuxing Li, Jingzhou Li, Renrong Liang, Ruiting Zhao, Benkuan Xiong, Houfang Liu, He Tian, Yi Yang, and Tian-Ling Ren. Switching dynamics of ferroelectric $\text{HfO}_2\text{-ZrO}_2$ with various ZrO_2 contents. *Applied Physics Letters*, 114(14):142902, April 2019. ISSN 0003-6951, 1077-3118. doi: 10.1063/1.5093793. URL <http://aip.scitation.org/doi/10.1063/1.5093793>.
- [120] Ee Wah Lim and Razali Ismail. Conduction Mechanism of Valence Change Resistive Switching Memory: A Survey. *Electronics*, 4:586–613, September 2015. doi: 10.3390/electronics4030586.
- [121] Damir R. Islamov, Vladimir A. Gritsenko, Timofey V. Perevalov, Vladimir A. Pustovarov, Oleg M. Orlov, Anna G. Chernikova, Andrey M. Markeev, Stefan Slesazeck, Uwe Schroeder, Thomas Mikolajick, and Gennadiy Ya Krasnikov. Identification of the nature of traps involved in the field cycling of $\text{Hf}_{0.5}\text{Zr}_{0.5}\text{O}_2$ -based ferroelectric thin films. *Acta Materialia*, 166:47–55, March 2019. ISSN 13596454. doi: 10.1016/j.actamat.2018.12.008. URL <https://linkinghub.elsevier.com/retrieve/pii/S1359645418309509>.
- [122] V.A. Gritsenko, T.V. Perevalov, and D.R. Islamov. Electronic properties of hafnium oxide: a contribution from defects and traps. *Phys. Rep.*, 613:1–20, 2016. doi: 10.1016/j.physrep.2015.11.002.

- [123] Pauline Calka, Małgorzata Sowinska, Thomas Bertaude, Damian Walczyk, Jarek Dabrowski, Peter Zaumseil, Christian Walczyk, Andrei Gloskovskii, Xavier Cartoixà, Jordi Suñé, and Thomas Schroeder. Engineering of the Chemical Reactivity of the Ti/HfO₂ Interface for RRAM: Experiment and Theory. *ACS Applied Materials & Interfaces*, 6(7):5056–5060, April 2014. ISSN 1944-8244, 1944-8252. doi: 10.1021/am500137y. URL <https://pubs.acs.org/doi/10.1021/am500137y>.
- [124] Ilia Valov, Rainer Waser, John R. Jameson, and Michael N. Kozicki. Electrochemical metallization memories—fundamentals, applications, prospects. *Nanotechnology*, 22(28):289502, June 2011. doi: 10.1088/0957-4484/22/28/289502. URL <https://doi.org/10.1088%2F0957-4484%2F22%2F28%2F289502>.
- [125] D. Ielmini, F. Nardi, and C. Cagli. Physical models of size-dependent nanofilament formation and rupture in NiO resistive switching memories. *Nanotechnology*, 22(25):254022, May 2011. doi: 10.1088/0957-4484/22/25/254022. URL <https://doi.org/10.1088%2F0957-4484%2F22%2F25%2F254022>.
- [126] Corvin Liaw, Michael Kund, Doris Schmitt-Landsiedel, and Ingolf Ruge. The conductive bridging random access memory (CBRAM): A non-volatile multi-level memory technology. In *ESSDERC 2007 - 37th European Solid State Device Research Conference*. IEEE, 2007. doi: 10.1109/essderc.2007.4430919. URL <https://doi.org/10.1109%2Fessderc.2007.4430919>.
- [127] Rainer Waser. *Nanoelectronics and Information Technology: Advanced Electronic Materials and Novel Devices*. John Wiley & Sons, Weinheim, May 2012. ISBN 978-3-527-40927-3. Google-Books-ID: 1PgYS7zDCM8C.
- [128] P Gonon, M Mougenot, C Vallée, C Jorel, V Jousseau, H Grampeix, and F El Kamel. Resistance switching in HfO₂ metal-insulator-metal devices. *J. Appl. Phys.*, page 10, 2010.
- [129] S. U. Sharath, T. Bertaude, J. Kurian, E. Hildebrandt, C. Walczyk, P. Calka, P. Zaumseil, M. Sowinska, D. Walczyk, A. Gloskovskii, T. Schroeder, and L. Alff. Towards forming-free resistive switching in oxygen engineered HfO_{2-x}. *Applied Physics Letters*, 104(6):063502, February 2014. ISSN 0003-6951. doi: 10.1063/1.4864653. URL <https://aip.scitation.org/doi/10.1063/1.4864653>. Publisher: American Institute of Physics.
- [130] Sankaramangalam Ulhas Sharath, Stefan Vogel, Leopoldo Molina-Luna, Erwin Hildebrandt, Christian Wenger, Jose Kurian, Michael Duerrschnabel, Tore Niermann, Gang Niu, Pauline Calka, Michael Lehmann, Hans-Joachim Kleebe, Thomas Schroeder, and Lambert Alff. Control of Switching Modes and Conductance Quantization in Oxygen Engineered HfO_x-based Memristive Devices. *Advanced Functional Materials*, 27(32):1700432, July 2017. doi: 10.1002/adfm.201700432. URL <https://doi.org/10.1002%2Fadfm.201700432>.
- [131] Doo Seok Jeong. *Resistive switching in Pt/TiO₂/Pt*. PhD thesis, Forschungszentrum, Zentralbibliothek, Jülich, 2009. OCLC: 554098634.
- [132] Terence Mittmann, Michail Michailow, Patrick D. Lomenzo, Jan Gärtner, Max Falkowski, Alfred Kersch, Thomas Mikolajick, and Uwe Schroeder. Stabilizing the ferroelectric phase in HfO₂-based films sputtered from ceramic targets under ambient oxygen. *Nanoscale*, November 2020. ISSN 2040-3372. doi: 10.1039/D0NR07699F. URL <https://pubs.rsc.org/en/content/articlelanding/2021/nr/d0nr07699f>. Publisher: The Royal Society of Chemistry.

- [133] H. Hieber. Aging properties of gold layers with different adhesion layers. *Thin Solid Films*, 37(3):335–343, September 1976. ISSN 0040-6090. doi: 10.1016/0040-6090(76)90603-9. URL <https://www.sciencedirect.com/science/article/pii/0040609076906039>.
- [134] Matteo Todeschini, Alice Bastos da Silva Fanta, Flemming Jensen, Jakob Birkedal Wagner, and Anpan Han. Influence of Ti and Cr Adhesion Layers on Ultrathin Au Films. *ACS Applied Materials & Interfaces*, 9(42):37374–37385, October 2017. ISSN 1944-8244. doi: 10.1021/acsami.7b10136. URL <https://doi.org/10.1021/acsami.7b10136>. Publisher: American Chemical Society.
- [135] H. Y. Lee, P. S. Chen, T. Y. Wu, Y. S. Chen, C. C. Wang, P. J. Tzeng, C. H. Lin, F. T. Chen, C. H. Lien, and M.-J. Tsai. Low power and high speed bipolar switching with a thin reactive Ti buffer layer in robust HfO₂ based RRAM. *2008 IEEE International Electron Devices Meeting*, 2008. doi: 10.1109/IEDM.2008.4796677.
- [136] Eduardo Perez, Cristian Zambelli, Mamathamba Kalishettyhalli Mahadevaiah, Piero Olivo, and Christian Wenger. Toward Reliable Multi-Level Operation in RRAM Arrays: Improving Post-Algorithm Stability and Assessing Endurance/Data Retention. *IEEE Journal of the Electron Devices Society*, 7:740–747, 2019. ISSN 2168-6734. doi: 10.1109/JEDS.2019.2931769. URL <https://ieeexplore.ieee.org/document/8781843/>.
- [137] Furqan Zahoor, Tun Zainal Azni Zulkifli, and Farooq Ahmad Khanday. Resistive Random Access Memory (RRAM): an Overview of Materials, Switching Mechanism, Performance, Multilevel Cell (mlc) Storage, Modeling, and Applications. *Nanoscale Research Letters*, 15, April 2020. ISSN 1931-7573. doi: 10.1186/s11671-020-03299-9. URL <https://www.ncbi.nlm.nih.gov/pmc/articles/PMC7176808/>.
- [138] S. Makram-Ebeid and M. Lannoo. Quantum model for phonon-assisted tunnel ionization of deep levels in a semiconductor. *Phys. Rev. B*, 25:6406–6424, 1982. doi: 10.1103/PhysRevB.25.6406.
- [139] K. A. Nasyrov and V. A. Gritsenko. Transport mechanisms of electrons and holes in dielectric films. *Physics-Uspekhi*, 56(10):999, 2013. ISSN 1063-7869. doi: 10.3367/UFNe.0183.201310h.1099. URL <https://iopscience.iop.org/article/10.3367/UFNe.0183.201310h.1099/meta>. Publisher: IOP Publishing.
- [140] D.R. Islamov, V.A. Gritsenko, and A. Chin. Charge transport in thin hafnium and zirconium oxide films, Optoelectron. *Instrum. Data Process*, 53:184–189, 2017. doi: 10.3103/S8756699017020121. URL <https://doi.org/10.3103/S8756699017020121>.
- [141] Wolfgang Gös. *Hole Trapping and the Negative Bias Temperature Instability*. PhD thesis, TU Wien, Wien, 2011. URL <http://www.iue.tuwien.ac.at/phd/goes/diss.html#dissap1.html>.
- [142] D. Pantel and M. Alexe. Electroresistance effects in ferroelectric tunnel barriers. *Physical Review B*, 82(13):134105, October 2010. ISSN 1098-0121, 1550-235X. doi: 10.1103/PhysRevB.82.134105. URL <https://link.aps.org/doi/10.1103/PhysRevB.82.134105>.
- [143] E. O'Reilly, A. Lindsay, Stanko Tomic, and M. Kamal-Saadi. Tight-binding and k.p models for the electronic structure of Ga(In)NAs and related alloys. *Semiconductor Science and Technology - SEMICOND SCI TECHNOL*, 17:870–879, August 2002. doi: 10.1088/0268-1242/17/8/316.

- [144] F. Marsiglio and R. L. Pavelich. The tight-binding formulation of the Kronig-Penney model. *Scientific Reports*, 7(1):17041, December 2017. ISSN 2045-2322. doi: 10.1038/s41598-017-17223-2. URL <http://www.nature.com/articles/s41598-017-17223-2>.
- [145] Christoph W. Groth, Michael Wimmer, Anton R. Akhmerov, and Xavier Waintal. Kwant: a software package for quantum transport. *New Journal of Physics*, 16(6):063065, June 2014. ISSN 1367-2630. doi: 10.1088/1367-2630/16/6/063065. URL <https://doi.org/10.1088%2F1367-2630%2F16%2F6%2F063065>. Publisher: IOP Publishing.
- [146] R. K. Pandey, Rajesh Sathiyanarayanan, Unoh Kwon, Vijay Narayanan, and K. V. R. M. Murali. Role of point defects and HfO₂/TiN interface stoichiometry on effective work function modulation in ultra-scaled complementary metal–oxide–semiconductor devices. *Journal of Applied Physics*, 114(3):034505, July 2013. ISSN 0021-8979. doi: 10.1063/1.4816090. URL <https://aip.scitation.org/doi/full/10.1063/1.4816090>.
- [147] J. Robertson, O. Sharia, and A. A. Demkov. Fermi level pinning by defects in HfO₂-metal gate stacks. *Applied Physics Letters*, 91(13):132912, September 2007. ISSN 0003-6951. doi: 10.1063/1.2790479. URL <https://aip.scitation.org/doi/10.1063/1.2790479>.
- [148] John Robertson. Band offsets and work function control in field effect transistors. *Journal of Vacuum Science & Technology B: Microelectronics and Nanometer Structures Processing, Measurement, and Phenomena*, 27(1):277–285, January 2009. ISSN 1071-1023. doi: 10.1116/1.3072517. URL <https://avs.scitation.org/doi/full/10.1116/1.3072517>.
- [149] Alexander A. Demkov, O. Sharia, X. Luo, G. Bersuker, and J. Robertson. Modeling complexity of a complex gate oxide. *Microelectronic Engineering*, 86(7):1763–1766, July 2009. ISSN 0167-9317. doi: 10.1016/j.mee.2009.03.116. URL <http://www.sciencedirect.com/science/article/pii/S0167931709002858>.
- [150] C. Sun, S. M. Lu, F. Jin, W. Q. Mo, J. L. Song, and K. F. Dong. Control the switching mode of Pt/HfO₂/TiN RRAM devices by tuning the crystalline state of TiN electrode. *Journal of Alloys and Compounds*, 749:481–486, June 2018. ISSN 0925-8388. doi: 10.1016/j.jallcom.2018.03.320. URL <http://www.sciencedirect.com/science/article/pii/S0925838818311976>.
- [151] M. H. Park, T. Schenk, C. M. Fancher, E. D. Grimley, C. Zhou, C. Richter, J. M. LeBeau, J. L. Jones, T. Mikolajick, and U. Schröder. A comprehensive study on the structural evolution of HfO₂ thin films doped with various dopants. *Journal of Materials Chemistry C*, 5(19):4677–4690, 2017. ISSN 2050-7526, 2050-7534. doi: 10.1039/C7TC01200D. URL <http://xlink.rsc.org/?DOI=C7TC01200D>.
- [152] Max Falkowski, Christopher Künneth, Robin Materlik, and Alfred Kersch. Unexpectedly large energy variations from dopant interactions in ferroelectric HfO₂ from high-throughput ab initio calculations. *npj Computational Materials*, 4(1):1–9, December 2018. ISSN 2057-3960. doi: 10.1038/s41524-018-0133-4. URL <https://www.nature.com/articles/s41524-018-0133-4>. Number: 1 Publisher: Nature Publishing Group.
- [153] Max Falkowski and Alfred Kersch. Optimizing the Piezoelectric Strain in ZrO₂- and HfO₂-Based Incipient Ferroelectrics for Thin-Film Applications: An Ab Initio Dopant Screening Study. *ACS Applied Materials & Interfaces*, 12(29):32915–32924, July 2020. ISSN 1944-8244. doi: 10.1021/acsami.0c08310. URL <https://doi.org/10.1021/acsami.0c08310>. Publisher: American Chemical Society.

- [154] Robin Materlik. *Stabilization of Ferroelectricity in Hafnia, Zirconia and their Mixtures by Dopants and Interface Energy: First Principles Calculations and a Phenomenological Model.* PhD thesis, TUM, Munich, 2019.
- [155] Min Hyuk Park, Young Hwan Lee, Han Joon Kim, Yu Jin Kim, Taehwan Moon, Keum Do Kim, Seung Dam Hyun, Thomas Mikolajick, Uwe Schroeder, and Cheol Seong Hwang. Understanding the formation of the metastable ferroelectric phase in hafnia–zirconia solid solution thin films. *Nanoscale*, 10(2):716–725, January 2018. ISSN 2040-3372. doi: 10.1039/C7NR06342C. URL <https://pubs.rsc.org/en/content/articlelanding/2018/nr/c7nr06342c>.
- [156] M. Dawber, K.M. Rabe, and J.F. Scott. Physics of thin-film ferroelectric oxides. *Reviews of Modern Physics*, 77(4):1083–1130, 2005. doi: 10.1103/RevModPhys.77.1083.
- [157] Limei Jiang, Yichun Zhou, Yi Zhang, Qiong Yang, Yijia Gu, and Long-Qing Chen. Polarization switching of the incommensurate phases induced by flexoelectric coupling in ferroelectric thin films. *Acta Materialia*, 90:344–354, May 2015. ISSN 1359-6454. doi: 10.1016/j.actamat.2015.02.039. URL <http://www.sciencedirect.com/science/article/pii/S1359645415001500>.
- [158] Q. Yang, J. X. Cao, Y. C. Zhou, Y. Zhang, Y. Ma, and X. J. Lou. Tunable oxygen vacancy configuration by strain engineering in perovskite ferroelectrics from first-principles study. *Applied Physics Letters*, 103(14):142911, September 2013. ISSN 0003-6951. doi: 10.1063/1.4824215. URL <https://aip.scitation.org/doi/10.1063/1.4824215>.
- [159] Qiong Yang, Juexian Cao, Yichun Zhou, Lihong Sun, and Xiaojie Lou. Dead layer effect and its elimination in ferroelectric thin film with oxide electrodes. *Acta Materialia*, 112:216–223, June 2016. ISSN 1359-6454. doi: 10.1016/j.actamat.2016.04.036. URL <http://www.sciencedirect.com/science/article/pii/S1359645416302932>.
- [160] R.R. Mehta, B.D. Silverman, and J.T. Jacobs. Depolarization fields in thin ferroelectric films. *Journal of Applied Physics*, 44(8):3379–3385, 1973. doi: 10.1063/1.1662770.
- [161] G. Gerra, A. K. Tagantsev, N. Setter, and K. Parlinski. Ionic Polarizability of Conductive Metal Oxides and Critical Thickness for Ferroelectricity in BaTiO₃. *Physical Review Letters*, 96(10):107603, March 2006. doi: 10.1103/PhysRevLett.96.107603. URL <https://link.aps.org/doi/10.1103/PhysRevLett.96.107603>.
- [162] Massimiliano Stengel, David Vanderbilt, and Nicola A. Spaldin. Enhancement of ferroelectricity at metal–oxide interfaces. *Nature Materials*, 8(5):392–397, May 2009. ISSN 1476-4660. doi: 10.1038/nmat2429. URL <https://www.nature.com/articles/nmat2429>.
- [163] A.M. Bratkovsky and A.P. Levanyuk. Abrupt appearance of the domain pattern and fatigue of thin ferroelectric films. *Physical Review Letters*, 84(14):3177–3180, 2000. doi: 10.1103/PhysRevLett.84.3177.
- [164] X. J. Lou. Polarization fatigue in ferroelectric thin films and related materials. *Journal of Applied Physics*, 105(2):024101, January 2009. ISSN 0021-8979. doi: 10.1063/1.3056603. URL <https://aip.scitation.org/doi/full/10.1063/1.3056603>.
- [165] Z. Ye, M. H. Tang, Y. C. Zhou, X. J. Zheng, C. P. Cheng, Z. S. Hu, and H. P. Hu. Modeling of imprint in hysteresis loop of ferroelectric thin films with top and bottom interface layers.

- Applied Physics Letters*, 90(4):042902, January 2007. ISSN 0003-6951. doi: 10.1063/1.2433026. URL <https://aip.scitation.org/doi/full/10.1063/1.2433026>.
- [166] B. Chen, H. Yang, J. Miao, L. Zhao, L. X. Cao, B. Xu, X. G. Qiu, and B. R. Zhao. Leakage current of Pt/(Ba_{0.7}Sr_{0.3})TiO₃ interface with dead layer. *Journal of Applied Physics*, 97(2):024106, December 2004. ISSN 0021-8979. doi: 10.1063/1.1828219. URL <https://aip.scitation.org/doi/full/10.1063/1.1828219>.
 - [167] N. Gong, X. Sun, H. Jiang, K. S. Chang-Liao, Q. Xia, and T. P. Ma. Nucleation limited switching (NLS) model for HfO₂-based metal-ferroelectric-metal (MFM) capacitors: Switching kinetics and retention characteristics. *Applied Physics Letters*, 112(26):262903, June 2018. ISSN 0003-6951, 1077-3118. doi: 10.1063/1.5010207. URL <http://aip.scitation.org/doi/10.1063/1.5010207>.
 - [168] Muhammad Mustafa Hussain. *Advanced Nanoelectronics: Post-Silicon Materials and Devices*. Wiley-VCH Verlag GmbH & Co. KGaA, Weinheim, Germany, December 2018. ISBN 978-3-527-81186-1 978-3-527-34358-4. doi: 10.1002/9783527811861. URL <http://doi.wiley.com/10.1002/9783527811861>.
 - [169] Manoj Kumar Majumder. *Introduction to Microelectronics to Nanoelectronics: Design and Technology*. CRC Press, Milton, UNITED KINGDOM, 2021. ISBN 978-0-367-50237-9 978-1-00-022308-8 978-1-00-022309-5 978-1-00-022307-1. URL <https://go.openathens.net/redirector/umoncton.ca?url=https%3A%2F%2Fbookcentral.proquest.com%2Flib%2Fumoncton-ebooks%2Fdetail.action%3FdocID%3D6356174>. OCLC: 1203058272.
 - [170] T. Olsen, U. Schröder, S. Müller, A. Krause, D. Martin, A. Singh, J. Müller, M. Geidel, and T. Mikolajick. Co-sputtering yttrium into hafnium oxide thin films to produce ferroelectric properties. *Applied Physics Letters*, 101(8):082905, August 2012. ISSN 0003-6951. doi: 10.1063/1.4747209. URL <https://aip.scitation.org/doi/10.1063/1.4747209>. Publisher: American Institute of Physics.
 - [171] Anton E. O. Persson, Robin Athle, Pontus Littow, Karl-Magnus Persson, Johannes Svensson, Mattias Borg, and Lars-Erik Wernersson. Reduced annealing temperature for ferroelectric HZO on InAs with enhanced polarization. *Applied Physics Letters*, 116(6):062902, February 2020. ISSN 0003-6951. doi: 10.1063/1.5141403. URL <https://aip.scitation.org/doi/10.1063/1.5141403>. Publisher: American Institute of Physics.
 - [172] R. Materlik, C. Künneth, T. Mikolajick, and A. Kersch. The impact of charge compensated and uncompensated strontium defects on the stabilization of the ferroelectric phase in HfO₂. *Appl. Phys. Lett.*, 111, 2017. doi: 10.1063/1.4993110.
 - [173] M. Hoffmann, U. Schroeder, T. Schenk, T. Shimizu, H. Funakubo, O. Sakata, D. Pohl, M. Drescher, C. Adelmann, R. Materlik, A. Kersch, and T. Mikolajick. Stabilizing the ferroelectric phase in doped hafnium oxide. *Journal of Applied Physics*, 118(7):072006, August 2015. ISSN 0021-8979. doi: 10.1063/1.4927805. URL <https://aip.scitation.org/doi/10.1063/1.4927805>. Publisher: American Institute of Physics.
 - [174] Milan Pešić, Franz Paul Gustav Fengler, Luca Larcher, Andrea Padovani, Tony Schenk, Everett D. Grimley, Xiahan Sang, James M. LeBeau, Stefan Slesazeck, Uwe Schroeder, and Thomas Mikolajick. Physical Mechanisms behind the Field-Cycling Behavior of HfO₂-Based

- Ferroelectric Capacitors. *Advanced Functional Materials*, 26(25):4601–4612, July 2016. ISSN 1616301X. doi: 10.1002/adfm.201600590. URL <http://doi.wiley.com/10.1002/adfm.201600590>.
- [175] Andreas Dörfler, Gitanjali Kolhatkar, Ulrich Wagner, and Andreas Ruediger. The effects of thin film homogeneity on the performance of ferroelectric tunnel junctions. *Journal of Physics: Condensed Matter*, 32, January 2020. doi: 10.1088/1361-648X/ab6d15.
- [176] Bernhard Mittermeier, Andreas Dörfler, Anna Horoschenkoff, Rajesh Katoch, Christina Schindler, Andreas Ruediger, and Gitanjali Kolhatkar. CMOS Compatible $\text{Hf}_{0.5}\text{Zr}_{0.5}\text{O}_2$ Ferroelectric Tunnel Junctions for Neuromorphic Devices. *Advanced Intelligent Systems*, 1(5):1900034, July 2019. ISSN 2640-4567, 2640-4567. doi: 10.1002/aisy.201900034. URL <https://onlinelibrary.wiley.com/doi/abs/10.1002/aisy.201900034>.
- [177] Fredrik Bagge Carlson. MonteCarloMeasurements.jl: Nonlinear Propagation of Arbitrary Multivariate Distributions by means of Method Overloading. *arXiv:2001.07625 [cs, stat]*, January 2020. URL <http://arxiv.org/abs/2001.07625>. arXiv: 2001.07625.
- [178] J. Bezanson, A. Edelman, S. Karpinski, and V. Shah. Julia: A Fresh Approach to Numerical Computing. *SIAM Review*, 59(1):65–98, January 2017. ISSN 0036-1445. doi: 10.1137/141000671. URL <https://pubs.siam.org/doi/10.1137/141000671>.
- [179] Christopher Künneth, Robin Materlik, and Alfred Kersch. Modeling ferroelectric film properties and size effects from tetragonal interlayer in $\text{Hf}_{1-x}\text{Zr}_x\text{O}_2$ grains. *Journal of Applied Physics*, 121(20):205304, May 2017. ISSN 0021-8979, 1089-7550. doi: 10.1063/1.4983811. URL <http://aip.scitation.org/doi/10.1063/1.4983811>.
- [180] Fabian Ambriz Vargas. Ferroelectric $\text{Hf}_{0.5}\text{Zr}_{0.5}\text{O}_2$ ultra-thin films prepared by on-axis radio frequency magnetron sputtering for ultra-fast and high density nonvolatile memories. Technical report, Université du Québec, Québec, 2016.
- [181] F. Ambriz-Vargas, R. Thomas, and A. Ruediger. *Ferroelectric $(\text{Hf}, \text{Zr})\text{O}_2$ Thin Films for High-Density Nonvolatile Memories*. Springer Nature Singapore Pte Ltd, 2018.
- [182] Gunther Jegert, Alfred Kersch, Wenke Weinreich, and Paolo Lugli. Ultimate scaling of $\text{TiN}/\text{ZrO}_2/\text{TiN}$ capacitors: Leakage currents and limitations due to electrode roughness. *Journal of Applied Physics*, 109(1):014504, January 2011. ISSN 0021-8979, 1089-7550. doi: 10.1063/1.3531538. URL <http://aip.scitation.org/doi/10.1063/1.3531538>.
- [183] David Stirzaker. *Probability and random variables: a beginner's guide*. Cambridge University Press, Cambridge ; New York, 1999. ISBN 978-0-521-64297-2 978-0-521-64445-7.
- [184] Thomas P. Dence. A Brief Look into the Lambert W Function. *Applied Mathematics*, 04(06):887–892, 2013. ISSN 2152-7385, 2152-7393. doi: 10.4236/am.2013.46122. URL <http://www.scirp.org/journal/doi.aspx?DOI=10.4236/am.2013.46122>.
- [185] Min Hyuk Park, Han Joon Kim, Yu Jin Kim, Woongkyu Lee, Hyo Kyeom Kim, and Cheol Seong Hwang. Effect of forming gas annealing on the ferroelectric properties of $\text{Hf}_{0.5}\text{Zr}_{0.5}\text{O}_2$ thin films with and without Pt electrodes. *Applied Physics Letters*, 102(11):112914, March 2013. doi: 10.1063/1.4798265. URL <https://doi.org/10.1063%2F1.4798265>.

- [186] C.-H. Chang and J.-G. Hwu. Characteristics and Reliability of Hafnium Oxide Dielectric Stacks With Room Temperature Grown Interfacial Anodic Oxide. *IEEE Transactions on Device and Materials Reliability*, 9(2):215–221, June 2009. ISSN 1530-4388, 1558-2574. doi: 10.1109/TDMR.2008.2012057. URL <http://ieeexplore.ieee.org/document/4785213/>.
- [187] R. Mahapatra, Je-Hun Lee, S. Maikap, G. S. Kar, A. Dhar, Nong-M. Hwang, Doh-Y. Kim, B. K. Mathur, and S. K. Ray. Electrical and interfacial characteristics of ultrathin ZrO_2 gate dielectrics on strain compensated SiGeC/Si heterostructure. *Applied Physics Letters*, 82(14):2320–2322, April 2003. ISSN 0003-6951, 1077-3118. doi: 10.1063/1.1566480. URL <http://aip.scitation.org/doi/10.1063/1.1566480>.
- [188] J. F. Conley, Y. Ono, R. Solanki, G. Stecker, and W. Zhuang. Electrical properties of HfO_2 deposited via atomic layer deposition using $Hf(NO_3)_4$ and H_2O . *Applied Physics Letters*, 82(20):3508–3510, May 2003. ISSN 0003-6951, 1077-3118. doi: 10.1063/1.1575934. URL <http://aip.scitation.org/doi/10.1063/1.1575934>.
- [189] Lun Xu, Tomonori Nishimura, Shigehisa Shibayama, Takeaki Yajima, Shinji Migita, and Akira Toriumi. Kinetic pathway of the ferroelectric phase formation in doped HfO_2 films. *Journal of Applied Physics*, 122(12):124104, September 2017. ISSN 0021-8979, 1089-7550. doi: 10.1063/1.5003918. URL <http://aip.scitation.org/doi/10.1063/1.5003918>.
- [190] Takahisa Shiraishi, Kiliha Katayama, Tatsuhiko Yokouchi, Takao Shimizu, Takahiro Oikawa, Osami Sakata, Hiroshi Uchida, Yasuhiko Imai, Takanori Kiguchi, Toyohiko J. Konno, and Hiroshi Funakubo. Impact of mechanical stress on ferroelectricity in $(Hf_{0.5}Zr_{0.5})O_2$ thin films. *Applied Physics Letters*, 108(26):262904, June 2016. ISSN 0003-6951, 1077-3118. doi: 10.1063/1.4954942. URL <http://aip.scitation.org/doi/10.1063/1.4954942>.
- [191] Mark Kracklauer, Fabian Ambriz-Vargas, Gitanjali Kolhatkar, Bernhard Huber, Christina Schindler, and Andreas Ruediger. Oxygen vacancy filament-based resistive switching in $Hf_{0.5}Zr_{0.5}O_2$ thin films for non-volatile memory. *Advanced Materials Letters*, 10(6):405–409, 2019.
- [192] Thomas Breuer. Development of ReRAM-based Devices for Logic- and Computation-in-Memory Applications. *Forschungszentrum Jülich GmbH*, 51, 2017. ISSN 1866-1777. URL http://juser.fz-juelich.de/record/841561/files/Information_51.pdf.
- [193] Matthew Dawber, Dong Jin Jung, and James F. Scott. Perimeter effect in very small ferroelectrics. *Applied Physics Letters*, 82(3):436–438, January 2003. ISSN 0003-6951, 1077-3118. doi: 10.1063/1.1536022. URL <http://aip.scitation.org/doi/10.1063/1.1536022>.
- [194] V.A. Gritsenko, D.R. Islamov, T.V. Perevalov, V.S. Aliev, A.P. Yelisseyev, E.E. Lomanova, V.A. Pustovarov, and A. Chin. The oxygen vacancy in hafnia as a blue luminescence center and a trap of charge carriers. *J. Phys. Chem. C* 120:19980–19986, 2016. doi: 10.1021/acs.jpcc.6b05457.
- [195] Herng Yau Yoong, Haijun Wu, Jianhui Zhao, Han Wang, Rui Guo, Juanxiu Xiao, Bangmin Zhang, Ping Yang, Stephen John Pennycook, Ning Deng, Xiaobing Yan, and Jingsheng Chen. Epitaxial Ferroelectric $Hf_{0.5}Zr_{0.5}O_2$ Thin Films and Their Implementations in Memristors for Brain-Inspired Computing. *Advanced Functional Materials*, 28(50):1806037, 2018. ISSN 1616-3028. doi: 10.1002/adfm.201806037. URL <https://onlinelibrary.wiley.com/doi/abs/10.1002/adfm.201806037>. eprint: <https://onlinelibrary.wiley.com/doi/pdf/10.1002/adfm.201806037>.

- [196] Lin Chen, Tian-Yu Wang, Ya-Wei Dai, Ming-Yang Cha, Hao Zhu, Qing-Qing Sun, Shi-Jin Ding, Peng Zhou, Leon Chua, and David Wei Zhang. Ultra-low power $\text{Hf}_{0.5}\text{Zr}_{0.5}\text{O}_2$ based ferroelectric tunnel junction synapses for hardware neural network applications. *Nanoscale*, 10(33):15826–15833, August 2018. ISSN 2040-3372. doi: 10.1039/C8NR04734K. URL <https://pubs.rsc.org/en/content/articlelanding/2018/nr/c8nr04734k>.
- [197] Christian Keysers and Valeria Gazzola. Hebbian learning and predictive mirror neurons for actions, sensations and emotions. *Philosophical Transactions of the Royal Society B: Biological Sciences*, 369(1644), June 2014. ISSN 0962-8436. doi: 10.1098/rstb.2013.0175. URL <https://www.ncbi.nlm.nih.gov/pmc/articles/PMC4006178/>.
- [198] Guo-qiang Bi and Mu-ming Poo. Synaptic Modifications in Cultured Hippocampal Neurons: Dependence on Spike Timing, Synaptic Strength, and Postsynaptic Cell Type. *Journal of Neuroscience*, 18(24):10464–10472, December 1998. ISSN 0270-6474, 1529-2401. doi: 10.1523/JNEUROSCI.18-24-10464.1998. URL <https://www.jneurosci.org/content/18/24/10464>. Publisher: Society for Neuroscience Section: ARTICLE.
- [199] Sung Hyun Jo, Ting Chang, Idongesit Ebong, Bhavitavya B. Bhadviya, Pinaki Mazumder, and Wei Lu. Nanoscale Memristor Device as Synapse in Neuromorphic Systems. *Nano Letters*, 10(4):1297–1301, April 2010. ISSN 1530-6984. doi: 10.1021/nl904092h. URL <https://doi.org/10.1021/nl904092h>. Publisher: American Chemical Society.
- [200] S{"\o"}ren Boyn, Julie Grollier, Gwendal Lecerf, Bin Xu, Nicolas Locatelli, Stéphane Fusil, Stéphanie Girod, Cécile Carrétéro, Karin Garcia, Stéphane Xavier, Jean Tomas, Laurent Bellaïche, Manuel Bibes, Agnès Barthélémy, Sylvain Saighi, and Vincent Garcia. Learning through ferroelectric domain dynamics in solid-state synapses. *Nature Communications*, 8: 14736, April 2017. ISSN 2041-1723. doi: 10.1038/ncomms14736. URL <http://www.nature.com/doifinder/10.1038/ncomms14736>.
- [201] Rui Guo, Yaxiong Zhou, Lijun Wu, Zhuorui Wang, Zhishuh Lim, Xiaobing Yan, Weinan Lin, Han Wang, Herng Yau Yoong, Shaohai Chen, Ariando, Thirumalai Venkatesan, John Wang, Gan Moog Chow, Alexei Gruverman, Xiangshui Miao, Yimei Zhu, and Jingsheng Chen. Control of Synaptic Plasticity Learning of Ferroelectric Tunnel Memristor by Nanoscale Interface Engineering. *ACS Applied Materials & Interfaces*, 10(15):12862–12869, April 2018. ISSN 1944-8244. doi: 10.1021/acsami.8b01469. URL <https://doi.org/10.1021/acsami.8b01469>. Publisher: American Chemical Society.
- [202] Sergey Zhukov, Yuri A. Genenko, and Heinz von Seggern. Experimental and theoretical investigation on polarization reversal in unfatigued lead-zirconate-titanate ceramic. *Journal of Applied Physics*, 108(1):014106, July 2010. ISSN 0021-8979, 1089-7550. doi: 10.1063/1.3380844. URL <http://aip.scitation.org/doi/10.1063/1.3380844>.
- [203] Vishal Boddu, Florian Endres, and Paul Steinmann. Molecular dynamics study of ferroelectric domain nucleation and domain switching dynamics. *Scientific Reports*, 7(1):806, December 2017. ISSN 2045-2322. doi: 10.1038/s41598-017-01002-0. URL <http://www.nature.com/articles/s41598-017-01002-0>.
- [204] A. Gruverman, B. J. Rodriguez, C. Dehoff, J. D. Waldrep, A. I. Kingon, R. J. Nemanich, and J. S. Cross. Direct studies of domain switching dynamics in thin film ferroelectric capacitors. *Applied Physics Letters*, 87(8):082902, August 2005. ISSN 0003-6951, 1077-3118. doi: 10.1063/1.2010605. URL <http://aip.scitation.org/doi/10.1063/1.2010605>.

- [205] A Chouprik, A Chernikova, A Markeev, V Mikheev, D Negrov, M Spiridonov, S Zarubin, and A Zenkevich. Electron transport across ultrathin ferroelectric $\text{Hf}_{0.5}\text{Zr}_{0.5}\text{O}_2$ films on Si. *Microelectronic Engineering*, page 4, 2017.
- [206] A. Zaman. *Characterization of Tantalum Nitride Thin Films Synthesized by Magnetron Sputtering*. PhD thesis, 2014.
- [207] A. Mirfazli. *Characterization of Piezoelectric AlN Thin Films Deposited on Si by RF reactive Magnetron Sputtering at Low Temperature For Acoustic Wave Devices*. PhD thesis, 2004.
- [208] H. S. Nalwa. Handbook of thin film materials. In Hari Singh Nalwa, editor, *Handbook of Thin Films*, pages xxiii–xxvi. Academic Press, Burlington, 2002. ISBN 978-0-12-512908-4. doi: 10.1016/B978-0125129084/50003-5. URL <https://www.sciencedirect.com/science/article/pii/B9780125129084500035>.
- [209] Stanislaw Halas and Tomasz Durakiewicz. Work functions of elements expressed in terms of the Fermi energy and the density of free electrons. *Journal of Physics: Condensed Matter*, 10(48):10815–10826, December 1998. ISSN 0953-8984, 1361-648X. doi: 10.1088/0953-8984/10/48/005. URL <https://iopscience.iop.org/article/10.1088/0953-8984/10/48/005>.
- [210] Mark T. Greiner, Lily Chai, Michael G. Helander, Wing-Man Tang, and Zheng-Hong Lu. Transition Metal Oxide Work Functions: The Influence of Cation Oxidation State and Oxygen Vacancies. *Advanced Functional Materials*, 22(21):4557–4568, November 2012. ISSN 1616301X. doi: 10.1002/adfm.201200615. URL <http://doi.wiley.com/10.1002/adfm.201200615>.
- [211] L. P. B. Lima, J. A. Diniz, I. Doi, and J. Godoy Fo. Titanium nitride as electrode for MOS technology and Schottky diode: Alternative extraction method of titanium nitride work function. *Microelectronic Engineering*, 92:86–90, April 2012. ISSN 0167-9317. doi: 10.1016/j.mee.2011.04.059. URL <http://www.sciencedirect.com/science/article/pii/S0167931711004850>.
- [212] S. Logothetidis, Efstathios Meletis, George Stergioudis, and Albert Adjaotor. Room temperature oxidation behavior of TiN thin films. *Thin Solid Films*, 338:304–313, January 1999. doi: 10.1016/S0040-6090(98)00975-4.
- [213] Jerry Wu, Yin-Lin Shen, Kitt Reinhardt, Harold Szu, and Boqun Dong. A Nanotechnology Enhancement to Moore’s Law. *Applied Computational Intelligence and Soft Computing*, 2013: 1–13, 2013. ISSN 1687-9724, 1687-9732. doi: 10.1155/2013/426962. URL <http://www.hindawi.com/journals/acisc/2013/426962/>.
- [214] Satish Kandlikar. Review and Projections of Integrated Cooling Systems for Three-Dimensional Integrated Circuits. *Journal of Electronic Packaging*, 136:024001, June 2014. doi: 10.1115/1.4027175.
- [215] Elisabetta Chicca, Fabio Stefanini, Chiara Bartolozzi, and Giacomo Indiveri. Neuromorphic Electronic Circuits for Building Autonomous Cognitive Systems. *Proceedings of the IEEE*, 102(9):1367–1388, September 2014. ISSN 1558-2256. doi: 10.1109/JPROC.2014.2313954. Conference Name: Proceedings of the IEEE.
- [216] L. Baldi, R. Bez, and G. Sandhu. Emerging Memories. *Solid-State Electronics*, 102:2–11, 2014.

- [217] Ekaterina Yurchuk. *Electrical Characterisation of Ferroelectric Field Effect Transistors based on Ferroelectric HfO₂ Thin Films*. Logos Verlag Berlin GmbH, June 2015. ISBN 978-3-8325-4003-6. Google-Books-ID: 9AybCgAAQBAJ.
- [218] T. Mikolajick, W. Hartner, I. Kasko, M.J. Kastner, N. Nagel, M. Moert, and C. Mazure. FeRAM Technology for High Density Applications. *Microelectronics Reliability*, 41:947–950, 2001.
- [219] Yuewei Yin and Qi Li. A review on all-perovskite multiferroic tunnel junctions. *J. Mater.*, 3(4):245–254, 2017. ISSN 23528486. doi: 10.1016/j.jmat.2017.09.001.
- [220] Darrell G. Schlom and Jeffrey H. Haeni. A Thermodynamic Approach to Selecting Alternative Gate Dielectrics. *MRS Bulletin*, 27(3):198–204, March 2002. ISSN 0883-7694, 1938-1425. doi: 10.1557/mrs2002.71. URL https://www.cambridge.org/core/product/identifier/S0883769400020479/type/journal_article.
- [221] Andreas Dörfler, Rajesh Katoch, Gitanjali Kolhatkar, Anna Horoschenkoff, and Andreas Ruediger. Tolerance and Stability in Ferroelectric Tunnel Junctions, July 2019. URL www.iee.et.tu-dresden.de/mem2019.
- [222] F. A. Kröger and H. J. Vink. Relations between the Concentrations of Imperfections in Crystalline Solids. volume 3 of *Solid State Physics*, pages 307 – 435. Academic Press, 1956. doi: 10.1016/S0081-1947(08)60135-6. URL <http://www.sciencedirect.com/science/article/pii/S0081194708601356>. ISSN: 0081-1947.
- [223] Sangheon Lee, Daeseok Lee, Jiyong Woo, Euijun Cha, Jaesung Park, and Hyunsang Hwang. Engineering Oxygen Vacancy of Tunnel Barrier and Switching Layer for Both Selectivity and Reliability of Selector-Less ReRAM. *IEEE Electron Device Letters*, 35:1022–1024, 2014. doi: 10.1109/led.2014.2347925.
- [224] Sören Boyn. *Ferroelectric tunnel junctions: memristors for neuromorphic computing*. PhD Thesis, Université Paris-Saclay, Paris, 2016. URL <https://tel.archives-ouvertes.fr/tel-01382194/document>.
- [225] Sergei Petrenko. Limitations of Von Neumann Architecture. In *Big Data Technologies for Monitoring of Computer Security: A Case Study of the Russian Federation*, pages 115–173. Springer International Publishing, Cham, 2018. ISBN 978-3-319-79036-7. doi: 10.1007/978-3-319-79036-7_3. URL https://doi.org/10.1007/978-3-319-79036-7_3.
- [226] Rui Guo, Weinan Lin, Xiaobing Yan, T. Venkatesan, and Jingsheng Chen. Ferroic tunnel junctions and their application in neuromorphic networks. *Applied Physics Reviews*, 7(1):011304, March 2020. ISSN 1931-9401. doi: 10.1063/1.5120565. URL <http://aip.scitation.org/doi/10.1063/1.5120565>.
- [227] P. Jesper Sjöström, Ede A. Rancz, Arnd Roth, and Michael Häusser. Dendritic excitability and synaptic plasticity. *Physiological Reviews*, 88(2):769–840, April 2008. ISSN 0031-9333. doi: 10.1152/physrev.00016.2007.
- [228] Spencer Allen Pringle. *Modeling and Implementation of HfO₂-based Ferroelectric Tunnel Junctions*. PhD thesis, Rochester Institute of Technology, June 2017. URL <https://scholarworks.rit.edu/theses>.

Appendix A

Appendix

A.1 Probing

A.1.1 X-ray Photoelectron Spectroscopy (XPS)

X-ray Photoelectron Spectroscopy is based on the photoelectric effect to probe the electronic structure of a material. The binding energies are measured from energy difference between incoming and scattered photons, as and ejected electrons. Using these binding energies as a fingerprint, chemical elements and compounds can be identified and quantified within the sample. Additionally, electronic parameters, such as the valence band minimum, band gap and Fermi level can be determined.

In the context of ferroelectric tunnel junctions, XPS has been successfully used to determine the interface potentials of a ferroelectric tunnel junctions, as shown by the previous work of Vargas [180] for TiN/Hf_{0.5}Zr_{0.5}O₂/Pt FTJs, see Fig. A.1.

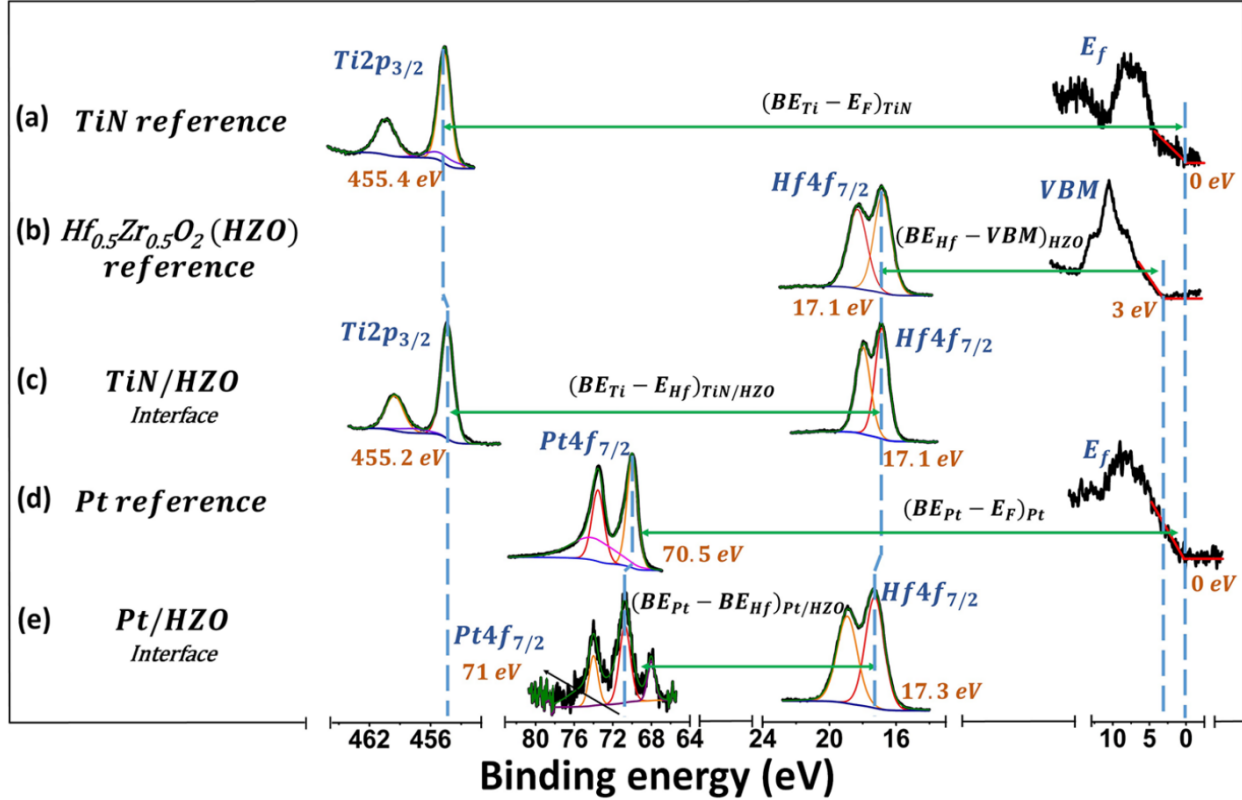


Figure A.1: XPS spectra taken on the (a) thick TiN film, (b) thick Hf_{0.5}Zr_{0.5}O₂/Pt interface, (c) TiN/Hf_{0.5}Zr_{0.5}O₂ interface, (d) bulk Pt film, and (e) Hf_{0.5}Zr_{0.5}O₂/Pt interface. ([180])

A.1.2 X-ray Spectroscopy (XRD)

X-ray spectroscopy is used to observe periodic structures in a sample. Based on Bragg's law, the diffracted X-ray beams form interference patterns over angular scanning regions. This allows to determine various kinds of crystal characteristics, such as lattice parameters, degree of polycrystallinity, as well as crystal orientation. Various scanning methods exist, such as the 2d reciprocal space maps shown in Fig. A.2, as well as more basic 2-Theta measurement (Fig. A.3).

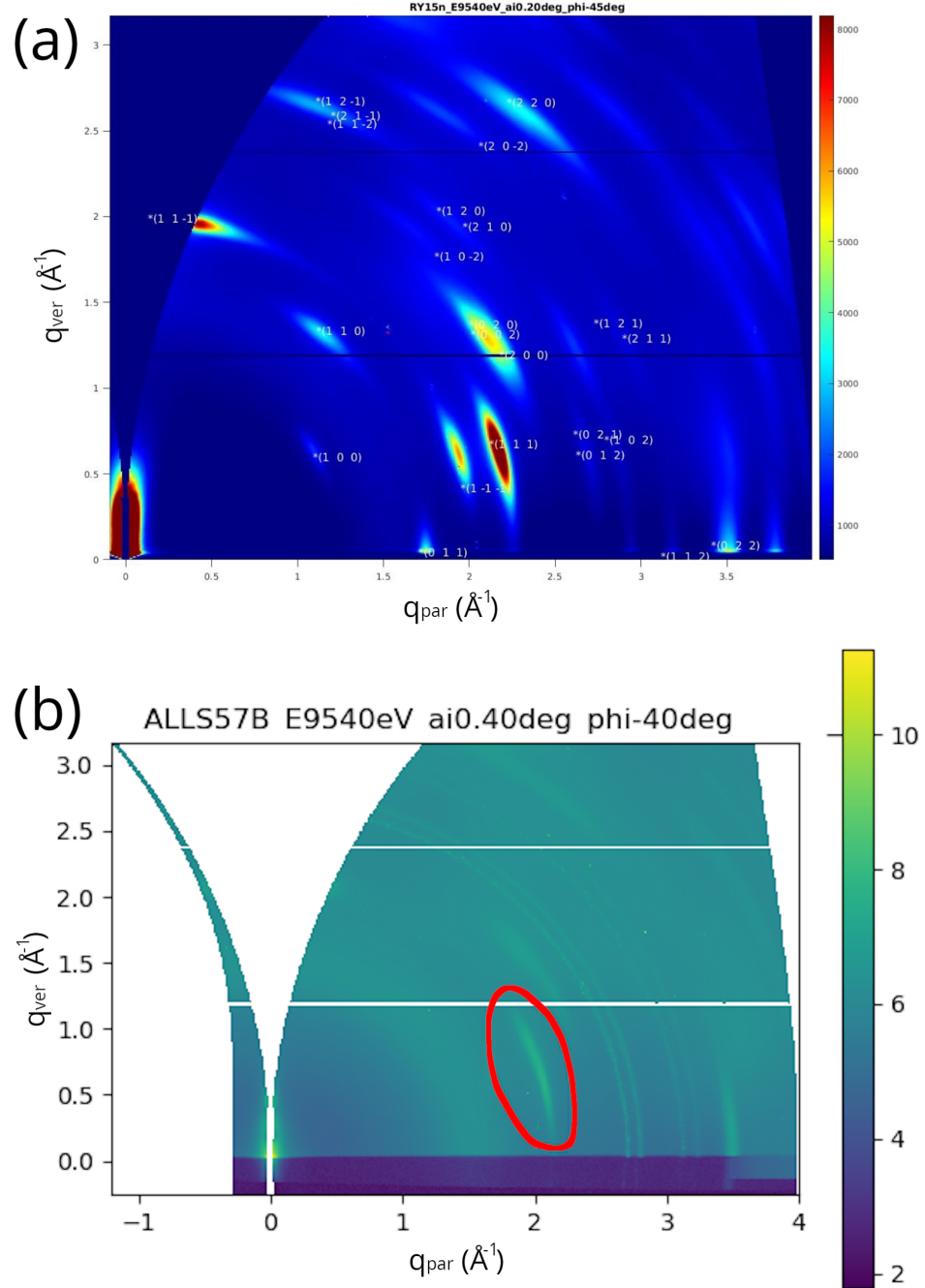


Figure A.2: XRD maps of the $\text{Hf}_x\text{Zr}_{1-x}\text{O}_2$ film. (a) Monoclinic phase with $(11\bar{1})$ parallel to surface. (b) Orthorhombic phase with (111) plane (red circle). The orthorhombic $(11\bar{1})$ axis is parallel to the surface.

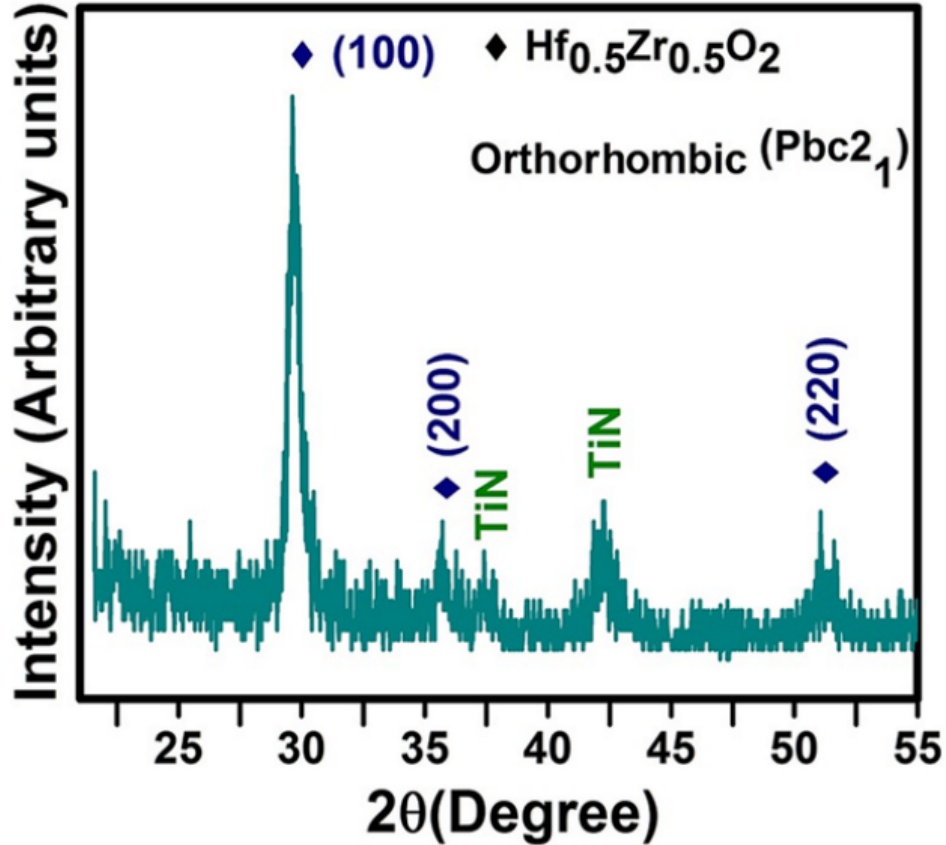


Figure A.3: Grazing incidence XRD measurements on $\text{Hf}_x\text{Zr}_{1-x}\text{O}_2$ film deposited on TiN. The spectrum reveals various crystal phases ([180])

A.1.3 X-ray reflectivity (XRR)

The X-ray reflectivity (XRR) is a means to determine properties of ultra-thin films, such as thickness, interface roughness and optical density. The technique allows thickness measurements in the range between 2 nm and 200 nm with a precision of ~ 0.2 nm on highly planar surfaces. Even multilayer films can be characterized, including their interface roughnesses and densities. A numerical model is fitted to the measured reflectometry profile, thereby determining the model parameters.

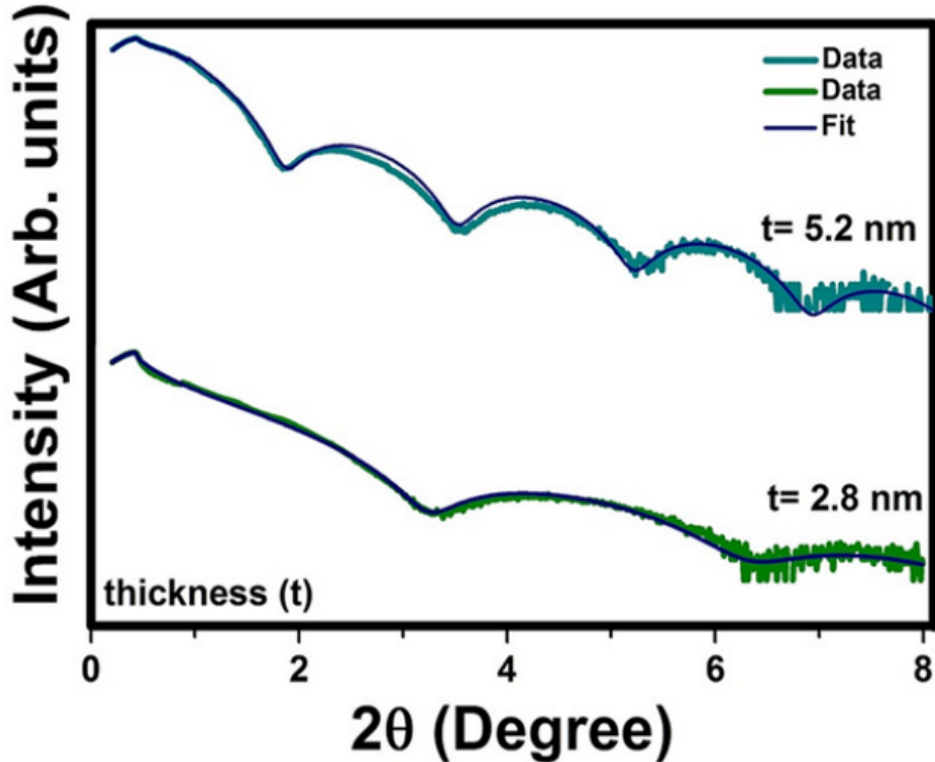


Figure A.4: XRR measurements on $\text{Hf}_x\text{Zr}_{1-x}\text{O}_2$ film deposited on TiN. The fitting determines the thickness to be 2.8 nm ([180])

A.1.4 Atomic and Piezoresponse Force Microscopy

The atomic force microscopy (AFM) is a piezoelectric nanopositioner that uses the voltage-displacement characteristic of piezoelectrics to probe a sample surface using a very fine cantilever with a conductive tip in tunneling distance to the surface. The interaction between the tip and the sample is controlled by a laser beam that reflects off the back of the cantilever, detecting tiny deflections using a quadrant photosensitive detector. The XY resolution is typically in the nanometer regime, the Z resolution in the angstrom regime.

The AFM is typically available in the operating modes: contact mode, tapping mode, piezoresponse force microscopy and conductive AFM mode. They are valuable techniques to visualize and probe surfaces with high spatial resolution. The AFM allows topographical imaging of deposited and annealed layers, while the PFM permits the probing and manipulation of ferroelectric domains. A typical PFM scan of the sputtered and annealed $\text{Hf}_x\text{Zr}_{1-x}\text{O}_2$ film is shown in Fig. A.5,

A.6. Especially for FTJ applications, PFM is an important and widely used tool to investigate the ferroelectric behavior of ultrathin (<3 nm) $\text{Hf}_x\text{Zr}_{1-x}\text{O}_2$ films [27, 58, 205].

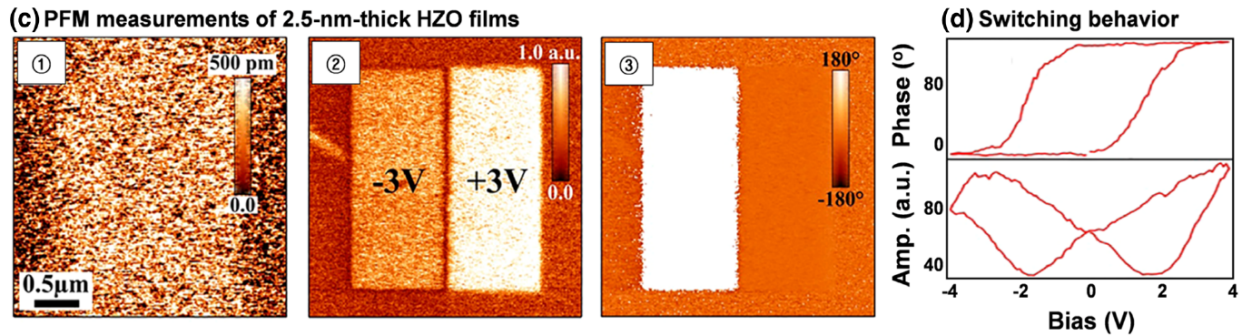


Figure A.5: PFM measurements on 2.5 nm thick $\text{Hf}_x\text{Zr}_{1-x}\text{O}_2$ films (image from Kim et al. [89]). 1: Surface profile. 2: PFM amplitude, 3: PFM phase. 4: PFM phase and amplitude hysteresis loops

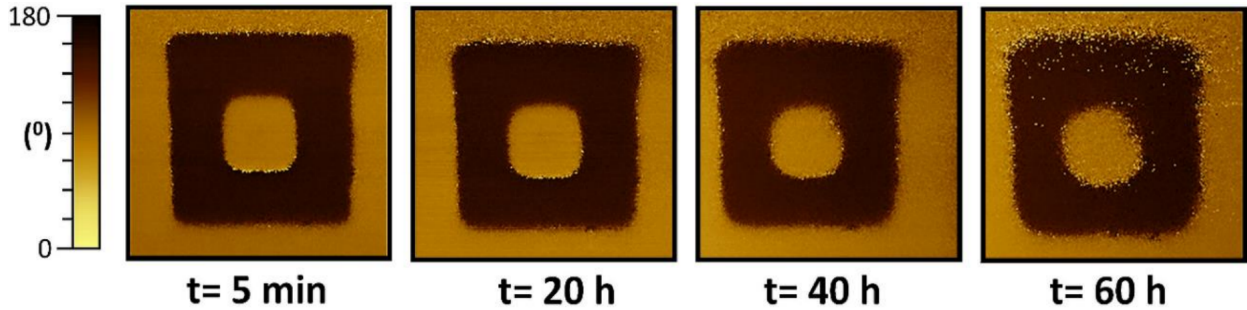


Figure A.6: PFM endurance measurements on 2.8 nm thick $\text{Hf}_{0.5}\text{Zr}_{0.5}\text{O}_2$ films (image from Vargas [180])

A.1.5 Transmission Electron Microscopy (TEM)

Transmission electron microscopy (TEM) employs a beam of electrons of sufficiently small wavelength to transmit through a sample. The sample is prepared as an ultrathin cross-section in the sub-micron range, in our case by a focused ion beam. The diffraction of the electron beam within the sample lattice is used to reconstruct the image.

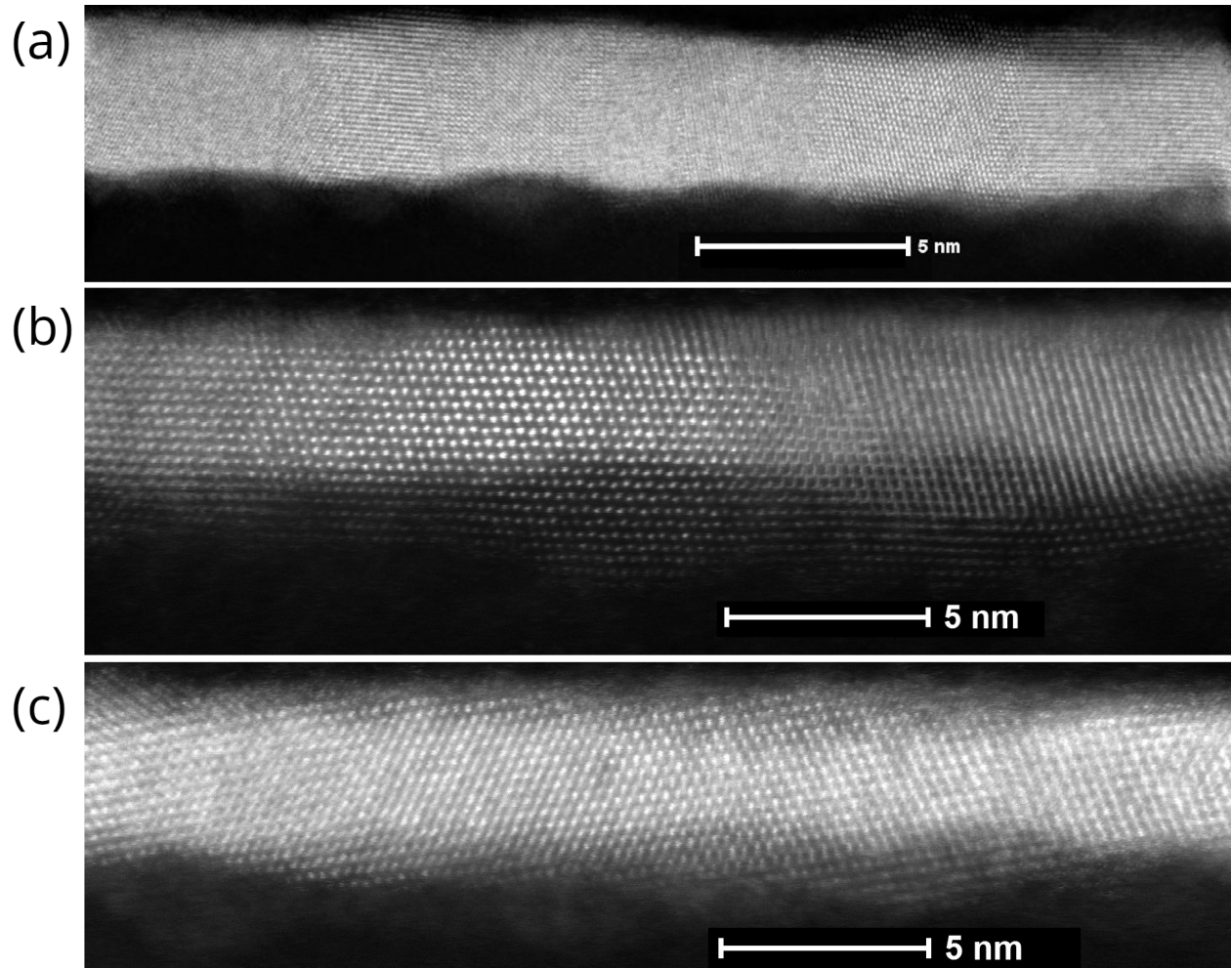


Figure A.7: TEM images of various $\text{Hf}_x\text{Zr}_{1-x}\text{O}_2$ films on SiO_2 . a) Polycrystalline domains visible, mostly monocline. b) and c) Larger domains, mostly orthorhombic phase.

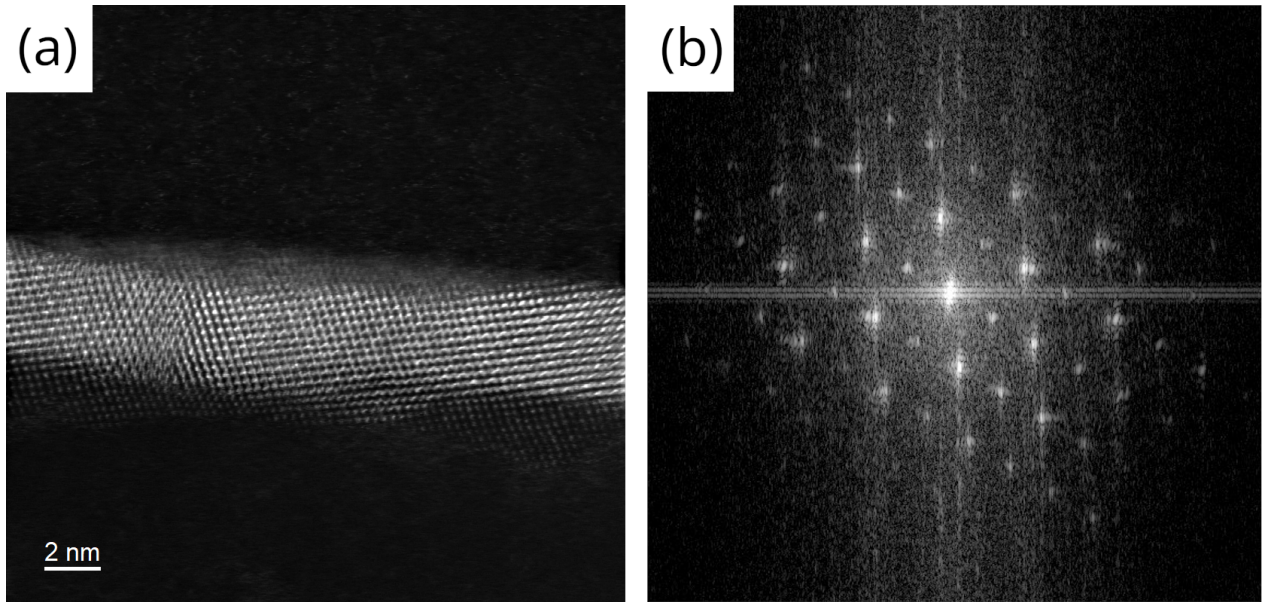


Figure A.8: TEM image of 3 nm $\text{Hf}_x\text{Zr}_{1-x}\text{O}_2$ film. (a) Cartesian representation and (b) Corresponding diffraction pattern.

A.2 Manufacturing methods

A.2.1 Magnetron Sputter deposition

Besides computer hard disks, optical and surface hardening coatings, sputtering is widely used in the semiconductor industry to deposit thin films of various materials in integrated circuit processing. Due to the low substrate temperatures used, sputtering is an ideal method to deposit contact metals for thin-film transistors. A large variety of materials, even with very high melting points are easily sputtered. Compared to chemical vapor deposition (CVD) or ALD, reactive formation gases are not required.

The system used in this thesis is a reactive radio frequency magnetron sputtering device. The setup depicted in Fig. A.9. The chamber gas is used to supply oxygen for the $\text{Hf}_x\text{Zr}_{1-x}\text{O}_2$ oxide, whilst nitrogen gas is used in the formation of the TiN bottom electrode. The plasma is created applying an electrical RF (radio frequency) signal to the magnetron, typically at 13.56 MHz [206, 207]. The RF sputtering works for non-conductive targets using capacitive currents that maintain the plasma.

The alternating magnetic field permeates the target and confines electron movement to the target surface, accelerating argon ions towards the surface.

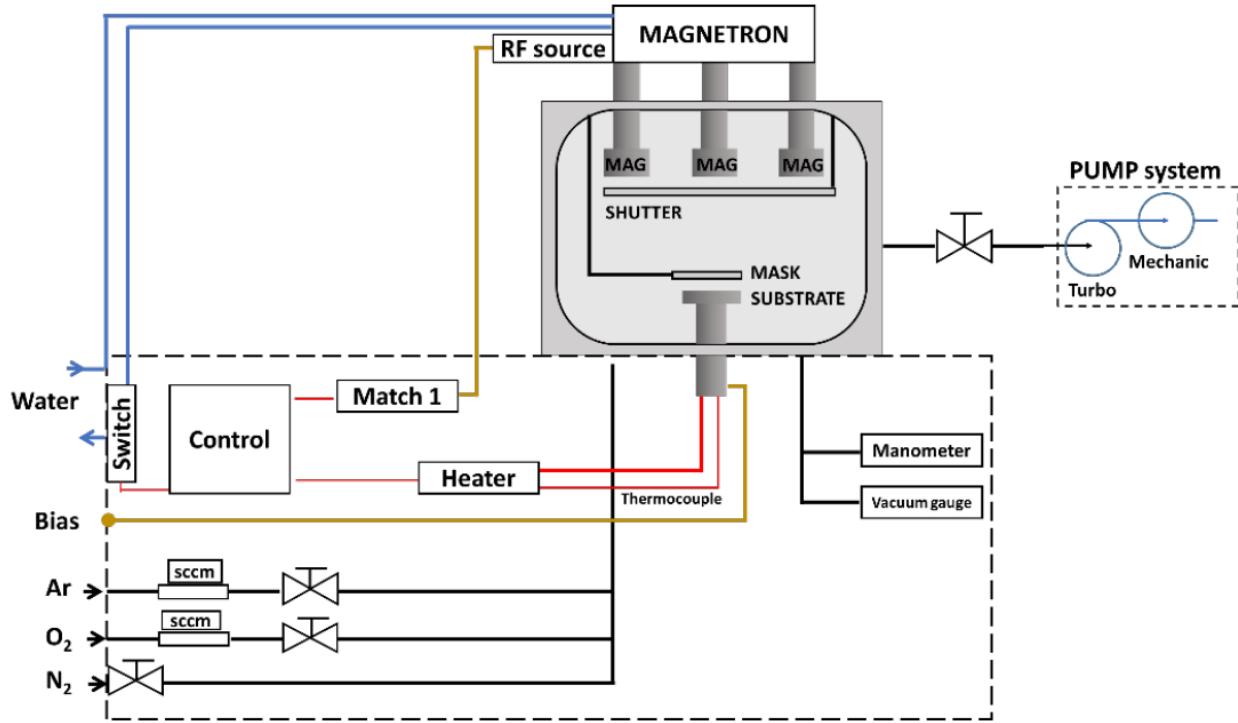


Figure A.9: Deposition system. SPT310 Plasmionique Inc. Reactive radio frequency magnetron sputtering device as used for the manufacturing of FTJs. The stainless steel chamber has a cylindrical shape with 20 cm in diameter and 31 cm height. The system has three water-cooled magnetron guns (1 inch diameter) mounted at the top of the chamber. The substrate holder is a 5 cm diameter plate to which the samples can be mounted and its temperature is controlled by a type K thermocouple and a PID controller. DC or RF power can be applied from any of the available power supplies to any of the three guns or substrate.

Film	bottom electrode	FE layer	top electrode A	top electrode B
Target	TiN 1" disk	Hf _{0.5} Zr _{0.5} O ₂ 1" disk	Pt 1" disk	Au 1" disk
Substrate	Si	TiN	Hf _{0.5} Zr _{0.5} O ₂	Hf _{0.5} Zr _{0.5} O ₂
Power	100 W	20 W	20 W	20 W
Sputtering medium	N ₂	Ar and O ₂ *	Ar	Ar
Chamber pressure	5 mTorr	5 mTorr	5 mTorr	5 mTorr
Substrate temperature	650°C	600°C	25°C	25°C
Pre-sputtering time	15 min	15 min	3 min	3 min
Deposition time	30 min	30 min	5 min	5 min

Table A.1: Summary of sputtering parameters used for the fabrication of FTJs with Pt and Au top electrodes. The target-substrate distance is 11 cm for all deposition steps.

*: Equal partial pressures

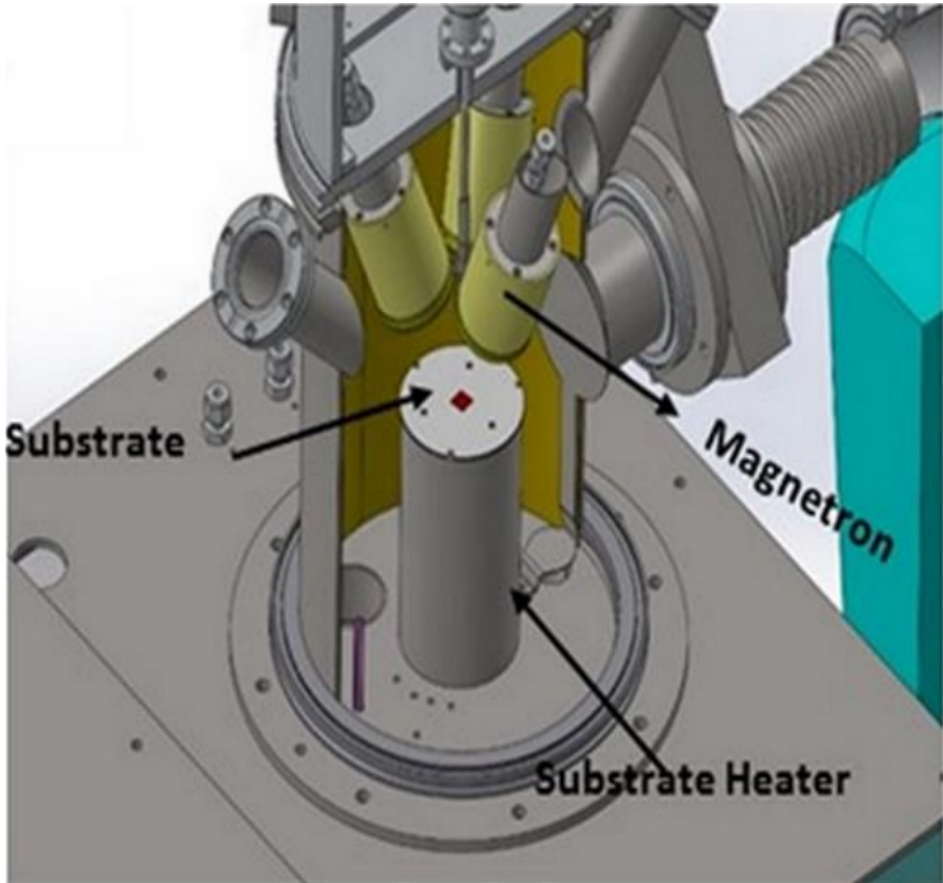


Figure A.10: Sputtering System (geometric model)

A.2.2 Atomic Layer Deposition (ALD)

Atomic layer deposition (ALD) is an alternative to the sputtering deposition process used in this work (see table 2.1). The cyclic process is carried out by dividing a conventional CVD process into a series of deposition cycles with self-saturating surface reactions. Each individual step deposits a single layer at a time. This allows the deposition of highly uniform films. Other deposition techniques initiate film growth by nucleation, which typically exhibit substantial compressive stress and a higher number of pinhole defects [208].

A.3 FTJ Measurement Setup

A measurement microscope was used for the electrical characterization, as shown in Fig. A.11. Two adjustable tungsten contact needles were used to contact the individual FTJs in the deposited pattern (Fig. A.12, A.12).

An exemplary resistive switching response of a pristine 3 nm Pt/Hf_{0.5}Zr_{0.5}O₂/TiN FTJ over pulse duration and amplitude is shown in Fig. A.14. The FTJ is exposed to a pulse of increasing time and voltage. After each pulse, the resistivity is measured at 400 mV, after which the device is reset to the LRS using a -1.4 V at 500 ms. The same measurement is done with reversed polarity, showing that the switching threshold for LRS to HRS is 250 mV higher than the inverse process. As can be seen in Fig. A.14, the device shows little time dependence in a largely reversible process, which is consistent with ferroelectric switching.



Figure A.11: Measurement Microscope

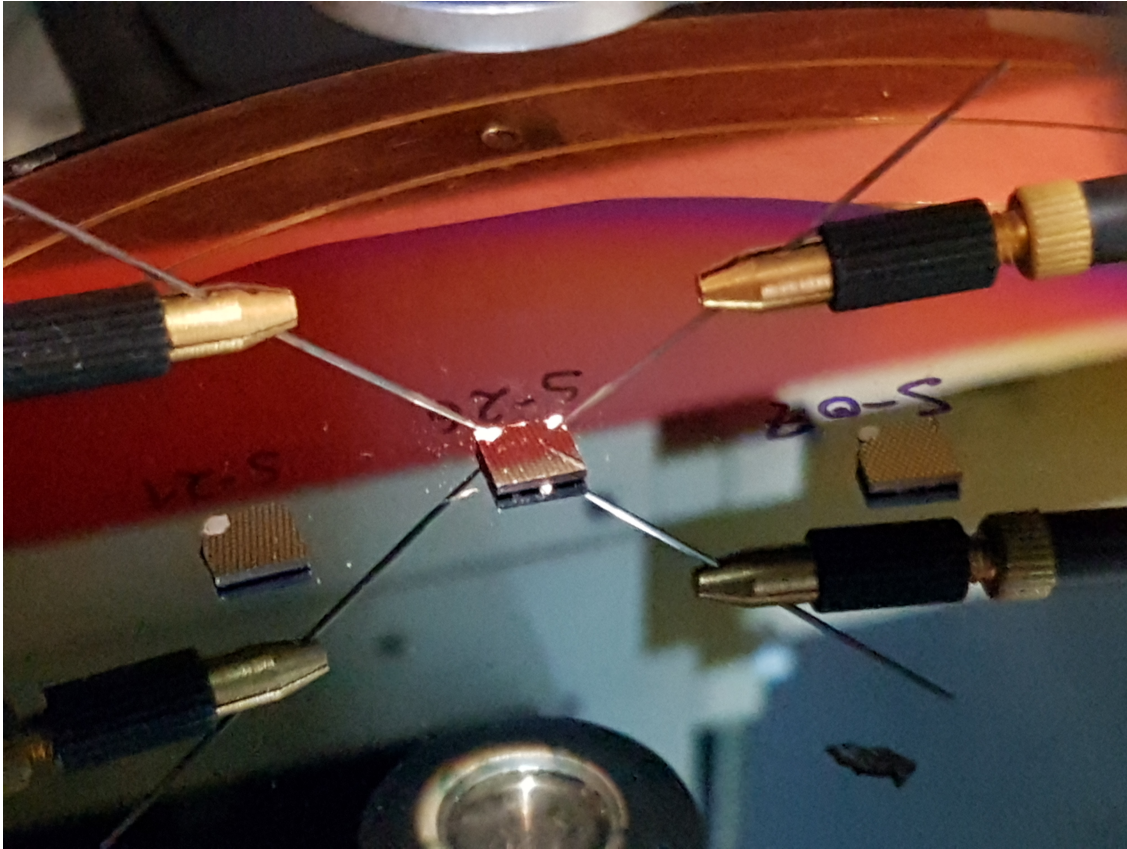


Figure A.12: Two Tip Measurement

A.3.1 Switching Behavior

Switching behavior of a pristine FTJ, measured over increasing pulse lengths and amplitudes. The TER switching is highly dependent on the voltage, and shows only marginal dependency on time. Fig. A.14 was performed directly after manufacturing. High overall current densities indicate significant deviations from the ideal 3 nm ferroelectric layer.

A.3.2 FTJ Valency Switching

A.3.3 Endurance

The endurance of the device is closely coupled to the vacancy mechanism. Although the resistive switching grows significantly during long-term operation of the device at elevated voltages, the total conductivity increases rapidly. Fig. A.17 shows this mode of degradation in a 3.5 nm

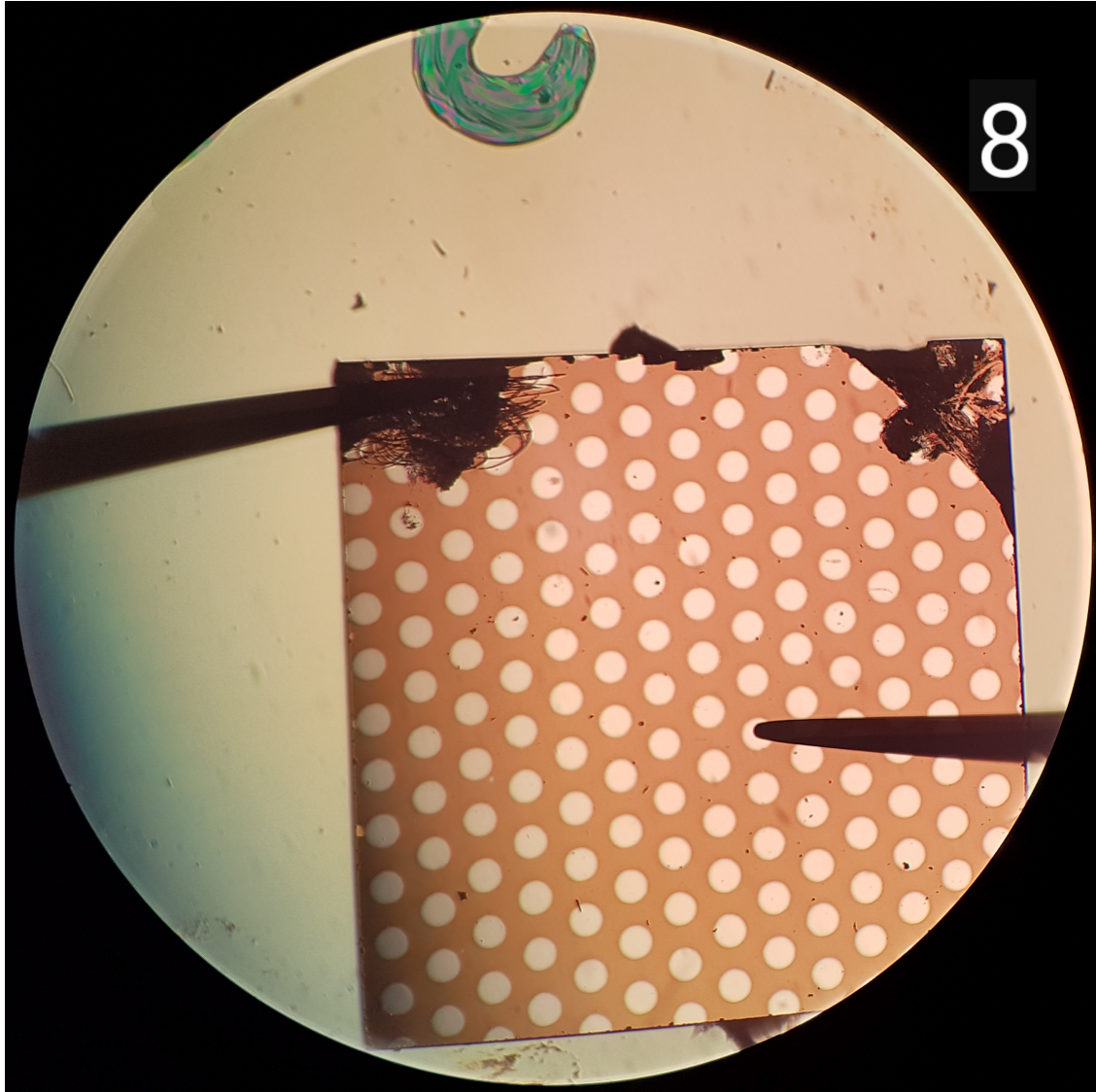


Figure A.13: FTJ, microscope view

Parameter	value	unit	description
u_i	0.445	nm^{-3}	Initial concentration
k^+	0.00338	s^{-1}	Generation rate
k^-	0.560	s^{-1}	Annihilation rate
β	0.914	1	Asymmetry factor
f	0.0120	1	Exponential factor
φ^+	2.94	eV	Vacancy generation barrier
φ^-	1.11	eV	Vacancy annihilation barrier
D	0.0320	$\text{nm}^2 \text{s}^{-1}$	Diffusion coefficient
v_d	3.77×10^{-4}	$\text{nm s}^{-1} \text{V}^{-1}$	Voltage-induced drift

Table A.2: Valency mechanism model parameters.

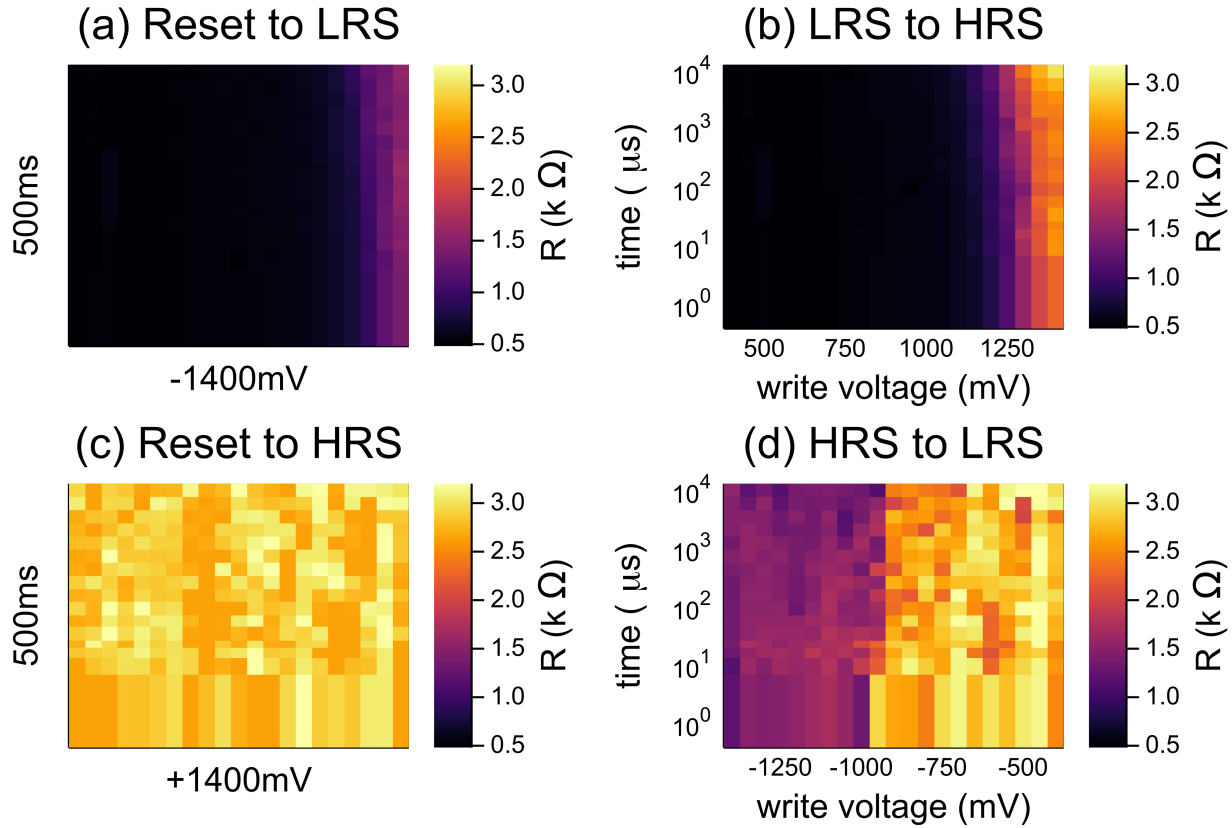


Figure A.14: Resistive switching over pulse duration and amplitude of a pristine $\text{Hf}_{0.5}\text{Zr}_{0.5}\text{O}_2$ FTJ of a nominal thickness of 3 nm. The small resistivities were measured at 400 mV, indicating significant leakage current.

TiN/Hf_{0.5}Zr_{0.5}O₂/Au device, operated by pulse sequences as shown in Fig. A.18. After long-term cycling, delamination of the top electrode is observed (Fig. A.19).

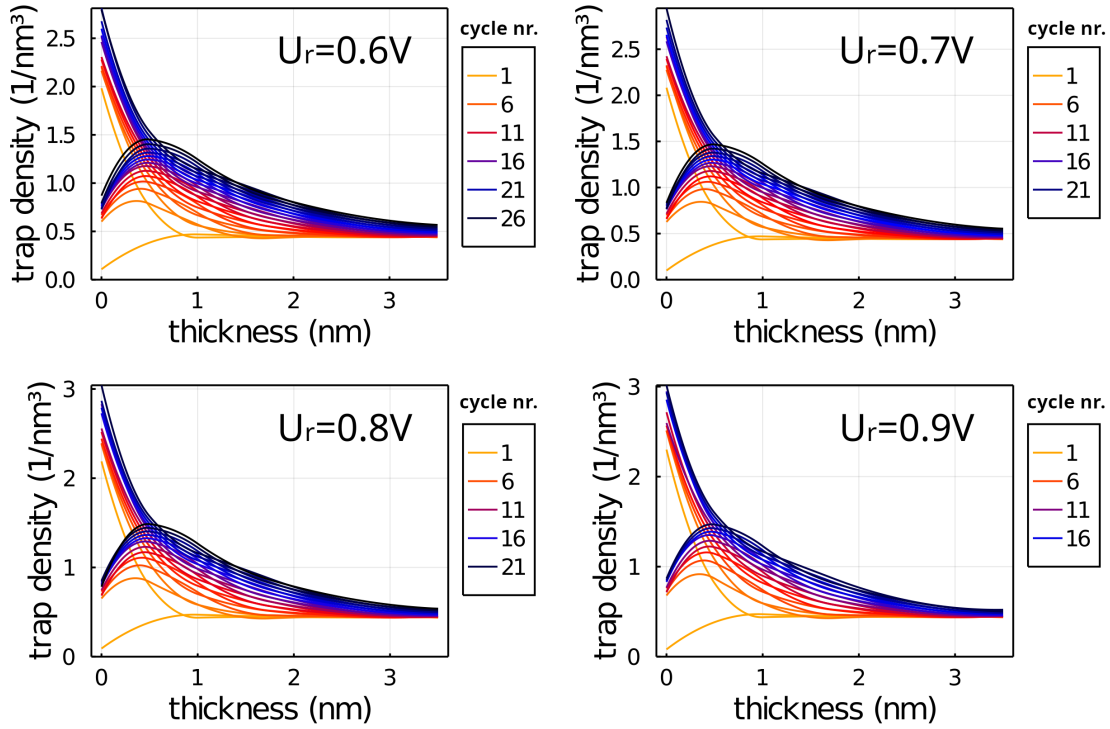


Figure A.15: Vacancy convection-diffusion FDM model for the pulse sequence, fitted to the measured pulse sequence at $U_r = 0.7V$. The left side is the chemically active $\text{Hf}_{0.5}\text{Zr}_{0.5}\text{O}_2/\text{Pt}$ interface, while the right TiN electrode is assumed to be inert.

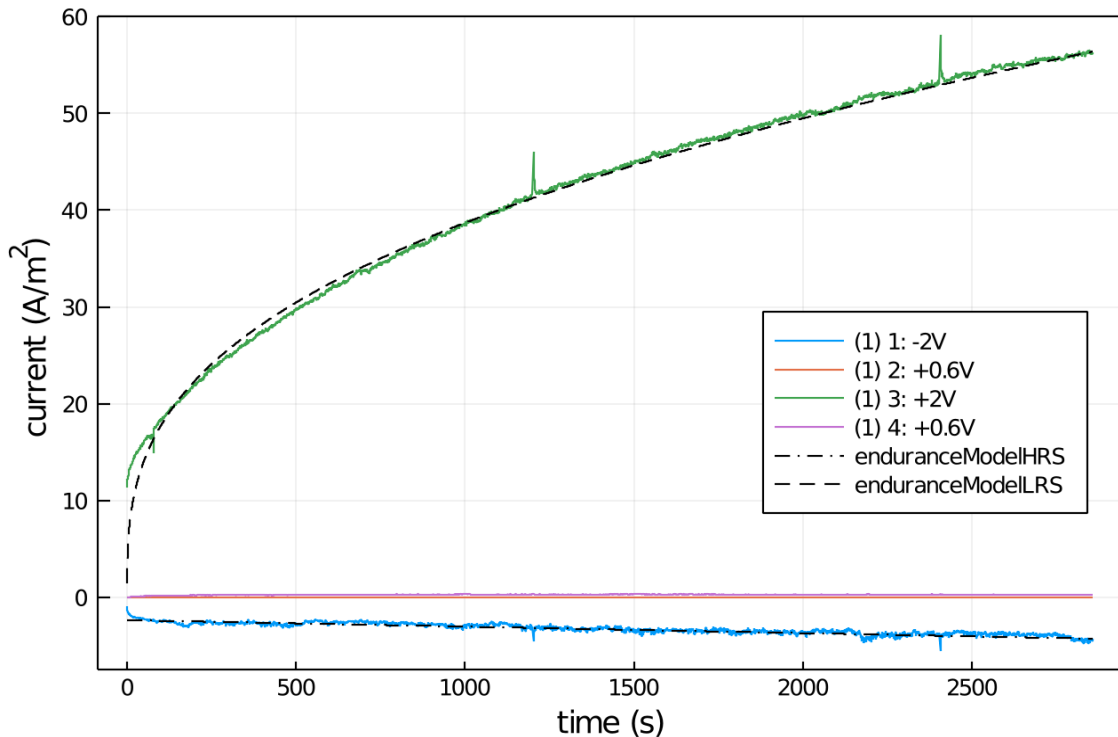


Figure A.17: Endurance over Pulses, 3000s

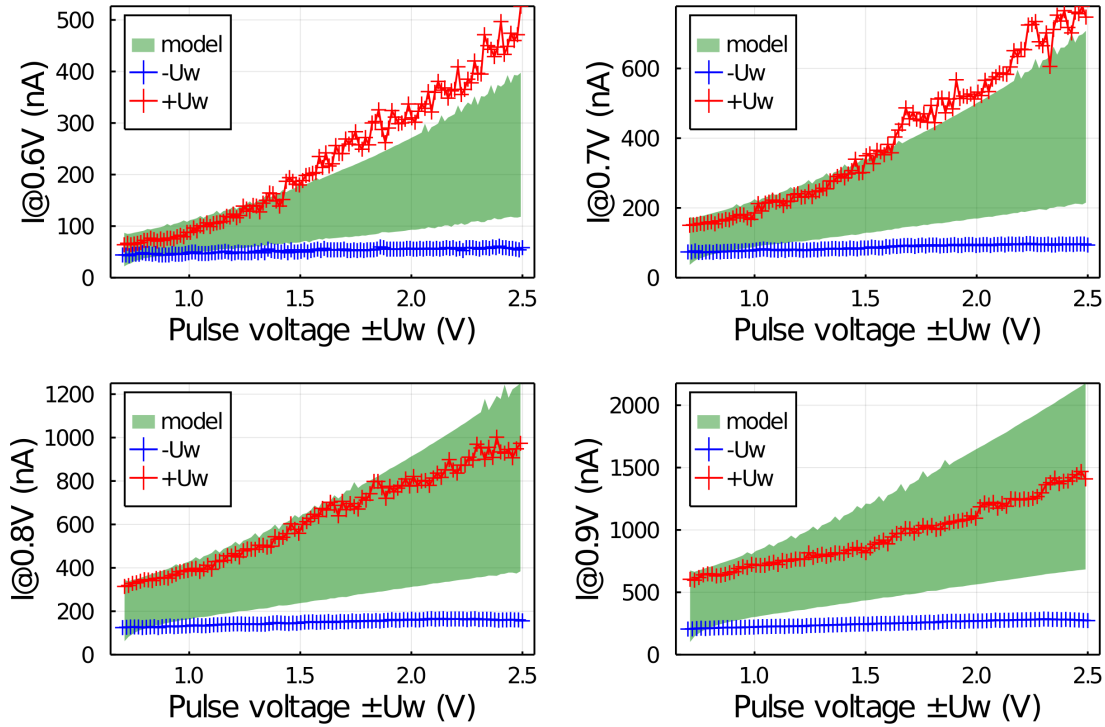


Figure A.16: Current density from the valency switching model (red) compared to the measured values of the pulse sequence successively increasing write pulse amplitudes between $U_r = \pm 0.6\text{ V}$ and $\pm 2.5\text{ V}$ (Fig. 4.10). The four shown measurements were done in sequence.

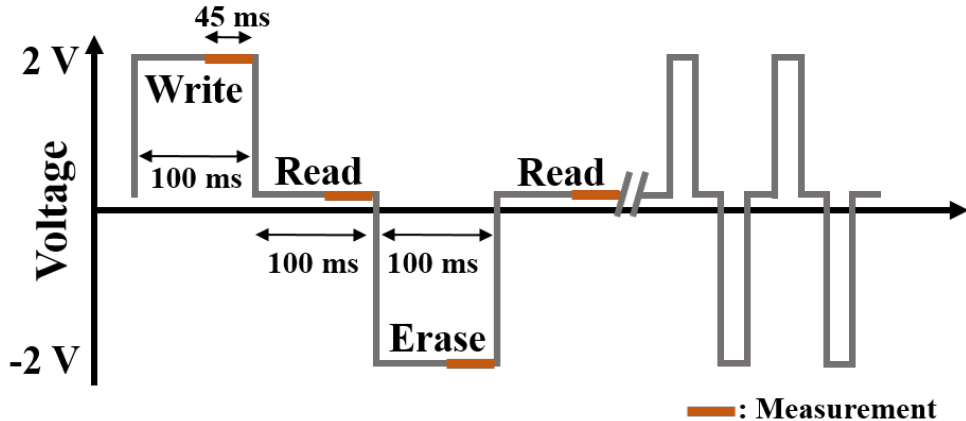


Figure A.18: Endurance Pulse Sequence

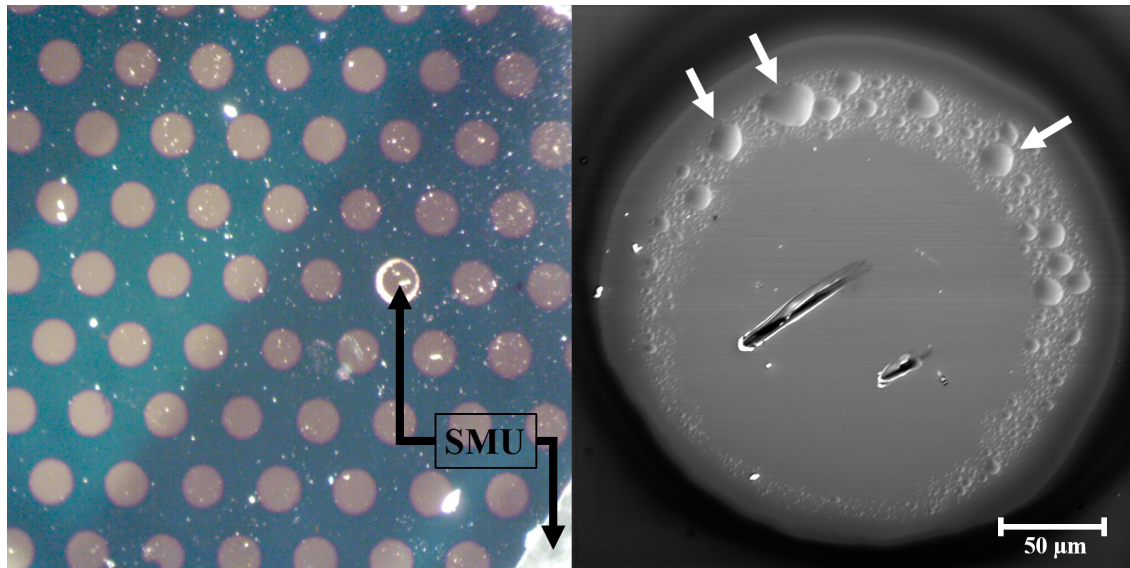


Figure A.19: Delamination of top electrode. Left: Microscopy. Right: SEM image. Over long-term, high-voltage pulse sequences, the creation of vacancies releases oxygen at the top electrode interface, producing device failure by electrode delamination.

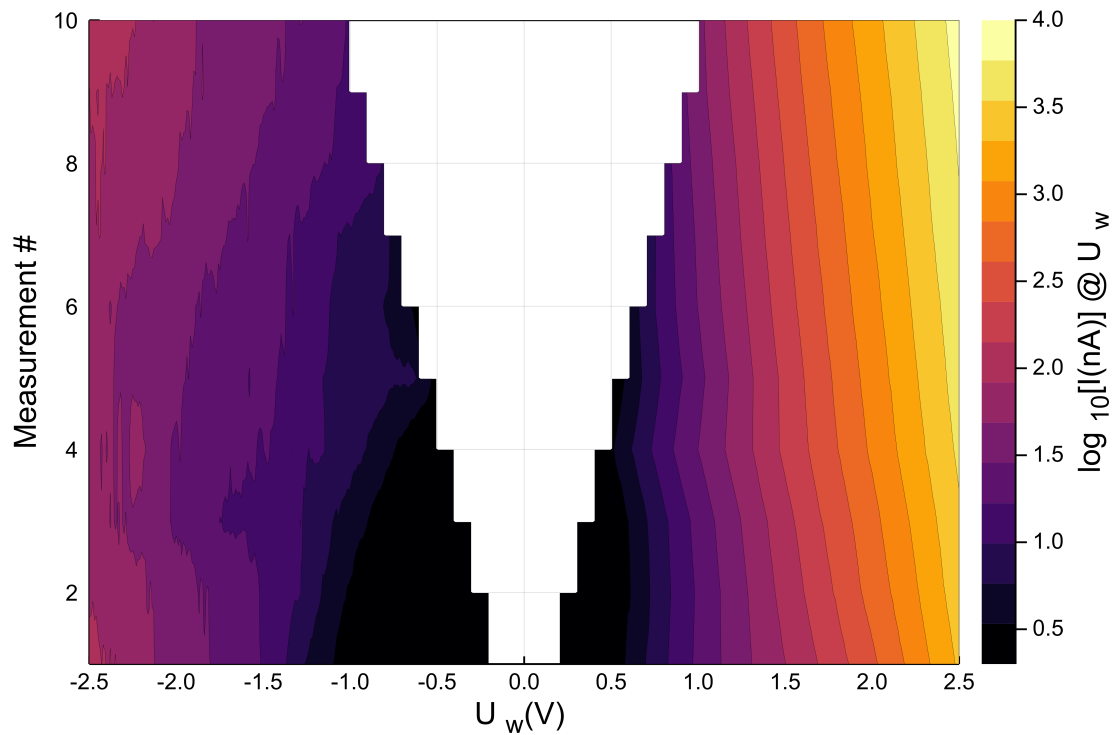


Figure A.20: Current over write voltage. Identical sequence as in Fig. 4.10, but measurements taken at the write voltages.

A.4 Work Function in Electrode Materials

An overview of work functions in metals, metal oxides and TiN is found in Halas and Durakiewicz [209], Greiner et al. [210], Lima et al. [211], respectively. The work function of TiN is given as 4.2 eV, however this can vary with structural and composition parameters [212].

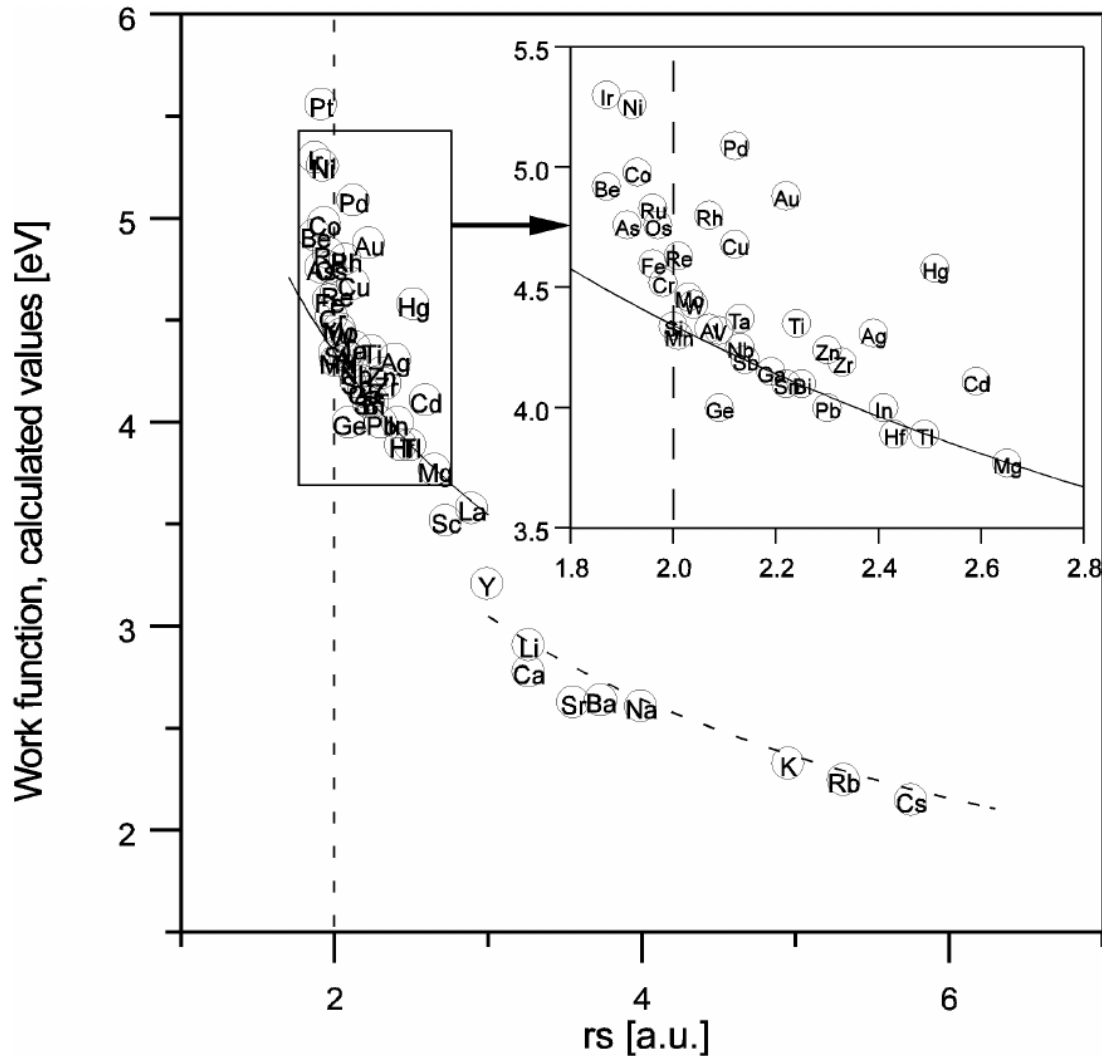


Figure A.21: Work function over density of free electrons [209]. Pt and Au provide some of the largest work functions (5.5 eV and 4.9 eV respectively)

Sommaire Récapitulatif

La jonction tunnel ferroélectrique :

Modélisation pour les applications

mémoires et neuromorphiques

1 Introduction

La miniaturisation successive de la taille des structures a indéniablement été une force motrice pour l'avancée de la nano fabrication ainsi que de la technologie des mémoires et de l'informatique durant les récentes décennies [213]. Cette progression vers des dispositifs moins coûteux, puis rapides et à faible consommation d'énergie avec de plus grandes capacités dans chaque production de dispositif est en train d'atteindre ses limites physiques et technologiques, de manière évidente dans la lithographie de haute résolution, dans les effets de parasites électriques et les interférences, ainsi que la nécessité de refroidissement qui limite la réduction de taille et l'intégration 3D [214]. D'une part, ce développement a déclenché les efforts des manufacturiers à concevoir des puces optimisées pour une application spécifique; d'autre part, la recherche d'un changement de paradigme dans lequel la technologie de l'information surmonte les défis mentionnés plus haut gagne du terrain. En plus de la quête de vouloir remplacer les composants individuels de logique et de mémoire, la recherche sur l'intelligence artificielle et les réseaux neuronaux inspirés de la biologie a démontré que l'architecture classique du CPU or du TPU est mal adaptée pour la recréation d'un tel système

[215], principalement à cause de la séparation de la logique et de la mémoire, de la consommation en puissance, des unités d'opération dédiées, centralisés et synchrones, ainsi que la limitation à des interconnexions logiques 2D. Tous ces points peuvent être résolus en principe, tel que démontré par son homologue biologique, le cerveau. De nouveaux candidats pour la mémoire, qui combinent les avantages du DRAM, du SRAM et de la mémoire flash sont actuellement à l'étude [31, 216].

1.1 Motivation

Parmi ces mémoires, le type qui utilise la ferroélectricité comme moyen de stocker de l'information est une variante de dispositif très prometteuse. Ces dispositifs peuvent être divisés en deux sous-types: la mémoire ferroélectrique qui intègre des condensateurs ferroélectriques ou des oxydes de grille et qui fonctionnent en piégeant et en relâchant les charges pendant l'inversion de la polarisation [217, 218], ainsi que des jonctions tunnel ferroélectrique (FTJ) qui modulent leur état résistif en fonction de la polarisation [31, 219]. Les deux sous-types ont démontré leur capacité à fonctionner comme des mémoires, mais ont récemment attiré les regards provoqués par la découverte révolutionnaire d'une phase ferroélectrique de l'oxyde de hafnium en 2011 par Böscke et al. [7]. Le dispositif FTJ a une structure de mémoire extrêmement simple qui ne consiste en rien d'autre que de deux électrodes métalliques séparées par une couche nanométrique ferroélectrique (1 à 4 nm) [13, 14, 47]. Leur fonctionnement s'appuie sur un phénomène physique nommé électrorésistance par effet tunnel (TER – tunneling electrorésistance). Ce phénomène décrit la dépendance de la résistance électrique à la polarisation du ferroélectrique (FE). Cet état de la polarisation peut être commuté par un champ externe qui dépasse le champ électrique coercitif à l'intérieur du FE. L'asymétrie entre les deux états résistifs (état résistif élevé (HRS) et état résistif faible (LRS)) est due aux propriétés différentes des matériaux qui constituent les électrodes, ce qui module la hauteur ou la largeur effective de la barrière tunnel. Ces états résistifs peuvent alors être utilisés pour représenter les états binaires digitaux ‘1’ et ‘0’ pour stocker l'information. Bien que son existence ait été prédite théoriquement depuis des décennies [8], l'effet TER a été démontré pour la première fois sans ambiguïté en 2009 par Garcia et al. [9], en se servant de couches ultra-minces de titanate de baryum (BaTiO_3) ferroélectrique. Leurs travaux ont initié d'intenses recherches sur les propriétés des mé-

moires FTJ. Plusieurs avantages de ces mémoires ont été démontrés, notamment une endurance élevée ($\sim 10^6$ cycles) [10, 11], une haute vitesse d’opération (état ON/OFF peuvent être écrits par des impulsions), une consommation faible en puissance électrique [12], une densité de données élevée et une architecture crossbar simple [14, 47]. Malgré les propriétés excellentes dont les mémoires FTJ font preuve en théorie, leur intégration comme mémoire commerciale a été freinée par trois facteurs majeurs : premièrement, leur compatibilité avec le procédé CMOS à cause des conditions nécessaires auxquelles doivent être soumis le bilan thermique, le gaz azoté (mélange de H₂ et de N₂), et la faible affinité des pérovskites à l’oxygène produit une interface avec le silicium de qualité piètre [15–18, 220]. Deuxièmement, la nécessité d’avoir des films ferroélectriques ultra-minces est requise par le mécanisme de l’effet tunnel. La diminution de la taille des ferroélectriques mène à la dégradation de leurs propriétés ferroélectriques. Troisièmement, le défi technologique de fabriquer des films reproductibles et très homogènes et les incertitudes qui en résultent dans la récupération d’informations. Étant donné que la conductivité électrique d’une jonction de tunnel dépend exponentiellement de sa largeur, même de légères variations dans l’homogénéité génèrent de grosses variations dans les propriétés électriques. Les phases ferroélectriques découvertes dernièrement des couches ultramince de HfO₂ dopé et de Hf_xZr_{1-x}O₂ ont une compatibilité CMOS excellente et un faible bilan thermique [7, 22], permettant ainsi de satisfaire les exigences du premier point. En effet, les oxydes individuels HfO₂ et ZrO₂ sont des matériaux diélectriques ayant fait leurs preuves dans l’industrie des semiconducteurs [23–25, 142]. Bien que le nouveau matériau règle le problème de l’incompatibilité fondamentale aux CMOS, sa nature polycristalline et la nécessité à avoir une phase ferroélectrique stable ne sont pas pleinement maîtrisées. Nous étudions la faisabilité théorique et pratique d’un tel dispositif FTJ, notamment les deuxième et troisième points sur l’adaptabilité à grande échelle et les exigences technologiques de production. Dans le but d’établir les FTJ comme des dispositifs de mémoires, la compréhension du mécanisme de transport de charges, les exigences de la production et la durabilité des dispositifs requièrent une amélioration. Plus particulièrement, une étude en profondeur des relations entre les propriétés des interfaces ferroélectrique/métal et les facteurs affectant le transport de charge doivent être compris dans le but d’optimiser la performance de ces dispositifs ferroélectriques à couche mince [14]. Nous nous penchons aussi sur les limitations de la jonction de tunnel, notamment sa dégradation vers le mode à commutation basée sur les

lacunes de lacune (vacancy switching mode). Enfin, nous finissons avec un cas d'étude de nos FTJ dans une configuration de réseaux de neurones à impulsions.

1.2 Objectifs de Recherche

Cet ouvrage se veut une étude des défis et des propriétés caractéristiques des jonctions de tunnel ferroélectriques (FTJ) qui sont fondés sur la phase ferroélectrique récemment découverte du $\text{Hf}_{0.5}\text{Zr}_{0.5}\text{O}_2$. Nous exposons les grandes lignes des mécanismes physiques fondamentaux et explorons les espaces des paramètres de conception. À partir de cette base théorique, nous soulignons les défis pratiques de l'épaisseur et de l'homogénéité du film et développons un modèle pour quantifier ces exigences de conception. Nous fabriquons les FTJ par dépôt par pulvérisation cathodique magnétron par condition réactive. Par ce procédé, nous recherchons des dispositifs qui manifestent une commutation résistive significative. Ensuite, nous caractérisons la durabilité électrochimique du dispositif en effleurant des voltages de claquage. Le premier mode de défaillance est en conformité avec la commutation de vacance (vacancy switching), un mécanisme qui manifeste encore une fois une commutation résistive. Nous avons l'intention de créer un modèle qui décrit ces claquages successives. Des modèles appropriés devaient être trouvés par l'auteur. À partir de ces modèles, les propriétés caractéristiques tels que les comportements ferroélectrique et électrique, la nécessité que le film soit homogène, la dégradation du dispositif et d'autres comportements intéressants découverts dans des expériences devaient être étudiés. Avec ces résultats, la pertinence des FTJ au sujet des applications dans les mémoires, de même que dans un cas d'étude d'un réseau de neurones à impulsions devaient être analysées.

2 Contexte Théorique

Pour comprendre les jonctions tunnel ferroélectriques, il est critique de comprendre les propriétés des matériaux dans le dispositif, ce qui comprend les interactions électrostatiques entre la polarisation ferroélectrique et les électrodes. Cela constitue un fondement pour la description de la barrière de tunnel, qui définit le mécanisme de commutation résistive. Finalement, l'évolution dans le

temps de la commutation ferroélectrique nécessite une discussion de la dynamique de commutation ferroélectrique.

2.1 Le Champ de Déplacement Électrique

Le comportement d'un diélectrique est décrit par

$$D_i = \varepsilon_{ij} E_j \quad (\text{A.1})$$

où D_i est le champ de déplacement électrique dans la direction i , E_j est le champ électrique dans la direction j et ε_{ij} , la permittivité diélectrique. Dans 20 classes de cristaux non-centrosymétriques sur 21, il existe au moins une composante non nulle de la constante piézoélectrique d_{ijk} . Ces cristaux sont polarisés quand ils sont soumis à un stress mécanique σ_k et vice versa. Ainsi, Eq. A.1 devient

$$D_i = \varepsilon_{ij} E_j + d_{ik} \sigma_k \quad (\text{A.2})$$

Sur les 20 groupes piézoélectriques, il en existe 10 qui ont un axe polaire unique. Ces derniers sont appelés pyroélectriques. La grandeur de leur polarisation est dépendante de la température. Elle est quantifiée par le coefficient pyroélectrique p_i , qui ajoute une contribution additionnelle au champ de déplacement électrique:

$$D_i = \varepsilon_{ij} E_j + d_{ik} \sigma_k + p_i \Delta T \quad (\text{A.3})$$

Finalement, certains cristaux pyroélectriques ont un état de polarisation qui peut être commuté entre au moins deux états stables par l'application d'un champ électrique. Ces cristaux sont appelés ferroélectriques. Leur polarisation inhérente et spontanée P_{Si} affecte directement le champ de déplacement électrique:

$$D_i = \varepsilon_{ij} E_j + d_{ik} \sigma_k + p_i \Delta T + P_{Si} \quad (\text{A.4})$$

Une vue d'ensemble graphique de la classification des cristaux est donnée en Fig. A.22. Il est à noter que la piézoélectricité et la pyroélectricité sont seulement des critères nécessaires, mais pas

suffisants pour la ferroélectricité. L'orientation de la polarisation spontanée est une contribution dominante au champ de déplacement électrique dans la plupart des ferroélectriques.

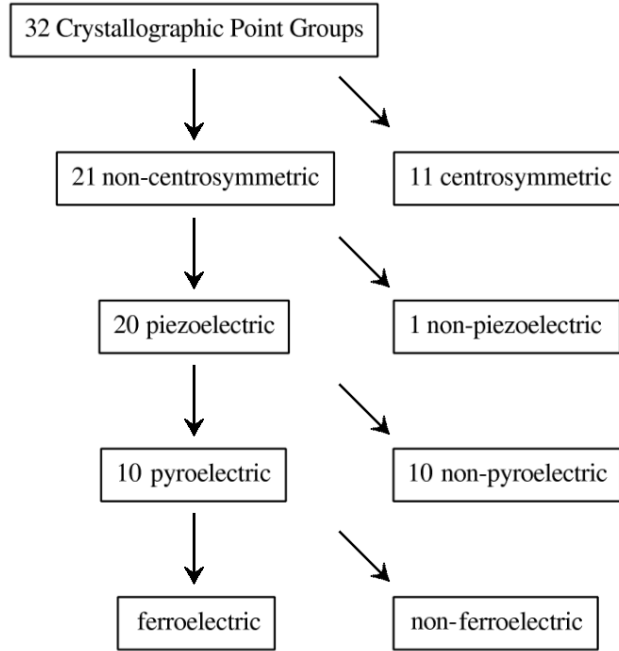


Figure A.22: Classification hiérarchique des matériaux qui démontrent un effet ferroélectrique. Contrairement aux autres groupes, la propriété ferroélectrique n'est pas uniquement définie par la classe du cristal.

2.2 Ferroélectricité

Un ferroélectrique est défini comme un matériau qui manifeste une polarisation permanente qui peut être réorientée par l'application d'un champ électrique. Contrairement aux autres groupes présentés en Fig. A.22, la différence par rapport aux pyroélectriques ne se trouve pas dans la structure du cristal, mais seulement dans la capacité des ferroélectriques de changer de polarisation. Ce changement de polarisation peut être visualisé par la courbe d'hystérésis présentée sur la Fig. A.23a. Dans un cristal non polarisé, la polarisation est orientée aléatoirement, la polarisation macroscopique est donc nulle. Si l'on applique un très faible champ électrique, la relation entre la polarisation P et le champ électrique E aura un comportement similaire à un diélectrique ordinaire, et si l'on retire le champ, cela aura pour effet de ramener la polarisation totale à zéro. Une augmentation suffisante du champ électrique amènera la polarisation à être alignée dans une direction [35]. Dans cet état

de saturation, la polarisation est proportionnelle au champ électrique appliqué

$$\partial P_i = \chi_{ij} \partial E_j = (\varepsilon_{ij} - 1) \partial E_j \quad (\text{A.5})$$

La polarisation P_i englobe les moments électriques dipolaires permanent et induit dans le matériau. Elle est mesurée en unités de charge surfaciques C/m². Dans la théorie de Ginzburg-Landau [36], une approche de la courbe d'hystérésis ferroélectrique est dérivée. En se basant sur un modèle d'énergie libre, la théorie peut être utilisée pour décrire la courbe d'hystérésis ferroélectrique. La polarisation dans le cas uniaxial est exprimée à l'aide du polynôme implicite comme suit:

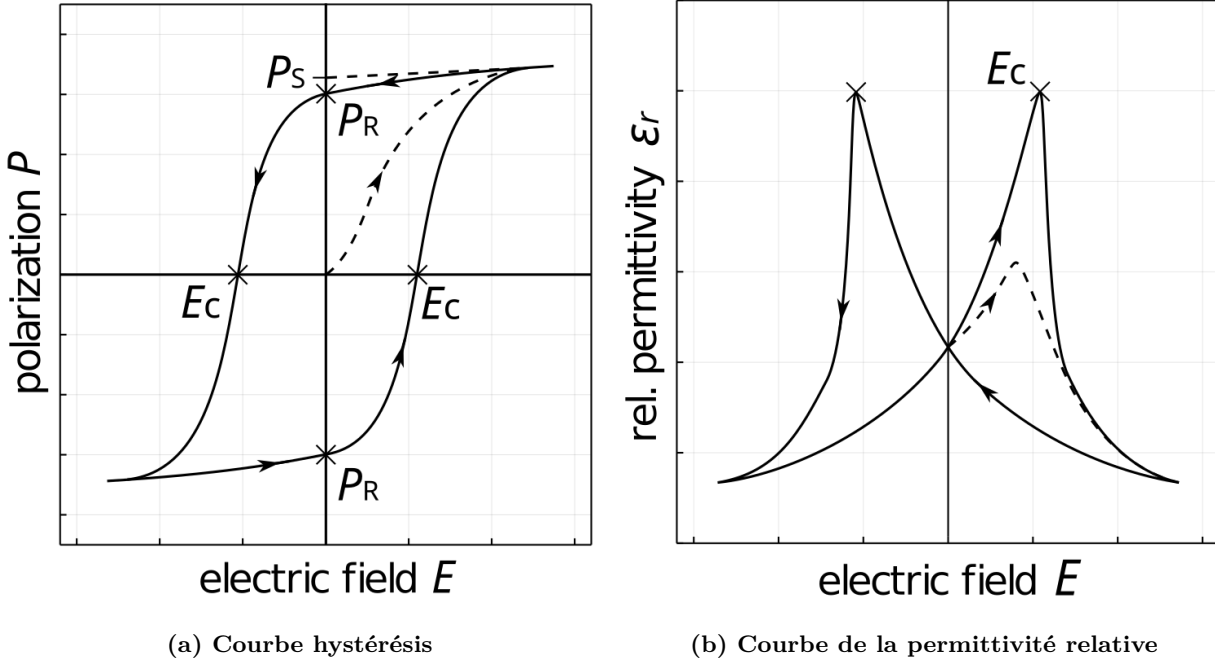
$$E = \alpha_0(T - T_0)P + \alpha_{11}P^3 + \alpha_{111}P^5 + \dots \quad (\text{A.6})$$

où les paramètres α et T_0 peuvent être obtenus par des méthodes expérimentales ou des calculs ab initio. Lorsque l'on résout cette équation pour trouver la valeur de P , la courbe d'hystérésis caractéristique qui a la forme de S peut être tracée. La section 2.5.1 décrit une application de ce modèle. Un modèle heuristique qui inclut également un renversement de P incomplet est donné par Lue et al. [37].

2.3 Matériaux Ferroélectriques

D'un point de vue cristallographique, seuls les cristaux polaires non-centrosymétriques peuvent être ferroélectriques. Ceci est dû à l'axe de polarisation intrinsèque qui est incompatible avec l'opérateur de symétrie inversion. La polarisation dans un ferroélectrique se développe comme conséquence d'une séparation de charges dans la phase cristalline. Quand la polarisation est inversée, il se produit un déplacement relatif des atomes entre deux états thermodynamiquement stables. Cela implique que ledit matériau perd sa propriété ferroélectrique quand il dépasse sa température de Curie T_c .

Les représentants les plus remarquables des ferroélectriques sont les pérovskites tels que le BaTiO₃, Pb(Zr, Ti)O₃ and LiNbO₃, de même que les matériaux organiques, tel que le polytrifluoroéthylène (PVDF) [38]. La structure de la fluorine orthorhombique du ferroélectrique HfO₂ et ZrO₂ est mon-



(a) Courbe hystérésis

(b) Courbe de la permittivité relative

Figure A.23: La courbe d'hystérésis caractéristique d'un ferroélectrique. Initialement, les domaines FE orientés aléatoirement peuvent ne pas manifester de polarisation macroscopique (ligne pointillée). Sous l'effet du champ électrique externe, le cristal devient de plus en plus polarisé de telle sorte que sa polarisation s'approche asymptotiquement à la limite de saturation $\partial P / \partial E = \varepsilon_0 \chi$. La polarisation rémanente P_R demeure, et peut être ensuite inversée par un champ électrique de sens opposé. La facilité avec laquelle la polarisation est inversée dépend du comportement de nucléation et de croissance des domaines renversés, ce qui dépend du matériau ferroélectrique et des paramètres tels que la fréquence appliquée.

trée en Fig. A.24. Les antiferroélectriques, qui sont intimement reliés aux ferroélectriques, manifestent aussi des dipôles inversibles dans le cristal. Cependant, contrairement aux ferroélectriques, des dipôles adjacents s'alignent antiparallèles de manière à annuler toute polarisation macroscopique.

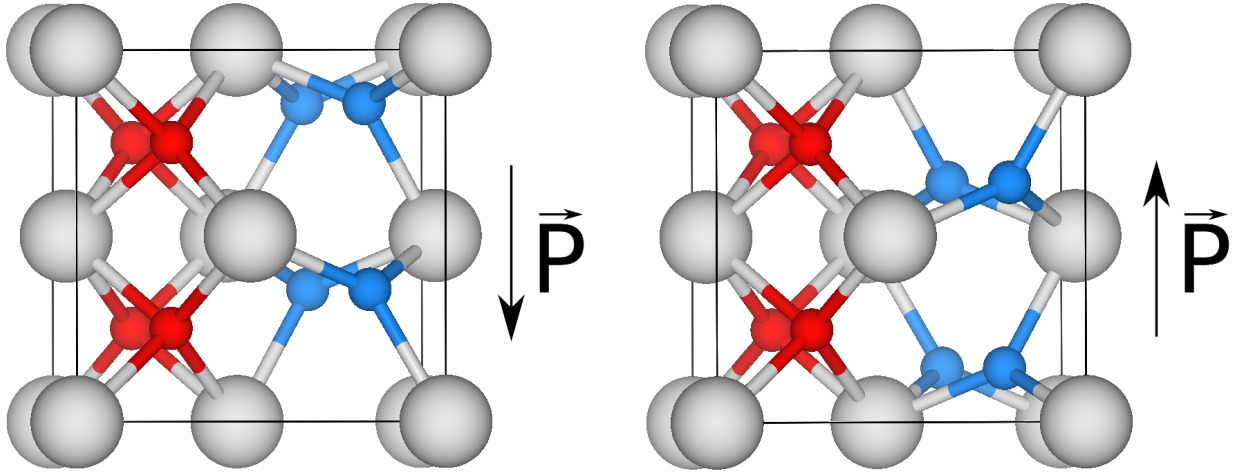


Figure A.24: Phase orthorhombique d'un ferroélectrique (No. 29) telle qu'observée dans le $\text{Hf}_{0.5}\text{Zr}_{0.5}\text{O}_2$. En gris: atomes Hf/Zr. En rouge ou en bleu: atomes d'oxygène. En bleu: atome d'oxygène dans un site bistable où il peut pivoter. À gauche: polarisation vers le bas. À droite : polarisation vers le haut. L'axe horizontal est aligné avec le paramètre de maille b, tandis que l'axe vertical est aligné avec le paramètre de maille c.

2.4 La Loi de Kay-Dunn

En 1962, H. Kay et J. Dunn ont décrit la dépendance du champ coercitif E_c à l'épaisseur du film d par une loi semi-empirique [39]

$$E_c \propto d^{-2/3} \quad (\text{A.7})$$

La dérivation de l'équation suppose des électrodes parfaites qui n'induisent aucun champ électrique interne dans le film ferroélectrique, ce qui implique que le champ coercitif mesuré entre les électrodes est identique à celui de l'échantillon Dawber et al. [40]. ont démontré que cette loi est vraie pour divers matériaux (PVDF, $\text{Pb}[\text{Zr}_x\text{Ti}_{1-x}]\text{O}_3$, KNO_3) pour des films ayant une épaisseur de 100 um jusqu'à aussi peu que 1 nm (voir Fig. A.25). Les effets d'interface tel que l'écrantage par des charges sur des distances finies ont pour effet d'altérer le champ coercitif mesuré. Dans le cas d'une polarisation spontanée très grande par rapport à la constante diélectrique du film $4\pi P_s \gg \varepsilon_0 \varepsilon_r E$, le champ coercitif effectif est réduit étant donné que le champ de dépolariation aide le processus de commutation [40]. Dans ce cas, la loi de Kay-Dunn peut être considérée comme une limite supérieure au champ coercitif.

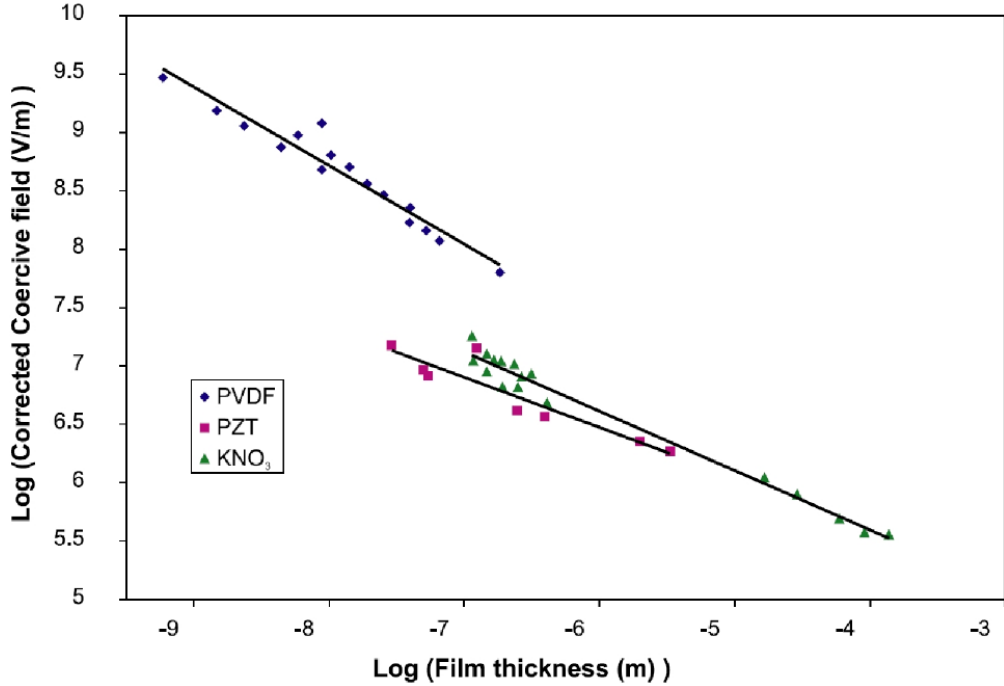


Figure A.25: Loi de Kay-Dunn : Variation du champ coercitif en fonction de l'épaisseur de divers films ferroélectriques (échelle logarithmique) [42].

2.5 La Conduction dans les Ferroélectriques

Bien que tous les matériaux ferroélectriques soient des isolants, il existe une série de mécanismes qui permettent la conduction [60]. Dans cet ouvrage, nous résumons quelques-uns de ces mécanismes pertinents à notre étude des jonctions de tunnel.

La Conduction Thermoïonique

Le mécanisme Schottky décrit l'excitation thermique des porteurs de charge dans la bande de conduction d'un isolant [61]. Une équation qui décrit le courant thermoïonique est donnée dans la section 2.7.4. Le mécanisme dépend de la hauteur de la barrière et de la température, mais est indépendant de la largeur de la barrière et devient négligeable à des largeurs de barrière qui sont de l'ordre du nanomètre; puisque les mécanismes de tunnel croissent exponentiellement [54].

Effet Tunnel Direct

Le mécanisme de conduction tunnel direct résulte de la probabilité de transmission mécanique quantique de porteurs de charge à travers des barrières potentielles, et devient pertinent pour les couches minces dans à l'échelle nanométrique [62]. Direct tunneling directly transports particles between the electrodes, assuming negligible scattering within the barrier. Effet tunnel direct transporte directement les particules entre les électrodes, en supposant que la diffusion à la barrière est négligeable. Dans le cas d'une barrière de potentiel trapézoïdale, l'approximation Wentzel-Kramers-Brillouin (WKB) donne [63]

$$j_{DT} = C \frac{\exp \left[\alpha \left(\left(\phi_2 - \frac{eV}{2} \right)^{3/2} - \left(\phi_1 + \frac{eV}{2} \right)^{3/2} \right) \right]}{\alpha^2 \left[\sqrt{\phi_2 - \frac{eV}{2}} - \sqrt{\phi_1 + \frac{eV}{2}} \right]^2} \sinh \left[\frac{3eV}{4} \alpha \left(\sqrt{\phi_2 - \frac{eV}{2}} - \sqrt{\phi_1 + \frac{eV}{2}} \right) \right] \quad (\text{A.8})$$

où $C = -\frac{4em_{ox}}{9\pi^2\hbar^3}$, $\alpha = \frac{4d\sqrt{2m_{e,ox}}}{3\hbar(\phi_1+eV-\phi_2)}$, m_{ox} est la masse effective des électrons à effet tunnel, ϕ_1 et ϕ_2 sont les potentiels d'interface.

L'équation ne dépend que des deux potentiels d'interface $\phi_{1,2}$ par polarisation et de la masse effective $m_{e,ox}$, tout en présentant un comportement exponentiel avec l'épaisseur d .

Effet Tunnel de Fowler-Nordheim

Par rapport à l'effet tunnel direct, l'effet tunnel de Fowler-Nordheim nécessite des tensions plus élevées [64, 65]. La tension appliquée réduit le potentiel d'interface de l'isolant en dessous du niveau d'énergie des électrons en opposition à l'électrode. Par conséquent, la distance tunnel est réduite. Le courant qui en résulte est donné par [63]

$$j_{FN} = \frac{e^3 m}{8\pi h m_{ox} \phi_{1,2}} E^2 \exp \left[-\frac{8\pi\sqrt{2m_{ox}}}{3he} \frac{\phi_{1,2}^{3/2}}{E} \right] \quad (\text{A.9})$$

où $\phi_{1,2}$ est le potentiel de barrière de l'interface de tension négative.

Mécanismes de Défauts

Les défauts déforment localement la forme de la barrière potentielle. Ces défauts peuvent être le résultat de la polycristallinité, des défauts de fabrication ou de fatigue dus à une polarisation répétée de commutation. Les parois des domaines ferroélectriques peuvent également présenter un comportement conducteur [67]. En plus de la dégradation de propriétés de commutation ferroélectrique, les défauts ponctuels tels que les lacunes d'oxygène permettent à Poole-Frenkel ainsi qu'à la conduction par saut de piège à piège (multi piégeage) (trap-to-trap hopping conduction), entre autres [60]. . La conduction à sauts a précédemment été liée aux courants de fuite dans les oxydes d'hafnium et zirconium $\text{Hf}_{0.5}\text{Zr}_{0.5}\text{O}_2$ [68–72]. Le modèle quantitatif basé sur le mécanisme de sauts est développé dans la section 4.2.

Autres Mécanismes

À haute tension, il se produit une rupture diélectrique qui génère des porteurs de charge supplémentaires dans le diélectrique et dégrade rapidement l'isolant [73, 74]. Un transport de charge de catégorie spéciale est le courant de déplacement transitoire. Il se produit lors de la commutation ferroélectrique : la polarisation est dépassée lorsque le champ coercitif bascule, des charges supplémentaires sont libérées. Ce comportement peut être modélisé par un condensateur variable [108] comme indiqué au point 2.5.1.

2.6 La Jonction Tunnel Ferroélectrique

Une jonction tunnel ferroélectrique est constituée d'une couche ferroélectrique de quelques nanomètres d'épaisseur, pris en sandwich entre deux électrodes métalliques asymétriques, ou une électrode métallique et une électrode semi-conductrice [75]. En fonction de la direction de polarisation, la couche mince ferroélectrique entre les électrodes module la résistance entre les électrodes de manière significative. Cet effet est connu sous le nom d'effet d'électrorésistance à effet tunnel (TER) [76]. Bien que théoriquement prédit par Esaki en 1971 [8], le premier effet expérimental a été réalisé en 2006 par Tsymbal et Kohlstedt Tsymbal and Kohlstedt [13]. Alors qu'initialement les pérovskites fer-

roélectrique, tels que BaTiO_3 et $\text{Pb}(\text{Zr}, \text{Ti})\text{O}_3$ ont été utilisés, les propriétés uniques et avantageuses de la phase orthorhombique ferroélectrique récemment découverte dans le HfO_2 en 2011 par Böscke et al. [7] a suscité un nouvel intérêt pour le concept des mémoires ferroélectrique à jonction tunnel (FTJ).

Le mécanisme physique de la commutation des TER est basé sur l'effet de la polarisation sur la barrière tunnel. La nature asymétrique des électrodes produit différentes distributions de charges miroirs qui s'accumulent aux interfaces, en fonction de la direction de la polarisation. Lorsque la polarisation pointe vers une électrode, une région de charge spatiale positive se forme, ce qui augmente le potentiel d'interface. L'électrode opposée présente un effet inverse, diminuant son potentiel d'interface. L'asymétrie des propriétés de blindage des électrodes provoque des changements d'ampleur différente, ce qui entraîne une modification de la hauteur moyenne des barrières. L'état de polarisation avec une hauteur de barrière moyenne inférieure est appelé un état de basse résistance (LRS), celui dont la hauteur de la barrière est la plus élevée est un état de haute résistance (HRS). Ce mécanisme est décrit à la Fig. A.26.

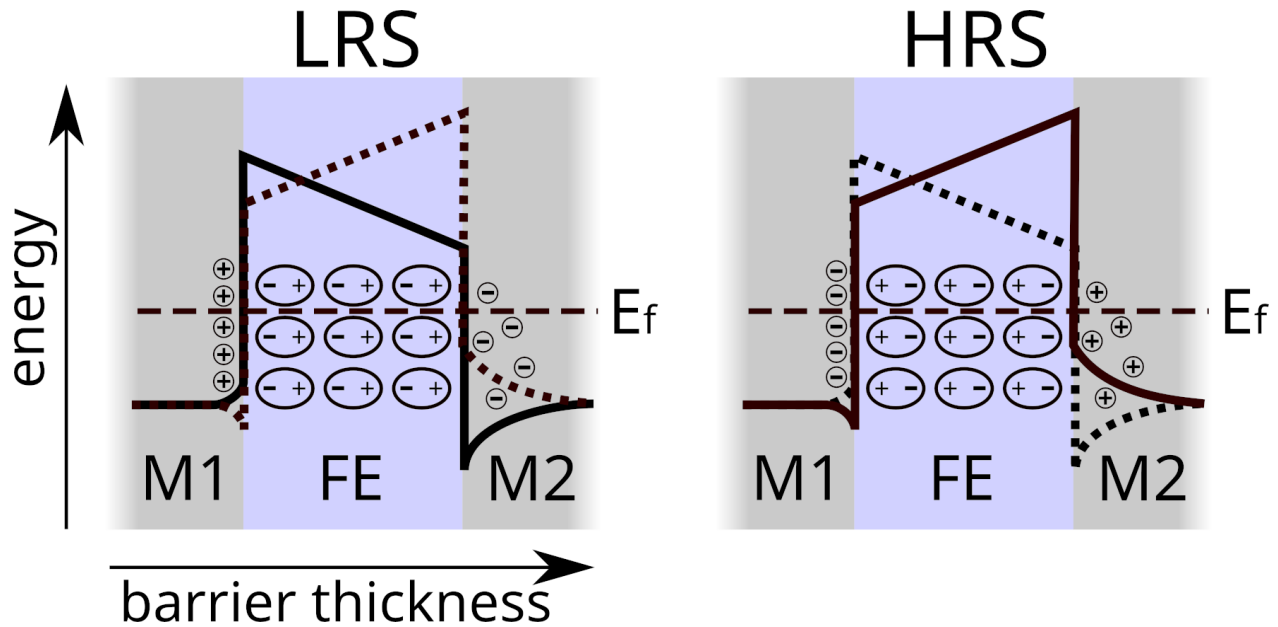


Figure A.26: Schémas illustratifs des états LRS et HRS de la commutation resistive (schéma). La ligne pleine est la barrière tunnel. À gauche : la couche ferroélectrique FE est polarisée vers l'électrode de faible blindage électrostatique M2, provoquant une baisse significative de la barrière potentielle à l'interface M2, avec un effet opposé et plus petit à M1. À droite : lorsque la polarisation est inversée, la barrière de potentiel augmente de manière significative à M2, avec un effet opposé et plus faible à M1.

Le schéma de la Fig. 1.1 présente le changement de la barrière tunnel. Deux régimes tunnel de base peuvent être directement dérivés de ce modèle : dans le cas d'une tension de polarisation modérée, le mécanisme de l'effet tunnel direct, où le courant de tunnel traverse une barrière trapézoïdale de hauteur commutable aura lieu. Ce mécanisme est indépendant de la polarité de la polarisation. En cas de tension de polarisation élevée, un côté de la barrière descend en dessous de la bande de conduction de l'électrode opposée. Cela réduit efficacement la barrière tunnel à une forme triangulaire de largeur réduite, également connue sous le nom de tunnel Fowler-Nordheim en cas de tension de polarisation élevée, un côté de la barrière descend en dessous de la bande de conduction de l'électrode opposée. Cela réduit efficacement la barrière tunnel à une forme triangulaire de largeur réduite, également connue sous le nom de barrière tunnel de Fowler-Nordheim (FNT).

Outre le mécanisme de la FNT, il existe deux mécanismes supplémentaires qui affectent la largeur de barrière effective : la longueur de l'écran de l'électrode, et l'effet piézoélectrique inverse. La polarisation ferroélectrique est masquée sur une distance finie par les électrodes, ce qui donne un espace et une flexion correspondante de la bande de conduction. La flexion est vers le bas dans cas où la polarisation pointe vers l'interface, et vice versa. Comme la longueur de l'écran diminue avec la densité des porteurs libres, elle est généralement négligeable pour les électrodes métalliques idéales. Cependant, dans le cas d'électrodes semi-conductrices ou d'électrodes de pauvres interfaces, cet effet peut avoir un impact significatif sur le dispositif [77]. L'effet piézoélectrique inverse couple directement le champ électrique appliqué à la largeur de la barrière. Les valeurs des pics en Si:HfO₂ de $d33 = 20pm/V$ [78] et les champs de $300MV/m$ signifient que cet effet reste dans la gamme subpourcentage de l'épaisseur initiale.

2.7 Les Parois des Domaines Ferroélectriques

La commutation ferroélectrique progresse à travers le cristal en étendant ou en diminuant les domaines avec une l'alignement spécifique de polarisation [84]. Les parois des domaines décrivent les interfaces entre ces domaines. Selon l'alignement de la paroi de domaine et les polarisations voisines, différents types de parois de domaine et de mouvement de domaines peuvent être distingués [85]. Le cas le plus simple de commutation d'un ferroélectrique uni axial sans défaut est illustré à la

Fig. A.27. En général, les parois de domaine peuvent être considérées comme des surfaces élastiques en mouvement qui peuvent être ralenties ou bloquées par des défauts chargés à l'intérieur du cristal [86, 87], ce qui conduit à une réduction de la capacité de commutation [85].

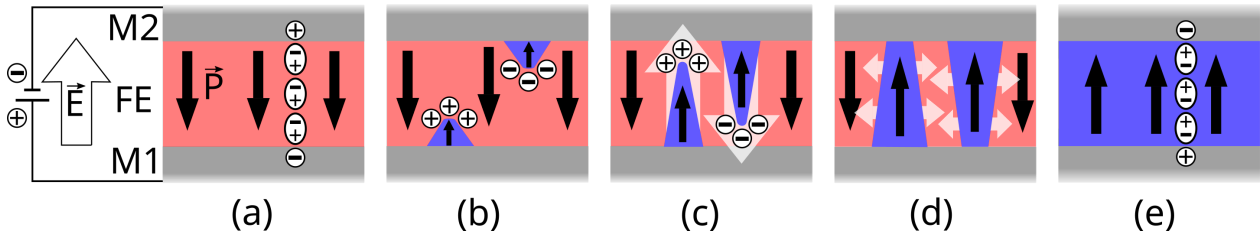


Figure A.27: Processus de commutation de domaine (schéma). Cinq états de commutation de polarisation sont présentés. (a) Au départ, la polarisation ferroélectrique est entièrement descendante. (b) Quand un certain seuil de tension est dépassé, la nucléation d'un domaine inversé est initiée. (c) Poussé par des charges au niveau de la paroi du domaine, il se propage rapidement à travers le domaine. (d) Avec des polarisations principalement orientées parallèlement à la paroi du domaine, un état énergétique beaucoup plus stable est formé, ce qui entraîne une croissance latérale lente. (e) Complètement commuté domaine.

3 Résultats

Dans ce travail, nous examinons trois thèmes principaux : La première section décrit l'impact théorique de l'homogénéité de l'épaisseur de la couche mince sur les propriétés électriques du FTJ. La deuxième section présente le modèle de lacune, qui décrit la génération de lacune d'oxygène et la dégradation du dispositif dans le cadre d'un effet tunnel assisté par pièges (trap-assisted tunneling). Enfin, nous étudions nos FTJ dans une configuration de réseau de neurones et enfin le mécanisme de lacunes et le comportement de commutation qui en découle, et qui conduit la dégradation des dispositifs, en particulier à des tensions élevées. Cela nous permettra de formuler des exigences pour

la fabrication de couches minces. La description du comportement de commutation des neurones définit des paramètres clés, tels que le taux d'apprentissage, la stabilité et la symétrie.

3.1 Les Effets de l'Homogénéité des Couches Minces

Comme l'épaisseur d'une couche mince ferroélectrique appliquée à un dispositif ferroélectrique à jonction de tunnel (FTJ) réduit à plusieurs nanomètres, le comportement de transport des électrons, provoquant deux états de résistance connus sous le nom d'effet d'électrorésistance par effet tunnel (TER), peut être décrit par le mécanisme de l'effet tunnel direct [142]. Afin de décrire les FTJ fabriqués, il est essentiel de quantifier les variations des caractéristiques électriques avec l'homogénéité de la structure fabriquée. Nous présentons les résultats théoriques des effets des variations d'épaisseur dans un dispositif FTJ, en utilisant le système Pt/Hf_xZr_{1-x}O₂/TiN avec une structure Hf_{0.5}Zr_{0.5}O₂ de 3 nm d'épaisseur comme barrière tunnel, et montrer les effets des inhomogénéités d'épaisseur et ce qui en résultent sur la performance du système. Le comportement exponentiel des courants tunnel en fonction de l'épaisseur de la couche est un facteur critique dans des appareils reproductibles. Vous trouverez des détails supplémentaires dans la section 4.1 et dans notre article correspondant [221].

L'approximation WKB à travers une barrière trapézoïdale quantifie la densité de courant J en fonction de l'épaisseur de la barrière d et de la tension U . L'expression analytique [57, 59, 88] peut s'écrire selon l'équation suivante:

$$J(d) = \frac{C}{d^2} e^{Dd} \times \sinh(Ed) \quad (\text{A.10})$$

Avec les paramètres C, D, E

$$C = \frac{4em_e}{9\pi^2\hbar^3} \frac{1}{\alpha^2 \left[\left(\phi_2 - \frac{eU}{2} \right)^{1/2} - \left(\phi_1 + \frac{eU}{2} \right)^{1/2} \right]^2} \quad (\text{A.11a})$$

$$D = \alpha \left[\left(\phi_2 - \frac{eU}{2} \right)^{3/2} - \left(\phi_1 + \frac{eU}{2} \right)^{3/2} \right] \quad (\text{A.11b})$$

$$E = \frac{3}{4} \left| U \alpha \left[\left(\phi_2 - \frac{eU}{2} \right)^{1/2} - \left(\phi_1 + \frac{eU}{2} \right)^{1/2} \right] \right| \quad (\text{A.11c})$$

où α est

$$\alpha = \left(\frac{-4\sqrt{2m_e}}{3\hbar \left[\left(\phi_2 - \frac{eU}{2} \right) - \left(\phi_1 + \frac{eU}{2} \right) \right]} \right) \quad (\text{A.11d})$$

Dans cette équation, ϕ_1 and ϕ_2 sont les barrières potentielles de l'interface trapézoïdale (voir Fig. 4.2), m_e est la masse effective des électrons, U et d sont les tensions de fonctionnement et l'épaisseur, respectivement. On notera que l'équation ne nécessite que 3 paramètres liés au matériau.

En utilisant des approximations pour le petit et le grand régime de tension (voir les équations 4.3a, b), l'effet de la répartition des épaisseurs sur la densité de courant peut être exprimé par les distributions

$$pdf_{Js}(j) = pdf_d \left(-\frac{W_{Js}}{D} \right) \times \left| \frac{W_{Js}}{jD(W_{Js} + 1)} \right| \quad (\text{A.12a})$$

$$pdf_{Jl}(j) = pdf_d \left(-\frac{2W_{Jl}}{D + E} \right) \times \left| \frac{W_{Jl}}{j(D + E)(W_{Jl} + 1)} \right| \quad (\text{A.12b})$$

avec $W_{Js} = W \left(\frac{-CDE}{j} \right)$ et $W_{Jl} = W \left(\frac{-\sqrt{2}C(D+E)}{4\sqrt{j}} \right)$, où W est la branche principale de la fonction Lambert W [184]. En supposant que la probabilité de distribution de l'épaisseur normale pdf_d pour les petits écarts σ autour de l'épaisseur moyenne d_0 , la distribution de la densité de courant est calculée à partir de l'équation A.12(a) et A.12(b). Les deux sont présentés dans la Fig. 4.5(a),

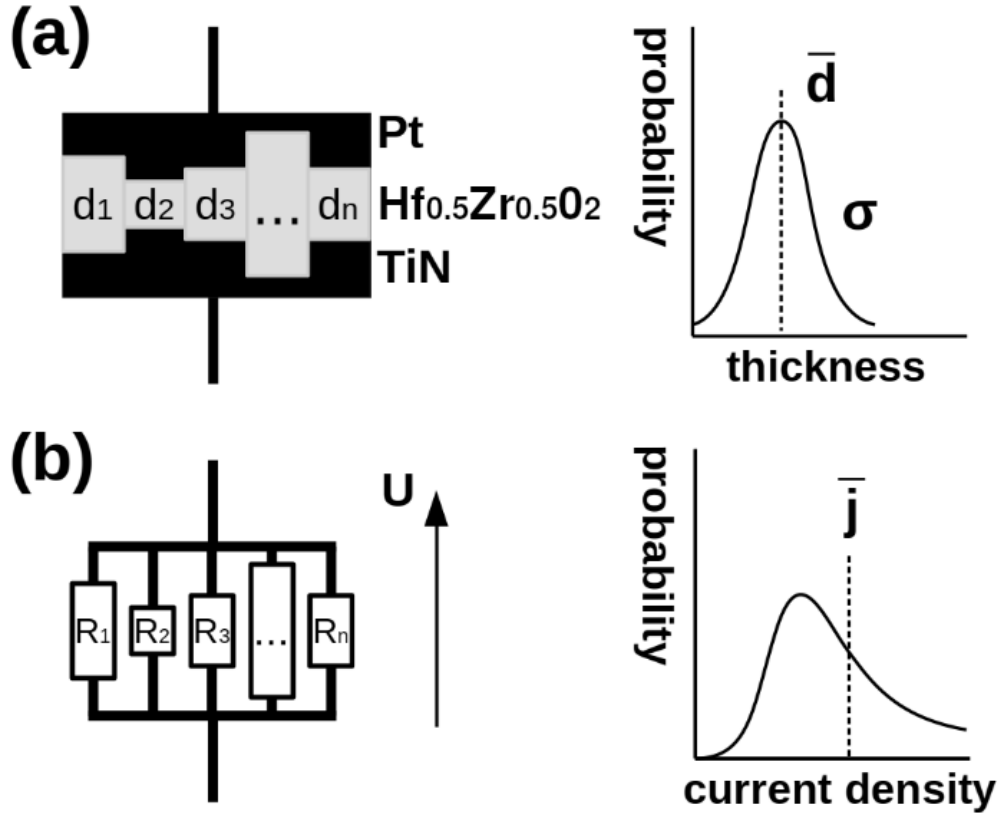


Figure A.28: Modèle de conductivité de $\text{Hf}_x\text{Zr}_{1-x}\text{O}_2$. L'épaisseur locale de la couche résulte en une densité de courant locale à tension U . (a) Représentation de la rugosité comme une distribution des épaisseurs. (b) Modèle de résistance parallèle donnant la distribution de la densité de courant pour une tension fixe.

(b) à des tensions correspondant à leur champ d'application.

Les résultats de j_{LRS} et j_{HRS} pour la LRS et la HRS sont illustrés dans la Fig. A.29(a) sur l'écart standard de l'épaisseur σ . Il montre que les densités actuelles augmentent de manière exponentielle avec écart standard de l'épaisseur σ . L'épaisseur du FTJ doit donc être extrêmement homogène pour permettre des conductances reproductibles. Cette exigence se produit lorsque les grains fonctionnent comme un réseau de résistances parallèle. En conséquence, la résistance du réseau est dominée par de plus petites résistances parallèles.

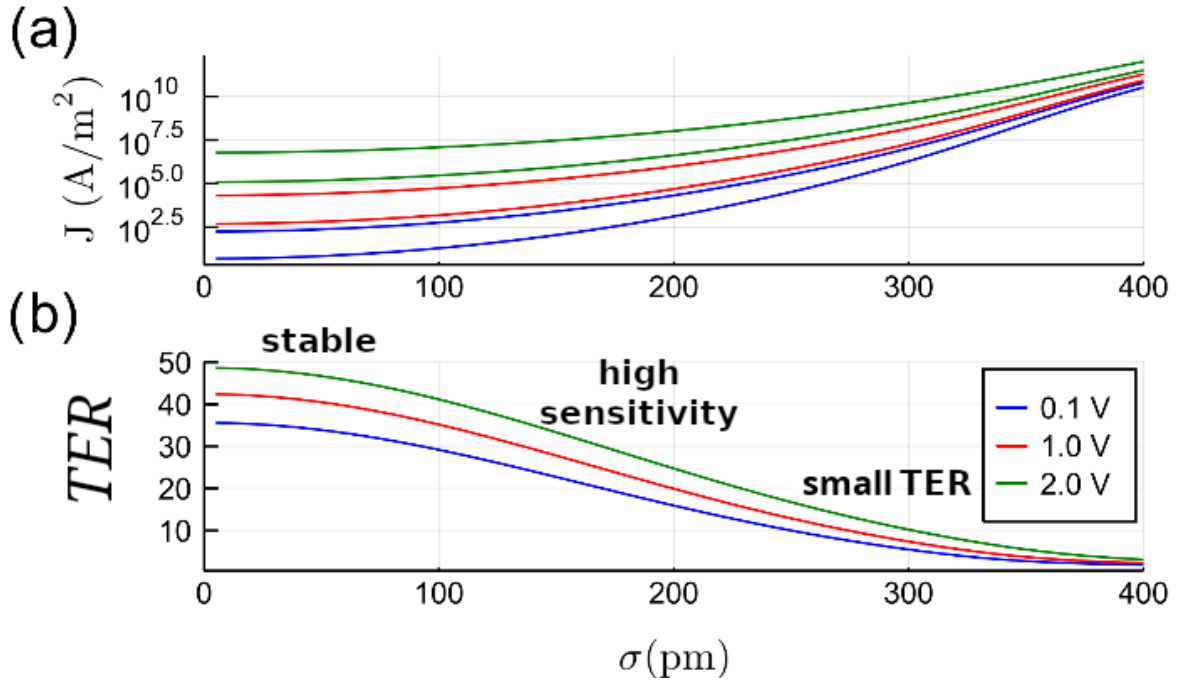


Figure A.29: (a) Densité de courant moyenne de l'état LRS et de l'état HRS pour trois tensions à une épaisseur de $d_0 = 3\text{nm}$. (b) Rapport moyen du TER sur le type d'écart. Le rapport est stable pour les petits écarts et tombe rapidement au-dessus lorsque σ dépasse $\approx 0.1\text{nm}$. Le rapport TER suit une décroissance de forme gaussienne de commutation résistive avec la variation croissante de l'épaisseur. On peut constater que l'inhomogénéité de l'épaisseur a un impact significatif sur le rapport TER.

En résumé, nous obtenons une estimation analytique simple de l'impact de l'homogénéité de l'épaisseur sur les résistivités des états LRS et HRS des jonctions tunnel ferroélectriques en nous basant sur le modèle WKB. Ceci est illustré par une hétérostructure TiN/Hf_{0.5}Zr_{0.5}O₂/Pt. Une augmentation exponentielle de la conductance et une probabilité accrue de panne électrique sont quantitativement prédictes. Nous calculons une dégradation du ratio TER avec des inhomogénéités de surface croissante, qui est la clé d'une récupération fiable des informations. La grande sensibilité des courants tunnel par rapport à l'épaisseur rend cet effet critique lors de l'étude de la stabilité du dispositif. Cela signifie également que la majeure partie du courant sera transférée par une petite fraction de domaine ferroélectrique. Grands écarts statistiques entre les différents FTJ doivent être pris en considération lors de la planification de paramètres des appareils individuels et les circuits globaux.

3.2 Mécanisme de Valence et Endurance

Dans cette section, nous étudions le fonctionnement du FTJ à des tensions élevées, en exposant un autre mécanisme de conduction qui s'avère être responsable de la dégradation et de dysfonctionnements du dispositif. Plus de détails, sont présentés dans la section 4.2. Contrairement à l'isolant idéal discuté précédemment, nous pouvons également observer une composante du cycle qui dépende du mécanisme de conduction à des tensions élevées. Ce mécanisme est identifié dans la littérature [123–126] par des réactions électrochimiques formées et qui annihilent les lacunes d'oxygène aux interfaces métal/isolant. Ce phénomène est utilisé dans les dispositifs ReRAM à base d'oxyde métallique, la commutation résistive étant généralement basée sur la dérive des lacunes d'oxygène. Ces lacunes peuvent être produites soit lors d'un cycle d'électroformation ou sont déjà dans la structure de l'isolant [127–130].

La différence de potentiel redox entre les électrodes détermine la symétrie du comportement de commutation de l'appareil. La réduction dans l'isolant selon la notation de Kröger-Vink [222] commence par la dislocation d'un atome d'oxygène à l'interface [223] avec une tension positive appliquée de l'extérieur $U > 0$



où $\frac{1}{2}\text{O}_2$ désigne l'oxygène provenant de l'isolant, physiosorbé au grain de l'électrode. Une fois que les lacunes se forment près de l'interface, ils forment une voie de migration pour l'oxygène plus profond, permettant à la réaction de se poursuivre. Avec une électrode métallique inerte et imperméable à la diffusion d'oxygène, l'oxygène s'accumule à l'interface [224]. Comme les métaux typiques des électrodes supérieures, tels que le Pt ou l'Au, sont relativement tendres et minces, cette recombinaison peut former des vides, détachant localement l'interface [131]. De là, une perte irréversible d'oxygène dans l'isolant et une dégradation permanente de système en est la conséquence. Dans le cas extrême de ce processus a été observé dans des FTJ testés à la fatigue, conduisant finalement à la délamination de l'électrode (Fig. A.19).

Pour déterminer l'évolution des pièges et les courants de fuite qui en résultent, nous utilisons le modèle PATT (phononassisted tunneling between traps) initialement proposé par Makram-Ebeid and Lannoo [138]. Il a été démontré que ce modèle de transport décrit de manière adéquate le comportement électrique dans le $\text{Hf}_{0.5}\text{Zr}_{0.5}\text{O}_2$ ferroélectrique et non ferroélectrique [68–72]. Le transport de charges peut être décrit par le modèle Shockley-Read-Hall [139, 140] (voir section 2.6.2). Dans les profonds pièges et pour une densité de pièges suffisante, le mécanisme de transport par sauts peut être exprimé comme suit [68]

$$\left(\frac{\partial n_t}{\partial t} \right)_{tun} = -a\nabla(n_t(1 - n_t/N)P) = -\frac{1}{q}\nabla J \quad (\text{A.14})$$

avec la concentration d'électrons dans la bande de conduction et pièges n , n_t et v la vitesse des électrons, et P_{ion} , P_{tun} le taux d'ionisation des pièges et le taux de l'effet tunnel interpièges. La section de capture du piége, la densité de piége et le potentiel de tension sont respectivement σ , N et U . La distance moyenne du piége est $a = 1/\sqrt[3]{N}$, et F est le champ électrique. Les conditions aux limites de cette équation différentielle partielle sont données par les taux de réaction de Eq. A.13. Ils sont décrits par les fonctions d'Arrhenius (équation 4.15). En utilisant la densité d'inoccupation décrite par l'équation A.14, la densité de courant électrique peut être calculée par le modèle PATT (équation A.14). Le paramètre P est la vitesse de transmission entre les pièges, qui est donnée par [70, 121]:

$$P = \int_{W>0} \frac{\hbar W}{m^* a^2 k T Q_0} \exp\left(-\frac{(Q - Q_0)^2 - (Q - qFa/Q_0)^2}{2kT}\right) - \frac{4}{3} \frac{\sqrt{2m^*}(W^{3/2} - (W - qFa)^{3/2})}{qF\hbar} dQ \quad (\text{A.15a})$$

$$W = Q_0(Q - Q_0) + W_{opt} \quad (\text{A.15b})$$

$$Q_0 = \sqrt{2(W_{opt} - W_t)} \quad (\text{A.15c})$$

m^* st la masse effective du porteur de charge, T est la température, Q est la coordonnée de configuration d'un système électron-phonon piégé, F est le champ électrique local, $-W$ est l'énergie de l'électron piégé en dessous de la bande de conduction, et Q_0 est la coordonnée de configuration qui quantifie l'interaction électron-phonon [121].

Dans notre dispositif expérimental, nous étudions des FTJs de 3.5 nm TiN/Hf_{0.5}Zr_{0.5}O₂/Au et les exposons à des cycles répétés d'impulsions, comme le montre la Fig. A.30. Nous ajustons le modèle de dérive-diffusion transitoire des lacunes à des mesures périodiques de tension croissante, comme le montre la Fig. A.31. La série complète de mesures est présentée dans la section 4.2. Un résultat exemplaire pour la série 0.7 V-2.5 V series est présenté dans la Fig. A.32 (la courbe bleue).

En utilisant le modèle de dérive-diffusion des lacunes avec la vitesse de réaction à l'interface comme conditions limites, nous obtenons la distribution des lacunes au sein de l'isolant. À partir de cette distribution, le PATT est résolu pour calculer le courant. Comme le modèle PATT contient des paramètres connus pour Hf_{0.5}Zr_{0.5}O₂ [70, 121], nous ajustons les paramètres de l'équation différentielle partielle à la mesure. La prédition du modèle est illustrée dans la Fig. A.32 (la courbe rouge). L'évolution résultante correspondant à la population des lacunes est présentée à la Fig. A.31.

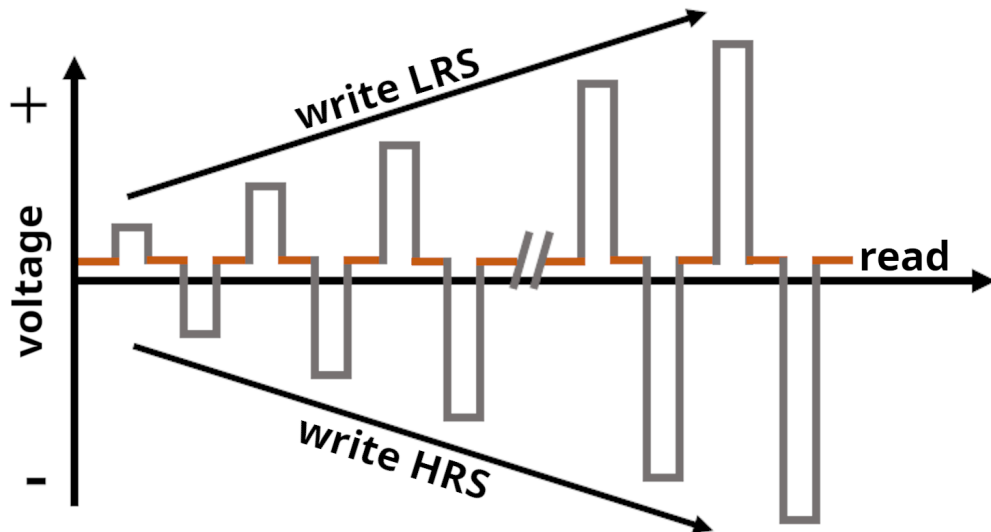


Figure A.30: Séquence d'alternance des impulsions d'écriture et de lecture. La tension des impulsions d'écriture augmente successivement. Après chaque impulsion d'écriture, le courant est mesuré sur une impulsion de lecture constante (lignes rouges). Les deux impulsions de lecture et d'écriture ont une longueur fixe de 100 ms.

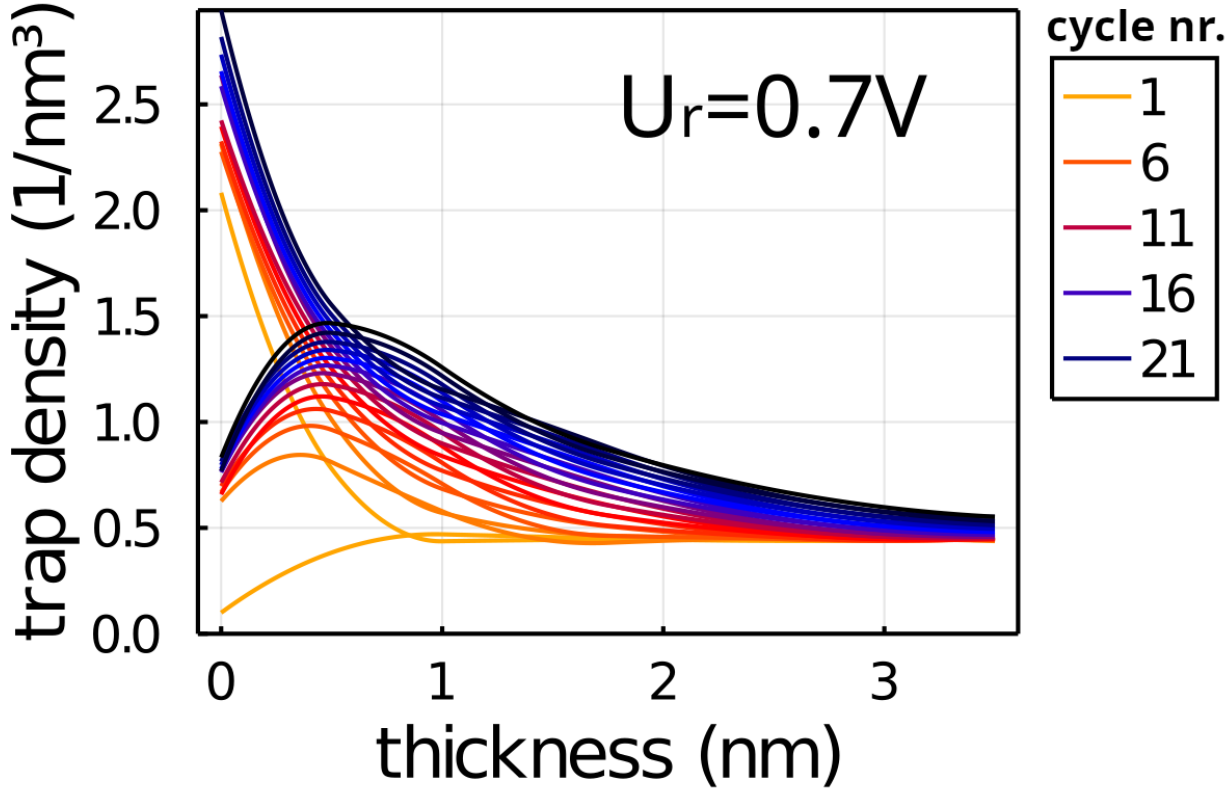


Figure A.31: Modèle FDM de convection-diffusion des lacunes pour la séquence d’impulsions, adapté à la séquence d’impulsions à $U_r = 0.7V$. Le côté gauche est l’interface $\text{Hf}_{0.5}\text{Zr}_{0.5}\text{O}_2/\text{Au}$ interface, tandis que le côté droit est l’électrode TiN qui supposée être inerte.

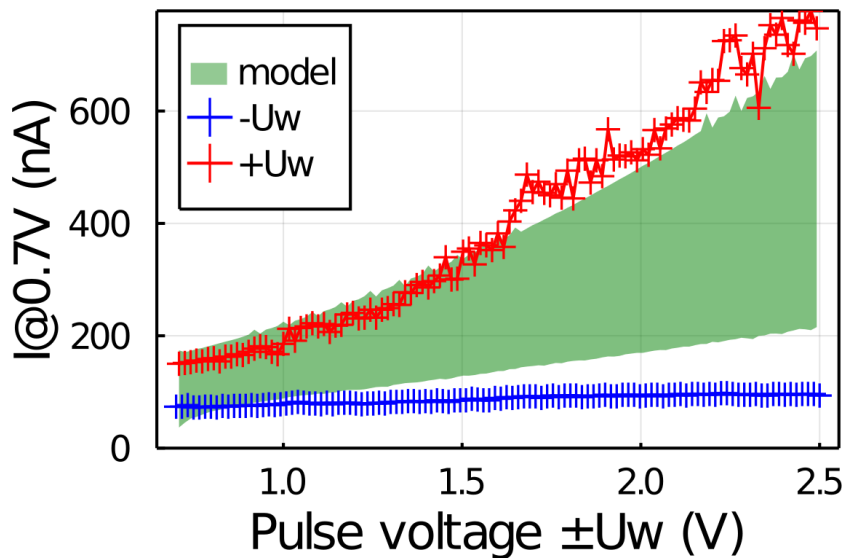


Figure A.32: Densité de courant du modèle de commutation de valence (rouge) comparée aux valeurs mesurées de la séquence d’impulsions à une tension de lecture de $U_r = 0.7V$ (Fig. 4.10).

Le modèle est capable de reproduire l'évolution temporelle des courants mesurés avec des paramètres des modèles physiques. Les courants de l'état HRS devraient augmenter plus rapidement que les courants mesurés, ce qui signifie que l'état LRS est prédit avec précision. Les écarts entre le modèle et la mesure peuvent être attribués aux assumptions du modèle, telles que l'approximation 1D. La densité moyenne prévue des lacunes d'oxygène est d'environ 0.5nm^{-3} . Il s'agit d'une lacune pour 8 cellules unitaires, ce qui est un résultat plausible.

3.3 Jonctions Tunnels Ferroélectriques pour les Dispositifs Neuromorphiques

Dans cette section, nous évaluons les propriétés du FTJ en ce qui concerne sa capacité à émuler les synapses dans un réseau neuronal. L'influence du potentiel d'action sur le taux d'apprentissage est étudiée, et un modèle basé sur la commutation limitée par la nucléation (NLS) est utilisé pour décrire expérimentalement le changement de la résistivité observé.

Alors que les algorithmes d'apprentissage machine sont de plus en plus élaborés, leurs réseaux neuronaux artificiels sous-jacents reposent généralement sur l'architecture informatique binaire de von Neumann [225]. Par contre, les réseaux neuronaux des matériaux offrent une série d'avantages en raison de leur étroite ressemblance à leurs homologues biologiques : Lorsqu'ils sont intégrés dans un système de neurones de pointe, la mémoire résistive peut modéliser les synapses biologiques par commutation progressive, ce qui permet d'unifier mémoire et les opérations logiques [226]. Le processus d'apprentissage dans un système neuronal biologique peut être compris en termes de la loi de Hebb: lorsque deux neurones s'allument en même temps, leurs potentiels de tension chevauchent dans le temps, en augmentant ou en diminuant leur connexion à la synapse, en fonction de leur ordre temporel. Ceci peut aussi référer à "potentialisation de long terme (LTP)" et à "une dépression de à long terme (LTD)" [227]. Le processus comporte des modifications à court et à long terme du système, comme l'activation rapide de récepteurs supplémentaires, et des processus plus lents tels que les changements dans la synthèse des protéines et l'expression des gènes, ainsi que la capacité pour développer de nouvelles connexions entre les axones et les dendrites [197].

Les tests de la plasticité fonction du temps d'occurrence des impulsions "Spike-timing-dependent plasticity (STDP)" sont une technique de choix pour évaluer la capacité du matériau à imiter la plasticité synaptique [198, 199]. Le STDP imite l'activité neuronale du cerveau, où deux neurones stimulent la synapse qui les interconnecte en appliquant une impulsion de tension [196, 200, 201]. Cette impulsion réfère au potentiel d'action, et le décalage horaire entre les deux potentiels d'action définit le renforcement ou l'affaiblissement de la synapse, ce qui décrit comme un dispositif de commutation résistif. Les mesures du STDP révèlent directement le taux d'apprentissage de la synapse, qui est un paramètre important pour la formation d'une ANN et, et élargie l'influence de son algorithme de formation. Il a été démontré que les dispositifs de mémoire résistive peuvent imiter un comportement synaptique similaire [176, 195, 196]. Les composantes à court et à long terme de commutation ferroélectrique (Fig. A.27) font de la jonction tunnel de $\text{Hf}_{0.5}\text{Zr}_{0.5}\text{O}_2$ un candidat fiable pour la construction d'analogues artificiels aux synapses (voir Fig. A.33).

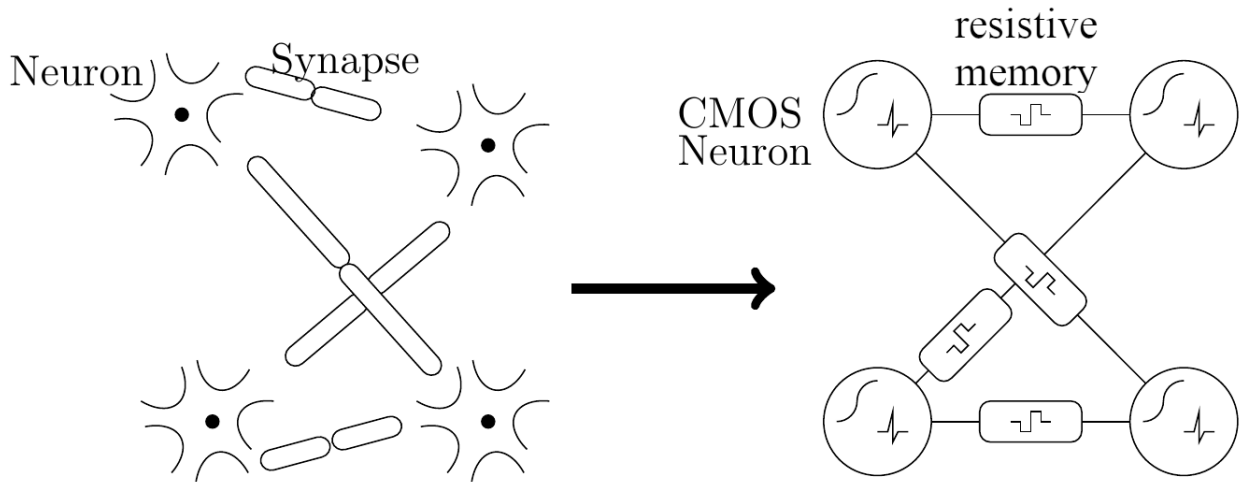


Figure A.33: Synapses et neurones. Représentation d'un réseau de neurones biologiques (à gauche), et sa reconstruction artificielle (à droite)[228]. Les neurones génèrent des pics de potentiel électrique. En fonction de la superposition temporelle des pics d'entrée au niveau de la mémoire résistive, sa résistance augmente ou diminue.

Dans le cadre d'un réseau de neurones à impulsions "spiking neural network (SNN)", la plasticité synaptique, c'est-à-dire le changement de la résistance de la synapse, dépend du décalage temporel Δt entre l'action pré et post-synaptique [215] comme le montre la Fig. 4.14. La mesure clé dans cette configuration est la réponse de résistivité $\frac{\Delta R}{R_0}$ pour une superposition de deux potentiels d'action

avec décalage temporel Δt . Nous définissons

$$\frac{\Delta R}{R_0}(\Delta t) = \frac{R_{after}(\Delta t) - R_{before}(\Delta t)}{\min\{R_{before}(\Delta t), R_{after}(\Delta t)\}} \quad (\text{A.16})$$

où R_{after} and R_{before} sont les valeurs de résistance de la synapse mesurées après et avant l'application la superposition des potentiels d'action, respectivement. Le dénominateur utilise la valeur minimale de R_{after} et R_{before} comme le facteur d'échelle.

Pour quantifier et pouvoir comparer les mesures individuelles du STDP entre elles, les fonctions STDP $\Delta R/R_0(\Delta t)$ sont dotées d'un modèle exponentiel

$$\frac{\Delta R}{R_0}(\Delta t) = A_+ \exp(-\Delta t/\tau_+) \quad \text{for } \Delta t > 0 \quad (\text{A.17a})$$

$$\frac{\Delta R}{R_0}(\Delta t) = A_- \exp(-\Delta t/\tau_-) \quad \text{for } \Delta t < 0 \quad (\text{A.17b})$$

avec les deux facteurs d'échelle linéaires A_+ , A_- et les deux temps caractéristiques τ_+ , τ_- .

Les mesures STDP ont été effectuées avec un testeur de mémoire résistive ArCOne (ArC Instruments), qui est utilisé pour créer deux pics à décroissance exponentielle avec un décalage temporel relatif Δt . Les jonctions tunnel étudiées sont des échantillons de TiN/Hf_{0.5}Zr_{0.5}O₂/Pt avec une largeur de barrière de 2.5 nm.

Pendant les mesures, la jonction tunnel ferroélectrique est commutée par une série de STDP pour les décalages positifs et négatifs de Δt entre 20 et 320 μs . Cette mesure est répétée pour des impulsions d'amplitudes entre 0.8 V et 1.1 V, ce qui donne effectivement une impulsion presque rectangulaire pour un petit Δt , et un pic de tension qui diminue de façon exponentielle avec l'augmentation de Δt . Avant et après chaque impulsion, la résistivité est mesurée à 0.2 V. L'orientation des grains estimée par l'équation A.18 est présentée à la Fig. A.35 (zone verte).

La disposition des grains peut être considérée comme approximativement parallèle [179] en raison des diamètres de grains qui sont généralement aussi grands que l'épaisseur de la couche [15]. Ainsi, la structure est modélisée comme un réseau de résistance parallèle où le courant total est donné par la somme des courants sur les grains individuels. Le mode de l'effet tunnel direct 1D est utilisé pour

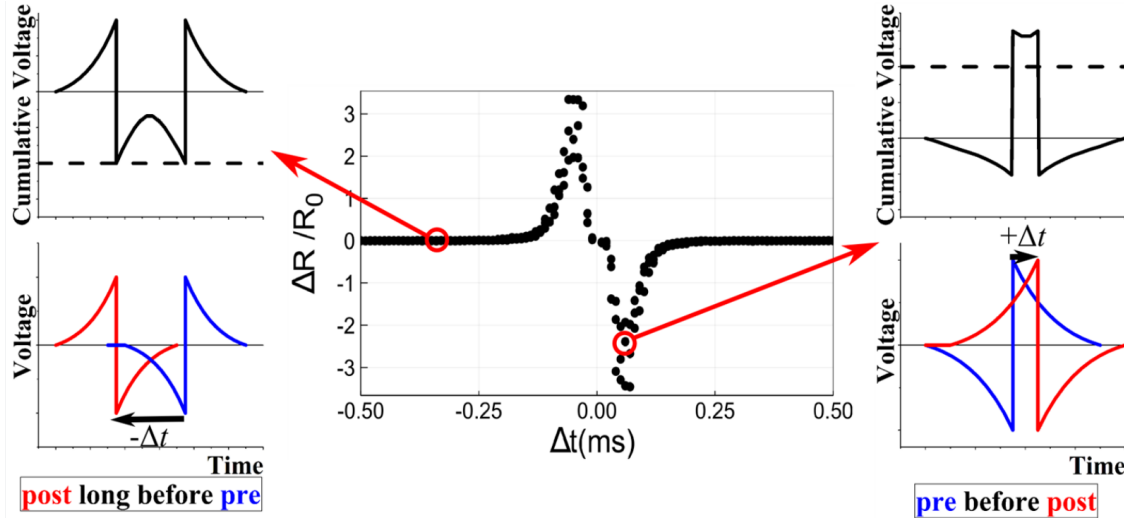


Figure A.34: Schéma de la différence de la variable temps Δt entre le potentiel d'action pré- et post-synaptique créer une plasticité synaptique dans le STDP. Le diagramme de dispersion montre le changement de résistance du FTJ en fonction de Δt (fonction STDP). Pour un petit Δt positif, le chevauchement des deux actions entraîne une diminution de la résistance. Les courbes rouge et bleue représentent respectivement le potentiel d'action pré et post-synaptique. La courbe noire est la superposition des deux potentiels d'action pour un Δt donné. Pour un Δt largement négatif, la tension résultante est trop faible pour déclencher un changement de résistance.

modéliser la densité de courant [63]. Les densités de courant des états LRS et HRS sont calculées à partir des fonctions tunnel trapézoïdales. La combinaison linéaire avec la fraction granulaire g dans l'état LRS se lit alors

$$j(g) = g j_{LRS}(U, d) + (1 - g) j_{HRS}(U, d) \quad (\text{A.18})$$

où $j(g)$ est la densité de courant d'une fraction g des grains orientée vers l'état faible résistance. Les densités de courant actuelles j_{LRS} et j_{HRS} sont extraites des mesures expérimentales, en utilisant un préfacteur commun. Ainsi, la résistivité est donnée par

$$R(g) = \frac{U}{A j(g)} \quad (\text{A.19})$$

où A est la surface du FTJ, et $U = 200$ mV est la tension appliquée.

Nous utilisons un modèle NLS pour décrire les résultats expérimentaux dans la gamme de tension observée. Ce modèle est une extension du modèle classique Kolmogorov-Avrami-Ishibashi (KAI), qui décrit la dynamique de commutation ferroélectrique dans les couches minces polycristallines

[202]. Comme le précisent Li et al. [119], le modèle NLS est applicable au $\text{Hf}_{0.5}\text{Zr}_{0.5}\text{O}_2$ ferroélectrique et fournit une expression analytique pour le l'inversion de la polarisation en fonction du champ et du temps. Avec la polarisation initiale entièrement polarisée en une direction $\Delta P = 0$ at $t = 0$), la commutation est décrite par [119]

$$\Delta P(t) = P_s \operatorname{erfc} \left\{ \left[\frac{E_a}{E_f(t) [\log(t/\tau_0)]^{1/n}} - 1 \right] / \sqrt{2}\sigma \right\} \quad (\text{A.20})$$

où $E_f(t)$ est le champ électrique appliqué à l'extérieur, P_s , E_a , τ_0 , n , et σ sont des paramètres du matériau, $\operatorname{erfc}(x)$ est la fonction d'erreur complémentaire. Alors que cette équation décrit l'inversion de polarisation à partir de $\Delta P(t) = 0$ au temps $t = 0$, our devices possess an intrinsic bias that leaves an initial non-zero mean polarization. nos appareils possèdent un biais intrinsèque qui laisse une polarisation initiale moyenne non nulle. Par conséquent, nous résolvons d'abord l'équation pour obtenir le temps initial t_{init} correspondant à la polarisation initiale de notre appareil. Ensuite, les impulsions STPD peuvent être traitées comme un rectangle pour un petit Δt , et l'évolution de la polarisation est obtenue en résolvant l'équation A.20 avec un incrément de temps Δt .

Comme le comportement de commutation du dispositif est asymétrique, la constante de temps caractéristique τ_0 , l'activation du champ E_a , la déviation standard σ de E/E_f , et l'exposant empirique n sont déterminés individuellement pour les deux orientations. L'orientation moyenne du grain est déterminée par la polarisation $\Delta P = 2P_s$. La comparaison entre le modèle et les résultats expérimentaux est présentée dans la Fig. A.35. Dans cette figure, le FTJ commence à un Δt de 20 μs pour l'état LRS. L'appareil passe ensuite de l'état LRS à l'état HRS par $+\Delta t$ et $-\Delta t$ pour chaque incrément de temps. La partie inférieure de chaque courbe correspond donc à au HRS, tandis que la partie supérieure correspond au LRS.

En commençant par un petit Δt , le passage au HRS maximum prend environ 60 μs . Après le passage au HRS, l'appareil passe au LRS initial, ce qui permet d'aplatir la partie supérieure des courbes. Pour Δt au-dessus de 150 μs et des amplitudes maximales du potentiel d'action de 1.0 V et 1.1 V, la quantité de grains échangés dans le cadre du SRL augmente. Cela suggère qu'il faut plus de $+\Delta t$ pour la commutation des domaines restants dans le LRS. La commutation rapide observée pour le faible $+\Delta t$ s'explique par la formation de noyaux à polarisation inversée, tandis que le mécanisme

plus lent (Δt au-dessus de 150 μs) est un l'expansion successive des parois de domaine existant qui se produit lorsque le champ électrique est trop faible pour induire la nucléation [203]. L'asymétrie pourrait être due à la structure électronique asymétrique des interfaces, de différentes contraintes interfaciales ou des contributions des défauts chargés.

En utilisant le modèle décrit ci-dessus, les courbes STDP sont reproduites, comme l'illustre la Fig. 4.20a. Pour ce faire, les valeurs de résistance obtenues à partir de l'orientation des grains calculée sont tracées en fonction de Δt . La Fig. 4.20a montré un comportement similaire à celui du STDP expérimental, où la résistance de FTJ varie en fonction de Δt . Ces courbes modélisées ont été ajustées à l'aide de l'équation A.17 pour étudier l'effet de l'amplitude du potentiel d'action sur l'échelle et les paramètres exponentiels comme le montre la Fig. 4.20b,c.

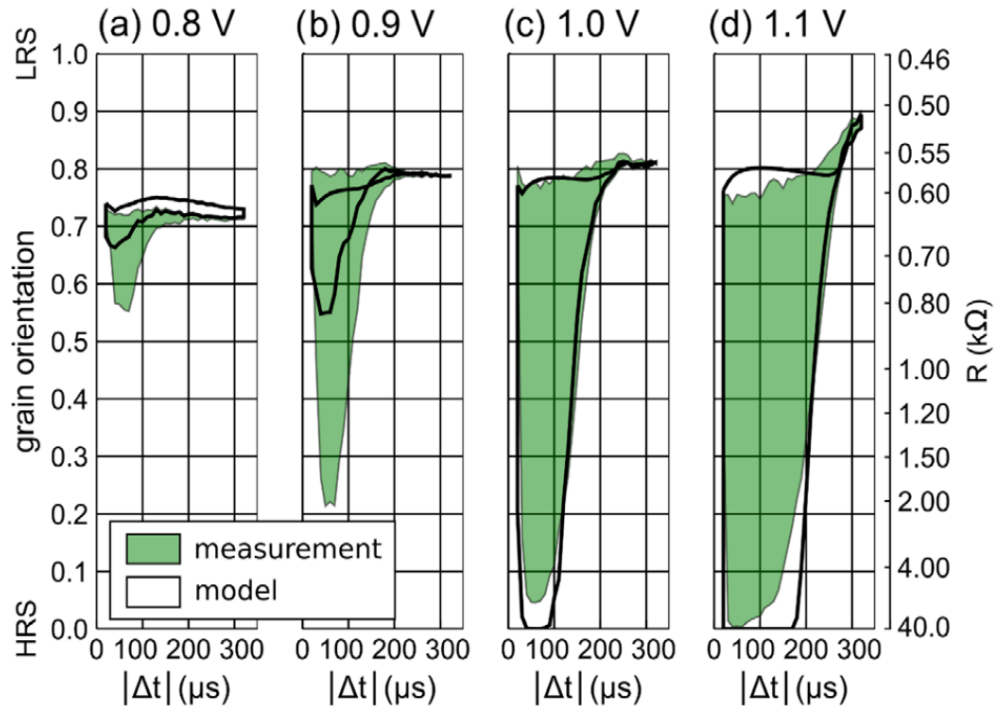


Figure A.35: Commutation résistive pour des impulsions STDP variables avec des amplitudes a) 0.8 V b) 0.9 V c) 1.0 V, et d) 1.1 V et décalages Δt . La zone verte correspond à la commutation de l'orientation du grain induite par deux pics qui se chevauchent avec Δt dans les orientations positives et négatives. La ligne noire montre le modèle de prédiction en commençant par la valeur mesurée.

Nous concluons que le taux d'apprentissage des synapses est défini par l'amplitude de tension des potentiels d'action. Conformément à nos résultats expérimentaux (figure 4.17), le paramètre

d'échelle augmente exponentiellement avec l'amplitude maximale du potentiel d'action, tandis que les paramètres exponentiels restent constants. Entre 0.7 V et 1.0 V, les paramètres d'échelle augmentent de 0.01 à 100. Le pic de 1.1 V peut indiquer le début de la commutation de valence, puisque le LRS commence à dériver de manière significative. Ce résultat expérimental est supporté par un modèle du comportement de commutation graduelle, qui repose sur un changement progressif de la polarisation des grains du $\text{Hf}_{0.5}\text{Zr}_{0.5}\text{O}_2$. Ce modèle de nucléation de commutation limité (NLS) [119, 202] confirme nos conclusions expérimentales.

4 Résumé et Conclusions

Alors que les FTJs ont longtemps été discutés théoriquement, ils n'ont été démontrés expérimentalement qu'en 2009 [9]. Avec la découverte en 2011 d'une phase ferroélectrique dans le HfO_2 [7], un matériau avec des caractéristiques uniques est devenu disponible. Bien que les recherches sur ce matériau soient toujours en cours, son évolutivité ainsi que sa compatibilité CMOS font du $\text{Hf}_{0.5}\text{Zr}_{0.5}\text{O}_2$ un excellent candidat pour les systèmes FTJ. Nous nous appuyons sur les travaux antérieurs Vargas [180], qui a développé un modèle quantitatif pour le diagramme de bande qui a depuis été soutenu par Yoon et al. [59].

Tout d'abord, nous avons commencé notre étude des propriétés de transport de charges électroniques dans les FTJs. Sur la base de l'équation WKB, nous avons développé un modèle analytique qui estime l'effet important de l'épaisseur de la couche sur les performances électriques du matériau [175]. L'expression analytique simple décrit l'impact des inhomogénéités d'épaisseur sur la conductivité électrique, les rapports de commutation TER qui sont essentiels pour la récupération des informations, et la probabilité de panne électrique. De là découlent les exigences de fabrication pour une conception reproductible. Les résultats ont été déterminés en étudiant les hétérostructures $\text{TiN}/\text{Hf}_{0.5}\text{Zr}_{0.5}\text{O}_2/\text{Pt}$. La nature exponentielle des courants tunnel par rapport à l'épaisseur rend cet effet essentiel lors de la conception des FTJs et l'étude de la stabilité, où une réduction de l'épaisseur par une seule cellule unitaire peut augmenter la conductance par 3 ordres de magnitude.

Dans la deuxième partie, nous avons étudié la commutation à des champs élevés, où nous avons constaté que la commutation TER est remplacée par un processus différent. La dérive de la résistance sur les cycles de commutation est conforme au mécanisme de commutation de valence. Nous avons développé un modèle d'éléments finis qui décrit la formation des lacunes d'oxygène aux électrodes et la diffusion subséquente dans le domaine. Couplé au modèle PATT (phonon-assisted tunneling between traps) [122, 194] et les équations de Shockley-Read-Hall [139, 140], nous avons réussi à obtenir une description modèle en bon accord avec nos résultats expérimentaux.

Notre troisième étude est consacrée à l'application des FTJs dans un réseau de neurones à impulsions [176]. Les caractéristiques de commutation graduelles rendent le FTJ fiable pour des applications multiniveaux ou analogiques [11, 12] et un candidat intéressant pour le réseau de neurones à impulsions [204]. Dans notre configuration, le FTJ TiN/Hf_{0.5}Zr_{0.5}O₂/Pt agit comme une synapse artificielle. Les mesures de la plasticité fonction du temps d'occurrence des impulsions (STDP) [196, 200, 201] sont effectuées en variant les amplitudes et les largeurs du potentiel d'action. Une analyse quantitative des fonctions STDP résultantes montre que le taux d'apprentissage de la synapse dépend principalement de l'amplitude du potentiel d'action. Nous avons démontré que le modèle de commutation limitée par la nucléation (NLS) model [119, 202] est en bon accord avec nos résultats expérimentaux.